

Università degli Studi di Napoli “Federico II”

SCUOLA POLITECNICA E DELLE SCIENZE DI BASE
Doctorate Programme in Industrial Engineering, XXXI Cycle

*Dissertation presented in partial fulfillment of the requirements for the
degree of Doctor of Philosophy in Industrial Engineering*

Preliminary and Advanced Structural Design of a Three-Modal Camber Morphing Wing Flap for Large Civil Aircraft Applications

Tutors:

Prof. Ing. Francesco Marulo

Prof. Ing. Leonardo Lecce

Prof. Ing. Rosario Pecora

Prof. Ing. Francesco Amoroso

Candidate:

Francesco Rea

December 2018

Ai miei genitori e a mio fratello,

Abstract

Researchers and engineers design modern aircraft wings to reach high levels of efficiency with the main outcome of weight saving and airplane lift-to-drag ratio increasing. Future commercial aircraft need to be mission-adaptive to improve their operational efficiency.

Within the framework of Clean Sky 2 Airgreen 2 (REG-IADP) European research project, a novel multifunctional morphing flap technology was investigated to improve the aerodynamic performances of the next Turboprop regional aircraft (90 passengers) along its flight mission. The proposed true-scale device (5 meters span with a mean chord of 0.6 meters) is conceived to replace and enhance conventional Fowler flap with new functionalities. Three different functions were enabled: overall airfoil camber morphing up to $+28^\circ$ (mode 1), $\pm 10^\circ$ (upwards/downwards) deflections of the flap tip segment (mode 2), flap tip twist of $\pm 5^\circ$ along the outer flap span (mode 3). Morphing mode 1 is supposed to be activated during take-off and landing only to enhance aircraft high-lift performances and steeper initial climb and descent. Thanks to this function, more airfoil shapes are available at each flap setting and therefore a dramatic simplification of the flap deployment system may be implemented. Morphing modes 2 and 3 are enabled in cruise and off-design flight conditions to improve wing aerodynamic efficiency. The proposed structural concept consists of a multi-box arrangement activated by segmented ribs with embedded inner mechanisms to realize the transition from the baseline configuration to different target aero-shapes while withstanding the aerodynamic loads.

Lightweight and compact actuating leverages driven by electromechanical motors were properly integrated to comply with demanding requirements for real aircraft implementation: minimum actuating torque, minimum number of motors, reduced weight, and available design space. The methodology for the kinematic design of the inner mechanisms is based on a building block approach where the instant centres analysis tool is used to preliminary select the locations of the hinges' leverages.

The structural layout of an Adaptive Twist composite Tab was considered as a promising concept to balance the conflicting requirements between load-carrying capability and shape adaptivity in morphing lightweight structures.

Finally, the embedded system functionality of the actuation system coupled with the structural skeleton is fully investigated by means of detailed finite element simulations. Results of actuation system performances, and aeroelastic deformations considering limit aerodynamic loads demonstrate the potential of the proposed structural concepts to be energy efficient, and lightweight for real aircraft implementation.

Contents

1	Introduction	18
1.1	General Overview	18
1.2	Research Background	19
1.3	Research Objective	20
1.4	Research Method	21
2	Morphing Structures: State of research for Large Aircraft applications	22
2.1	Introduction	22
2.2	Components of a Wing Morphing Structural System	23
2.2.1	Structural Skeleton	23
2.2.2	Actuation Systems	24
2.3	NASA Research & the Mission Adaptive Wing Project	25
2.3.1	Other NASA Studies	28
2.4	DLR Research & the <i>Adaptiver Flügel</i> (ADIF) Project	30
2.5	Recent Research Projects in Europe	32
2.5.1	Smart Intelligent Aircraft Structures (SARISTU)	33
2.6	Evolution of High-Lift Systems on Large Commercial Airplane	35
2.7	Beyond the State of the Art	37
3	Clean Sky 1 Research Project	39
3.1	Green Regional Aircraft (GRA-ITD)	39
3.2	Preliminary Studies on Morphing Flap Feasibility (GRA Phase 1)	41
3.3	Morphing Inner-Section Flap (GRA Phase 2)	44
3.3.1	Morphing Architecture	45
3.3.2	Finite Element model of the full-scale prototype	50
3.3.3	Limit Load reproduced in the Ground Static Test	52
3.3.4	Static Analysis	53
3.3.5	Overview of the Experimental Tests Performed	57

3.3.6	Functionality Test	57
3.3.7	Ground Static Test	58
3.4	Conclusions	63
4	Clean Sky 2 Research Project	64
4.1	Regional Integrated Aircraft Development Platform (REG-IADP)	64
4.1.1	The Adaptive Electric Wing (WP 2.1)	65
4.2	Multifunctional Morphing Flap (WP 2.1.2)	66
4.2.1	Mission Requirements and Requested Performances	68
4.2.2	Aerodynamic Design Load Conditions	70
5	Three Modal Morphing Fowler Flap (3MMF)	74
5.1	Working Principles and Design Approach	74
5.2	The Smart Rib Concept	75
5.2.1	Binary Crossed Link (BCL) Mechanism	76
5.2.2	Kinematic Requirements and Performance	82
5.2.3	Inner Mechanisms Analysis with the Instant Centres (ICs) tool	88
5.2.4	Force Analysis of Single Input-Single Output Linkage Systems	93
5.2.5	Finalized Layout (3D-CAD)	100
5.2.6	Structural Design of the Smart Rib	100
5.3	The Span-wise 3MMF Structural Skeleton	105
5.3.1	Structural Sizing of the Multi-Box Arrangement	105
5.4	The Actuation System	112
5.4.1	Through Shafts Solution: concept explained	112
5.4.2	COTS selection & Mechanical Arrangement Definition	113
5.5	The Adaptive Twist Composite Tab	116
5.5.1	Working Principles and main design parameters	116
5.5.2	Torsion Equation for Thin-Walled Closed Section Beams	117
6	Assessment of the 3MMF concept	125
6.1	Finalized Concept	125
6.2	Aerodynamic Design and Performance Assessment	130
6.2.1	Full-Camber Morphing Mode 1	131
6.2.2	Tab rigid rotation and twist (Mode 2 & 3)	137
6.3	Finite Element (FE) Model	140
6.3.1	FE Modelling Guidelines	141
6.3.2	Modal Analysis	144
6.4	Structural assessment of the full-metallic 3MMF	148

6.5	Structural assessment of the composite ATT	153
6.6	Estimated Weight	158
6.7	Mechanical Power	162
7	Conclusions & Recommendations	163

List of Figures

2.1	MAW project [7].	27
a	Outboard trailing-edge hinge moments caused by aerodynamic ($90 \cdot 10^3 \text{ in}\cdot\text{lb} = 10168 \text{ N}\cdot\text{m}$) and flexing loading ($10 \cdot 10^3 \text{ in}\cdot\text{lb} =$ $1129 \text{ N}\cdot\text{m}$) [7].	27
b	Morphing LE and TE [7].	27
2.2	Variable-Geometry Wing Camber for Transport Aircraft [11].	28
2.3	L-1011 aircraft with a variable camber [11].	29
a	Family of polars of the L-1011 with variable camber for different TE deflection ($M_\infty = 0.83$).	29
b	Maximum increment of L/D (<i>left</i>), and optimal TE angle (<i>right</i>).	29
2.4	ADIF (DLR): the Adaptive Airfoil concept, combination of variable cam- ber and bump systems [15].	31
2.5	Flap with eccentric beam device: position of the actuator [21].	32
2.6	SARISTU research project: final demonstrator [22].	34
a	Adaptive Trailing-Edge device (ATED): (<i>left</i>) rib, (<i>right</i>) elastic skin [28].	34
b	Full-scale Wind Tunnel demonstrators with three morphing de- vices [22].	34
2.7	Evolution of flap design on large commercial airplanes [32].	35
2.8	Airbus A350XWB high-lift trailing-edge system [34].	36
2.9	Fairing-less deployment system with a variable-camber (morphing) flap.	37
3.1	Flap airfoil [42]: (<i>left</i>) target geometry; (<i>right</i>) Morphing "finger-like" rib layout.	42
3.2	Morphing Flap (GRA Phase 1)[42]: (<i>left</i>) crossed links; (<i>right</i>) transmis- sion line.	43
3.3	Morphing outer section flap, investigation domain (GRA-ITD, phase 2).	45
3.4	Segmented rib (GRA-ITD, phase 2).	46

a	Symbol used.	46
b	Stephenson's Six-bar [47] linkages (K1 and K2).	46
3.5	Morphing outer-section flap (GRA-ITD Phase 2): final demonstrator.	48
a	Final prototype	48
b	Actuation group assembly.	48
3.6	Morphing outer-section flap (GRA-ITD Phase 2): actuations and segmented skin.	49
a	Actuation groups span-wise location (1^{st} , 3^{rd} , 5^{th} , and 7^{th} bay).	49
b	Segmented skin.	49
3.7	Technical data of COTS actuation system parts.	50
a	Hollow-shaft brushless motor data.	50
b	Gearbox data.	50
3.8	Morphing Flap FE model, modal shapes pertaining to rigid modes.	51
a	Rigid Mode 1, $f = 8.124 * 10^{-4}$ Hz.	51
b	Rigid Mode 2, $f = 4.68 * 10^{-3}$ Hz.	51
3.9	Limit load condition: 3D pressure distribution.	52
a	3D pressure distribution.	52
b	Pressure per each $Area(Bay_i, Block_j)$	52
3.10	Lumped forces system used in the Ground Static Test (GST).	53
a	Forces values.	53
b	Lumped forces system.	53
3.11	Morphing Flap FE model, Displacements [mm].	55
a	FE model with skin at Limit Load condition.	55
b	FE model without skin at Limit Load condition.	55
3.12	Bi-modal Flap, VM stress [MPa]. (a) Spars, (b) Ribs, (c) Leverages, (d) Links.	56
3.13	Bi-modal morphing flap (CS1): functionality test.	58
a	Setup hardware.	58
b	Functionality test: (<i>left</i>) full-camber mode, (<i>right</i>) tip deflection upward.	58
3.14	GST (Ground Static Test) Setup Hardware.	60
3.15	Ground Static Test (GST) results.	61
a	MDS and MSS data.	61
b	Stain Gauges (SG) data obtained.	61
3.16	Bi-Modal Morphing Flap: actuation torques correlation between FEM and GST.	62
a	Forward actuation groups.	62

	b	Rear actuation groups.	62
4.1		CS2 TP90: main views.	67
4.2		TP90 outboard flap.	69
	a	Outboard Flap geometric data: tip chord (633mm), root chord (869mm), span (5154mm).	69
	b	Tip Section (Outboard flap): minimum design space.	69
4.3		Flap configurations: (<i>left</i>) deployed, (<i>right</i>) stowed.	70
4.4		Limit Load condition for 3MMF preliminary design.	72
	a	Outboard Flap 3D pressure distribution: landing configuration.	72
	b	Total forces acting on each $Area(Bay_i, Block_j)$	72
5.1		Binary Crossed Link (BCL) Mechanism: working principle.	77
5.2		Airfoil camber line.	78
5.3		Sensitivity of Link hinges (L1 and L2).	80
5.4		Link (L1) kinematic design.	81
	a	Link hinges for $r = 15.7$ mm and $\theta = 22.5^\circ$	81
	b	Rib block angles (δ_1 and δ_2) as function of link rotation θ_L	81
	c	Final link hinges ($L1$ and $L2$) located in tip section.	81
5.5		Flow-chart of the actuation system design process.	82
5.6		Kinematic model of the inner mechanism: (a) full leverage can be seen as six-bar linkage plus a four-bar linkage; (b) Vector loop equations.	83
5.7		Kinematic design of the inner mechanism (IM1) located in rib block B1.	86
	a	Links lengths within the minimum available design space of the tip TE section.	86
	b	Links Angles as function of the crank angle input rotation.	86
5.8		Kinematic design of the inner mechanism (IM2) located in rib block B2.	87
	a	Links lengths within the minimum available design space of the tip TE section.	87
	b	Links Angles as function of the crank angle input rotation.	87
5.9		Inner mechanism (IM1): mechanical advantage as function of crank angle θ_1	90
5.10		Inner mechanism (IM2) instant centers analysis.	91
	a	Construction of instant center by means AK lines.	91
	b	ICs matrix of the linkage (IM2): main hinges (labeled in green), first order ICs (labeled in blue), second order IC (labeled in orange), and required ICs for MA estimation (marked in red).	91

5.11	Inner mechanism (IM2) mechanical advantage (MA) evaluation by means of ICs.	92
a	Evolution of instant centers (ICs) along AK lines.	92
b	Mechanical Advantage of IM2 (orange), and Output angle (blue) as function of crank rotation.	92
5.12	Inner mechanism full-force analysis (nomenclature).	93
5.13	Nomenclature of terms used for margin of safety evaluation.	96
a	Failure by pin shear [64].	96
b	Pin Bending Strength, method for determining the arm [64].	96
5.14	Inner mechanism (IM2): links forces and MA.	98
a	Forces as function of the input crank angle θ_1	98
b	Mechanical Advantage of IM2 (orange), and Output angle (blue) as function of crank rotation.	98
5.15	Inner mechanism (IM2): margin of safety for bolts as function of crank rotation θ_1	99
a	Margin of Safety (M.S.) for Shear.	99
b	Margin of Safety (M.S.) for Bending.	99
5.16	Smart rib: finalized layout (3D-CAD).	101
a	Side view.	101
b	Exploded view.	101
5.17	Smart rib FE simulation: limit load for morphing mode 1.	102
a	Displacement [mm], Max value 58 mm.	102
b	Von Mises Stress [MPa], Max value 550 MPa.	102
5.18	Smart rib FE simulation: limit load for morphing mode 2.	104
a	Displacement [mm], Max value 15.5 mm.	104
b	Von Mises Stress [MPa], Max value 484 MPa.	104
c	Mechanical Advantage estimated by ICs tool and NASTRAN (SOL400).	104
5.19	3MMF Multi-box arrangement: lumped elastic properties.	105
5.20	3MMF Multibox arrangement: beam model.	108
a	Fairing-less Deployment System hosted in the 3MMF skeleton.	108
b	Beam model of each flap box.	108
c	Continuous-beam model.	108
5.21	3MMF Multibox arrangement: bending moments and shear forces distributions.	109
5.22	3MMF Multibox arrangement: results of pre-design process.	111
a	Distribution of Bending stiffnesses for each box.	111

b	Limit Load Condition, Von Mises Stress distribution [MPa].	111
5.23	3MMF actuation system: through shafts solution.	113
a	Transmission shafts.	113
b	High speed and low speed shafts (section view).	113
5.24	3MMF actuation system: COTS components and IM mechanical arrange- ment.	114
a	Motors and power-off brakes.	114
b	IM mechanical arrangement.	114
5.25	Adaptive Twist composite Tab (ATT) concept. (a) Investigation domain; (b) Enabled functionalities: rigid deflection (<i>upper</i> , mode 2), "continuous" span-wise twist (<i>lower</i> , mode 3).	116
5.26	Adaptive Twist composite Tab (ATT) structural layout.	117
5.27	Adaptive Twist composite Tab (ATT) section layout.	118
5.28	Required moments by actuation systems (\mathcal{M}_{OUT}) for half-tab twist.	123
a	\mathcal{M}_{OUT} required at tip section for half-tab twist.	123
b	\mathcal{M}_{OUT} required at root section for half-tab twist.	123
5.29	Thin-walled Closed-Section beam: torsional moments distributions.	124
a	The Saint-Venant part of Torsional Moment T_{SV} [N*m].	124
b	The warping part of Torsional Moment T_w [N*m].	124
c	The warping part of Torsional Moment T_w [N*m] as function of $y * \beta$	124
6.1	3MMF finalized concept.	127
a	3D-CAD (isometric view).	127
b	Actuation System based on a segmented through shaft (section view).	127
c	Two bays full-camber evolution.	127
6.2	3MMF morphing modes.	128
a	Full camber morphing mode 1	128
b	Flap Tip upwards/downwards deflection (morphing mode 2).	128
c	Flap Tip segmented twist (morphing mode 3).	128
6.3	ATT composite tab installed on the 3MMF skeleton.	129
6.4	ATT composite tab structural layout.	129
6.5	ATT composite tab: continuous span-wise twist from tip to root ($-5^\circ/0^\circ/+$ 5°).	130
6.6	TP90 landing configuration.	133
a	Maximum Fowler motion (230mm) and 3MMF in landing config- uration.	133

b	Fairing-less Deployment System hosted in the 3MMF skeleton.	133
c	Fowler motion provided by deployment system.	133
6.7	Configurations considered for morphed flap (Mode 1) at landing conditions.	134
a	Angles nomenclature (<i>left</i>); Linking beam element marked in yellow (L, <i>right</i>).	134
b	Airfoil shapes considered in CFD simulations.	134
c	Rib-block angles obtained as function of linking beam element rotation θ_L	134
6.8	Process used for the generation of the morphed 3D flap configurations.	135
a	Geometry definition for Mode 1 in landing conditions.	135
b	CFD grid used for Mode 1.	135
6.9	Computed stall process for the optimum morphed flap configuration [76].	135
6.10	TP-90 regional airplane: High-Lift Performance in Take-off and Landing conditions [76].	136
a	Landing conditions: droop nose + morphing flap Mode 1.	136
b	Take-off conditions: droop nose + flap (without morphing)	136
6.11	TP-90 Polar in climb condition without morphing (at $M_\infty = 0.36$ and $4572m$) [76].	138
6.12	TP-90 Polar in climb condition with TE morphing mode 2 & 3 (at $M_\infty = 0.36$ and $4572m$) [77].	139
a	TE rigid rotation (<i>left</i>), TE twist morphing law (<i>right</i>).	139
b	C_L versus aerodynamic efficiency L/D	139
6.13	3MMF Finite-Element Model: details of the smart rib.	143
a	Rib blocks (CHEXA elements).	143
b	Inner mechanisms IM1 & IM2 (CHEXA elements).	143
c	Linking beam element (CHEXA) and hinge (CBAR with MPCs).	143
d	Segmented Skin (CQUAD4 elements).	143
e	Spars (CQUAD4 elements).	143
6.14	3MMF finite-element model.	144
6.15	Modal analysis: rigid modes.	146
a	1 st Rigid mode $f = 2.49 * 10^{-3}$ Hz.	146
b	2 nd Rigid mode $f = 4.57 * 10^{-3}$ Hz.	146
c	3 rd Rigid mode $f = 2.68 * 10^{-2}$ Hz.	146
d	4 th Rigid mode $f = 0.74$ Hz.	146
6.16	Modal analysis: elastic modes.	147
a	1 st Elastic mode $f = 25.2$ Hz.	147
b	2 nd Elastic mode $f = 33.4$ Hz.	147

c	3 rd Elastic mode $f = 49.2$ Hz.	147
6.17	3MMF finite-element model: BCs for static analysis.	148
6.18	3MMF static analysis with LL: displacements [mm].	149
6.19	3MMF static analysis with LL: reaction moments at each IM crank.	150
6.20	3MMF static analysis with LL: VM stress [MPa].	151
a	Upper and lower skin, Max Value 197MPa.	151
b	Spars, Max Value 266MPa.	151
c	Rib blocks, Max Value 278MPa.	151
6.21	3MMF static analysis with LL: VM stress [MPa].	152
a	Inner Mechanisms, Max Value 406MPa.	152
b	Linking beam element, Max Value 302MPa.	152
c	Hinge fittings, Max Value 255MPa.	152
6.22	ATT structural concept.	153
6.23	ATT thickness distribution.	154
6.24	Continuous span-wise TE twist (Mode 3): $+5^\circ$ (root); 0° (central); -5° (tip).	155
6.25	Rigid downward deflection equal to $+5^\circ$ (Mode 2): Strain Distribution [μ Strain].	156
6.26	Actuating torques required by the actuation systems for enabling morphing TE modes during high speed climb flight conditions ($M_\infty = 0.36$ at 4572m). 157	
6.27	Continuous span-wise TE twist (Mode 3): $+2^\circ$ (root); $+3^\circ$ (central); $+4^\circ$ (tip).	157
a	Displacement distribution [mm].	157
b	Strain Distribution [μ Strain].	157
6.28	Fuel weight decrease as function of 3MMF technology weight increase.	160
6.29	Actuating torque provided by each actuation system hosted in 3MMF block B2.	162

List of Tables

3.1	Bi-modal morphing flap.	63
4.1	CS2 TP90 main data.	68
4.2	Limit Load Condition considered for tab preliminary design.	73
a	TP90 aerodynamic model for evaluation of tab design loads (with DLM code).	73
5.1	IM2 geometric values used for MS evaluation.	97
5.2	Harmonic-Drive (CPL-17A) gearbox datasheet [65].	115
5.3	Kollmorgen (KBMS-10x04) brushless motor data-sheet [66].	115
5.4	Tab section properties.	122
6.1	3MMF final weight.	161

List of Acronyms

3MMF	Three-Modal Morphing Flap
A/C	aircraft
ACARE	Advisory Council for Aviation Research and innovation in Europe
AFP	Automatic Fiber Placement
ATL	Automatic Tape Layup
ATT	Adaptive Twist Tab
BDF	Bulk Data File
CAD	Computer-Aided Design
CBAR	Simple Beam Element Connection (see Ref. [88])
CBEAM	Beam Element Connection (see Ref. [88])
CBUSH	Generalized Spring-and-Damper Connection (see Ref. [88])
CFD	Computational fluid dynamics
CHEXA	Six-Sided Solid Element Connection (see Ref. [88])
CIRA	Centro Italiano Ricerche Aerospaziali
CONM2	Concentrated Mass Element Connection, Rigid Body Form (see Ref. [88])
COTS	Commercial Off-the-Shelf
CQUAD4	Quadrilateral Plate Element Connection (see Ref. [88])

CROD	Rod Element Connection
CS	Clean Sky
CTETRA	Four-Sided Solid Element Connection (see Ref. [88])
CTRIA3	Triangular Plate Element Connection (see Ref. [88])
DLM	Doublet Lattice Method
DLR	Deutsches Zentrum für Luft- und Raumfahrt e.V.
DOF	Degree of Freedom
DOC	Direct Operating Cost
DOFs	Degrees Of Freedom
EMA	electromechanical actuator
FE	Finite Element
FEM	Finite Element Model
GST	Ground Static Test
HA	Hinge Axis
HD	Harmonic Drive
IC	Instant Center
IM	Inner Mechanism
ITD	Integrated Technology Demonstrator
LA	Load Alleviation
LC	Load control
L/D	Lift over Drag ratio
LDG	Landing

LE	Leading Edge
LNC	Low Noise Configuration
LL	Limit Loads
LVDT	Linear variable displacement transducer
MA	Mechanical Advantage
MAW	Mission Adaptive Wing
MPC	Multi Point Constraint (see Ref. [88])
MTOW	Maximum Take-Off Weight
MZFW	Maximum Zero Fuel Weight
NASA	National Aeronautics and Space Administration
NLF	Natural Laminar Flow
ONERA	Office National d'Etudes et de Recherches Aéropatiales
PDU	Power Distribution Unit
RBE2	Rigid Body Element, Form 2 (see Ref. [88])
TACT	Transonic aircraft technology
TE	Trailing edge
TO	Take-off
TP90	Turbo-Prop 90 passengers
TRL	Technology Readiness Level
UNINA	UNiversity of Naples
USAF	United States Air Force
VM	Von Mises
WT	Wind Tunnel

Chapter 1

Introduction

1.1 General Overview

Early transport aircraft used simple high-lift devices to provide better airplane control and to improve pilot vision by producing low-speed flight [1]. The introduction and improvement of more complex high-lift devices in transport aircraft was mainly due to the development of powerful engines, which increased substantially the speed and the wing loading of the aircraft, and the limitations on runway lengths.

Due to economical considerations the wing profiles were optimised for cruise flight efficiency, but at low speeds they are rather inefficient, needing lots of lift to achieve the required Lift over Drag ratio (L/D). Hence, in order to cope with the high wing loadings and to achieve the required additional lift for take-off and landing, it was necessary to introduce high-lift devices.

The design of high-lift systems plays an important part in the process of defining the size and performance of modern aircraft and has taken a very important role in the design process of the whole aircraft. The design process of high-lift devices has been heavily scrutinized and has become of great importance for aircraft manufacturers.

For typical subsonic transports, the high-lift systems are about 5 to 11% of the total cost of the aircraft [1], and they have a large impact on the performance of the aircraft. The commercial transport market has become so competitive that an enormous and constant effort is expended on ways to reduce the direct operation costs. When it comes to high-lift devices, aircraft manufactures focus on the improvement and optimization of the currently used high-lift device concepts.

The introduction of high-lift devices in the leading and trailing edge of the wing provides the aircraft with the means to adjust and comply with the low-speed requirements for take-off and landing, while maintaining the "optimized" wing profile for cruise flight

efficiency. Though, because the wing profile is set during the cruise, without the possibility of variations, in specific occasions the wing might not be working in optimum conditions, incurring higher levels of drag and ultimately consuming more fuel.

The three-modal camber morphing wing flap concept provides a solution to this problem by allowing the wing to adapt to the different flight cruise conditions, hence improving the performance of the aircraft. The advantages of the Three-Modal Morphing Flap concept have been acknowledged, but no feasible practical design has yet been achieved or developed in the area of commercial transport.

Current improvements in computational capabilities, development of new design tools and the introduction of new technologies provide the means for a possible improvement of the traditional design methodologies and/or a breakthrough in the design of a novel multi-functional morphing flap concept.

1.2 Research Background

Aircraft versatility is growingly becoming an added value for daily operations. To date, airplanes are provided by numerous control systems which enable wing adaptation for several flight conditions. In fact, lifting devices such as flaps, slats, aileron and spoilers, are essential to increase wing chord, camber and therefore the lift distribution during the entire mission envelope.

However, several new sensors, control systems and new actuators have been developed over the last few years. These developments allow designers to distribute actuation forces and power optimally and more efficiently.

The next technological challenge worth to be embraced is switch to a more or all-electric aircraft. The first step, to be tackled, will be to replace the heavy conventional hydraulic actuators with a distributed span-wise arrangement of smaller electromechanical actuators (EMAs). This will bring several benefits at the aircraft level. First of all, a full electrical system reduces classical drawbacks of hydraulic systems and overall complexity, also providing maintenance benefits. Lack of supply buses, improved torque control, enhanced efficiency, removal of fluid losses and flammable fluids are only some of the benefits that can be achieved with (EMA) actuators. On the other hand, a general limit of electro-mechanic actuators is the possibility of jamming failures that can lead to critical aircraft failure conditions, as well as the limited electro-mechanical power provided.

Based on (EMA) actuators, a novel device capable of answering at the request of aircraft versatility providing several morphing modes can bring several benefits along the flight mission profile.

However, the application of an innovative technology in a new aircraft can be pursued

only when:

- interfaces and links with other technologies necessary to the aircraft operation must be properly resolved;
- solutions must be acceptable to the aeronautics market; indeed, they have to consider aspects like: certification and safety, reliability during operations, costs, and maintenance process;
- demonstration of feasibility to fulfil the criteria of aircraft manufacturing industry (i.e. in series production).

1.3 Research Objective

A novel multi-functional morphing flap technology was requested to improve the aerodynamic performances of the next TP90 aircraft along its entire flight mission. The morphing flap system layout added new and more demanding functionalities. Three different functions are now being considered:

- Morphing mode 1: overall airfoil camber morphing (up to 28° equivalent rigid deflection);
- Morphing mode 2: $+10^\circ / -10^\circ$ (upwards/downwards) deflection of the flap tip segment (from the 90% to 100% of the local chord);
- Morphing mode 3: Tip twist ($\pm 5^\circ$ along the outer flap span);

Morphing mode 1 is supposed to be activated when the flap is deployed during take-off and landing only to enhance A/C high-lift performances also allowing for steeper initial climb and descent, noise-abatement trajectories. Thanks to this function, more airfoil shapes are available at each flap setting and therefore a dramatic simplification of the flap's deployment systems may be expected: actuation tracks could be hosted into wing airfoil shape without external fairing needs. Basically, very simple conventional track systems (i.e. curved beam) without external fairings are not able to comply with high-lift requirements in landing and take-off configurations; therefore, further increase in high-lift performance are obtained using the overall airfoil camber morphing (mode 1) in the Fowler flap extended configuration.

Morphing modes 2 and 3 are related to the last chord-wise segment of the flap and are activated in climb, cruise, and off-design flight conditions when the flap is stowed in the

wing. Thanks to these modes, load control (LC) functionalities may be implemented to improve wing aerodynamic efficiency.

The smart function of the ribs, namely their capability to drive morphing as an inner movable articulation of the flap structure, was preserved.

Because of three different operating modes, the novel full-scale outboard flap will be named from now on Three-Modal Morphing Flap (3MMF).

The core of the three-modal morphing flap (3MMF) layout is the smart function of the articulated (finger-like) ribs: namely their capability to provide the morphing as an inner movable articulation of the flap structure. Ribs' architecture and the associated mechanics was instead fully analysed to enable several morphing modes through a more compact and robust design.

1.4 Research Method

The research starts with the analysis of the design requirements, required for enabling proper characteristics of the Three-Modal Morphing Fowler Flap. Starting from the external aerodynamic shape, main design constraints were identified, and the preliminary concept was proposed.

After that, the preliminary structural layout was defined; main effort was placed on the assessment of the actuation system and the structural architecture at limit and ultimate operative load conditions: limit aerodynamic loads were evaluated by means of high-fidelity CFD for landing configurations, and DLM code for dive speed flight conditions. Ultimate loads were obtained by applying a contingency factor of 1.5 to the limit ones.

Reliable Finite-Element models were developed to assess the structural behaviour of the device under the actions of aerodynamic limit loads. Actuating torques required for morphing operations were estimated and compared with the ones evaluated in the preliminary design of the actuation systems.

Finally, the mechanical arrangement of the final layout was defined with integration of properly selected Commercial Off-the-Shelf (COTS) components. Full explanation of the integration at aircraft level has been provided.

Chapter 2

Morphing Structures: State of research for Large Aircraft applications

2.1 Introduction

Modern transport aircraft wings have reached near-peak levels of energy-efficiency, allowing further improvements extremely difficult. Traditional aircraft design only optimizes to a single point in the flight envelope and fuel condition; therefore, all aircraft are suboptimal at every other point in the flight envelope. It is likely that more efficient aircraft, able to meet direct and indirect environmental requirements, will be achievable only by enhancing the aircraft's capability through adapting its wing configuration in flight, so as to always be in the optimal configuration.

This novel discipline of aeronautics is usually referred as morphing or smart structures. The main goal of this branch is to conceive a system with fully integrated devices (actuators and sensors) into a specific structural architecture. This system has to provide the additive capabilities to adapt its configuration when required while preserving the classical load-bearing characteristic proper to every aerospace structure.

The benefits of morphing structures are mainly [2]: flights with minimum drag, load control & alleviation, increasing the maximum & minimum speeds. The cost reductions mainly arise from the reduction in fuel burn. This is of great economic interest to airlines, because of the ever increasing fuel prices.

Dealing with commercial transport airplanes, the wing is the structural component most sensitive for flight performance. The wing shall support the aircraft mission in each condition. The idea of changing the wing shape has always been adopted by engineers, from the beginning of the human flight history. Wing shape change is necessary to adjust lift and drag to different flight stages, such as take-off, cruise and landing.

To fulfill these different offices, aircraft uses aerodynamic devices (such as flaps, slats, etc). Even if conventional hinge mechanisms are effective in controlling the airflow, it implies the presence of hardy control lines as well as complex actuation devices which contribute to the growth of the wing structural weight. Generally, a single flapped and a triple flapped wing, weight respectively 30% and 100% more than a clean wing.

Back to the very early days of the aviation history, the possibility of changing the wing shape becomes an essential problem for generating the lift and maintaining lateral equilibrium. In 1903, the Wright Brothers achieved the first sustained, powered, heavier-than-air flight in a machine of their own design and construction [3]. Experimenting first with kites and gliders, they developed a revolutionary wing design that helped solve the crucial problem of lateral equilibrium: lateral control was realized by twisting the rear of their fabric-and-wood wings in opposite directions [4]. However soon after, as aircraft became heavier and faster, engineers were forced to switch to stiff wings retrofitted with flaps and ailerons to satisfy the need for higher wing loading; morphing of these surfaces was proved to be impractical because the higher structural stiffness required to withstand higher aerodynamic loads due to increased performances.

Morphing was adopted in some '70 and '80 aircraft. F-14 Tomcat and Tornado aircraft were able to change their sweep angles to strike a balance between range and speed by delaying the rise in drag for higher speeds. The Corcorde had the ability to change the fuselage nose angle around its pitch axis.

2.2 Components of a Wing Morphing Structural System

Morphing structural systems are mainly applied to wings, enabling limited changes of their geometry and preserving their capability to bear external and internal loads. The morphing system should be able to deform itself, as it is sufficiently rigid to resist the action of several external forces.

Each morphing system is characterized by two main components:

- Structural skeleton,
- Actuator system.

2.2.1 Structural Skeleton

The structural layout has the main goal to provide overall bearing property with minimal deviations in terms of displacement from the original configuration, while changing its shape. The structural skeleton is the body of the system and is the part that shall sustain

the upcoming load. A solution is to rely on the actuation system to absorb the incoming forces by means of kinetic chains and motors.

Because of that, the main role of the structural skeleton is to create suitable transmission patterns for the stress and strain field, so that it can be distributed uniformly inside the system, alleviating the actuator load. The structural skeleton also preserves the shape of the system for any deformed configurations. It hosts the actuation system, completed with its kinematics, and is designed to respect the connections with the rest of the structure.

2.2.2 Actuation Systems

Following these assumptions, the actuation system plays different roles in the set-up of the morphing device. It is connected to the structural skeleton and, in general, it has a structural role. In fact, if the structural skeleton is a pure kinematic chain, all the loads are transferred through its actuation arms. This is nothing new, as the usual flaps, slats, ailerons, and so on are working on this principle.

The real novelty is that the system is fully integrated within the main body and, because it must guarantee complex deformed shapes, with some continuity, it is made of several actuators. On one hand, it is necessary to keep a large number for a better load distribution and a proper actuation. On the other hand, safety and maintenance cost requirements would keep that number low to minimize overall impact.

The most important challenge for actuation system design is to have the minimum number of actuators with the most effective distribution of actuation on the entire system.

2.3 NASA Research & the Mission Adaptive Wing Project

In 1980, the Preliminary Design Department of Boeing, under NASA commissioned research, where the potential of variable wing geometry was discussed [5]. In detail, the study concerned with the potential of introducing systems to vary the wing camber continuously in cruise, to optimize selected aerodynamic reference parameters to reduce fuel consumption and operating costs.

The F-111 Mission Adaptive Wing (MAW) joint research program among Boeing, USAF, and NASA started in the early 1980s [6]. It proposed the use of adaptive leading and trailing edge surfaces to provide ideal wing shapes for selected flight conditions (Fig.2.1a). In detail, a General Dynamics F-111 fighter was retrofitted with wings whose camber could be actively modified by hydraulic actuators.

The LE on each wing consisted of one continuous segment flexed through linkages and nine rotary actuators driven by two PDU's (power distribution unit) at each end of the segment. Each of the three TE flap segments was controlled by individual systems. The three segments were necessary because of the higher aerodynamic hinge moment loading acting on the TE (Fig.2.1a). Each outboard, midspan, and inboard TE segment was driven by two PDU's located at each end of the respective segment. The midspan and outboard flaps provide, in part, the lateral control and are called flaperons. Rotary motion was transferred from the PDU's to the rotary actuators by a torque tube drive shaft. The PDU's and rotary actuators had a combined gear ratio of 975:1. In addition, the PDU's were mounted and grounded along a span-wise line near the wing box or on the added load-carrying structure. Electrical brakes were attached to the gearboxes on the TE PDU's and on the LE actuator shaft ends.

The trailing-edge concept, shown in Fig.2.1b, used a basic mechanism of a four-bar linkage driven by a rotary actuators. Each segment incorporated flexible fibreglass skins on the top panels and metal sliding panels on the bottom panels. The upper fibreglass skins are attached to the four-bar linkages with span-wise stringers and short links. The bottom panels were overlapped at the junction to provide a continuous and nearly uninterrupted surface to allow articulation of the mechanism. Flexing and controlling the camber of each segment involved deforming the upper panels of the LE and TE through a scissor and part-grounded linkage arrangement.

The lower panels were removable for inspection and maintenance. Two sets of mechanisms drove each flap segment with spanwise shafts connecting both mechanisms. All pivot points were self-aligning teflon-lined bearings to provide maintenance-free, lifetime durability and a close tolerance fit.

Hydraulic power for the variable-camber wing PDU's is derived from and connected

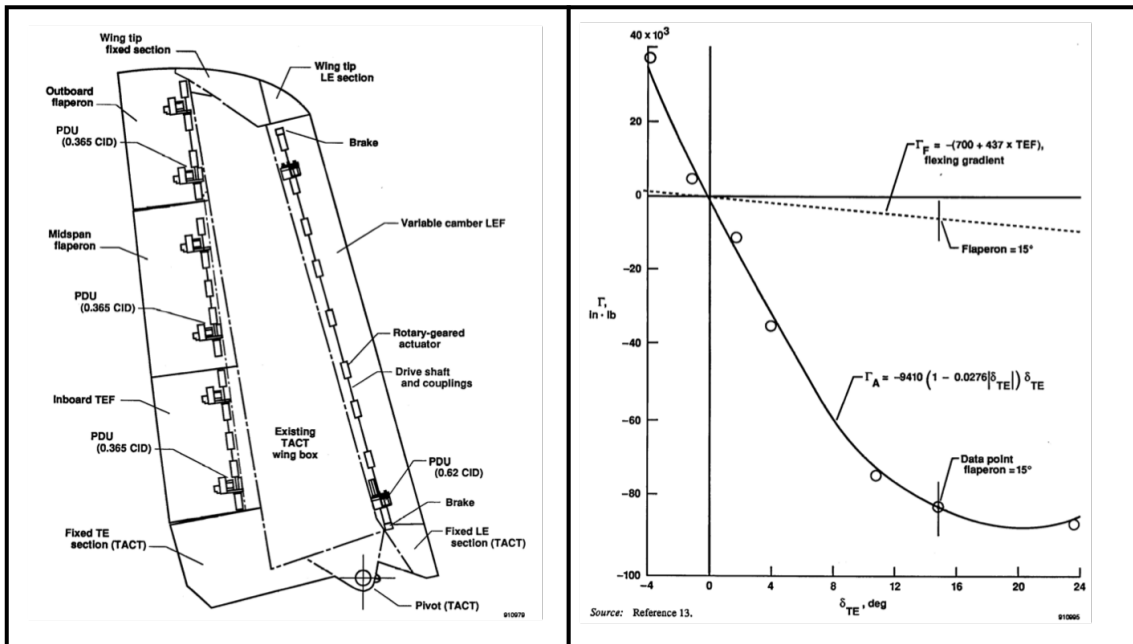
to the basic TACT/F-111 primary and utility hydraulic power supply systems. Addition of the 16 PDU's caused an increase in demand for hydraulic power which was considerably higher than the spoiler had previously required. Model studies determined that an increased hydraulic capacity was necessary. As a result, the stock F-111A hydraulic pumps were returned to the manufacturer for a 11-percent increase.

Each cambered segment was driven by two PDU's located on the end of each segment (2.1a). One PDU was powered by the primary system. The other PDU was powered by the utility system. The TE flaps and flaperons were driven by 628gal/min PDU motors.

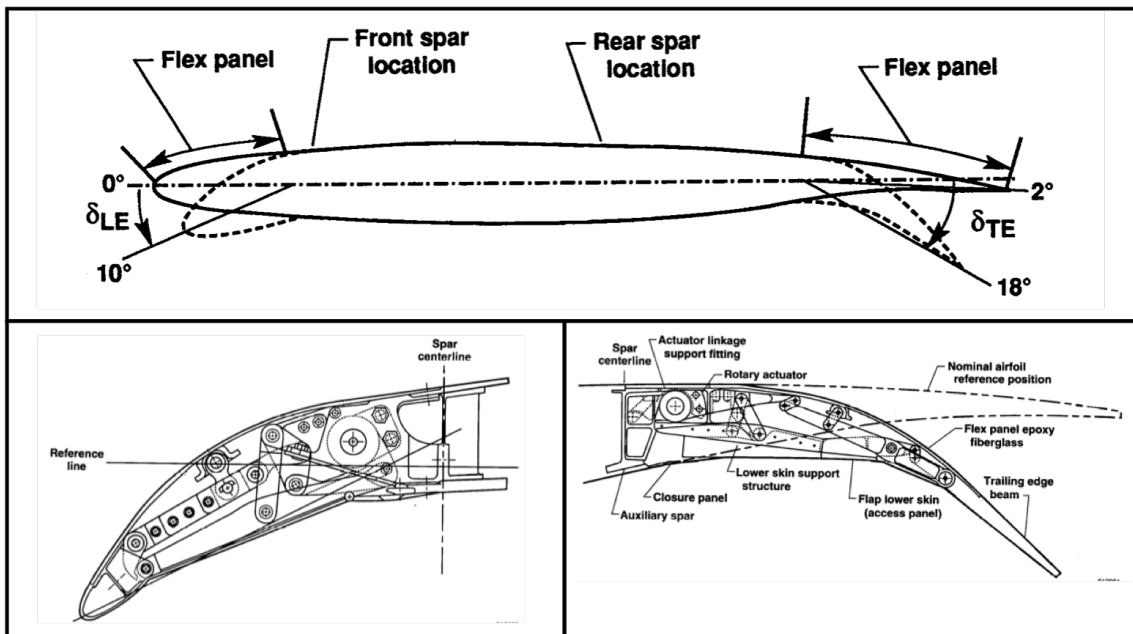
The aircraft actually had 59 flights between 1985 and 1989 [8]. Improved range, speed, and fuel efficiency were achieved by optimizing aerodynamic efficiency over operating C_L values by changing the airfoil shape. Deflections up to 10 and 18 degrees were respectively implemented, for both cruise and manoeuvre conditions [8]. There was a 40% drag benefit of the variable-camber airfoil over the fixed cruise airfoil at the maximum fixed cruise airfoil CL value ($C_{Lmax,cruise} = 1.02$) [8]. The wing-root bending moment could be reduced by 10–20% for the same load factor [8]-[9]. Conversely, the maximum load factor could be increased for the same wing-root bending moment from 4 to 5 g (25% increase in load factor) [8].

However, because of the elevated number hydraulic actuators, drawbacks resulted in severe power and weight penalties and a significant increase of the overall system complexity. During the entire program, the 46 rotary actuators never failed nor was it necessary to replace a rotary actuator unit. However, the 16 PDU's did require 37 component or full-assembly replacements [7]. Most of the initial replacements or overhauls were caused by localized contamination that developed within the first 400hr of system operation [7].

These difficulties almost completely vanished the attained aerodynamic benefits and generated serious doubts on the evolution of the concept [10]. After the first phase, investigations continued for more years, shifting the attention towards the system integration and the aircraft controllability [10].



(a) Outboard trailing-edge hinge moments caused by aerodynamic ($90 \times 10^3 \text{ in} \cdot \text{lb} = 10168 \text{ N} \cdot \text{m}$) and flexing loading ($10 \times 10^3 \text{ in} \cdot \text{lb} = 1129 \text{ N} \cdot \text{m}$) [7].



(b) Morphing LE and TE [7].

Figure 2.1: MAW project [7].

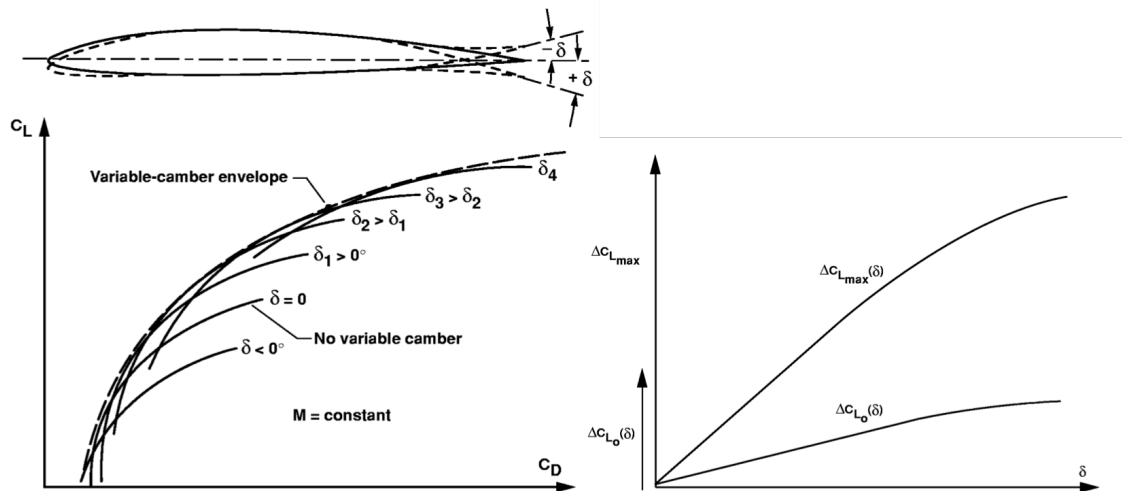


Figure 2.2: Variable-Geometry Wing Camber for Transport Aircraft [11].

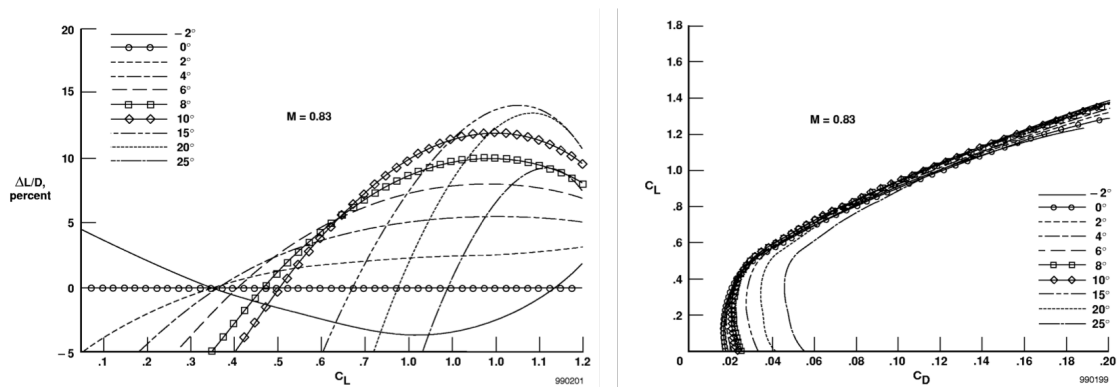
2.3.1 Other NASA Studies

In 1999, NASA published a systematic work on the estimated benefits of variable geometry wing camber control for transport aircraft [11]. Aerodynamic performance models allowed estimating optimal performance benefits of a variable camber wing for a transportation aircraft. The influence of camber variation was simulated as an aileron-type trailing-edge deflections (i.e. rigid deflection). The most important result was that by considering the complete wing trailing edge surfaces, drag could be reduced at virtually all points in the flight envelope [11].

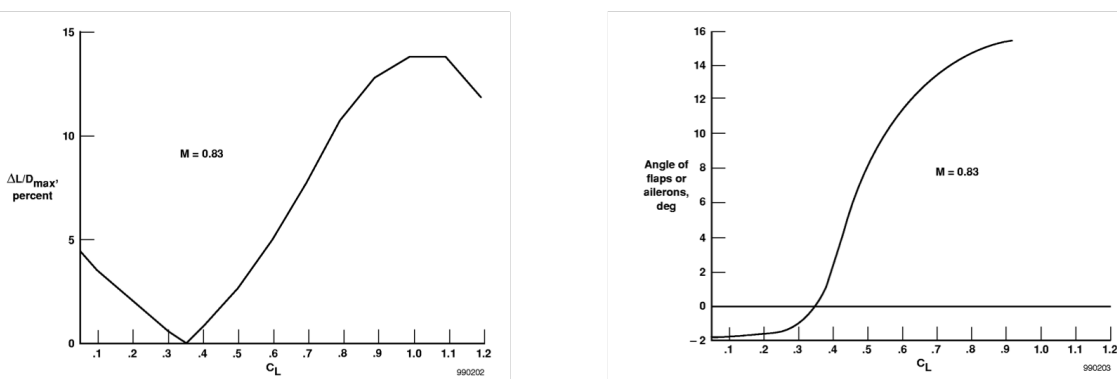
Modifying wing shape during cruise an optimum C_L/C_D curve can be obtained, as an envelope of the different variable-camber configurations enabled to compensate the aircraft weight reduction due to the fuel consumption. For instance, the overall benefit can thus be estimated by considering the variation of each drag polar (defined for a specific flight condition M_{infty}) as function of trailing-edge deflection (Fig.2.2) [11].

Starting from the complete drag polar equation for a reference vehicle (Lockheed L-1011), all the terms are computed from flight results at Mach equal to 0.83 and reported in the diagram in Fig.2.3 for different flap deflections. The aerodynamic trend represented above, shows that when deflection occurs, all the drag polars cross around a pivot point for relatively high-lift coefficients while shift on the left for low C_L .

Fig.2.3 shows the percent of change in L/D as a function of C_L respect to the uncambered configuration. The main result is that for $C_L = 0.35$ no benefits occur as it is clearly visible in the Fig.2.3.



(a) Family of polars of the L-1011 with variable camber for different TE deflection ($M_\infty = 0.83$).



(b) Maximum increment of L/D (left), and optimal TE angle (right).

Figure 2.3: L-1011 aircraft with a variable camber [11].

It is also important to see the flap deflection required to obtain the maximal L/D at a given C_L (Fig.2.3). The variation shows that for low lift coefficients it is required to deflect the trailing edge up (negative sense) in order to attain efficiency improvements otherwise increased down deflections (positive sense) are required for C_L greater than 0.35.

Cruise condition occurs at C_L in the range from 0.4 to 0.5 where it is evident that the improvements produced by variable camber wing are in the range of 1-3 percent which is related to the percent of fuel consumption. In this way, using a simple approach, the morphing benefits were demonstrated.

Further NASA studies were performed in NASA-TCAT program [12]. Different active trailing edge devices were tested on a wind tunnel model of a Beechcraft Premier I. The final Wind Tunnel Tests, supported by transonic CFD-calculations, showed that the cruise tab device improves aircraft performance at cruise speed as follows: 1) Total fuel burn reduced by up to 1.5%; 2) Mission range extended by 2.2% (long range cruise speeds); 3) Maximum speed increased by 2 to 4 knots.

2.4 DLR Research & the *Adaptiver Flügel* (ADIF) Project

In 1986, DGLR (the former DLR) published a first study concerning current trends in the commercial aircraft design [13]. Aerodynamic advances were outlined together with their expected impacts.

The results showed that variable-camber systems for a commercial aircraft using a simple trailing-edge device could lead to gains exceeding 10%, especially for non-standard conditions. In standard cruise regime, the benefits were estimated around 1%–3%. The report refers to contemporary studies carried out at those times in Europe by Airbus, trying to apply adaptive systems to A-330 and 340 series [14]. In detail, the work focused on the possible implementation and the overall integration of

- Transonic, variable-camber aerofoils for the control of the efficiency aerodynamic parameters and the buffeting alleviation, including load control.
- Transonic technologies for shock boundary layer control.
- Passive and active laminarization of transonic aerofoils.
- New propulsion systems, including prop-fan systems.

In 1995, at the DLR research centre, the ADIF (*Adaptiver Flügel*) project may be considered the first project on adaptive structural wings [15]-[16]. This first activity was related to numerical aerodynamic investigations, concerning with the alleviation of buffet phenomena. Deploying a properly contoured bump just under a shock wave could lead to achieve a nearly isentropic compression, attenuating the intensity of the shock itself [17].

The further inclusion of an adaptive trailing-edge gave the overall system capabilities of flow control. The "finger concept" substituted rigid with flexible ribs, realized by a continuous series of hinged plates (like a finger). Pin-jointed rib elements were used that rotated relative to each other via revolute and prismatic joints. The various elements were then linked together to reduce the degrees of freedom to two per rib for limiting the necessary number of actuators.

This morphing concept was intended for the Airbus A340-300 outboard Fowler flap. The dimensions include a flap chord length (inboard section) of 1680mm flap span length of 10,210mm and a rear spar height of 151mm [18]. The skin was allowed to slide on the ribs using roller bearings [19]. Linear electrical motors were used for two actuation schemes: 1) one actuator per rib connected to the first and second rib elements and 2) one actuator connected to a transmission beam and wedge [19].

Improved range, speed, and fuel efficiency were expected by optimizing aerodynamic efficiency over operating C_L values by changing the airfoil shape. A 3 – 10% L/D

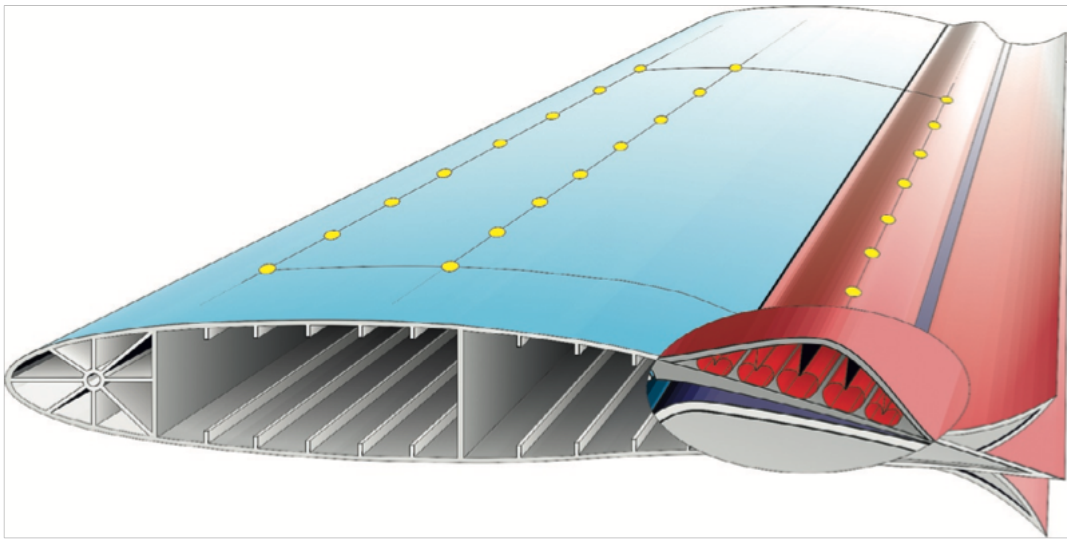


Figure 2.4: ADIF (DLR): the Adaptive Airfoil concept, combination of variable camber and bump systems [15].

improvement over a range of C_L values, and a possible C_L increase of 12% were expected [19]. In addition, the expected 12–15% reduction in wing-root bending moment could lead to improved manoeuvrability or reduced system weight (for the same original maximum load factor).

Wing camber variation may have the effect to either redistribute the wing lift in order to achieve an elliptical lift distribution ensuring the lowest induced drag or to move the lift resultant inboard, thus reducing the wing root bending moment with positive effect of the structural stress. This indicates another important application of the morphing structures: load control and gust load alleviation respectively in static and dynamic regime. It is clear that morphing structures technology can be tailored on the base of a specific application such as improve aerodynamic performance (increase L/D) or increase fatigue life by reducing bending stress.

2.5 Recent Research Projects in Europe

In 2008, the research project called 'Smart High Lift Devices for the Next Generation Wing' (SADE), conducted within the European Union Seventh Framework Programme, aimed to investigate and develop morphing concepts for the high lift devices of future aircraft wings.

The main objective pursued by SADE has been the development of a Smart Leading Edge and a Smart Single Slotted Flap to replace the conventional slats and flaps found on commercial aircraft wings. The use of a smart, gap-less leading edge device would contribute to achieve laminar flow over the wing and would help to reduce the noise and drag generated.

For the trailing edge, a distributed actuation concept was developed: an eccentric beam actuator (EBEAM) (firstly developed in the DARPA project [20]) was selected as solution for actuate morphing device with restricted volume as reported in Fig.2.5 [21]. The main component was a bent beam connected to a rotary actuator shaft that pushes its extremity upwards or downwards. The movement was then transmitted to the structures by means of discs located in correspondence of skin stringer which provide a surface along with the disc can slide acting like a rail.

As first option, the authors in [21] proposed to individually drive the beam by single actuators (required torque per each rib $58.2 Nm$) equally distributed. However, no further evidence on COTS electric motor and actuation mechanical arrangement definition (in the span-wise direction) was provided.

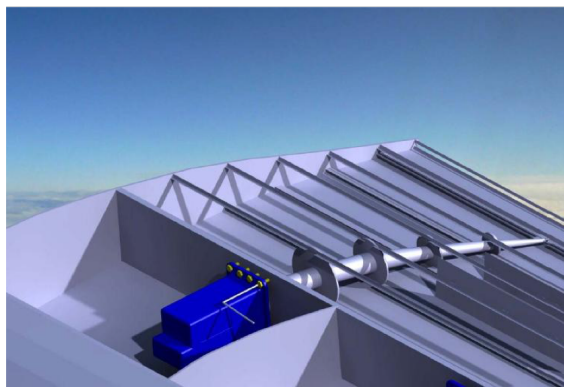


Figure 2.5: Flap with eccentric beam device: position of the actuator [21].

2.5.1 Smart Intelligent Aircraft Structures (SARISTU)

In 2010, the major research project ever carried out in Europe on adaptive structures was established (with a 51 million Euro budget and more than 60 partners involved). Airbus led the SARISTU program [22], which was articulated into several application scenarios. Each of them targeted at developing specific technologies to be integrated in two full-scale demonstrators.

Concerning the adaptive wing activities, a 5.5m span wing section hosted a complete set of three morphing devices.

An adaptive leading-edge aimed at increasing take-off and landing performance was designed by a research group led by the Deutsche Zentrum für Luft- und Raumfahrt (DLR) [23]. The system implemented a single electromechanical actuator [24] that forced mechanical deformation of a composite skin. It combined high bending resistance with reasonable in-plane deformability, taking advantage of the anisotropy properties.

Airbus led a team aimed at developing an innovative adaptive winglet system [25]. It targeted the possibility of giving the aircraft an effective device for gust alleviation [26]. It implemented a classical, large band electromechanical actuator driving a single-hinged (plain) flap.

The Italian Aerospace Research Centre (CIRA) guided a group focused on the design and the realization of an adaptive trailing edge device (ATED) [27], aimed at improving the aircraft performance in cruise, in terms of fuel consumption reduction, or equivalently, range increase [28]. A set of 10 flyable electrical actuators was used [29]: each one compact enough to be entirely integrated into the main body in spite of the limited available room. They drove a single degree of freedom (SDOF) kinematics [30], made of 3-hinge ribs (designed by UniNA [28]) and related structural components (stiffeners and spars) devoted to ensure the prescribed shape. A suited deformable skin was implemented to guarantee aerodynamic surface continuity, this time combining metal and special rubbers [31] as shown in Fig.2.6b.

All the devices were designed for sustaining real flight conditions for the referenced aircraft they were developed for, and realized according to the best practice, common to the aeronautical industry. The assembled wing, Fig.2.6a, underwent WT tests at TsAGI, the Russian Aeronautical Research Centre, where the three systems proved their capabilities in low speed flow ($M_\infty = 0.150$), April–June 2015.



(a) Adaptive Trailing-Edge device (ATED): (left) rib, (right) elastic skin [28].



(b) Full-scale Wind Tunnel demonstrators with three morphing devices [22].

Figure 2.6: SARISTU research project: final demonstrator [22].

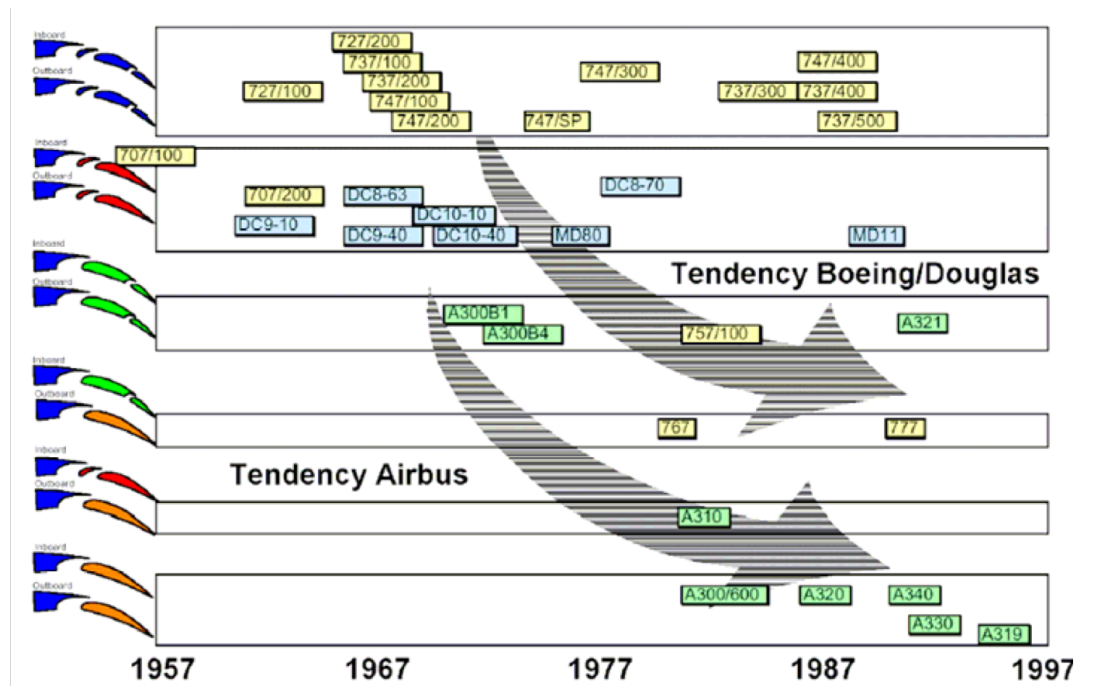


Figure 2.7: Evolution of flap design on large commercial airplanes [32].

2.6 Evolution of High-Lift Systems on Large Commercial Airplane

The state-of-the-art of commercial aircraft high-lift actuation systems mostly consists of mechanical transmission shafts moved by rotary or linear hydraulic actuators with common control valves. These architectures are designed to assure a synchronous, safe and reliable deployment during take-off and landing phases. Indeed, the main functionality of the high-lift devices is to provide lift increment at low speed condition (take-off and landing) so that the clean wing is optimized for the cruise speed regime.

There are several HLD (High-Lift Device) on commercial wing aircraft starting from simple plain flaps to Fowler flaps with single, double, and even the most complex triple slots (Boeing 747). The design and optimization of high-lift systems is one of the most complex task in aircraft design. It involves a close coupling of aerodynamics, structures and kinematics [33]. Over decades, the trend for HLD improvement has been strongly supported by more powerful aerodynamic optimization and CAD tools for complex structure simulations.

At the early stage, outstanding High-lift performance ($C_{L,max}$) was achieved by means

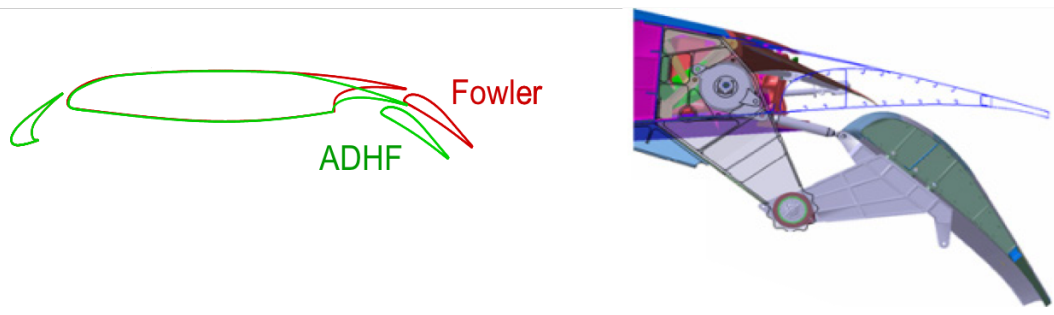


Figure 2.8: Airbus A350XWB high-lift trailing-edge system [34].

of multi-slotted trailing-edge flaps (Fig.2.7). However, these systems allowed to achieve satisfactory performance with penalties in structural complexity and weight and therefore in costs. Later on, the improvement in computation fluid dynamics has permitted to carefully optimize flap airfoil geometry parameters: gap, overlap, airfoil thickness and curvature. For this reason, the major trend was to decrease the number of slots focusing on optimization of Fowler deployment mechanism. On the other side, such Fowler mechanisms required even more complex kinematic actuation systems due to a combination of two movements: translation plus rotation.

The Fowler flap deployment mechanisms were designed by using linear or curved tracks coupled with multi-link system for the rotation. Such devices permits to match very demanding aerodynamic requirements with relatively structurally efficient system (the current system of A350XWB or Boeing 787). In the next future, further improvements in terms of an optimum balance among aerodynamic, structural weight and complexity for a standard single-slot fowler flap appears quite difficult.

Recent development programs at Airbus and Boeing extend the capabilities of a flap systems. The A350 XWB high lift systems incorporate additional functionalities that provide aircraft performance optimization during flight. The A350's flaps are a very simple drop-hinge design with a single slot between the trailing edge of the spoiler and the leading edge of the flap [34].

As the flap extends (Fig.2.8), the spoilers deflect downwards to control the gap and optimize the high-lift performance of flap. It constitutes a multi-purposes high lift system with augmented functionalities and furthermore it is a lightweight structures thanks to its low complexity link-based kinematic [35].

Moreover, for the first time, the flap system will have both the capability for differential inner and outer settings as well as a variable camber function. The design is composed of a gearbox with a motor installed between the outer and inner flap that enables a differential



Figure 2.9: Fairing-less deployment system with a variable-camber (morphing) flap.

control of the relative angle in order to shift inboard the resultant lift for a less bending moment. Furthermore, both inner and outer flaps can be moved together during the cruise to optimise the wing's camber for each phase of the flight and use the polar of drag to its most efficient configuration [34].

It is evident that today's research on high-lift system is moving toward both optimization of the Fowler mechanism deployment system and the external flap aerodynamic shape. The ultimate goal could be the development of innovative mechanisms with continuous curvatures, leading to the removal (or reduction) of slots in order to obtain the same performance with the less Fowler mechanism deflections. In other words, this means to conceive simple deployment system with a variable camber flap in Fig.2.9.

2.7 Beyond the State of the Art

The integration of innovative and affordable technologies in future aircraft platforms is a key success for manufacturers since it increases appeal and benefits for the customers (both airlines and passengers). Future technological improvements of morphing structures have to positively affect all the items contributing to the total cash operating costs such as fuel burn reduction, and reduced maintenance costs.

The actual application of a novel morphing technology can be pursued only when, as a minimum, the following conditions are fully met:

- interfaces and links with other technologies necessary to the aircraft operation must be properly resolved;
- solutions must be acceptable to the aeronautics market; indeed, they have to consider aspects like: certification and safety, reliability during operations, costs, and maintenance process;
- demonstration of feasibility to fulfil the criteria of aircraft manufacturing industry (i.e. in series production).

The research on next morphing technology should have as main goal to fulfil more demanding industrial requirements:

- integration at aircraft level;
- the minimization of spare parts;
- enhancement of the overall system robustness;
- the rationalization of actuation/structure interface;
- the simplification of the overall assembly;
- the reduction of installed power thanks to a lower number of actuators;
- effective distribution of actuators on the entire system for effective shape control.

These main guidelines will be followed during the design on a novel multi-functional morphing Fowler flap where the overall weight, installed power and aerodynamic performances will be constantly monitored and improved.

Chapter 3

Clean Sky 1 Research Project

This chapter will provide an overview on the Clean Sky Joint Undertaking main goals. Green Regional Aircraft ITD will be presented, and the LNC domain explained.

Preliminary Studies on Morphing Flap Feasibility were developed at UniNa during the GRA-ITD Phase 1 (2012-2014); after that, industrial requirements and enhanced functionalities were required during the GRA-ITD Phase 2 (2015-2016).

In the first part of the PhD programme, main activities were related to the advanced design and testing of a bi-modal full-scale outer section morphing flap. FE simulations and Ground Static Test results will be presented and discussed.

3.1 Green Regional Aircraft (GRA-ITD)

The aerospace sector is expected to increase worldwide at an average 4-5% per annum over the next few decades, which is significantly above global gross domestic product growth; in air transport terms, this implies a doubling of traffic about every 16 years [36]-[37]. It is evident that environmental requirements, such as emissions and noise, will play a dominant role in future transport aircraft development, becoming a driving force for aircraft design.

These are the main underlying reasons for which the Advisory Council for Aeronautics Research in Europe, in the 20-20 vision [36] and Flightpath 2050 initiatives [37], established the so-called greening of aircraft as a prime objective for future research activities related to aeronautics.

The green design criteria, as formulated in the Flightpath 2050 agenda, are represented by a 90% cut in NO_x emissions, 65% perceived aircraft noise levels, and a 75% cut in CO₂ emissions per passenger/ kilometre: all compared to the overall levels in 2000. The only ways of achieving these goals are through better engines, more aerodynamically efficient

wings and lighter structures.

In 2010, European Commission launched a major technology activity, intended in the end to address all more promising research topic in the aeronautical field. Clean Sky Joint Undertaking (CSJU) was established as a public-private partnership between the European Commission and the European aeronautics industry that coordinates and funds research activities to deliver significantly quieter and more environmentally friendly aircraft [38].

The CSJU managed the Clean Sky Programme (CS) where main strategic research areas were organized in Integrated Technology Demonstrators (ITDs). There were six main ITDs, each one co-led by two industry leaders for the full duration of the programme (2010-2016). Two ITDs mainly focused on enabling breakthrough technology for large commercial airplane (CS-25 category):

- The **Smart Fixed Wing Aircraft (SFWA) ITD**, co-led by Airbus and Saab, addressed the integration of passive flow, active flow, and load control technologies into new Smart Wing concepts. In this ITD, big effort was spent on enabling Natural Laminar Flow (NLF) technology on a transonic laminar wing profile with a standard aircraft internal primary structure. At the end of the BLADE Project (Breakthrough Laminar Aircraft Demonstrator in Europe), an Airbus' A340 laminar-flow test demonstrator aircraft was tested in flight [39].
- The **Green Regional Aircraft (GRA) ITD**, co-led by Leonardo Aircraft Division and Airbus D&S, delivered and integrated advanced technologies into real regional aircraft configurations.

More in detail, the GRA-ITD [40] was focused on developing new technologies to reduce noise and emissions, with particular focus around advanced low-weight and high performance structures, incorporation of all-electric systems, low noise/high efficiency aerodynamics, and environmentally optimised mission and trajectory management. Hence, the objective of the Green Regional Aircraft ITD was to mature, validate and demonstrate the technologies that best suit the environmental goals set for regional aircraft that will enter service from 2020 onwards.

Regional aircraft typically operate over airports located in the neighbourhood of densely populated areas, with a high frequency of taking-off and landing events and, hence, they strongly contribute to the impact of air transport on environmental noise and pollution.

Furthermore, due to the typical short range of regional aircraft, whose cruising flight distance is only about the 50% of the overall mission path, the climbing performance and the empty weight of the aircraft have both a strong influence on the entire mission fuel consumption and, again, on gaseous contaminants and noise emissions over airports

surrounding regions. For the above reasons, within the Low Noise Configuration (LNC) domain, promising breakthrough technologies were selected with a dual purpose:

- advanced aerodynamics and load control to enhance lift-to-drag ratio at various flight conditions, thereby reducing fuel consumption and air pollutant emissions, also allowing for steeper/noise-abatement climb paths;
- load alleviation to avoid aerodynamic loads exceeding given limits at critical conditions (gust and high-speed manoeuvre), thus optimising the wing structural design for weight saving.

Several concepts and respective technical solutions were investigated following a rigorous maturation road map; every concept was demonstrated in a realistic experimental environment, representative of the operational conditions expected in flight (TRL 5). More representative technologies developed were:

- Natural Laminar Flow (NLF) wing to improve aerodynamic efficiency in cruise
- Active control of wing movables for Load Control and Alleviation (LC&A) functions
- Droop nose: a gap-less high-lift device for the wing leading-edge
- Morphing flap: a novel single slotted high-lift device for the wing trailing-edge

3.2 Preliminary Studies on Morphing Flap Feasibility (GRA Phase 1)

Conventional aircraft Fowler flaps are pushed out behind the wing to increase lift at low speed on take-off and landing. Therefore, flaps allow the wing to be sized for cruise where most of the fuel is burned but still are able to safely take-off and land in reasonable distances.

In addition, conventional aircraft wings have slots to direct high-pressure air over the airfoil upper surface for maintaining flow attachment at high Fowler flap deflections. However, they generate noise and make flight less efficient and unable to respond to changes in flying conditions.

During the first phase of GRA-ITD Low Noise Configuration (LNC) domain, the design and the technological demonstration of a novel high-lift device enabling the camber variation of a flap segment was requested with the specific target to enhance the high lift performance of the 90-seats next generation green regional aircraft (CS-25 category [41]).

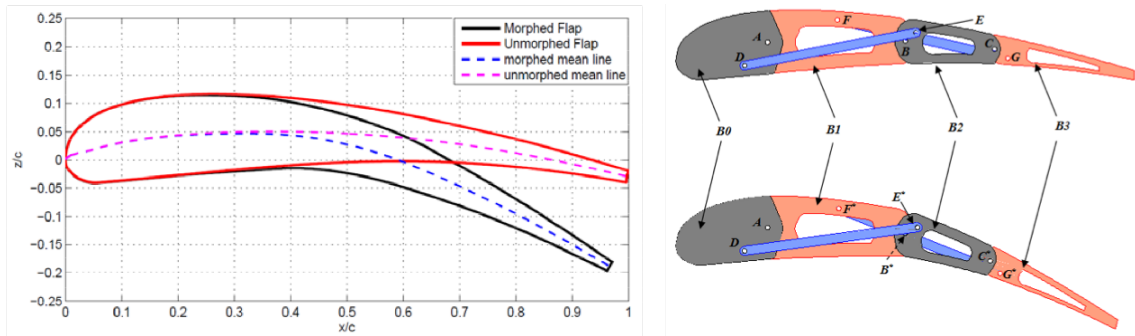


Figure 3.1: Flap airfoil [42]: (left) target geometry; (right) Morphing "finger-like" rib layout.

The basic idea driving the implementation of such technology was to replace a conventional double-slotted flap with a single-slotted morphing flap capable of increasing flapped wing $C'_{L,max}$ and stall angle while targeting to a reduced complexity of the flap architecture and of the associated deployment system. In addition, noise reduction can be obtained reducing the number of slots in the high-lift system.

Because of the specific demand of a product of industrial relevance, the reliability, the maintainability and above all the absence of out-of-the-standards solutions were considered as paramount requirements for the design of the morphing structure till from preliminary concept definition. To show the feasibility of the morphing solutions, the preliminary studies [42] were limited to a portion of the flap element obtained by slicing the actual flap geometry (0.62m chord) with two cutting planes distant 0.4m along the wing span.

Thanks to the limited span-wise size of the investigation domain, the flap tapering was neglected thus reducing the complexity of a 3D aero-structural problem to a 2D analysis. Target morphed shapes (Fig. 3.1 right) were evaluated on the base of 2D CFD optimization analyses [43] and were provided as input data for the design activities.

Referring to the unmorphed and morphed airfoils of the flap element, the conceptual layout of an articulated (finger-like) rib structure was assessed in order to physically realize the transition from the baseline airfoil configuration to the target one.

The rib structure (Fig. 3.1 left) was conceived as a mechanism characterized by four plates connected by hinges: B0, B1, B2 and B3. B0 and B2 had the same middle plane; B1 and B3 were staggered respect to them sharing always a common middle plane [44].

Each plate was connected to the adjacent one by a hinge located on rib camber line (points A, B and C, respectively at 20%, 50% and 70% of rib chord).

Plate B0 was linked to plate B2 by means of a rod element hinged at points D and E, hinges D and E being respectively located on B0 and B2. Plate B1 was linked to plate B3 through a second rod hinged at points F and G.

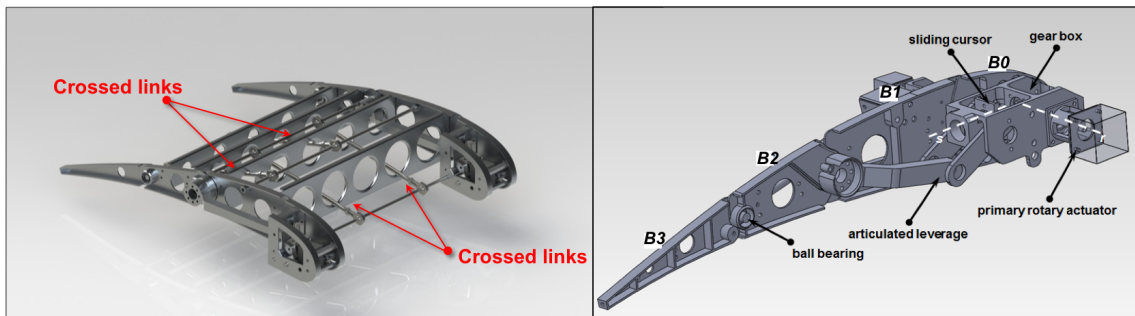


Figure 3.2: Morphing Flap (GRA Phase 1)[42]: (left) crossed links; (right) trasmission line.

Crossed links (DE and FG) positions were conceived in order to assure specific rotation ratios between adjacent plates and an overall plates movement useful to match the target morphed shape (Fig. 3.1 right). More in detail, considering plate B0 fixed on flap strut, a downward rotation of B1 around A by an angle of 3° makes all the other plate to move so that the final positions of hinges B and C (Fig. 3.1 left) are on the camber line of the morphed airfoil. Generally speaking, the rib architecture represents a single degree-of-freedom system; if a single plate was moved by a unique actuator, all the other plates were driven to move in compliance with the final shape to be achieved.

The actuation of the second rib block (B2) was obtained by means of an articulated leverage amplifying the displacements induced by the primary rotary actuator (Fig. 3.2). More in detail, a gear box converted the rotation of the actuator shaft (axis r of Fig. 3.2) into the rotation of an endless screw perpendicular to the shaft (axis s of Fig. 3.2); the rotation of the endless screw moves a cursor which slides along the endless screw and moves the second rib block by acting on the articulated leverage. All the other blocks follow the movement of the second block thanks to the crossed links between blocks B0-B2 and B1-B3 (Fig. 3.2).

At the end of GRA-LNC Phase 1 (2012-2014), a limited scale prototype was finally manufactured and tested. The structural layout was able to withstand static loads representative of the aerodynamic pressures expected in service [42]. At the end of the test campaign, experimental data confirmed the feasibility of a structural arrangement for camber morphing through a smart combination of conventional elements and materials.

The skeleton of the demonstrator was able to withstand aerodynamic design loads without detrimental deformations. However, crossed links (DE and FG, in Fig.3.1) located along the bay (Fig.3.2) experienced a difficult assembly process not compliant with required industrial standards.

The actuation system, based on an endless screw activating a leverage, was able to

provide shape transition and hold the demonstrator in a fixed position upon aerodynamic loads. However, because each rib required at least one actuation system, upscaling that concept to a true-scale flap demonstrator will require a large number of motors (up to 10 for a 3.6m demonstrator). Therefore, when a full-scale concept was required in the GRA-LNC Phase 2 (2015-2016), a new demonstrator with a new strategy was conceived.

3.3 Morphing Inner-Section Flap (GRA Phase 2)

After the promising results obtained during the first phase of the CleanSky GRA project, further activities were addressed to increase the TRL of the validated morphing flap technology. During the second phase of the Clean Sky GRA-ITD (2015-2016), a larger true-scale segment of the outer wing flap was selected as investigation domain for the new architecture in order to duly face the challenges posed by real wing installation issues especially with reference to the tapered geometrical layout and 3D aerodynamic loads distributions. In addition, a new wing load control device was required to enhance aerodynamic efficiency in all flight conditions and, hence, to reduce fuel consumption and pollution over the whole mission also allowing for steeper initial climb, noise-abatement flight trajectories.

For instance, the new innovative flap architecture was designed in order to enable two different morphing modes on the basis of the A/C flight condition:

- **Morphing mode 1:** overall camber morphing to enhance high-lift performances during take-off and landing (flap deployed);
- **Morphing mode 2:** tab-like wing tip rotation (flap stowed); upwards and downwards deflection of the flap tip during cruise and off-design flight phases (e.g. climb and descent) for load control at high speed.

The investigation domain covered the flap region spanning 3.6m from the wing kink (Fig. 3.3) and was characterized by a taper ratio equal to 0.75 with a root chord equal to 1.2m. The chord-wise extension of the flap tip - to be deflected according to morphing mode 2 - was set equal to the 10% of the local wing chord (red-coloured portion in Fig. 3.3). Maximum and minimum deflections required for a typical aircraft mission resulted respectively equal to $\pm 8^\circ$.

The dimensions of the flap tips and the deflection angles were defined on the basis of preliminary CFD analyses carried out at aircraft level and at cruise speed.

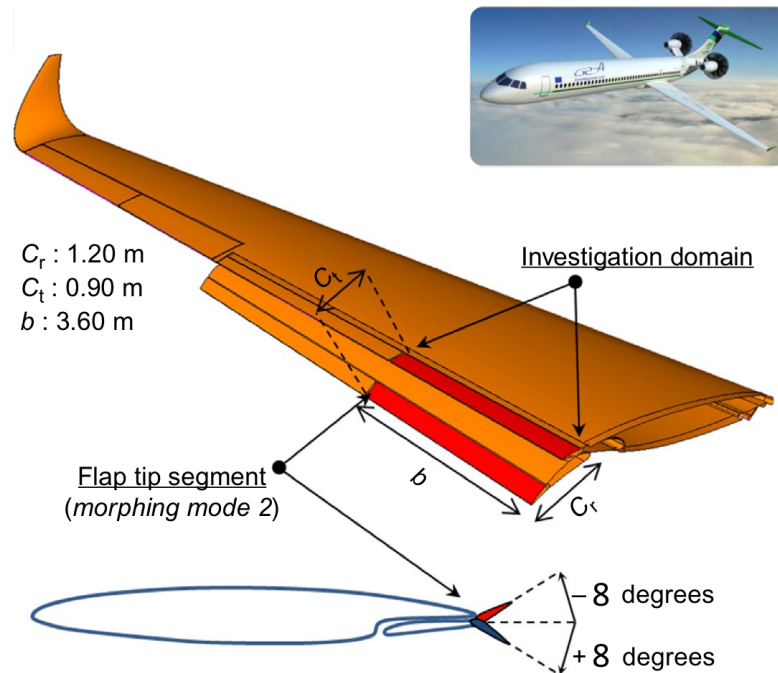


Figure 3.3: Morphing outer section flap, investigation domain (GRA-ITD, phase 2).

3.3.1 Morphing Architecture

The bimodal morphing capability was implemented by active ribs playing the role of inner movable articulation of the flap structure. The generic rib (Fig. 3.4) was segmented into four consecutive blocks (B0, B1, B2, B3) connected to each other by means of three frictionless cylindrical hinges located on the camber line (A, B, C).

Consecutive blocks can rotate respect to each other; hence, the rib mechanism uses a four segments polygonal line to approximate the camber line of the flap airfoil and to morph it into the desired configuration while keeping unchanged the airfoil thickness distribution.

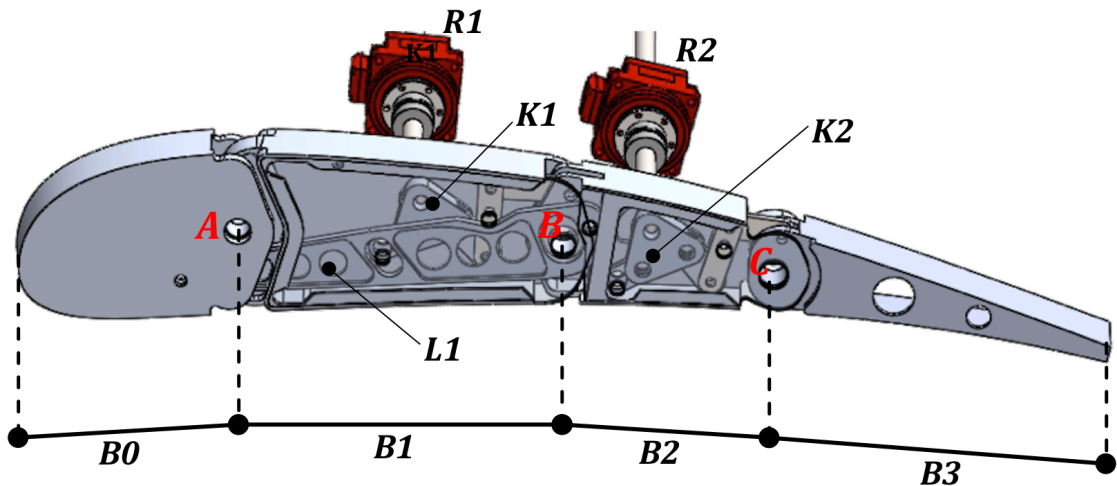
Blocks B0 and B2 are interconnected by means of a suitably shaped beam (L1) having two hinges at the edges; an internal leverage (K1) is hosted by block B1 and interconnects blocks B1 and B2. This leverage is activated by the external rotary actuator (R1) and amplifies its torque. The rotation induced by R1 makes the leverage K1 to move and therefore changes the relative position of block B2 with respect to block B1.

The position of the link L and of the pivots of the leverage M1 are selected in a way that, upon the rotation of R1 and R2 shafts, all the rib blocks rotate around hinges A,B,C according to specific angles compliant with the family of external morphed shapes to be matched. A secondary leverage (K2) links B3 to B2 and is driven by the rotation of the

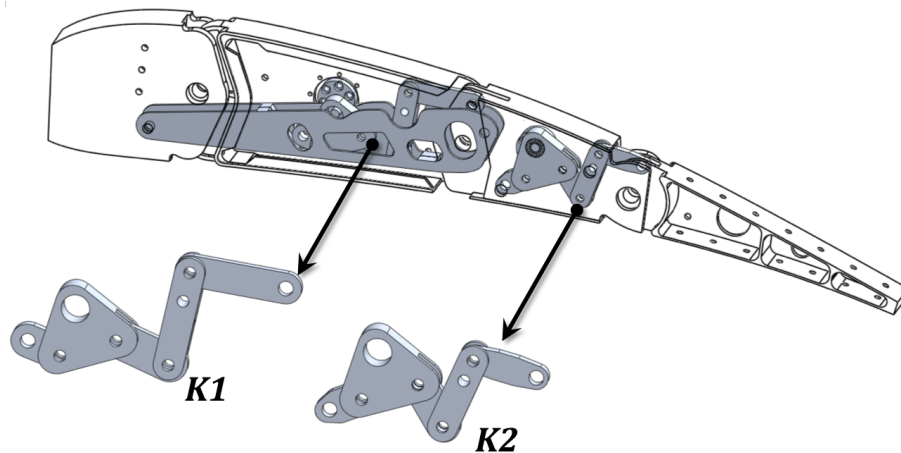
actuator R2.

The secondary leverage, hosted by block B2, amplifies the torque of the actuator R2 and makes B3 to rotate around the hinge C thus implementing the tab-like morphing.

During morphing mode 1, both K1 and K2 leverages are respectively activated by actuators R1 and R2 (camber variation, Fig.3.13). On the other hand, actuator R1 is powered off during morphing mode 2 (tip deflection, Fig.3.13).



(a) Symbol used.



(b) Stephenson's Six-bar [47] linkages (K1 and K2).

Figure 3.4: Segmented rib (GRA-ITD, phase 2).

All items of the actuation system are shown in Fig. 3.5b. The hollow shaft brushless motor (R1) provides the shaft torque, amplified by a HarmonicDrive® gearbox, to active the primary leverage (K1) connecting blocks B1 and B2. In such a way, relative rotation

between consecutive blocks B1 and B2 is obtained by means of torque provided by actuator (R1) amplified through the primary leverage (K1).

The secondary rotary actuator (R2) provides the shaft torque, amplified by another HarmonicDrive® gearbox, to the secondary leverage (K2) connecting consecutive blocks B2 and B3. Hence, the actuation torque is properly amplified through the secondary leverage (K2), and the tab-like morphing mode is properly enabled.

Motor parameters and performance data are reported in Fig.3.7a; torque amplifier parameters (i.e. Harmonic Drive) are summarized in Fig.3.7b.

The morphing rib layout was conservatively designed with reference to the flap tip section characterized by the minimum available room for actuation chains (K1, K2) installation. However, a parametric 3D-CAD was generated to quickly scale the tip rib layout according to the geometrical features of the other flap sections, equally spaced along the flap span by a distance of 0.485m and perpendicular to the flap trailing edge.

In addition, lengths of blocks B1 and B2, linking element (L1), and leverages (K1, K2) were kept equal for all flap sections thus obtaining hinge lines perpendicular to ribs' reference planes. The outer flap section had a taper ratio equal to 0.75, hence rib blocks B0 and B3 were properly scaled to match the chord of each flap section.

The ribs' kinematic was transferred to the overall flap structure by means of multi-box arrangement (Fig.3.7a). Each box of the structural arrangement was characterized by a single-cell configuration delimited along the span by homologue blocks of consecutive ribs, and along the chord by longitudinal stiffening elements (spars).

The articulation of the entire flap structure was enabled by actuation of the ribs; thus if the shape of each rib is prevented by locking the actuator shaft, the structural skeleton is elastically stable under the action of the external aerodynamic loads.

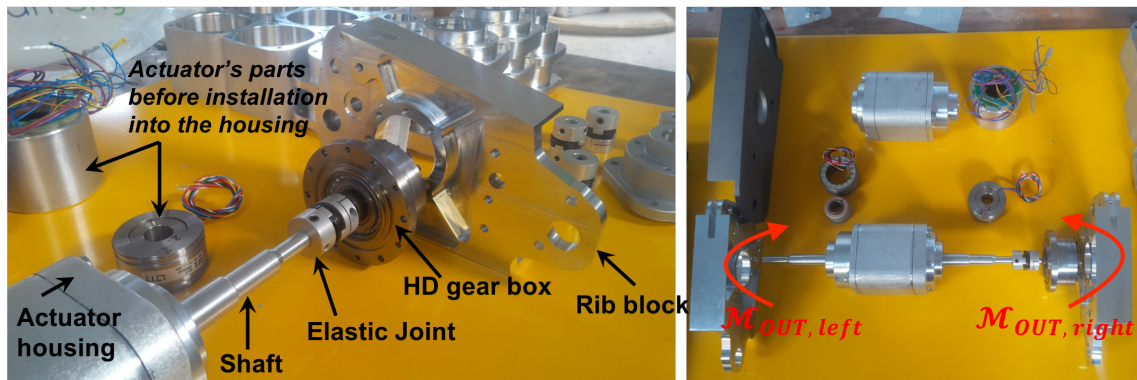
Segmented spars were then adopted to generate the multi-box arrangement elastically stable under bending and torsion. Two C-shaped (continuous) spars were positioned in correspondence of the 0% and 70% of the local airfoil chord in order to link all blocks B0 and B3 along the span. The spars were suitably conceived to provide the greatest contribute in carrying external loads while assuring adequate deformation levels to the entire assembly.

Both ribs and longitudinal stiffening components were properly shaped in order to enable the installation of a segmented skin solution characterized (on both upper and lower side) by four elements in Al2024-T4 sliding on each other as armadillo shells (Fig.3.6b). A segmented skin solution, with embedded silicon seals, was adopted on both upper and lower flap surface.

Each skin segment was properly screwed along spars and ribs' plates. Consecutive skin segments slide one on each other during the two different morphing modes, generating an



(a) Final prototype



(b) Actuation group assembly.

Figure 3.5: Morphing outer-section flap (GRA-ITD Phase 2): final demonstrator.

armadillo like covering structure.

Rubber seals were used to avoid friction between adjacent skin segments as well as to prevent airflow leakages. Al2024-T351 was considered for ribs, spars, linking beam elements (L1), and items of the actuation chains (K1, K2). The shape of the seals was defined by means of 3D-CAD kinematic analysis simulating flap morphing in both modes; these analyses also allowed for the verification of the implemented assembly tolerances while proving the absence of clashes between adjacent subcomponents in relative motion.

All metallic parts were produced by referring to numeric-control machining with the exception of the skin panels that were obtained by sheet forming. The thickness of components along the interface regions were increased with respect to the design values in order to allow for the implementation of screwed joints. Riveting was indeed avoided to safeguard the reversibility (and the costs) of the prototype's assembly process.

All parts' surfaces were treated and primer-painted before the final assembly; in

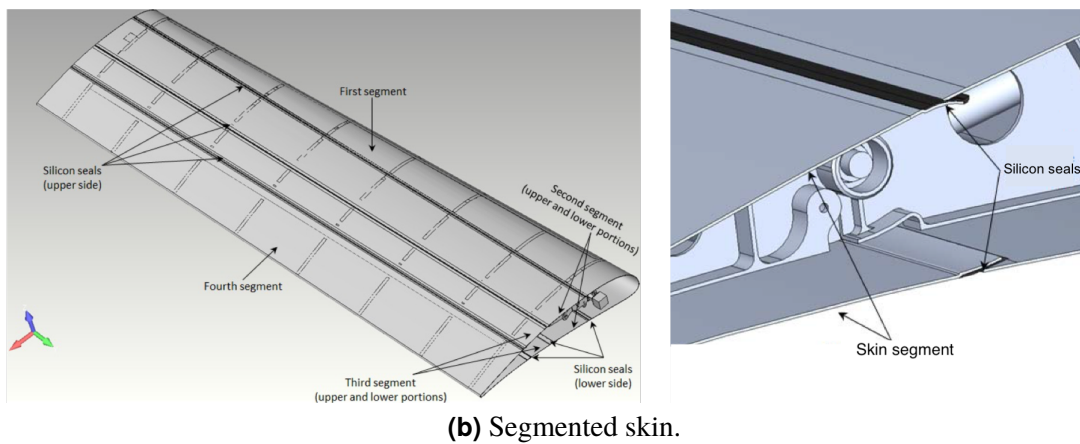
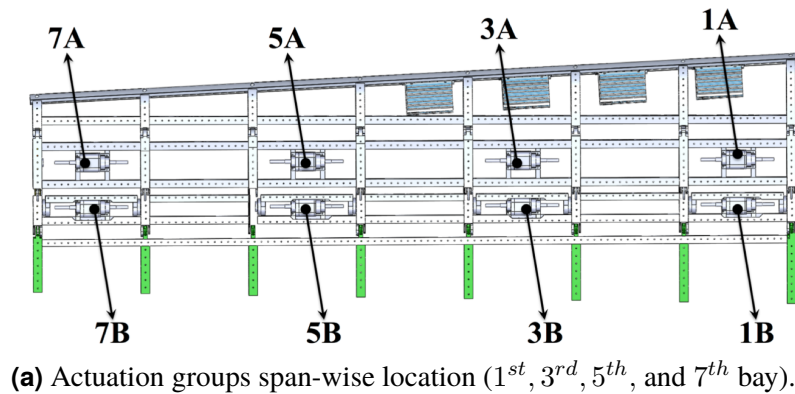


Figure 3.6: Morphing outer-section flap (GRA-ITD Phase 2): actuations and segmented skin.

Fig.3.5a the manufactured prototype is reported.

In Fig.3.5a the manufactured skin solution has been shown with reference to the fourth and fifth bays of the prototype. Gaps between consecutive skin modules were kept lower than 0.7 mm along the flap airfoil thickness direction. Trade off-studies were carried out to find out the minimum number of actuators required to morph the flap under the action of design aerodynamic loads. On the basis of the available space and taking in account specific constraints in terms of efficiency, power and reliability, the Kollmorgen® brushless motor KBMS-14 was down-selected ([50]).

Four actuation groups were considered adequate to move the entire device in operative conditions, they were respectively linked to the 1st, 3rd, 5th, and 7th bay (Fig.3.7a) and duly coupled to Harmonic-Drive® gearboxes (model HFUC-17-120-2UH-SP2983) hosted by ribs blocks and acting as amplifiers of the actuation torque (and reducers of the shaft rotation speed). In Fig.3.5b the assembly sequence of actuators, gearbox and rib blocks is described.

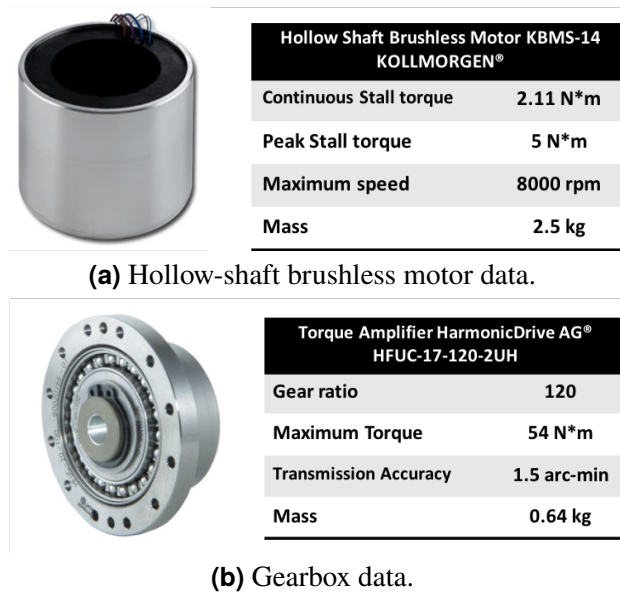


Figure 3.7: Technical data of COTS actuation system parts.

3.3.2 Finite Element model of the full-scale prototype

The 3D-CAD of the structural layout was used to address detailed stress verifications based on advanced FE models and analyses. The detailed modelling of such a complex morphing system involved the proper schematization of all sub-assemblies: ribs blocks, skin segments, spars, as well as cylindrical hinges, rivets and screws used to link parts while assuring required kinematic implementation.

Modelling guidelines were compatible with Finite Element Method approaches; element type, property and mesh size were rationally defined in order to get detailed and reliable distributions of stress and strains (especially around holes) while optimizing the computational time required for each analysis. The detailed Finite Element model was designed to be fully representative of the final flap layout (Fig.3.5a).

The blocks of each rib were modelled with tetra solid elements (CTETRA10 [88]); linking beam element (L1) and actuation chains (K1, K2) were modelled with hexa solid elements (CHEXA8 [88]). Longitudinal spars and skin segments were meshed with shell element (CQUAD4 [88]).

As fully explained in the previous Section 3.3.1, the articulation of the entire flap architecture was provided by means of actuator to segmented active ribs; in such a way, morphing modes were ensured. Hence, ribs' kinematic was properly preserved in the full-scale flap finite element model. All cylindrical hinges (A, B, C) connecting consecutive rib blocks and items of the actuation chains (K1, K2) were modelled with beam and rigid

body element (RBE2 [88]).

The pin, used for fastening together adjacent items, was modelled with a beam element (CBEAM [88]); torsional degree-of-freedom of one beam end was released in order to allow rotation around the cylindrical hinge axis. The connection, between each pin edge and the relative surface hole, was defined by means of rigid body element RBE2 [88]: with independent degrees-of-freedom specified at each pin edge, and dependent degrees-of-freedom associated to all grid points on each surface hole.

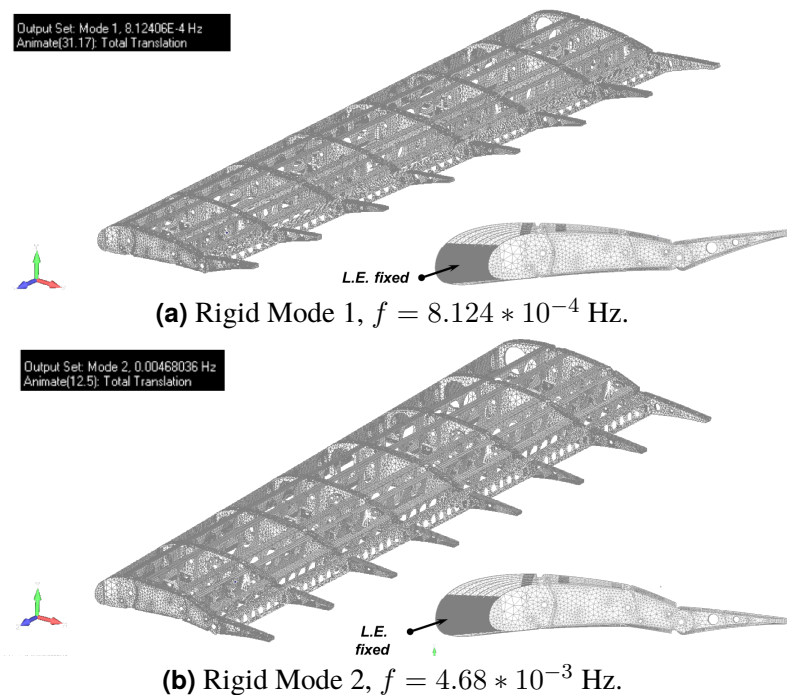


Figure 3.8: Morphing Flap FE model, modal shapes pertaining to rigid modes.

Per each articulated rib, two rotary actuators (R1, R2) provide the required torque to enable transition from the baseline configuration to the morphing modes.

A generalized spring-and-damper element CBUSH [88] was properly defined to model the stiffness of rotary actuator, shaft, and Harmonic Drive® gearbox in all directions.

In order to check kinematic consistency of the entire finite element model, a modal analysis was performed with the flap leading edge constrained in all degrees-of-freedom. Moreover, all actuator shafts, and harmonic drive gearboxes were removed: in such a way, all consecutive rib blocks might freely rotate around their respective hinge-axes.

Two rigid modes were found. As expected, the whole flap kinematics was properly modelled: the first modal shape replicates the tab-like mode (Fig.3.8a); the second modal shape combines the camber-morphing mode with the tab-like morphing mode (Fig.3.8b).

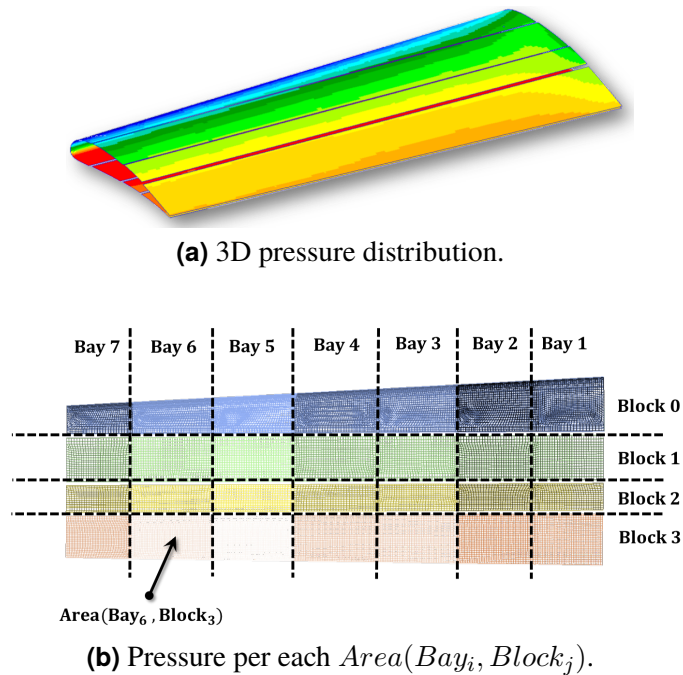


Figure 3.9: Limit load condition: 3D pressure distribution.

In addition, modal analysis results highlight the kinematics of the articulated rib: a double degree-of- freedom mechanism, one per each leverage/motor shaft interface.

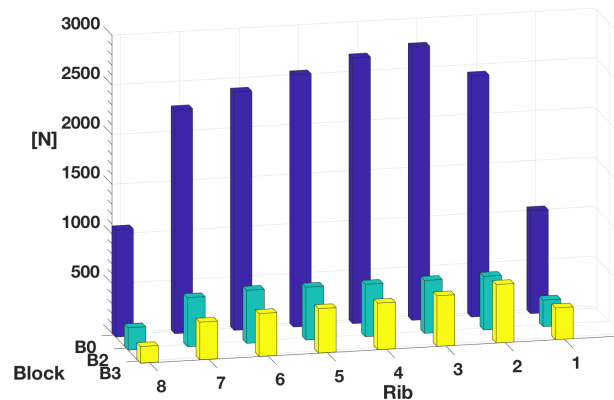
Once the reliability of the model was proved in terms of smooth simulation of morphing kinematics, actuators transmission line was re-connected to the ribs and actuators shaft rotation was prevented in order to address static analyses.

3.3.3 Limit Load reproduced in the Ground Static Test

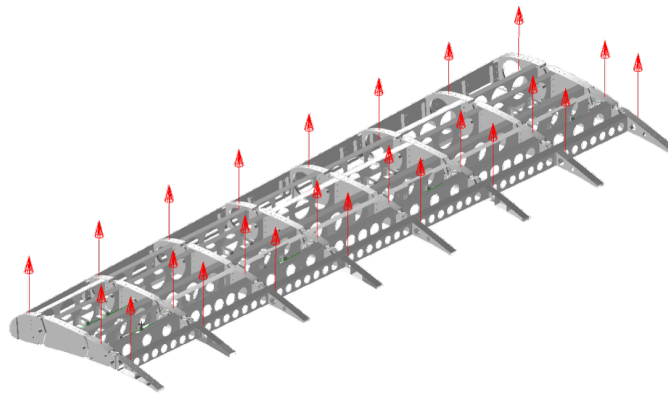
The 3D aerodynamic load distributions, related to different aircraft conditions and flap settings, were deeply analysed in order to validate the innovative outer wing flap architecture in the most critical and relevant environment. Among all 3D aerodynamic loads evaluated by means of CFD, the design load pressure distribution was attained at flight speed of 95 m/s at sea level, and flap deployed of 35 degrees. The 3D contour pressure distribution (Fig.3.9a) was properly reduced in a equivalent forces system applied on centre of blocks B0, B2, and B3 of each rib (Fig.3.10b).

The flap was constrained in correspondence of the blocks B1 belonging to the third and the sixth rib (from the root section) thus simulating a rigid deployment track.

Lumped forces pertaining to the pressure distributions along blocks B1 were transferred to adjacent blocks while preserving overall shear, bending moment and torque resultants.



(a) Forces values.



(b) Lumped forces system.

Figure 3.10: Lumped forces system used in the Ground Static Test (GST).

In addition, both load cases present the same total load resultant and moment distributions around blocks hinge (A, B, and C). Moreover, the equivalent forces system can be efficiently reproduced by means of a whiffle-tree load system in the Ground Static Test (GST). Total limit load resultant, applied on the flap structure, is equal to 20126N; resultant forces acting on each rib are summarized in Fig.3.10b.

3.3.4 Static Analysis

Linear static analyses were carried out in MD-Nastran® environment at both limit and ultimate (1.5 times the limit) loads conditions with locked actuator shafts. The flap was constrained in correspondence of the blocks B1 belonging to the third and the sixth rib (from the root section) thus simulating a rigid deployment track.

The morphing flap structure was placed in its baseline configuration and loaded by

the equivalent forces system pertaining to flap deployed configuration (Fig.3.10b). Such a combination of configuration and load was the most conservative for the following reasons:

- Aerodynamic loads acting in flap deployed configuration are higher than the one arising in baseline configuration;
- Aerodynamic loads pertaining to flap deployed configuration induce higher bending moments in wing rib structure when the rib is in its un-deflected position.

For the static analysis of the FE model with the skin, at limit load condition the maximum displacement of 102mm was found at the trailing edge root rib (Fig.3.11a).

For each condition the reaction couples at locked actuator shafts ($\mathcal{M}_{OUT,left}$ and $\mathcal{M}_{OUT,right}$) were calculated and verified to be less of the maximum actuation torque provided by the implemented system. The torque required to restore the un-deflected configuration was calculated by means of a dedicated linear analysis carried out on flap deformed shape with enforced motion of the actuator shafts. Also in this case, the obtained torque resulted compliant with actuation system performances.

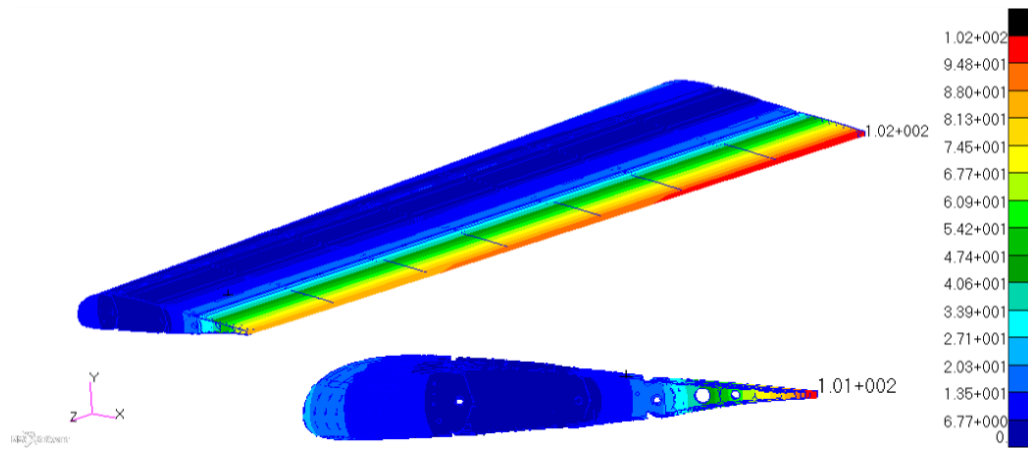
For the FE model without the skin, at limit load condition the maximum displacement was equal to 129mm at the trailing edge of the third rib.

For limit load condition, the reaction couples at locked actuator ($\mathcal{M}_{OUT,left}$ and $\mathcal{M}_{OUT,right}$) shafts were calculated and summarized in Fig.3.16.

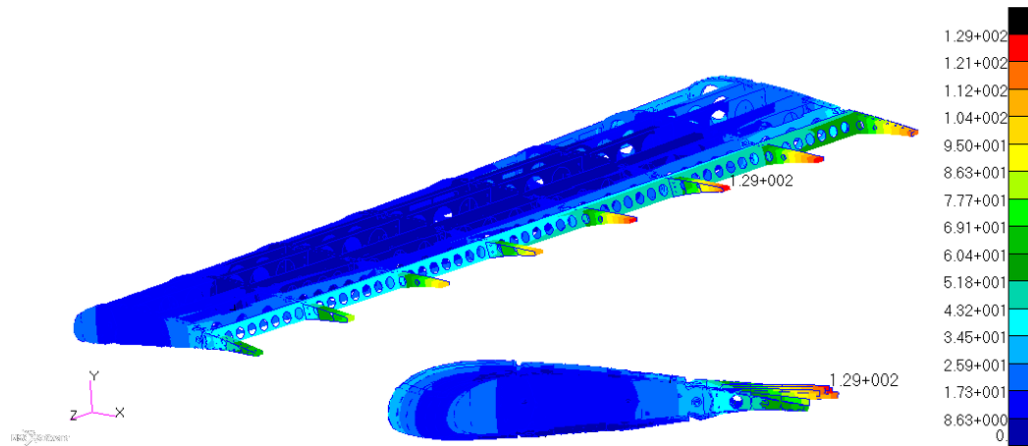
Comparing resistant torques (Fig.3.16) at limit load with torques provided by each actuation group ($\mathcal{M}_{act} = M_{mot} \cdot F_{HD}$, motor torque $\mathcal{M}_{act} = 1\text{Nm}$ amplified by the Harmonic-Drive® gear ratio $F_{HD} = 120$), a restore torque can be applied to deformed structure to compensate the elastic deformations.

As per the applicable sections of the airworthiness requirements [41], the absence of any local plasticization or elastic instability was verified up to limit loads while the clearance from any failure was proved up to the ultimate loads. Very low stress values were found along the skin, its participation in loads adsorption being reduced with respect to conventional arrangements.

As expectable, the highest stress values arose around the constrained regions simulating the links to the flap track. The highest stress concentration were detected in correspondence of the constrained blocks of rib 3 and 6 as well as in the internal elements of rib 3 and 6 mechanisms. The spars adjacent to the constrained ribs resulted consequently more stressed than the others. As evident from Fig.3.12, no elements of the load carrying structure was anyway interested by stress values greater them material allowable.



(a) FE model with skin at Limit Load condition.



(b) FE model without skin at Limit Load condition.

Figure 3.11: Morphing Flap FE model, Displacements [mm].

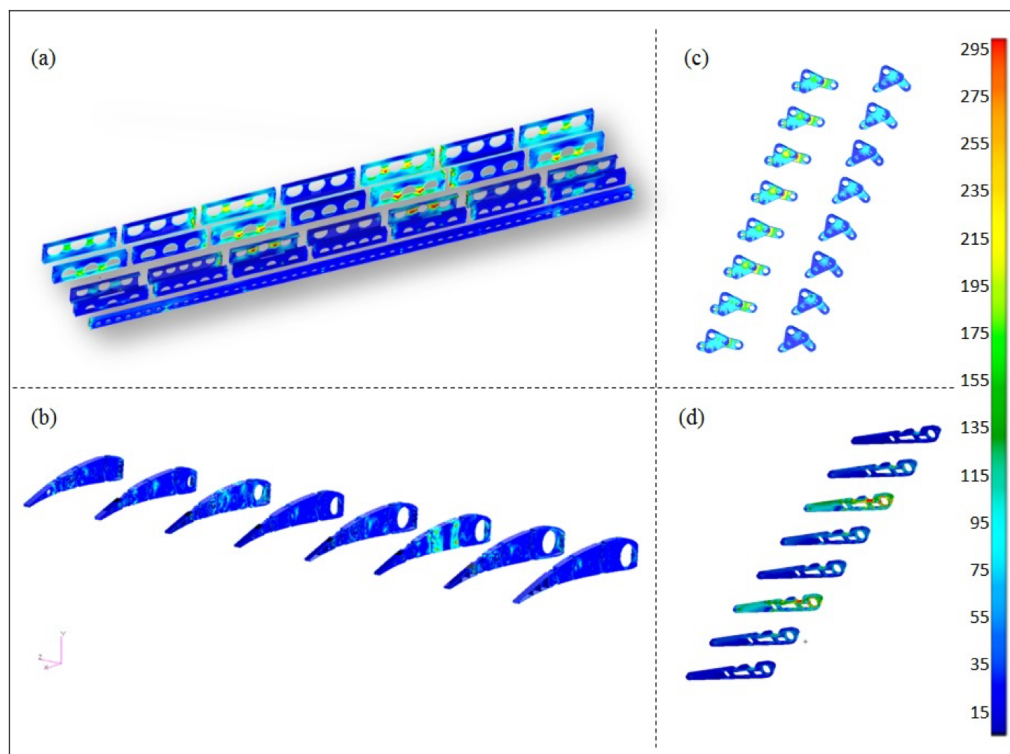


Figure 3.12: Bi-modal Flap, VM stress [MPa]. (a) Spars, (b) Ribs, (c) Leverages, (d) Links.

3.3.5 Overview of the Experimental Tests Performed

The morphing flap prototype was used as mechanical demonstrator to prove the adequacy of the adopted solutions with respect to design requirements and system specifications.

Two test campaigns were carried out: a functionality test campaign, and a static test campaign. The main objectives of each campaign have been outlined in the following subparagraphs together with a general description of performed pre-test activities and test outcomes.

In order to visually check the status of the inner structure and embedded equipment, skin modules were removed during all tests. For static tests, the applied load was reduced in order to compensate the increased structural elasticity due to the absence of the skin.

3.3.6 Functionality Test

These tests [50] were carried out to demonstrate that the flap was able to reproduce target morphed shapes in a controlled and repeatable manner. The target morphed shapes were considered successfully reached when the angles between adjacent rib blocks -obtained upon actuators activation- matched the design values pertinent to each morphing mode with a precision of 0.5° .

The first and the last sections of the flap were then equipped with additional high precision encoders measuring the relative rotations between blocks B0 and B1 and between blocks B2 and B3 (as shown in Fig.3.13a); due to the mechanical link between B0 and B2 it was considered un-relevant to place an additional encoder also between B1 and B2. Additional encoders were equipped with digital displays for real-time measure reading. The flap was then installed on an exhibition rig and secured to an external rig with a safety rope. Final target morphed shapes were reported in Fig.3.13b.



(a) Setup hardware.



(b) Functionality test: (left) full-camber mode, (right) tip deflection upward.

Figure 3.13: Bi-modal morphing flap (CS1): functionality test.

3.3.7 Ground Static Test

Static test was carried out to demonstrate the flap's capability of withstanding limit loads without permanent deformations, failures or buckling (as per part C of EASA airworthiness requirements CS-25 [41]). Due to the relevance of the loads to be applied (as reported in Sec.3.3.3), detailed numerical simulations of the test were carried out in order to:

- rationally address the experimental campaign, being prepared to detect (potentially dangerous) deviations between the actual and the expected structural behaviour of the device;
- properly define the most relevant area of the prototype for the installation of deformation and displacement sensors;
- properly verify the adequacy of the test rig and of the load transfer mechanism.

To this aim the detailed finite element model used during the flap design process (Sec.3.3.2) was assembled to the finite element model of the test rig, thus fairly reproducing the load transmission paths (whiffle-tree) and constraints conditions expected during the tests (3rd and 6th bays clamped).

In Fig.3.14 the assembled flap with the test rig setup hardware is depicted. A single lumped force of 1500kg (scaled limit load condition) was introduced to simulate the action of the hydraulic jack positioned at the top of the whiffle tree. The true limit load was properly scaled in order to account for the decreased stiffness of the test-article due to the absence of skin.

On the basis of pre-test analyses, strain gauges were positioned in the most stressed zones of the rib links and spar, being the max expected strain sensor (MSS) located on the second rib linking beam element (L1). LVDT sensors were used to measure the elastic deflection, the max expected deflection sensor (MDS) was the one at second rib tip. In Fig.3.14 the test set-up is reported with indication of MSS and MDS positions.

Load steps of 100kg up to 1500kg, with a loading speed of 10kgs, were considered adequate to avoid any dynamic amplification. A pause of 10s at the achievement of each load step was moreover set to check data acquisition; load levels were measured through a load cell installed between the hydraulic jack and the whiffle tree (Fig.3.14).

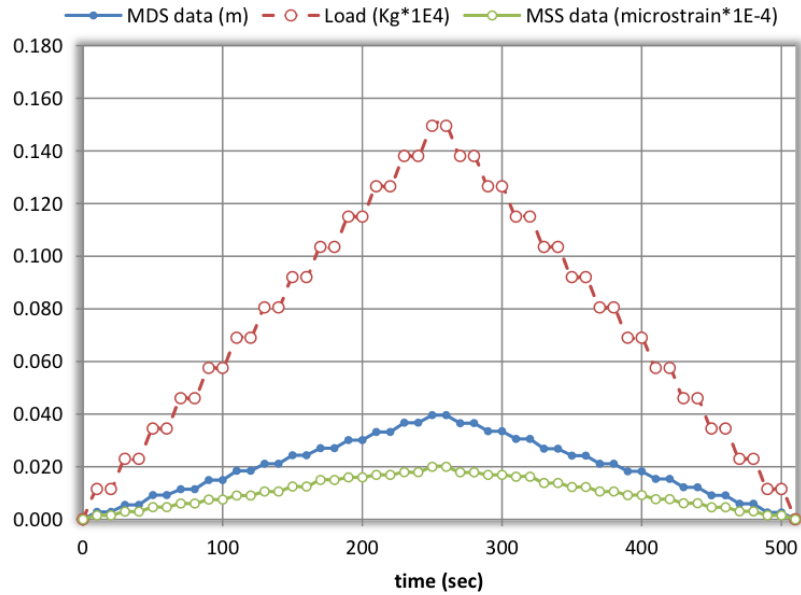
No failures occurred during tests. Load value, MDS and MSS recorded data have been plotted versus time in Fig.3.15; the full elastic recovery of the prototype is shown also by recorded data by strain gauges in Fig.3.15b. The maximum recorded deformation and displacement resulted in good agreement with numerical expectations.

Finally, motor torques (\mathcal{M}_{mot}) were monitored during the ground static test. Torques of each actuation group were estimated as follow: $\mathcal{M}_{act} = M_{mot} \cdot F_{HD}$, with \mathcal{M}_{mot} torque recorded by embedded motor sensors, and $F_{HD} = 120$ the Harmonic-Drive® gear ratio.

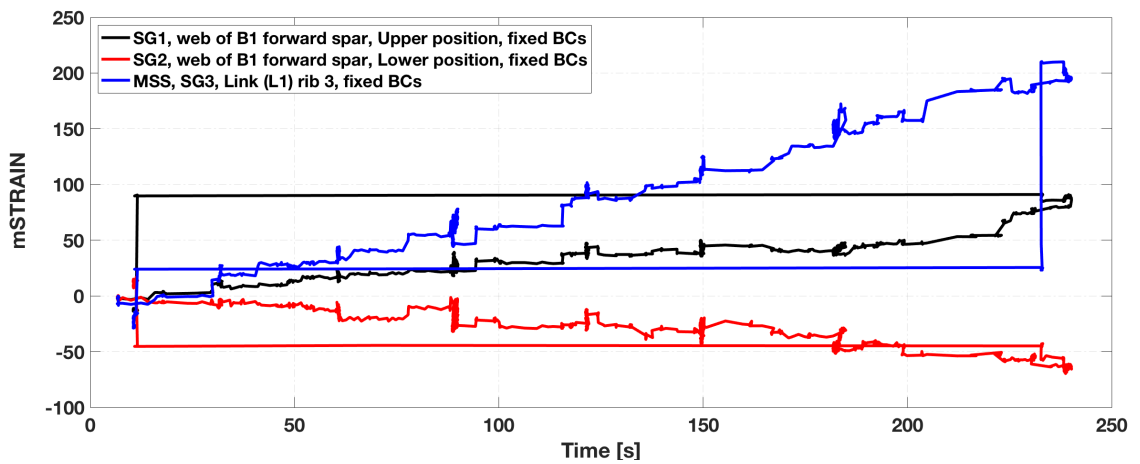
Maximum values of actuation torques, required to lock each rib leverage K1 and K2 in the baseline position, were attained at the maximum applied load. These values were in good agreement with the ones obtained by FE simulations (Fig.3.16). After the static test, the functionality of the flap was verified and no malfunctions were found.



Figure 3.14: GST (Ground Static Test) Setup Hardware.

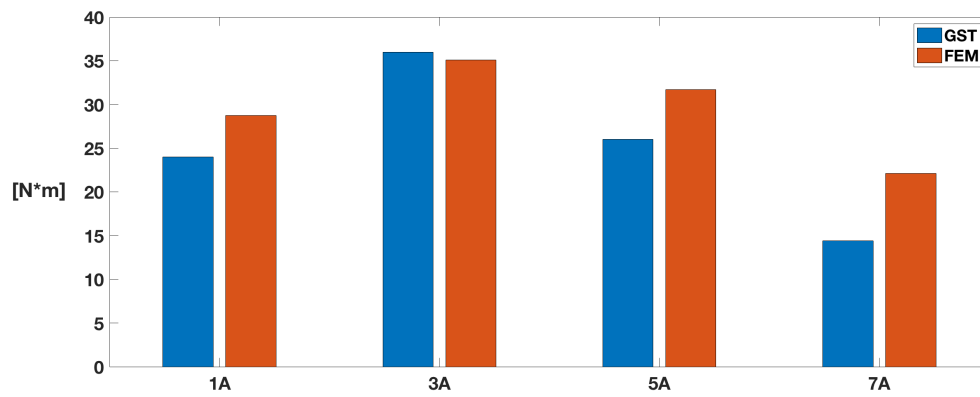


(a) MDS and MSS data.

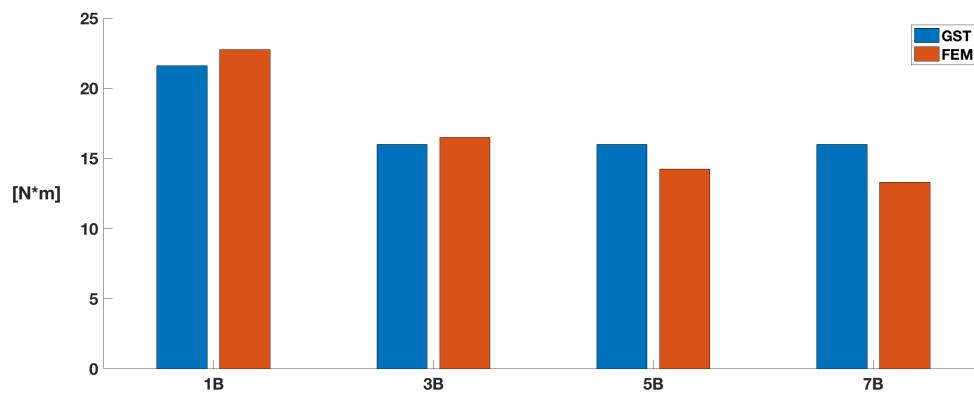


(b) Stain Gauges (SG) data obtained.

Figure 3.15: Ground Static Test (GST) results.



(a) Forward actuation groups.



(b) Rear actuation groups.

Figure 3.16: Bi-Modal Morphing Flap: actuation torques correlation between FEM and GST.

Table 3.1: Bi-modal morphing flap.

Component	Weight [Kg]
Multi-box skeleton (ribs, spars)	91.02
Segmented skin	36.76
16 HD gearboxes (2 per each rib)	11.52
8 brushless motors	20
8 shafts	4.72
8 controller	9
Total flap weight	173.02

3.4 Conclusions

The full-scale prototype was tested to:

- demonstrate the morphing capability of the conceived structural layout;
- demonstrate the capability of the morphing structure to withstand static loads representative of the limit aerodynamic pressures expected in service;

Rational approaches were implemented in an efficient test campaign providing the necessary database for the mechanical demonstration of the morphing structure. Test outcomes showed that:

- reliable, controllable and stable morphing compliant with design requirements is assured by the device for both morphing modes (1 and 2);
- no permanent deformations nor loss of functionality occurs up to the investigated limit load (2013 kg total normal load, scaled to 1500 kg due the absence of the skin during tests).

In addition, good correlation levels with respect to numerical expectations were observed both in terms of static deflections under applied loads and elastic deformations.

The reliability of modelling approaches, implemented during the design and pre-test phases, was therefore considered more than satisfactory. Final weight of the bi-modal morphing flap is reported in Tab.3.1.

Chapter 4

Clean Sky 2 Research Project

4.1 Regional Integrated Aircraft Development Platform (REG-IADP)

Following the success of the initial Clean Sky Programme, its successor, Clean Sky 2, was launched in 2015 as part of the Commission's Horizon 2020 Research and Innovation Programme. Clean Sky 2 aims to be the main contributor to the Commission's Flightpath 2050 goals set by ACARE [37] towards a more smart, green, and integrated transport. It will enable cutting-edge solutions for further gains in decreasing fuel burn and noise emissions. Clean Sky 2 will also contribute to maintaining global leadership in European aeronautics. This goal will be reached by jointly pursuing novel research on breakthrough innovations and demonstrating new vehicle technologies in operative environment.

The Clean Sky 2 Programme consists of three Innovative Aircraft Demonstrator Platform (IADPs) at vehicle level: Large Passenger Aircraft (LPA), Regional Aircraft (REG), and Fast Rotorcraft.

The Regional Aircraft IADP, led by *Leonardo Aircraft Division*, will bring the integration of technologies to a further level of complexity and maturity than before pursued in Clean Sky 1. The goal is to integrate and validate, at aircraft level, advanced technologies for regional aircraft so as to drastically de-risk their integration on future products.

The integration of innovative and affordable technologies in the future aircraft platforms is a key success factor for manufacturers since it increases appeal and benefits for the customers (both airlines and passengers). The airlines can get significant economic advantages from operating modern aircraft more efficient, eco-friendly, easier and cheaper to manage and maintain, saving money through the reduction of operating costs.

The technological improvements have positive impacts on all the items contributing

to the total cash operating costs such as fuel burn reduction, reduced maintenance costs, reduced navigation and airport fees due to structural weight saving (innovative aircraft architectures and lighter materials utilization). All these benefits and economic advantages will be even more evident for regional turboprop aircraft that are typically less expensive to operate than the regional jets. The technological enhancements have a significant appeal also on the passengers that can enjoy a better air travel experience thanks to higher comfort and lower noise levels.

The actual application of an innovative technology in a new aircraft can be pursued only when, as a minimum, the following conditions are met:

- interfaces and links with other technologies necessary to the aircraft operation must be properly resolved;
- solutions must be acceptable to the aeronautics market; indeed, they have to consider aspects like: certification and safety, reliability during operations, costs, and maintenance process;
- demonstration of feasibility to fulfil the criteria of aircraft manufacturing industry (i.e. in series production).

The reference REG-IADP platform is a regional aircraft (90 passengers, 5 abreast) with T-tail, high wing, and underwing mounted turboprop engines. Main views are reported in Fig.4.1. Main airplane parameters are summarized in Tab.4.1.

4.1.1 The Adaptive Electric Wing (WP 2.1)

Main objective of this work package is to further develop and mature the integration of wing technologies for future green regional aircraft, featuring advanced performances (high aerodynamic efficiency, load control & alleviation functions), low noise impact, innovative low-weight structural design, so contributing to a drastic reduction of the environmental impact of air transport over next decades.

- WP2.1.1 - Innovative Wing Structure D&M (Design & Manufacturing) will be devoted to i) reduction of the manufacturing costs, ii) improvement of automated manufacturing processes, iii) Development of an high automated process for the assembling of the Wing Box components.
- WP2.1.2 - Morphing Structures: advanced architectures will be developed to be adopted as wing control surfaces (small trailing edge devices & adaptive winglet) for loads control function and innovative high-lift devices (smart droop nose, morphing

flap) in order to achieve lighter and simplified actuation/kinematic systems. This project will provide technology maturation (TRL 4/5) for the structural-mechanics and materials aspects, including full-scale limited experimental validations.

- WP2.1.3 - Advanced HLD (High Lift Devices): Advanced highly-efficient low-noise HLD will be developed by considering especially architectures suitable for a NLF wing, in order to increase A/C high-lift performances in take-off and approach/landing conditions, and to reduce A/C community noise in approach/landing flight phases. Droop nose and morphing flap will be the HLD concepts considered as alternative solutions to conventional leading edge and trailing edge systems.
- WP2.1.4 - Load Control & Alleviation: (LC&A) technologies will be developed for a dual purpose: i) to optimise spanwise load distribution (LC function) so as to improve aerodynamic efficiency in all flight conditions, and ii) to avoid that wing bending and torsion moment from gust and/or manoeuvre loads may exceed given limits (LA function), thus optimising the wing structural design for weight savings.
- WP2.1.5 - Wing NLF (Natural Laminar Flow): Aerodynamic design of a Natural Laminar Flow (NLF) wing tailored to a future Turbo-Prop Green Regional A/C to reduce drag and enhance aerodynamic efficiency at cruise conditions. By taking into account the presence of wing-mounted propeller engines, the outboard panel of the wing will be designed to be laminar.

4.2 Multifunctional Morphing Flap (WP 2.1.2)

The bi-modal flap prototype investigated during the second phase of the CleanSky GRA (Sec.3.3) represented a promising structural architecture to be potentially implemented on large civil aircraft. This in force of its high reliability from the structural, actuation and control standpoints. On the other hand, weight and complexity of the finalized system could jeopardize the aerodynamic benefits obtained at aircraft level.

For this reason, targeting to an even more mature product, a new architecture was investigated within the "Morphing Structures" WP 2.1.2.

The overall flap structural layout was completely revised with the main outcome to fulfil more demanding industrial requests:

- integration of a fairing-less deployment system;
- the minimization of spare parts;

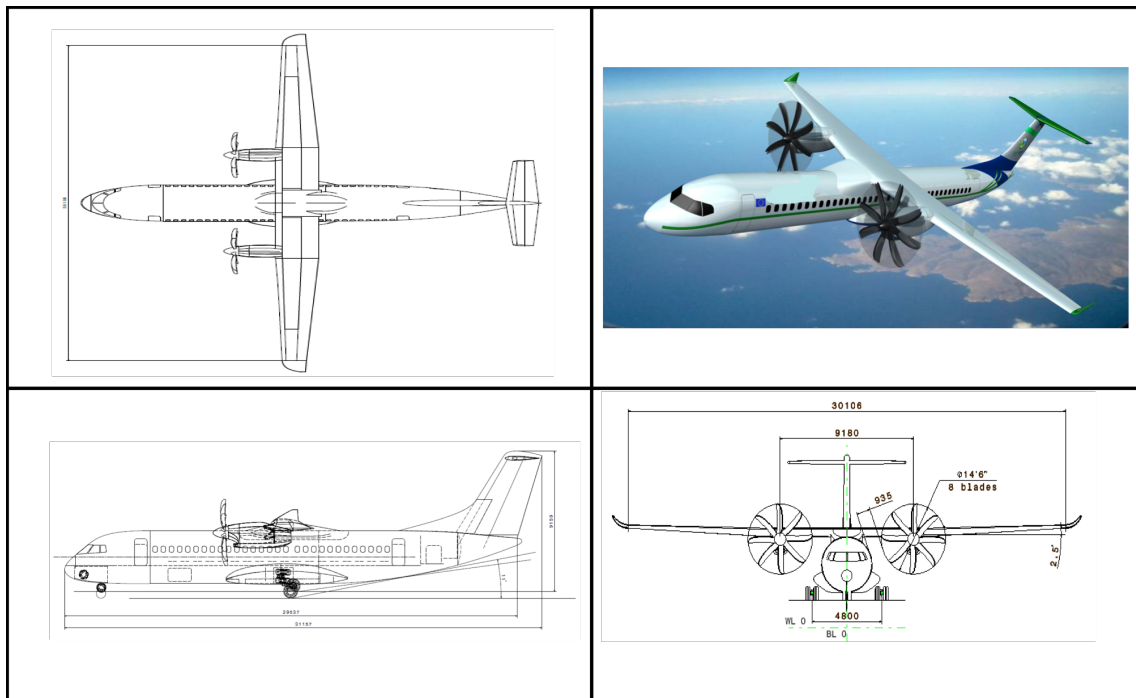


Figure 4.1: CS2 TP90: main views.

- enhancement of the overall system robustness;
- the rationalization of ribs-spar and ribs-gear box interface;
- the simplification of the overall flap assembly;
- the reduction of installed power thanks to a lower number of actuators;

Starting from the general bi-modal flap architecture in Sec.3.3.1, and experimentally validated by means of GST with real design loads (Sec.3.3.7), the new architecture was designed according to the challenges posed by real wing installation issues especially with reference to the minimum design space available at the tip section of the full-scale outboard flap region considering the aero-shape in Fig.4.2b (pertaining to a Natural Laminar Wing designed by Onera). It worth to notice that the design space at tip section (see Fig.4.2b) of the outer-board flap was reduced by a factor equal to 37% compared with the design space available at tip for the rib of the bi-modal flap (see Fig.3.4). This resulted in a more challenging design for the new concept. The full-scale outer Fowler flap region was selected as the investigation domain, spanning 5.15m from the wing kink, with a root chord equal to 0.87m and a taper ratio equal to 0.73.

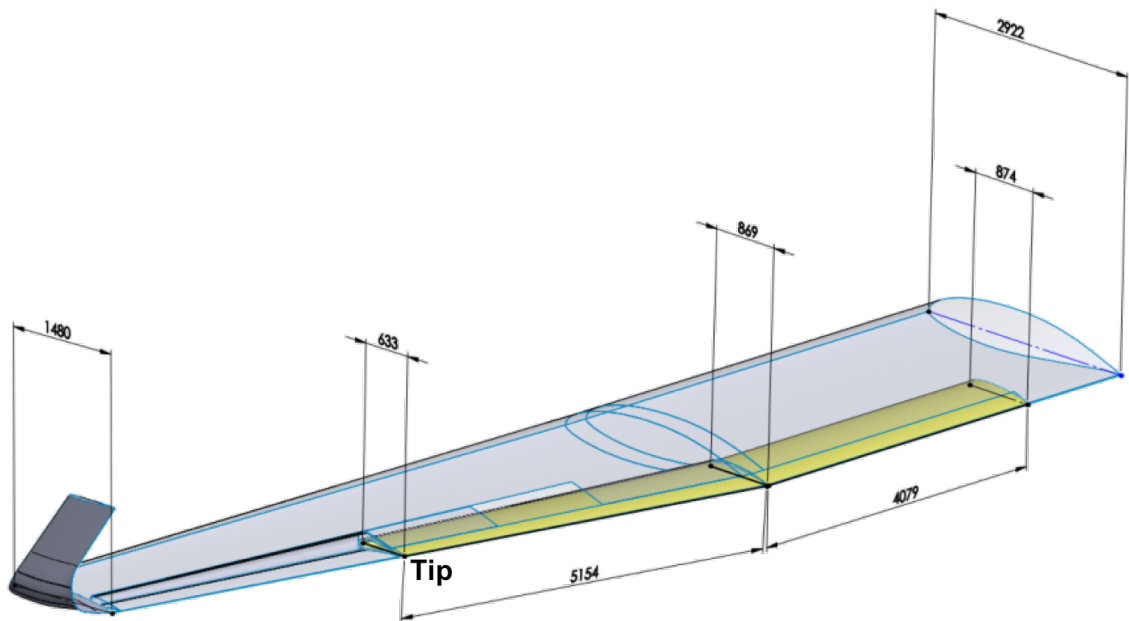
Table 4.1: CS2 TP90 main data.

Weights	
Maximum Take-Off Weight (MTOW)	33200 kg
Maximum Zero Fuel Weight (MZFW)	31200 kg
Operative Empty Weight (OEW)	19360 kg
Wing Geometry	
Span	29.65 m
Mean Aerodynamic Chord	2.56 m
Area	73.3m
Aspect Ratio	12
Taper Ratio (Tip/Root chord)	0.5
Front Spar Position (% chord)	16
Rear Spar Position (% chord)	60
Performance	
Cruise Altitude	6096m
Max cruise speed	$M_\infty = 0.56$, (270 KCAS)
Max altitude	8534m
Dive speed	$M_\infty = 0.67$, (315 KCAS)

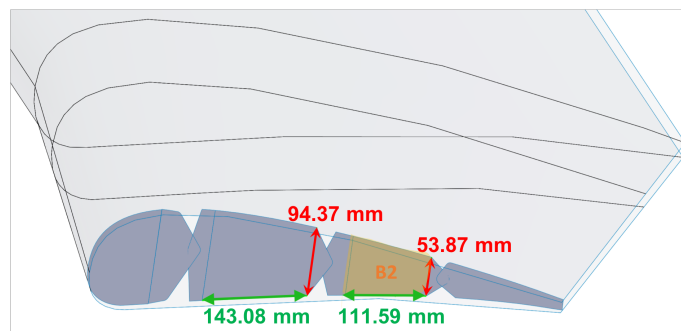
4.2.1 Mission Requirements and Requested Performances

Considering the challenging goals to improve aircraft high-lift performances (maximum attainable lift coefficient and stall angle) and noise emitted by the high-lift system, the driving idea was to replace a conventional double slotted flap with a single slotted morphing flap. This novel multi-functional morphing flap technology was requested to improve the aerodynamic performances of the next TP90 aircraft along its entire flight mission. The morphing flap system layout added new and more demanding functionalities. Three different functions are now being considered:

- Morphing mode 1: overall airfoil camber morphing (up to 28° equivalent rigid deflection);



(a) Outboard Flap geometric data: tip chord (633mm), root chord (869mm), span (5154mm).



(b) Tip Section (Outboard flap): minimum design space.

Figure 4.2: TP90 outboard flap.

- Morphing mode 2: $+10^\circ / -10^\circ$ (upwards/downwards) deflection of the flap tip segment (from the 90% to 100% of the local chord);
- Morphing mode 3: Tip twist ($\pm 5^\circ$ along the outer flap span);

Morphing mode 1 is supposed to be activated when the flap is deployed (Fig.4.3) during take-off and landing only to enhance A/C high-lift performances also allowing for steeper initial climb and descent, noise-abatement trajectories. Thanks to this function, more airfoil shapes are available at each flap setting and therefore a dramatic simplification of the flap's deployment systems may be expected: actuation tracks could be hosted into

wing airfoil shape without external fairing needs. Basically, very simple conventional track systems (i.e. curved beam) without external fairings are not able to comply with high-lift requirements in landing and take-off configurations; therefore, further increase in high-lift performance are obtained using the overall airfoil camber morphing (mode 1) in the Fowler flap extended configuration.

Morphing modes 2 and 3 are related to the last chord-wise segment of the flap and are activated in climb, cruise, and off-design flight conditions when the flap is stowed in the wing (Fig.4.3). Thanks to these modes, LC functionalities may be implemented to improve wing aerodynamic efficiency.

The smart function of the ribs, namely their capability to drive morphing as an inner movable articulation of the flap structure, was preserved; ribs' architecture and the associated mechanics was instead fully modified in order to improve the reliability and the efficiency of several morphing modes through a more compact and robust design.

Because of three different operating modes, the novel full-scale outboard flap will be named from now on Three-Modal Morphing Flap (3MMF).

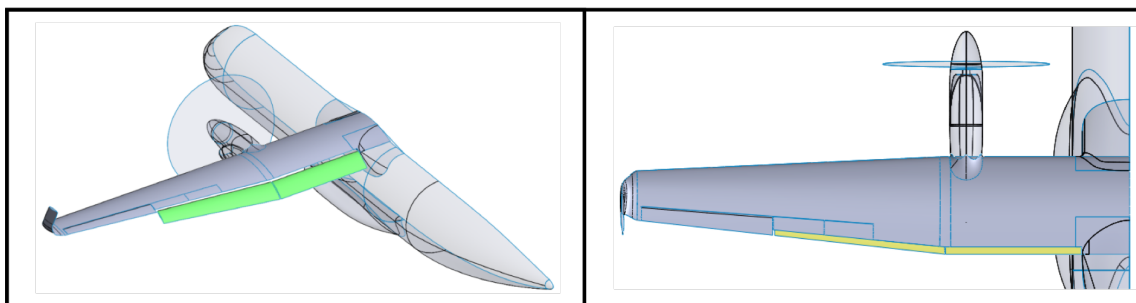


Figure 4.3: Flap configurations: (*left*) deployed, (*right*) stowed.

4.2.2 Aerodynamic Design Load Conditions

The 3D aerodynamic load distributions, related to different aircraft conditions and flap settings, were deeply analysed in order to validate the innovative outer-board flap architecture in the most critical and relevant environment.

According to regulations [41], during the structural design, the following assumptions for design loads have to be considered:

- **Limit Loads (LL)** are the maximum loads, which a flight vehicle may be subjected to during its life-time, when carrying out the required ground and flight operations. The limit loads must be carried by the structure without exceeding the yield stress

of the material used in the structure and that the deformation levels don't interfere with safe operation (as prescribed by *EASA CS 25.305(a)*).

- **Ultimate Loads (UL)** are the limit loads multiplied by a factor of safety, usually 1.5 for aircraft. The structure must have sufficient strength to carry the ultimate loads without failure.

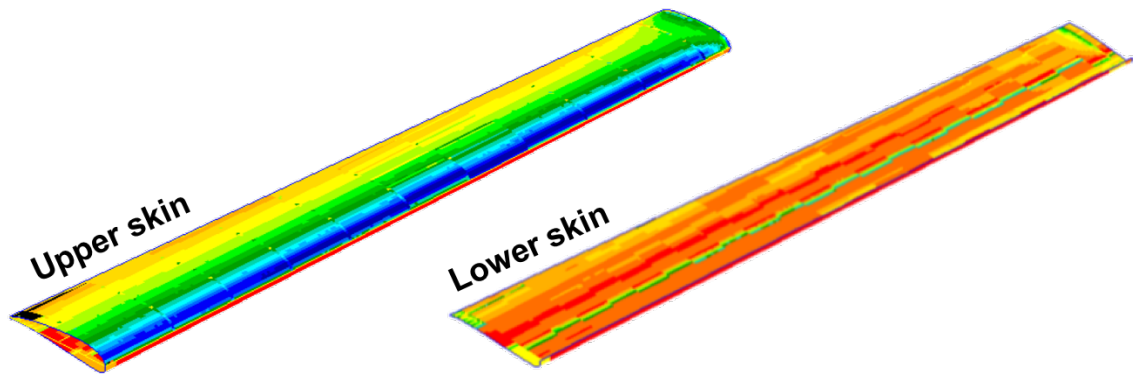
Considering the multi-functional capabilities to be enabled on the 3MMF concept, it is clear that a single limit load valid per each morphing modes can not be defined.

According to regulations [41], when the device operates as prescribed by mode 1 requirements, it has to be considered as a high-lift device. In such a case, among all 3D aerodynamic loads evaluated by means of CFD, the Limit Load (LL) condition was attained at the dynamic pressure of 5858Pa, with flap deployed (33°) in landing configuration, and aircraft angle of attack equal to 0.57° . The 3D contour pressure distribution is reported in Fig.4.4a; total forces acting on each $Area(Bay_i, Block_j)$ are shown in Fig.4.4b.

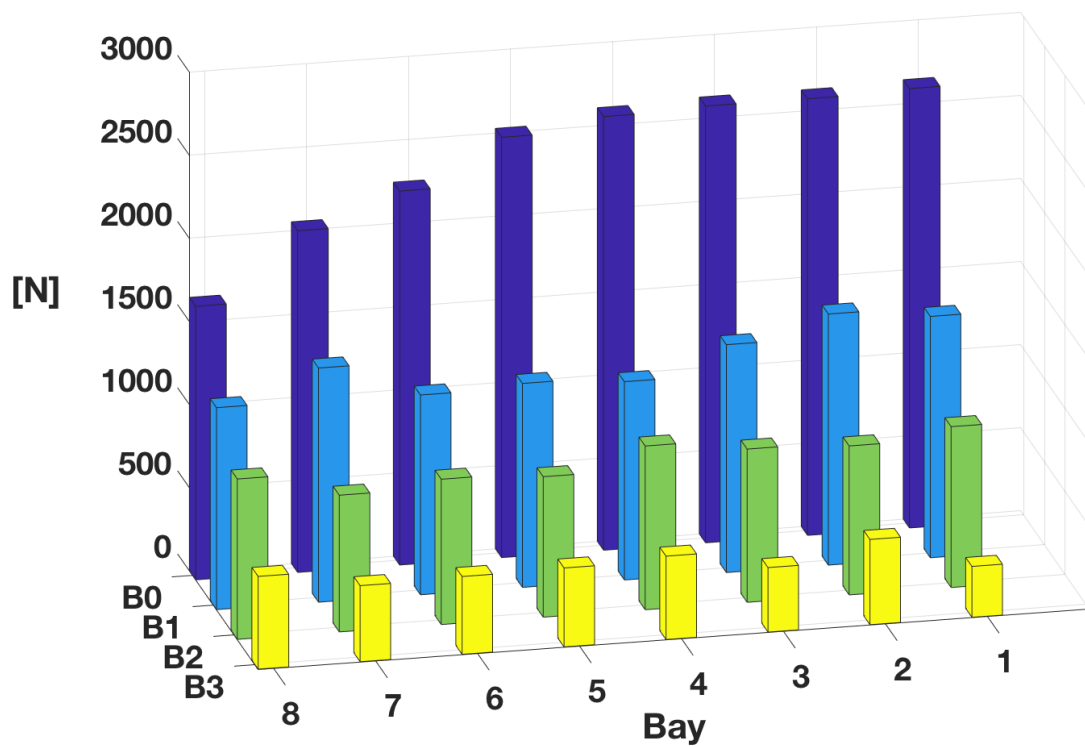
When the device operates as prescribed by mode 2 and 3 requirements, the flap tip segment (i.e. the tab or flap trailing-edge) must be considered as any movable control surface on a large airplane. According to regulations [41], a control surface must be able to provide a rotation angle equal to 33 per cent of its maximum value when the airplane is at its maximum speed. This condition will be considered as limit load for the tab preliminary design because, considering the complete airplane flight envelope, the highest dynamic pressure is reached at the dive speed.

Using an in-house 3D Doublet Lattice Method (DLM) code (Fig.4.2a), the limit load condition is summarized in Tab.4.2. In the preliminary design phase, the pressure distribution was considered uniform on tab upper and lower external surfaces. The maximum values of pressure coefficients (upper and lower) are reported in Tab.4.2.

It's worth to notice that the total actuation torque, provided by the tab actuation systems, has to be higher than the total aerodynamic hinge moment around tab hinge axis ($\mathcal{M}_{HA} = 475.8 \text{ Nm}$).

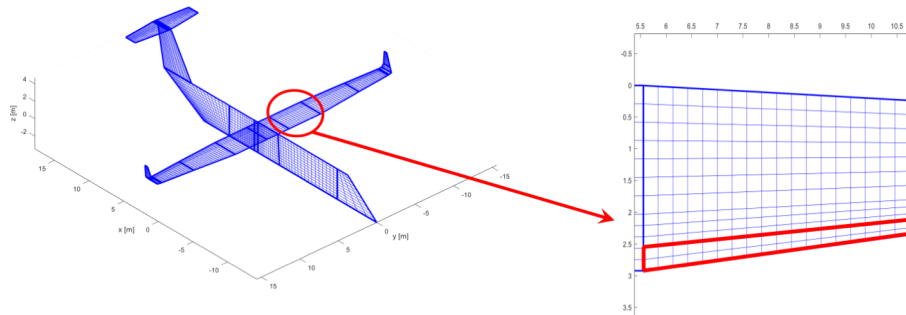


(a) Outboard Flap 3D pressure distribution: landing configuration.



(b) Total forces acting on each $Area(Bay_i, Block_j)$.

Figure 4.4: Limit Load condition for 3MMF preliminary design.



(a) TP90 aerodynamic model for evaluation of tab design loads (with DLM code).

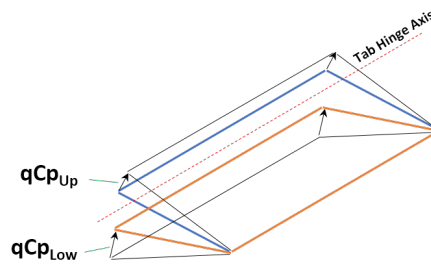


Table 4.2: Limit Load Condition considered for tab preliminary design.

Tab Geometric Data

Root chord,	0.222 m
Root chord as % of local wing chord,	10.57%
Tip chord,	0.167 m
Tip chord as % of local wing chord,	7.770%
Span,	5.154 m
Mean geometric chord,	0.236 m

Limit Load condition for tab design (DLM)

Rigid deflection (downward),	+3.33°
Dynamic pressure,	12005Pa
Pressure coefficient (upper), $C_{p,UP}$	0.3247
Dynamic pressure (upper), $q \cdot C_{p,UP}$	3898Pa
Force resultant (upper), F_{UP}	2378N
Pressure coefficient (lower), $C_{p,LOW}$	0.5011
Dynamic pressure (lower), $q \cdot C_{p,LOW}$	6015Pa
Force resultant (lower), F_{LOW}	3668N
Total Hinge Moment around tab hinge axis (H.A.), \mathcal{M}_{HA}	475.8Nm

Chapter 5

Three Modal Morphing Fowler Flap (3MMF)

5.1 Working Principles and Design Approach

The novel full-scale outboard 3MMF concept was based on the idea of segmentation of the traditional load-bearing box into a set of structural cells inter-connected by kinematic chains.

The smart function of the ribs, namely their capability to drive morphing as an inner movable articulation of the flap structure, was preserved from the demonstrator tested during GST (Sec.3.3.7). However, ribs' architecture and the associated mechanics were instead fully modified in order to improve the reliability and the efficiency of several morphing modes through a more compact and robust design. Kinematic chains must be able to provide several morphing modes and larger target shapes: up to 28° for the overall camber morphing, and $\pm 10^\circ$ for the flap tip segment.

A suitably designed actuation ensures the smoothness shape change of the overall system, from the baseline configuration to the target one, while significantly contributing to withstand external loads in all operative conditions [51].

Indeed, the mechanized system implements morphing through the rigid-body motion of stiff subcomponents (i.e. kinematic chains). Kinematic chains represent an effective way to implement morphing while ensuring high levels of compliance of the morphing structure with the airworthiness requirements. This can be seen as a direct consequence of standard materials and actuators used.

Because actuation power and structural integrity are of paramount importance [52], the design of the inner mechanisms was driven by an energy efficient approach for mechanical advantage improvement as well as an element based force analysis for structural

assessment.

After that, the finalized design of the smart rib will be assessed by means of preliminary FE models to support the definition of the mechanical arrangement of the inner mechanisms and the interface between the actuation system and the structural skeleton.

When the core of the morphing system (inner mechanisms and actuation systems) will be defined, the multi-box skeleton will be designed taking into account limit load conditions and track attachments of the fairing-less deployment system.

Finally, the Adaptive Twist composite Tab (ATT) concept will be introduced for enabling morphing mode 3 ("continuous" span-wise trailing-edge twist). A preliminary estimation of torsional moment required will be provided.

Generally speaking, the design methodology followed in this Chapter consists of four main steps:

- Shape transition design by means of a Binary Crossed Link (BCL) mechanism;
- Design of the inner mechanisms (by means of vector loop equations, Instant centre (IC), and element based force analysis);
- Structural design of the multi-box arrangement (based on the theory of thin-walled section beams);
- Preliminary evaluation of energy required for twisting flap trailing-edge.

5.2 The Smart Rib Concept

The most natural way to enable the transition of flap sections from the reference (baseline) shape to the target (morphed) one consists in the arrangement of a morphable layout for the ribs of the TE structure. The rib is assumed to be segmented in four consecutive blocks hinged to each other along the airfoil camber line (points $H01$, $H12$, $H23$ in Fig.5.1).

A large number of small blocks ensures more accurate reproduction of unmorphed/morphed camber lines; however, it can lead to considerable impacts on the feasibility of the structural arrangement as well as on its manufacturing and maintenance costs (high number of parts).

The introduced segmentation turns the airfoil camber line into an articulated polygonal line that can assume different shapes depending on the relative rotation between adjacent blocks. The number of blocks and their chord-wise extension are commonly defined in order to satisfactorily match the camber line in both baseline and morphed configurations while lowering the structural complexity as much as possible.

The shape transition is the same in all flap cross-sections and is usually described in terms of chord-wise extension of the morphable region (distance between $H01$ and TE in Fig.5.2), and morphed camber lines geometry (red coloured in Fig.5.2). Airfoil thickness distribution is constant and not affected by morphing.

In order to reduce number of actuators, three blocks ($B0$, $B1$, $B2$ in Fig.5.1) will be interconnected by a single linking beam element ($L1$). In addition, the rib tip segment ($B3$) can freely rotate around hinge $H23$. In such a way, when the flap is stowed in the wing, morphing modes 2 and 3 can be enabled with deflection of the flap tip segment alone ($B3$).

The active degrees of freedom (DOFs) of the smart rib mechanism can be evaluated as follows:

$$K = b - (l + 1) \quad (5.1)$$

where K denotes the active DOFs of the rib mechanism, b is the number of rib blocks, and l the number of linking beam elements. In addition, K is also equal to the number of actuators that should be installed to suppress and control the active DOFs of each smart rib. In Fig.5.1, l is equal to 1, b is equal to 4 and the smart rib mechanism clearly has two DOFs:

- **First DOF** defined by rib blocks $B0$, $B1$, $B2$ connected by a single link $L1$;
- **Second DOF** defined by rib blocks $B2$ and $B3$.

Linking beam $L1$ hinged to non-adjacent blocks ($B0$ and $B2$) force the camber line segments ($B0$, $B1$, $B2$) to rotate according to specific gear ratio. If the rotation of any of the blocks is prevented, no change in shape can be obtained; if one actuator moves any of the blocks, all the other blocks follow the movement according to the above-mentioned gear ratio.

Two inner mechanisms (one per each rib DOF) between adjacent blocks are clearly necessary to implement rotations requested by shape transitions defined by each morphing modes.

When both inner mechanisms (IM1 and IM2) will be activated, full-camber morphing mode 1 can be provided. Otherwise, modes 2 and 3 are enabled by the only inner mechanism hosted within block $B2$ (IM2).

5.2.1 Binary Crossed Link (BCL) Mechanism

The kinematic design of the BCL mechanism requires as preliminary input the definition of the target shapes.

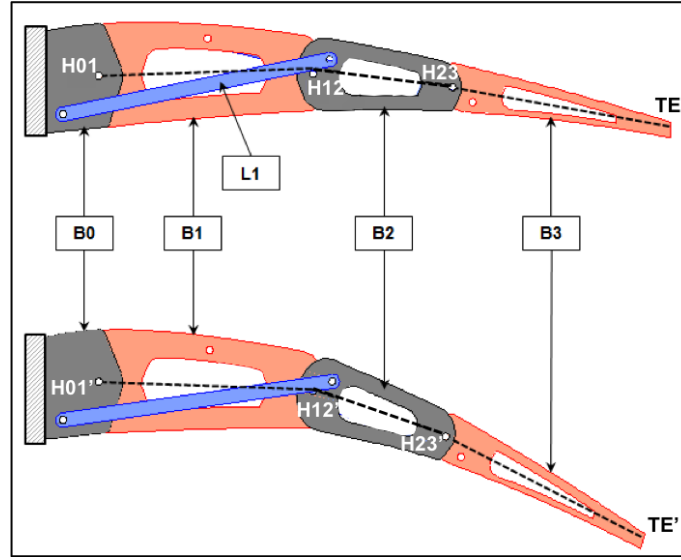


Figure 5.1: Binary Crossed Link (BCL) Mechanism: working principle.

The shape parameterization started with the assignment of the airfoil chord position (distance between $H01$ and TE in Fig.5.2) that will be affected by the morphing process and the deflection angle assumed (δ_{TE}). The latter is defined as the rigid rotation of the trailing-edge chord with respect to the fixed rib block (B0).

For a specific value of δ_{TE} , the camber line of the morphed airfoil can be analytically expressed by parabolic function. The analytical equation of a parabola requires three coefficients to be defined; therefore, three equations are needed to determine it. The conditions that were imposed to find the requested parameters are the following:

$$\begin{cases} (x_{TE}, y_{TE})_{rotated} \in y = a \cdot x^2 + b \cdot x + c \\ (x_{H01}, y_{H01}) \in y = a \cdot x^2 + b \cdot x + c \\ \frac{dy}{dx} = [\tan(\text{mean line})]_{(x_{H01}, y_{H01})} \end{cases} \quad (5.2)$$

The first two equations impose that the parabola passes through the trailing-edge tip and main hinge $H01$. Besides, to avoid profile first-order discontinuities, the parabola must be tangential to the original airfoil shape in correspondence of $H01$ as shown in Fig.5.2 and imposed in the last equation of the system Eq.5.2.

Such system can be synthetically expressed as:

$$\begin{pmatrix} a \\ b \\ c \end{pmatrix} = \begin{bmatrix} x_{H01}^2 & x_{H01} & 1 \\ 2 \cdot x_{H01} & 1 & 0 \\ x_{H01}^2 & x_{H01} & 0 \end{bmatrix}^{-1} \cdot \begin{pmatrix} y_{H01} \\ b \\ y_{TE} \end{pmatrix} \quad (5.3)$$

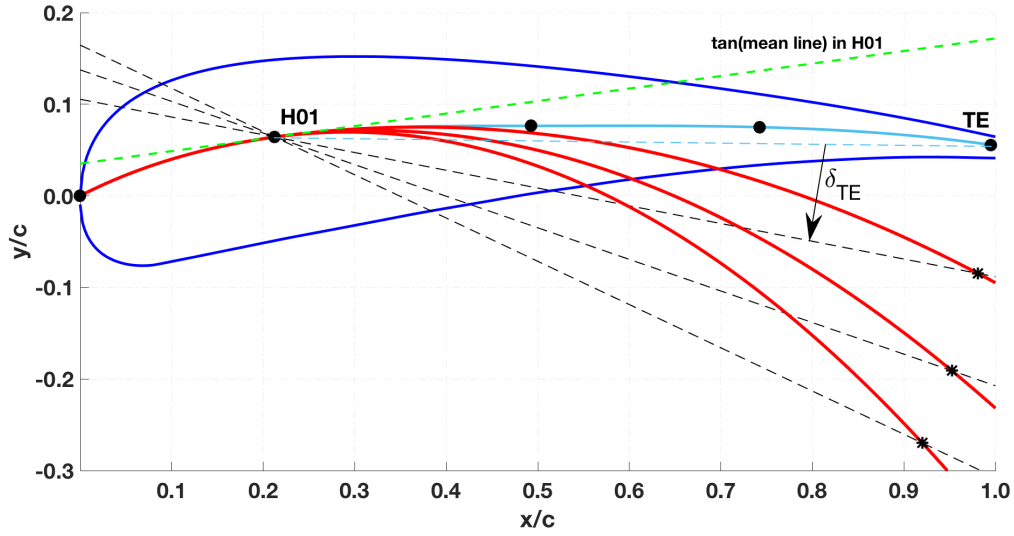


Figure 5.2: Airfoil camber line.

In Fig.5.2, the morphed camber line for three δ_{TE} are shown: 10° , 20° , 28° .

The shape transition analysis directly gives the position of camber line hinges ($H01$, $H12$, $H23$) and, indirectly, the amount of rotation required to each camber line segment to suitably fit the target morphed shape.

Let us now assume that the outcomes of the analysis are those sketched in Fig.5.1, in terms of the number of blocks and hinge positions along camber line in both unmorphed ($H01$, $H12$, $H23$) and morphed ($H01'$, $H12'$, $H23'$) configurations. The final results are represented by the rotations that the segments $H01 - H12$, $H12 - H23$, $H23 - TE$, have to make around $H01$, $H12$, $H23$ to turn the polygonal line $H01/H12/H23/TE$ into $H01'/H12'/H23'/TE'$.

The positions of the main hinges along the camber line (both in baseline and morphed configurations) are the input data of the problem, the positions of the link hinges ($L1$ and $L2$) are the unknown variables to be determined.

Because the position of each link is determined by the coordinates of its two hinges, the number of unknown variables is equal to four (two coordinates for each tip hinge).

The mathematical formulation of the problem consists in finding the vector \vec{v} ($= [x_{L1}, z_{L1}, x_{L2}, z_{L2}]$) defined over the domain \mathcal{D} and satisfying the equation:

$$\vec{w}_m = g(\vec{w}, \vec{v}) \quad (5.4)$$

where \mathcal{D} is the region delimited by the unmorphed airfoil.

$\vec{w} = [x_{H01}, z_{H01}, x_{H12}, z_{H12}, x_{H23}, z_{H23}, x_{TE}, z_{TE}]$ is the vector defining the positions

of the hinges $H01$, $H12$, $H23$ and of the airfoil tip point (TE) in unmorphed configuration; $\vec{w}_m = [x_{H01'}, z_{H01'}, x_{H12'}, z_{H12'}, x_{H23'}, z_{H23'}, x_{TE'}, x_{TE'}]$ is the vector defining the positions of the hinges $H01$, $H12$, $H23$ and of the airfoil tip point (TE) in morphed configuration; g is the mechanism *kernel function*, governing morphing kinematics. Such function is generally non-linear and non-invertible with respect to the variable \vec{v} . The space of the solutions of Eq. 5.4 can be found through a methodology consisting of three main steps.

Step 1. Forced reduction of the unknown variables.

The positions of the hinge L_2 is arbitrarily imposed in the domain \mathcal{D} . The unknown vector \vec{v} is then replaced by the following summation:

$$\vec{v} = \vec{v}_1 + \vec{t} \quad (5.5)$$

where $\vec{t} = [0, 0, x_{L_2}, z_{L_2}]$ is the vector defining the (imposed) positions of hinge L_2 ; $\vec{v}_1 = [x_{L_1}, z_{L_1}, 0, 0]$ is the vector defining the unknown position of the hinge L_1 .

Step 2. Solution of the linearised morphing equations.

In force of Eq. 5.5, the equation governing the morphing kinematics changes into:

$$\vec{w}_m = g(\vec{w}, \vec{t}) + g^*(\vec{v}_1) \quad (5.6)$$

where the kernel functions result decomposed into a non-linear and non-invertible part depending on variables \vec{w} , \vec{t} and into a generally linear and invertible part (marked with the apex “*”) depending on variable \vec{v}_1 . Because the positions of main hinges are all known when the morphed camber lines are defined (as in Fig.5.2), \vec{w}_m and $g(\vec{w}, \vec{t})$ are all known vectors defined in \mathcal{R}^4 . For this reason, Eq.5.6 can be solved algebraically to determine the unknown \vec{v}_1 .

Step 3. Iteration.

A new value for \vec{t} is imposed, and steps 1, 2 are repeated.

The iteration can be conceptually regarded as a function Γ operating on the variable \vec{t} (coordinates of hinge L_2) and providing as output vector \vec{v}_1 (coordinates of hinge L_1):

$$\Gamma : \forall \vec{t} \in \mathcal{D} \subset \mathcal{R}^4 \Rightarrow \vec{v}_1 = \Gamma(\vec{t}) \in \mathcal{D} \subset \mathcal{R}^4 \quad (5.7)$$

The function Γ (i.e., the iteration of the first two steps) allows for the evaluation of the locus described by the hinge L_1 while the position of the hinge L_2 range in the domain of the airfoil section.

A graphical representation of the hinge' locus obtained for the rib tip section has been reported in Fig.5.3. In this case, r is the distance of hinge L_2 from main hinge $H12$.

The best position of the hinges is considered to be the one ensuring the:

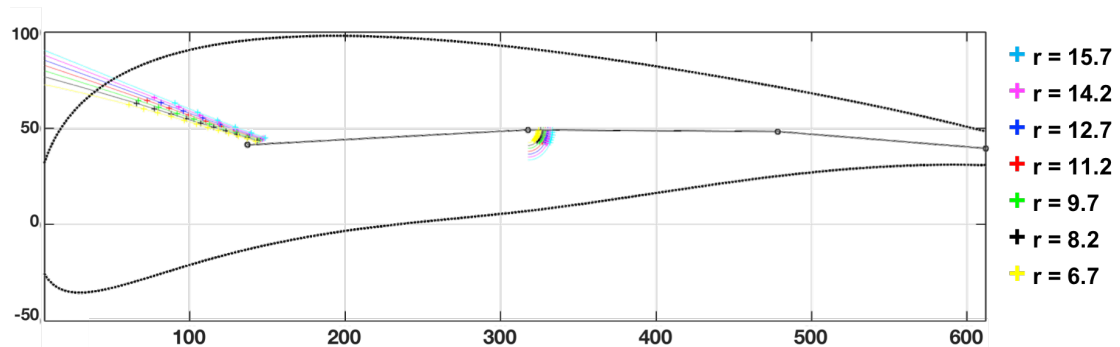
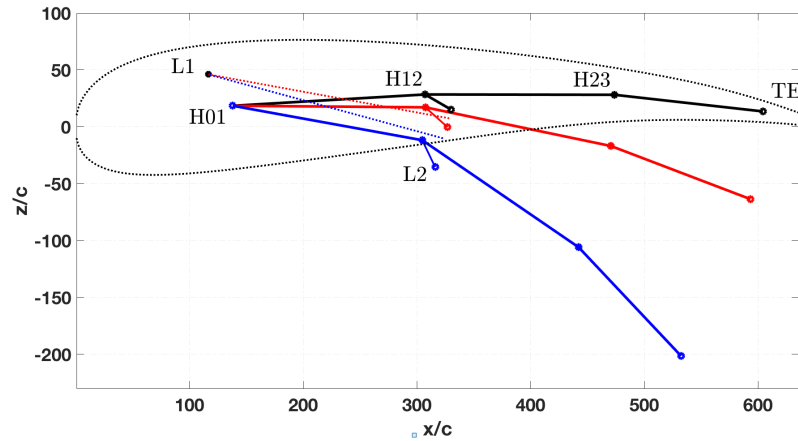


Figure 5.3: Sensitivity of Link hinges (L1 and L2).

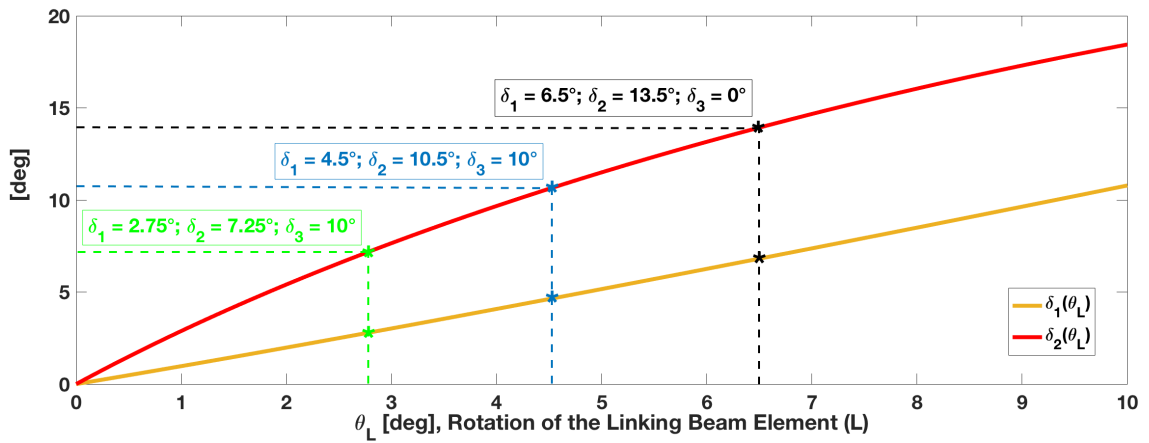
- Highest clearance from the camber line, thus avoiding dangerous alignment between link $L1$ and camber line hinges (potentially resulting in a bi-stable mechanism);
- Highest clearance from the airfoil boundary, thus avoiding interference problems between the physical hinges and the skin panels.

If the position vector $\overline{H12 - L2}$ is defined with complex notation ($\overline{H12 - L2} = r \cdot e^{j\theta}$), the final positions of link hinges are obtained for $r = 15.7$ mm and $\theta = 22.5^\circ$. The link ($L1 - L2$) is shown in Fig.5.4c.

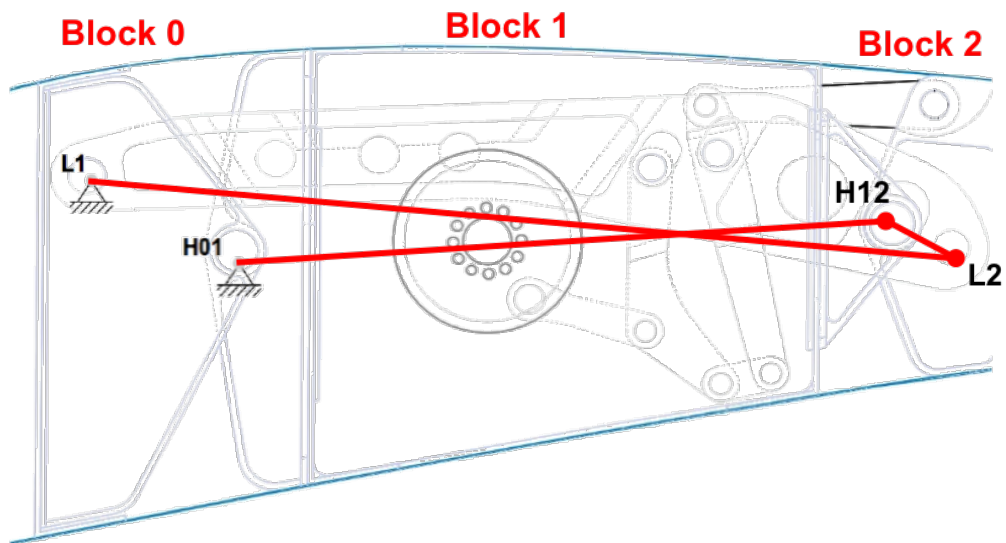
However, the linking beam element provides only a gear ratio between rib blocks $B1$ and $B2$; an inner mechanism (IM1) has to be designed to provide the angle δ_2 requested for shape transition.



(a) Link hinges for $r = 15.7$ mm and $\theta = 22.5^\circ$.



(b) Rib block angles (δ_1 and δ_2) as function of link rotation θ_L .



(c) Final link hinges ($L1$ and $L2$) located in tip section.

Figure 5.4: Link ($L1$) kinematic design.

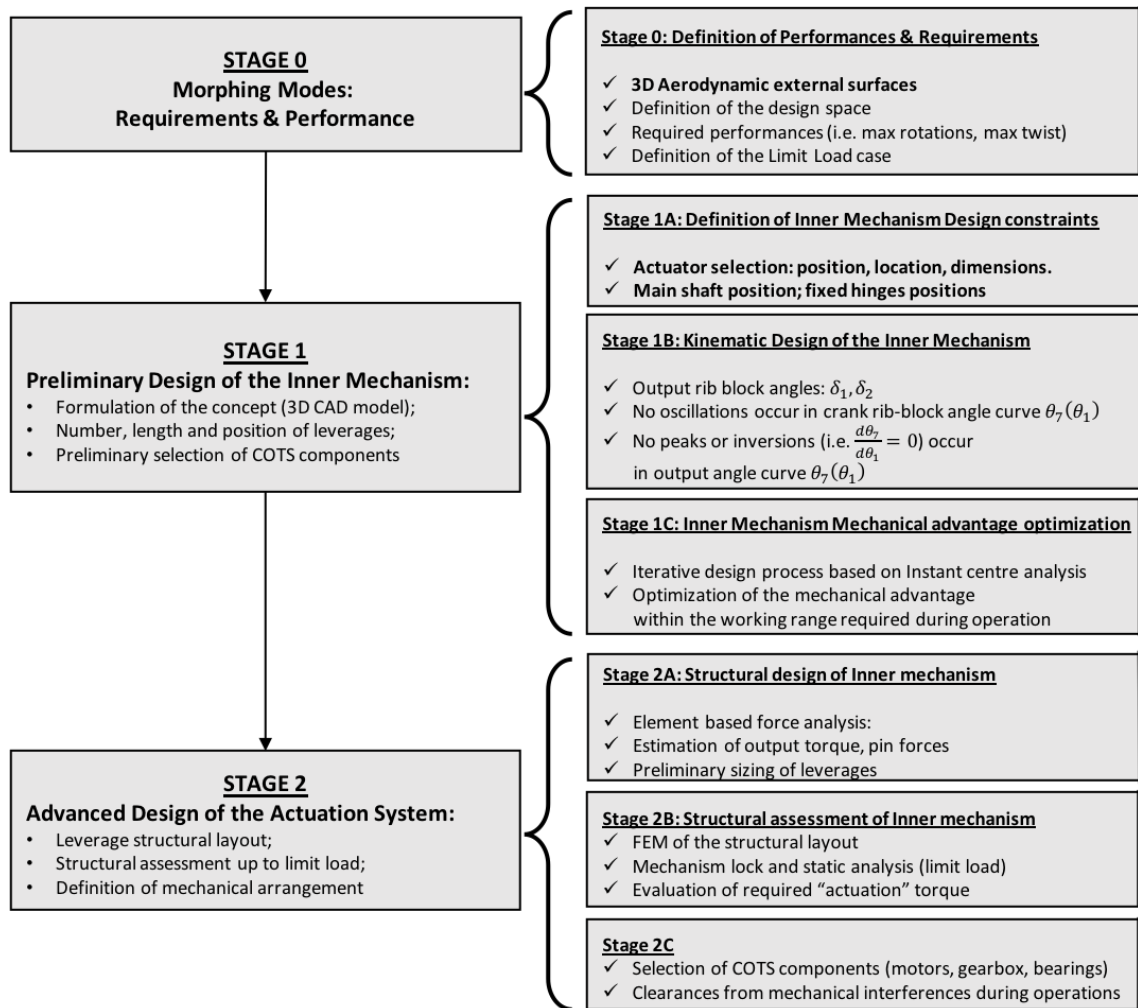


Figure 5.5: Flow-chart of the actuation system design process.

5.2.2 Kinematic Requirements and Performance

Generally, the core element of adaptive structures is the actuator-mechanism system. Interactions between the basic elements of this mechanized system and the external loads provide fundamental insight into the behaviour of the overall adaptive system.

Reduce parameters as power required and weight are of paramount importance to successfully integrate adaptive systems in large airplanes for improving performances and enlarge mission profiles.

In Fig. 5.5, the flow-chart of the actuation system design process is summarized.

The design engineer must ensure that the proposed mechanism will not fail under

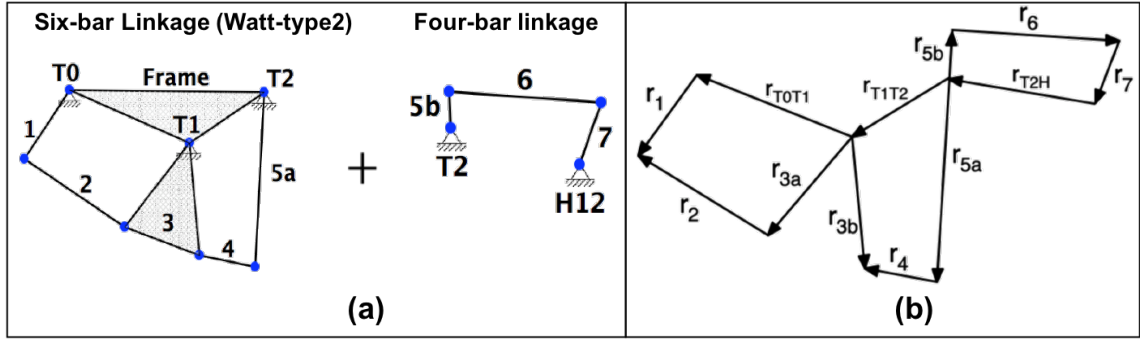


Figure 5.6: Kinematic model of the inner mechanism: (a) full leverage can be seen as six-bar linkage plus a four-bar linkage; (b) Vector loop equations.

operating conditions; however, the selected linkage has mainly to be synthesized with the principal goal to provide required kinematic performance by morphing operations.

The position of all the elements in the mechanism for each increment of input motion has to be evaluated and compared by expected kinematic performance to enable transition of the airfoil from the baseline configuration to the target shape. A first tentative linkage was selected (the one in Fig. 5.6): a Watt's Six-bar linkage plus a Four-bar linkage. In such a way, the hollow-shaft rotary brushless motor can transfer rotation from the crack element (link 1 in Fig. 5.6) to the output element (link 7 in Fig. 5.6).

As first step, link lengths and positions were defined as function of the input angle θ_1 as the full linkage is a one-DOF mechanism.

Indeed, assuming trial link lengths, unknown link angles were evaluated; each link location, represented as position vectors, was completely defined for each increment of input motion. The approach to linkage position analysis creates a vector loop (or several loops) around the linkage as first proposed by Raven [57].

In Fig. 5.6, the links are represented as position vectors that form a vector loop. The lengths of the vectors are the link lengths, which are assigned within the design space. The choices of vector directions and sense, as indicated by their arrowheads, lead to this vector loop equation [59]:

$$\begin{cases} \vec{r}_1 + \vec{r}_{T0T1} - \vec{r}_2 - \vec{r}_{3a} = 0 \\ \vec{r}_{3b} + \vec{r}_{T1T2} - \vec{r}_{5a} - \vec{r}_4 = 0 \\ \vec{r}_{5b} + \vec{r}_6 - \vec{r}_7 - \vec{r}_{T2H} = 0 \end{cases} \quad (5.8)$$

where each position vector is defined with complex number notation $\vec{r}_i = r_i \cdot e^{j\theta_i}$ (with $i = 1, \dots, 7$). Each vector loop can be expressed as Freudenstein's equation; if we solve

for angle θ_{3a} output of first vector loop equation, we have:

$$K_I \cdot \cos \theta_1 - K_{II} \cdot \cos \theta_{3a} + K_{III} = \cos(\theta_{3a} - \theta_1) \quad (5.9)$$

$$K_I = \frac{r_{T0T1}}{r_{3a}}; \quad K_{II} = \frac{r_{T0T1}}{r_4}; \quad K_{III} = \frac{r_{3a}^2 - r_2^2 + r_1^2 + r_{T0T1}^2}{2 \cdot r_{3a} \cdot r_1}; \quad (5.10)$$

Then, the first vector loop, expressed as Freudenstein's equation (Eq. 5.9), can be simplified as:

$$\theta_{3a} = 2 \cdot \tan^{-1} \left(\frac{-B \pm \sqrt{B^2 - 4 \cdot A \cdot C}}{2A} \right) \quad (5.11)$$

where link lengths and known input angle θ_1 terms have been collected as constants A , B , and C :

$$A = K_I \cdot \cos \theta_1 + K_{II} + K_{III} + \cos \theta_1 \quad (5.12)$$

$$B = -2 \cos \theta_1 \quad (5.13)$$

$$C = K_{III} - K_{II} - \cos \theta_1 + K_I \cdot \cos \theta_1 \quad (5.14)$$

The full inner mechanism is essentially three four-bar linkages in series, as shown in Fig. 5.6. These vector loop equations (Eq.5.8) can be solved in succession with the results of the first loop applied as input to the second loop. Note that there is a constant angular relationship between vectors r_{3a} and r_{3b} within ternary link 3.

The solution for the four-bar linkage (Eq.5.11) is simply applied twice in the Watt's Six-bar case:

$$\begin{cases} \theta_{3a} = f(r_1, r_2, r_{3a}, r_{T0T1}, \theta_1) \\ \theta_{5a} = g(r_{3b}, r_4, r_{5a}, r_{T1T2}, \theta_{3a}) \end{cases} \quad (5.15)$$

and one more time for the last four-bar linkage in Fig. 5.6:

$$\theta_7 = t(r_{5b}, r_6, r_7, r_{T2H}, \theta_{5a}) \quad (5.16)$$

The independent variable is θ_1 which will be controlled with the brushless motor. In such a way, each angle link was expressed as function of the crank angle θ_1 once the links lengths were defined within the minimum available design space of the tip trailing-edge section.

When the hollow-shaft brushless rotary motor is activated, the input rotation is transferred to the crank element (link 1). Leverage's output element (link 7) must provide adequate control action during trailing-edge evolution from baseline position to the target

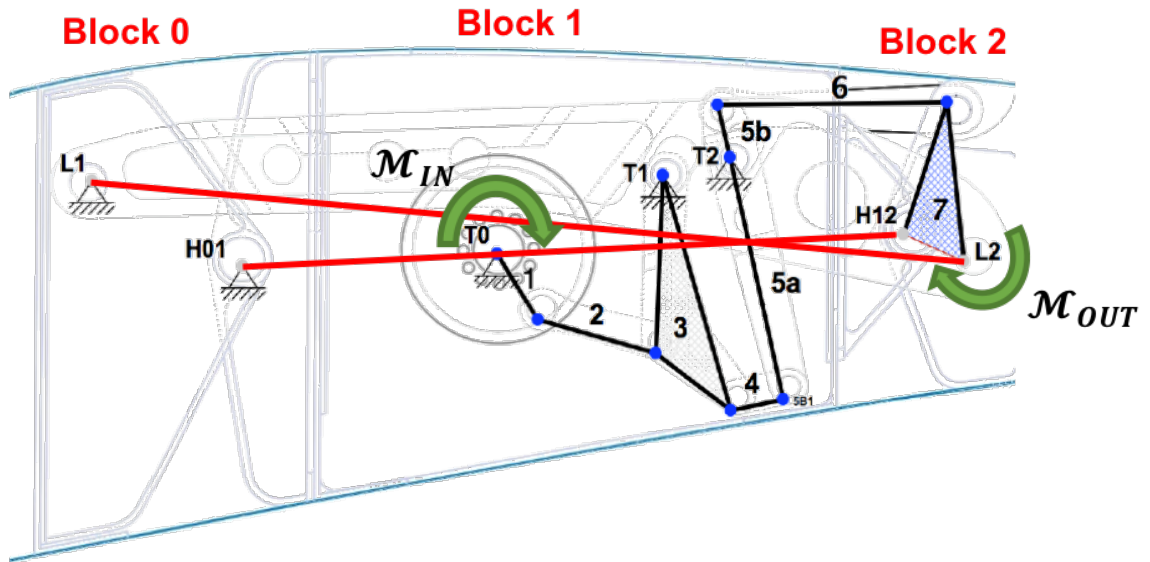
shape. In addition, the final output angle curve $\theta_7(\theta_1)$ must be able to fulfil performance requirements within the requested output angle range with the following additional criteria observed to assure effective shape transition during morphing operations:

$$\frac{d\theta_7}{d\theta_1} \neq 0 \quad \forall \theta_7(\theta_1) \in [-10^\circ; +10^\circ] \quad (5.17)$$

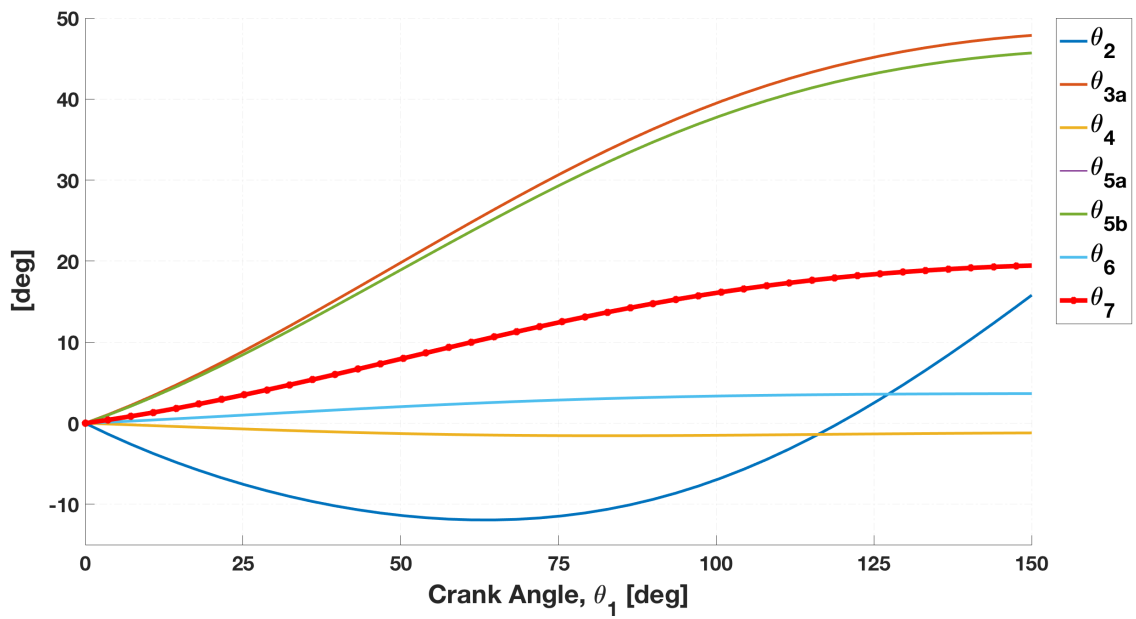
When this condition is verified, inversion points (i.e. toggle positions of the linkage) are avoided and smoothness transition from the baseline position to the target shape (and vice-versa) can occur.

In Fig.5.7a, the final inner mechanism (IM1) hosted within the rib block B1 is shown. In Fig.5.7b, as expected, IM1 provides the output angle θ_7 (red coloured in Fig.5.7b). This angle is equal to the rotation around hinge H12 ($\theta_7 = \delta_2$) defined in Fig.5.4b. As shown in Fig.5.7b, the maximum output angle is equal to $\theta_7 = \delta_2 = 16.67^\circ$.

In Fig.5.7a, the final inner mechanism (IM2) hosted within the rib block B2 is shown. In Fig.5.8b, starting from baseline position ($\theta_1 = 0^\circ$), IM2 provides output angle θ_7 within the required range $[-10^\circ; +10^\circ]$ for morphing modes 2 and 3. This angle is equal to the rotation around hinge H23 ($\theta_7 = \delta_3$) defined in Fig.5.4b.

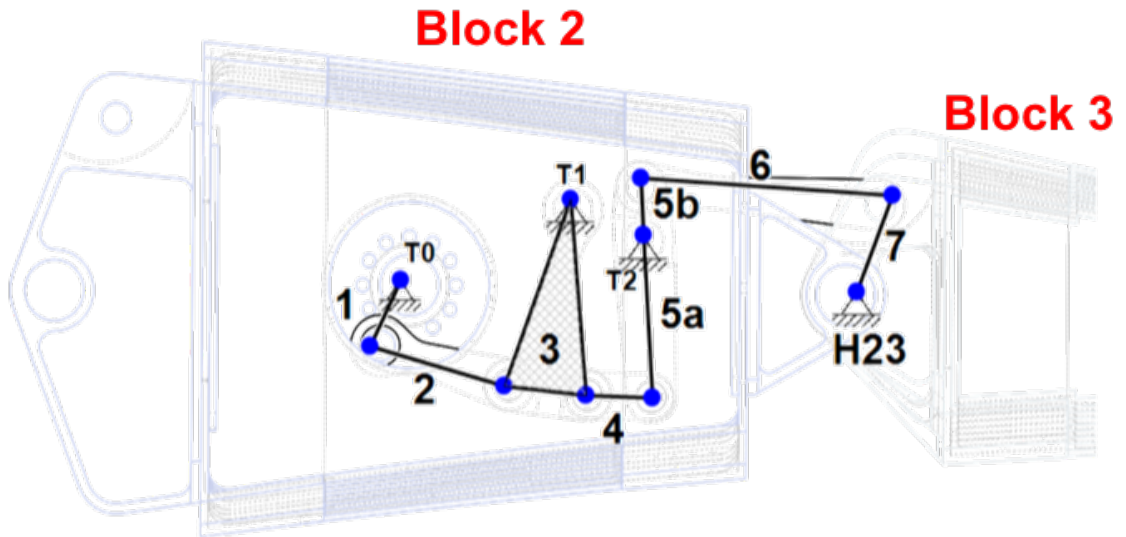


(a) Links lengths within the minimum available design space of the tip TE section.

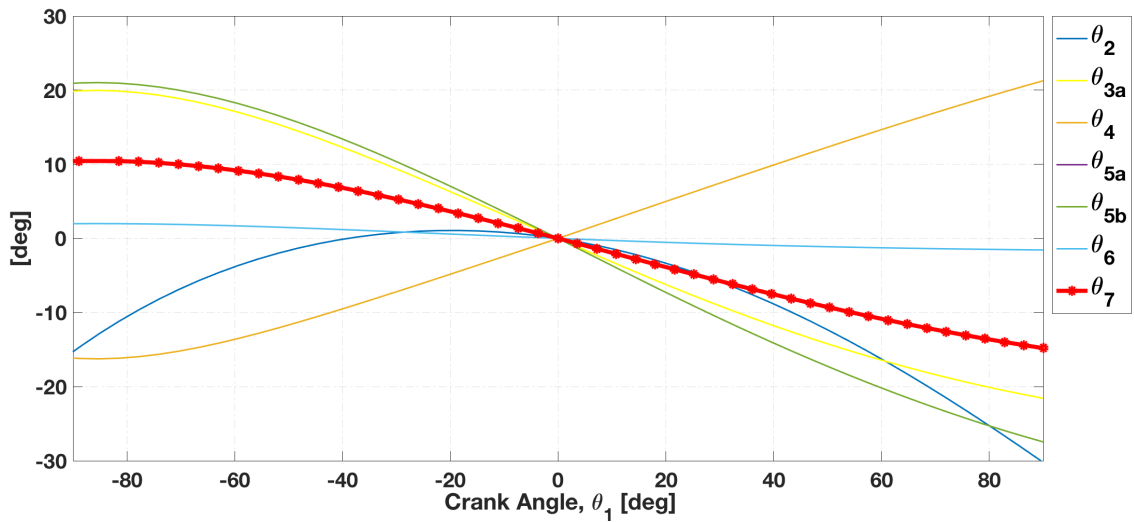


(b) Links Angles as function of the crank angle input rotation.

Figure 5.7: Kinematic design of the inner mechanism (IM1) located in rib block B1.



(a) Links lengths within the minimum available design space of the tip TE section.



(b) Links Angles as function of the crank angle input rotation.

Figure 5.8: Kinematic design of the inner mechanism (IM2) located in rib block B2.

5.2.3 Inner Mechanisms Analysis with the Instant Centres (ICs) tool

Modern adaptive systems, designed for large demonstrators, are commonly based on the seamless integration of actuators, mechanisms, and structures with the purpose of reshaping the external surface on demand [54].

Reduce parameters as power required and weight are of paramount importance to successfully integrate adaptive systems in large airplanes for improving performances and enlarge mission profiles.

For this reason, an energy-efficient perspective is crucial till from the preliminary design phase of the actuation system [55]. Parameters capable to express interactions between the basic elements of this mechanized system and the external loads have to be defined to provide insight into the behaviour of the overall adaptive system [56].

The mechanical advantage of a mechanism could be defined as the ratio of the output torque to the input one [60].

To cut down the capacities of electro-mechanical actuators, the mechanical advantage of the inner mechanism within the rib blocks working range angles should be as high as possible. For the inner mechanisms (IM1 and IM2) in Figures 5.7a-5.8a, the main output is the moment transferred around the main hinge axis (\mathcal{M}_{OUT}) and the input refers to the input torque applied to the crank (\mathcal{M}_{IN}).

Assuming the friction and inertia are ignored, according to the principle of virtual work [62], for the inner mechanism, the following relationship can be found:

$$\mathcal{P}_{IN} = \mathcal{M}_{IN} \cdot \omega_{IN} = \mathcal{M}_{OUT} \cdot \omega_{OUT} = \mathcal{P}_{OUT} \quad (5.18)$$

where ω_{IN} is the crank angular speed, and ω_{OUT} is the angular speed around the rib block hinge axis. According to the definition of instant centre of rotation, at a fixed instant of time, a linkage mechanism undergoing planar movement has a coincident point with the same speed for the input part and output part, thus the following relationship can be defined (*note*: symbols are referred to IM2 in Fig.5.10a):

$$\omega_{IN} \cdot \overline{IC_{12} - IC_{2B3}} = \omega_{OUT} \cdot \overline{IC_{1B3} - IC_{2B3}} \quad (5.19)$$

where IC_{12} is the instant center between frame and input part (crank), IC_{1B3} is the instant center between frame and output part, IC_{2B3} is the instant center between input part and output part; $\overline{IC_{12} - IC_{2B3}}$ is the distance of the instant centers IC_{12} and IC_{2B3} , $\overline{IC_{1B3} - IC_{2B3}}$ is the distance of instant centers IC_{1B3} and IC_{2B3} .

If we recall the validity of the Aronhold-Kennedy's theorem which deals with the three instant centers between three links of a system of rigid members [61]:

Aronhold-Kennedy's Theorem. *The three instantaneous centers of three bodies moving relative to one another must lie along a straight line.*

By returning to the inner mechanism obtained at the end of the kinematic design process (Fig.5.8a) with this theorem, we can further simplify eq.5.19 as follows:

$$\frac{\omega_{IN}}{\omega_6} \cdot \frac{\overline{IC_{26} - IC_{12}}}{\overline{IC_{26} - IC_{16}}} = \frac{\omega_{IN}}{\omega_{OUT}} \cdot \frac{\overline{IC_{6B3} - IC_{1B3}}}{\overline{IC_{6B3} - IC_{16}}} \quad (5.20)$$

where IC_{6B3} is a first order instant center, and IC_{26} is a second order instant center.

Therefore, the mechanical advantage of the inner mechanism can be defined as function of particular first order and second order Instant Centers (ICs) of the linkage:

$$M.A. = \frac{\mathcal{M}_{OUT}}{\mathcal{M}_{IN}} = \frac{\omega_{IN}}{\omega_{OUT}} = \frac{\overline{IC_{26} - IC_{16}}}{\overline{IC_{26} - IC_{12}}} \cdot \frac{\overline{IC_{6B3} - IC_{1B3}}}{\overline{IC_{6B3} - IC_{16}}} \quad (5.21)$$

where IC_{12} , IC_{16} and IC_{1B3} are the primary instant centres which respectively coincide with leverage's fixed hinges (1, 2), (1, 6) and (1, B3). Construction of required instant centres for the inner mechanism, as shown in Fig.5.10a, is based on intersection of proper Aronhold-Kennedy (AK) lines. All required ICs for the estimation of the mechanical advantage are summarized in the IC matrix of the linkage (Fig.5.10b).

If the IM2 main hinges (labelled in green in Fig.5.10b) of the inner mechanism are defined as output of the kinematic design process, in the first iteration the first order ICs (labelled in blue in Fig.5.10b) were evaluated by intersection of the respective Aronhold-Kennedy lines.

$$\mathbf{AK}_{124} : \begin{pmatrix} x_{12} \\ y_{12} \end{pmatrix} + \begin{bmatrix} 1 & 0 \\ 0 & 1 \end{bmatrix} \cdot \begin{pmatrix} (x_{14} - x_{12}) \cdot t_{124} \\ (y_{14} - y_{12}) \cdot t_{124} \end{pmatrix} = \begin{pmatrix} x_{24} \\ y_{24} \end{pmatrix} \quad (5.22)$$

$$\mathbf{AK}_{234} : \begin{pmatrix} x_{23} \\ y_{23} \end{pmatrix} + \begin{bmatrix} 1 & 0 \\ 0 & 1 \end{bmatrix} \cdot \begin{pmatrix} (x_{34} - x_{23}) \cdot t_{234} \\ (y_{34} - y_{23}) \cdot t_{234} \end{pmatrix} = \begin{pmatrix} x_{24} \\ y_{24} \end{pmatrix} \quad (5.23)$$

Full equation, expressed in the matrix form, has to be solved at each linkage position:

$$\mathbf{IC}(2, 4) : \begin{bmatrix} 1 & 0 & (x_{12} - x_{14}) & 0 \\ 0 & 1 & (x_{12} - x_{14}) & 0 \\ 1 & 0 & 0 & (x_{23} - x_{34}) \\ 0 & 1 & 0 & (y_{23} - y_{34}) \end{bmatrix} \cdot \begin{pmatrix} x_{24} \\ y_{24} \\ t_{124} \\ t_{134} \end{pmatrix} = \begin{pmatrix} x_{12} \\ y_{12} \\ x_{23} \\ y_{23} \end{pmatrix} \quad (5.24)$$

that, in compact form, can be written as: $\underline{\underline{\mathbf{M}}}_{24} \cdot \underline{\underline{\mathbf{IC}}}_{24} = \underline{\underline{\mathbf{Q}}}_{24}$.

First order ICs (2, 4)(4, 6)(6, B3) can be evaluated solving the equation:

$$\begin{bmatrix} M_{24} & 0 & 0 \\ 0 & M_{46} & 0 \\ 0 & 0 & M_{6B3} \end{bmatrix} \cdot \begin{pmatrix} IC_{24} \\ IC_{46} \\ IC_{6B3} \end{pmatrix} = \begin{pmatrix} Q_{24} \\ Q_{46} \\ Q_{6B3} \end{pmatrix} \quad (5.25)$$

In the second iteration, the second order ICs (2, 6) was finally evaluated from intersection of AK_{126} with AK_{246} :

$$\begin{bmatrix} 1 & 0 & (x_{12} - x_{16}) & 0 \\ 0 & 1 & (y_{12} - y_{16}) & 0 \\ 1 & 0 & 0 & (x_{24} - x_{46}) \\ 0 & 1 & 0 & (y_{24} - y_{46}) \end{bmatrix} \cdot \begin{pmatrix} x_{26} \\ y_{26} \\ t_{126} \\ t_{246} \end{pmatrix} = \begin{pmatrix} x_{12} \\ y_{12} \\ x_{24} \\ y_{24} \end{pmatrix} \quad (5.26)$$

Therefore, for each specific linkage position, the mechanical advantage was obtained using the ICs positions. In Fig.5.9, the MA of IM1 is reported. When the crank is activated the rib block B2 rotates from the baseline position to the maximum angle $\delta_2 = 16.67^\circ$ and the MA has a maximum value equal to 15.81 and a minimum value equal to 6.87.

In Fig.5.9, the MA of IM1 is reported. When the crank is activated the rib rotates from the baseline position to the maximum downward (*upward*) deflection equal to $+10^\circ$ (-10°). During the transition from the baseline position to the target shape, for each intermediate linkage position, all required instant centres were estimated to completely obtain the mechanical advantage curve as function of the input crank rotation. In Fig.5.11a, the evolution of each instant centre position is reported. The mechanical advantage for the working output angle range $[+10^\circ; -10^\circ]$ is within the range $[5.18; 8.97]$ (Fig.5.11b).

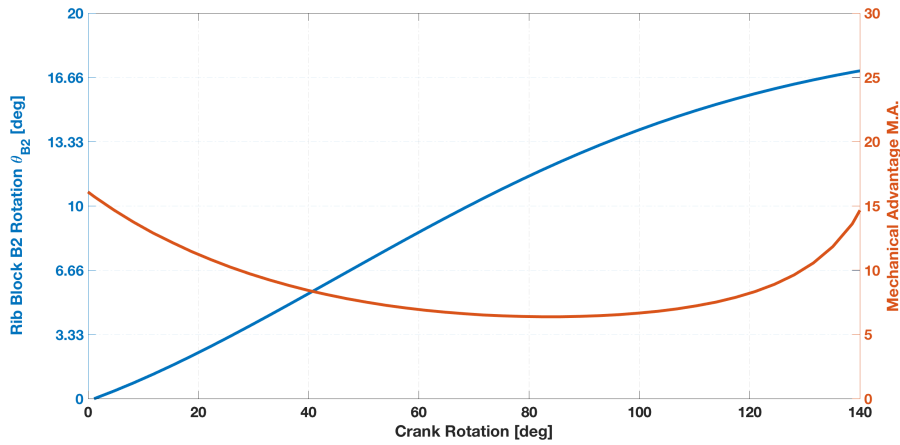
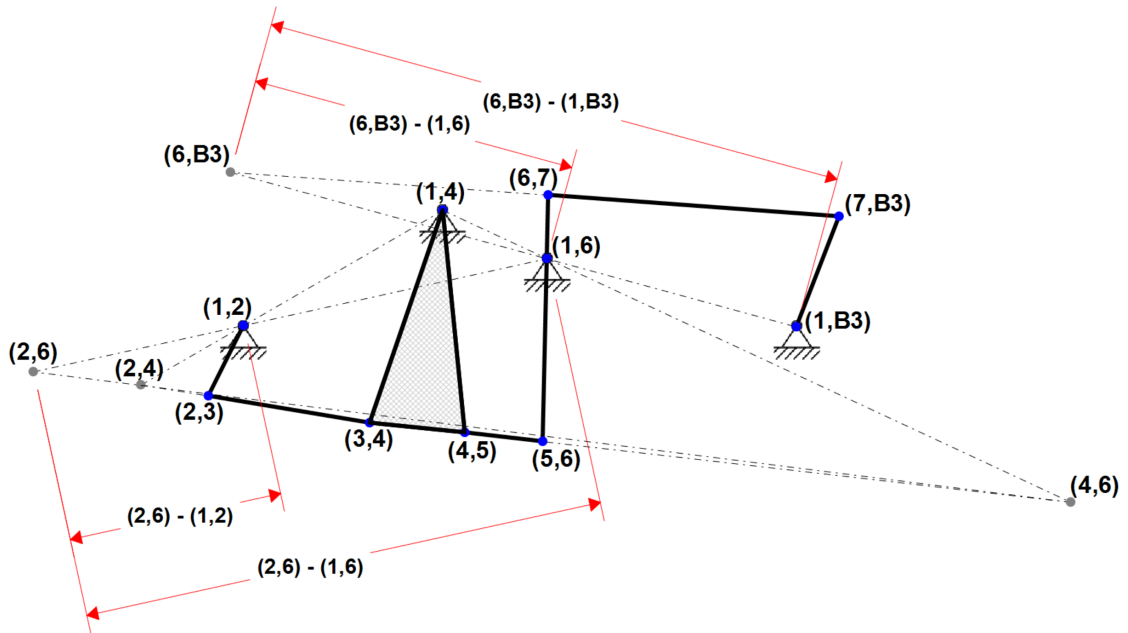


Figure 5.9: Inner mechanism (IM1): mechanical advantage as function of crank angle θ_1 .

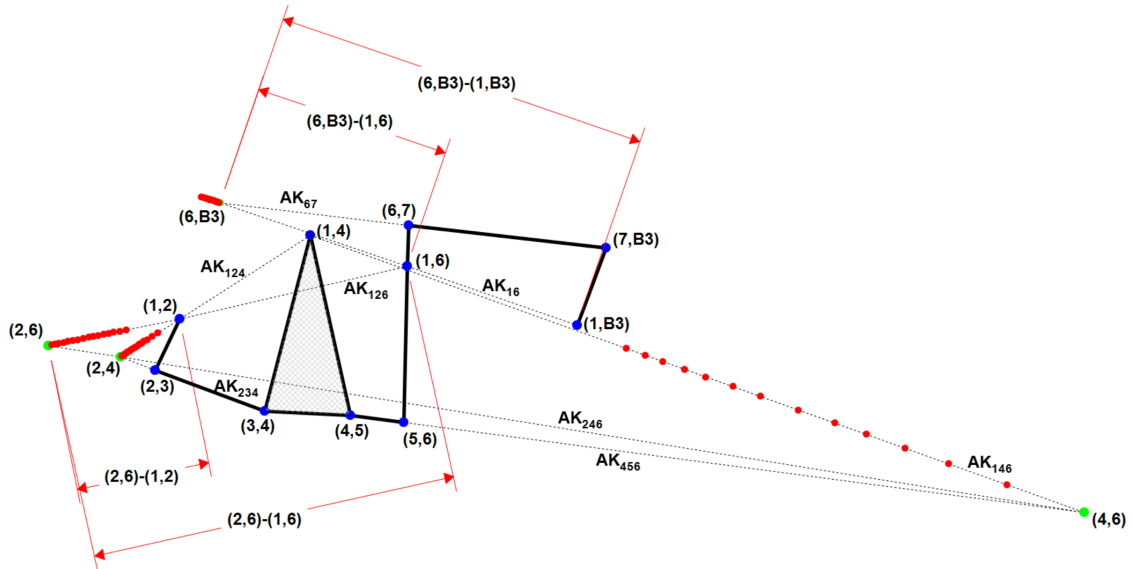


(a) Construction of instant center by means AK lines.

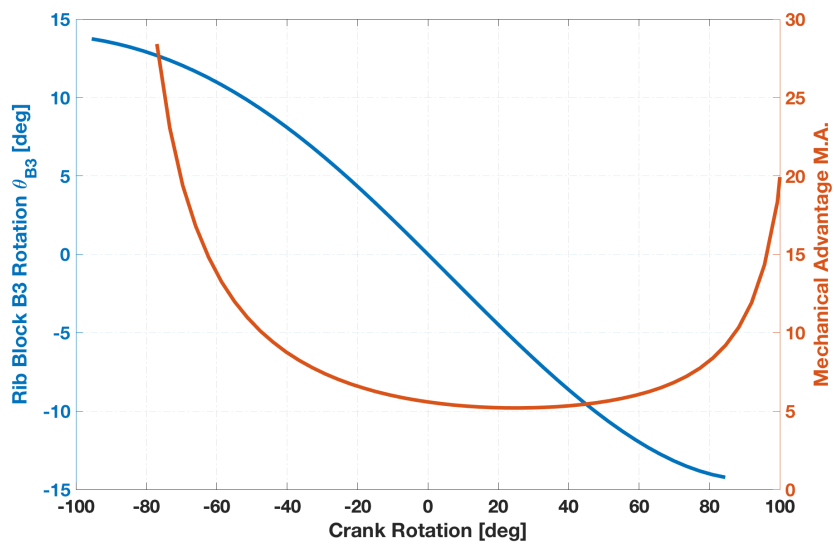
	1	2	3	4	5	6	7	B3
1	/	(1,2)	/	(1,4)	/	(1,6)	/	(1,B3)
2	(1,2)	/	(2,3)	(2,4)		(2,6)		
3	/	(2,3)	/	(3,4)				
4	(1,4)		(3,4)	/	(4,5)	(4,6)		
5				(4,5)	/	(5,6)		
6	(1,6)	<i>SYM</i>			(5,6)	/	(6,7)	(6,B3)
7	-					(6,7)	/	(7,B3)
B3	(1,B3)						(7,B3)	/

(b) ICs matrix of the linkage (IM2): main hinges (labeled in green), first order ICs (labeled in blue), second order IC (labeled in orange), and required ICs for MA estimation (marked in red).

Figure 5.10: Inner mechanism (IM2) instant centers analysis.



(a) Evolution of instant centers (ICs) along AK lines.



(b) Mechanical Advantage of IM2 (orange), and Output angle (blue) as function of crank rotation.

Figure 5.11: Inner mechanism (IM2) mechanical advantage (MA) evaluation by means of ICs.

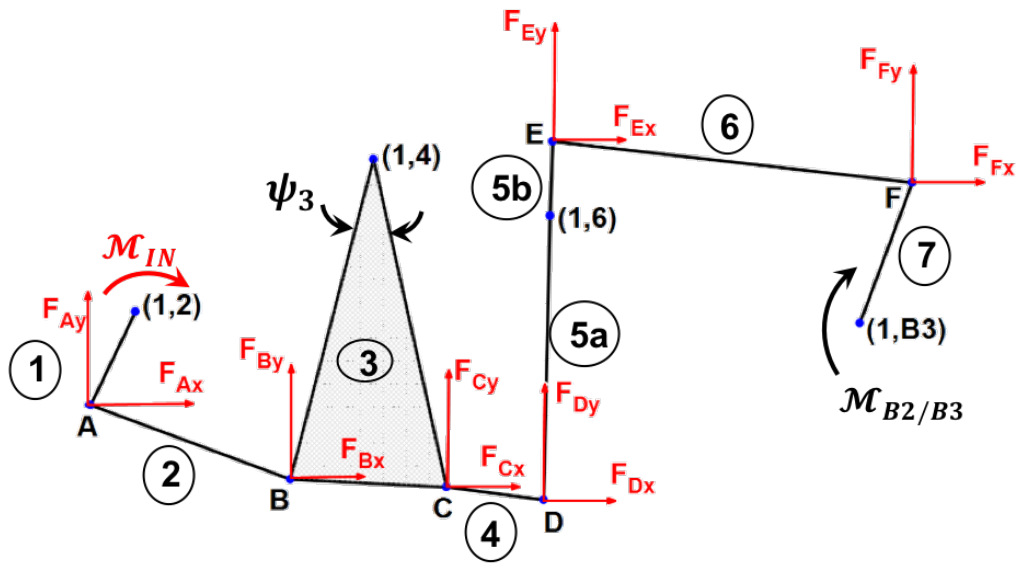


Figure 5.12: Inner mechanism full-force analysis (nomenclature).

5.2.4 Force Analysis of Single Input-Single Output Linkage Systems

A method for kinematic synthesis of a single-input single-output (SISO) linkage was proposed in Par.5.2.2 for use in the design of the kinematic chains of a smart rib.

Each mechanism (IM1 and IM2) uses a single actuator to provide the required output angle along the rib-block hinge during morphing operations. These inner mechanisms are comprised of a series of four-bar linkages connected together forming a multiple loop system that can provide smoothness transition from the baseline configuration to the target airfoil shape (i.e. mode 1, 2, and 3).

The kinematic synthesis method (Par.5.2.2) was able to determine the link sizes for the entire multi-loop system given a set of rib-block angle required for morphing.

After that, using the instant centres analysis tool in Par.5.2.2, fast evaluation of the linkages (IM1 and IM2) mechanical advantages was provided for the determination of the actuation torques provided in output along each rib-block hinge. Moreover, the ICs tool was able to preliminary estimate the amount of torque that the actuator needs to provide in order to hold the entire system in static equilibrium. These actuation torques were sufficient to counteract the aerodynamic moments experienced by each smart rib during limit load conditions. However, even if the instant centres analysis was fast and easy-to-program tool to estimate the mechanical advantage of selected mechanisms, this tool was not able to estimate the forces acting on each link during morphing operations.

For this purpose, a static force analysis was preliminary developed to capture the forces

applied on the entire linkage during morphing operations. In such a way, the result of this analysis was able to support the structural design of each link (length and position) as well as the selection of pin diameter required.

In what follows, first the analytical formulation of the problem is given; second, a full force modelling method is introduced for the specific linkage IM2 (located within rib-block B2); third, an analytical expression for the mechanical advantage is obtained, and finally simulations were carried out to estimate margin of safety for each link pin.

The full force modelling is based on the equations of equilibrium for each link. Fig.5.12 provides a diagram for full force modelling of a single inner mechanism (IM2). Here, $A, B, C, D, E,$ and F are the movable hinges connecting each link; $(1, 4), (1, 6)$ and $(1, B3)$ are the hinges fixed on the frame of each rib-block plate.

For the generic planar linkage under study with an external moment $\mathcal{M}_{B2/B3}$ applied, there is only one independent degree-of-freedom (DOF). For each assigned crank rotation θ_1 (i.e. the crank is the link 1 in Fig.5.12), an input moment (\mathcal{M}_{IN}) is required to maintain the system in equilibrium.

In total, there are thirteen unknown variables (marked in red in Fig.5.12) for the full linkage and only the external moment $\mathcal{M}_{B2/B3}$ is supposed to be known; this means that a determinate system of thirteen equations is required to fully define the linkage.

The following equilibrium conditions were imposed for each link:

- 1 equation (*moment equilibrium*) per each grounded link (i.e. 1, 3, 5, 7);
- 3 equations (*forces and moment*) per each not-grounded link (i.e. 2, 4, 6).

All the equilibrium equations can be arranged in matrix form:

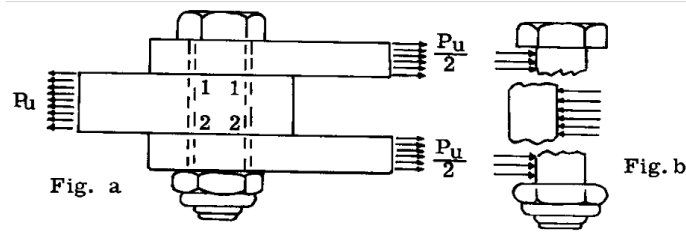
$$\{\underline{\mathbf{X}}\} = [\underline{\mathbf{A}}]^{-1} \cdot \{\underline{\mathbf{U}}\} \quad (5.27)$$

where: $\underline{\mathbf{X}}$ is a vector (13x1) of unknown variables (pin forces \mathcal{F}_i , and the input moment \mathcal{M}_{IN}); $\underline{\mathbf{U}}$ is a vector (13x1) of known variables (only the external aerodynamic moment in the rib-block hinge $\mathcal{M}_{B2/B3}$); $\underline{\mathbf{A}}$ is a banded matrix with 13x13 dimensions dependent by links lengths and angles.

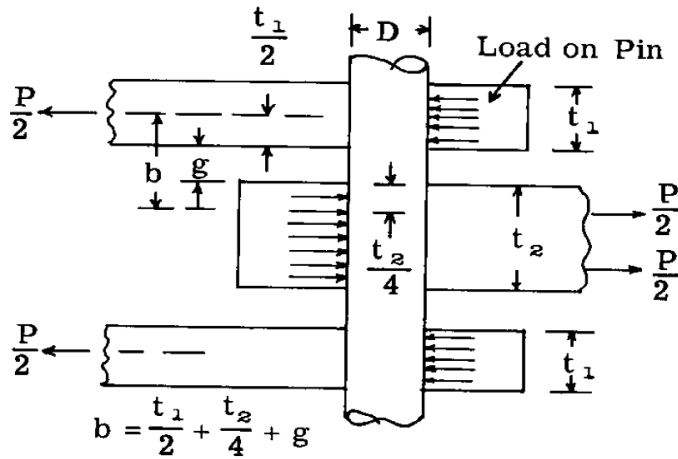
These matrices were defined as follows:

$$\{\underline{\mathbf{X}}\} = \left\{ \mathcal{M}_{IN} \ \mathcal{F}_{Ax} \ \mathcal{F}_{Ay} \ \mathcal{F}_{Bx} \ \mathcal{F}_{By} \ \mathcal{F}_{Cx} \ \mathcal{F}_{Cy} \ \mathcal{F}_{Dx} \ \mathcal{F}_{Dy} \ \mathcal{F}_{Ex} \ \mathcal{F}_{Ey} \ \mathcal{F}_{Fx} \ \mathcal{F}_{Fy} \right\}^T \quad (5.28)$$

$$\{\underline{\mathbf{U}}\} = \left\{ 0 \ 0 \ 0 \ 0 \ 0 \ 0 \ 0 \ 0 \ 0 \ 0 \ 0 \ 0 \ 0 \ -\mathcal{M}_{B2/B3} \right\}^T \quad (5.29)$$



(a) Failure by pin shear [64].



(b) Pin Bending Strength, method for determining the arm [64].

Figure 5.13: Nomenclature of terms used for margin of safety evaluation.

This formula has the benefit to provide direct relationship between the mechanical advantage of the inner mechanism and each link parameter: length r_i , and angle θ_i .

In the preliminary evaluation of force acting on the full linkage, an external aerodynamic torque $\mathcal{M}_{B2/B3}$ equal to 165 Nm was considered.

Imposing this value constant in the tab angle range $[-10^\circ; +10^\circ]$, we can estimate links forces as function of the crank input angle. As shown in Fig.5.14a, the highest force on not-grounded links is located on link 6. On the other hand, the highest force on grounded link is located on fixed hinge $T2$ (see Fig.5.8a) which connects the link 5 to the plates of rib-block B2.

According to Bruhn [64], pin can fail by shear. As the force P (see Fig.5.13a) is placed on the fitting it tends to shear the pin at sections. Let \mathcal{P}_{tu} represent the maximum or ultimate load on the fitting, the following formula for Margin of Safety can be assumed:

$$M.S.(Shear) = \frac{\mathcal{P}_{tu}}{1.5 * \text{Pin Force}} - 1 \quad (5.34)$$

Table 5.1: IM2 geometric values used for MS evaluation.

	t1 [mm]	t2 [mm]	g [mm]	b [mm]	Pin Diameter [mm]
A	10.25	8	7	16.125	6
B	4	8	1	7	6
T1	5.5	18	2	13.75	8
C	4	8	1	7	6
D	5	8	1	7.5	6
T2	5.5	10	6	13.75	8
E	5	10	0.5	8	6
F	4	9	2	8.5	6
B2/B3	10	25	2.5	20	10

In Fig.5.15a, results of M.S.(*Shear*) are summarized. Ultimate Shear strengths of AN steel pins, reported in [64], have been considered. All values are positive, and the minimum value is equal to 1.61 on hinge *F*.

In general static tests of single bolt fittings will not show a failure due to bolt bending failure [64]. However, it is important that sufficient bending strength will be provided to prevent permanent bending deformation of the fitting bolt under the limit loads so that bolts can be readily removed in maintenance operations. The following formula is used for evaluation of Margin of Safety:

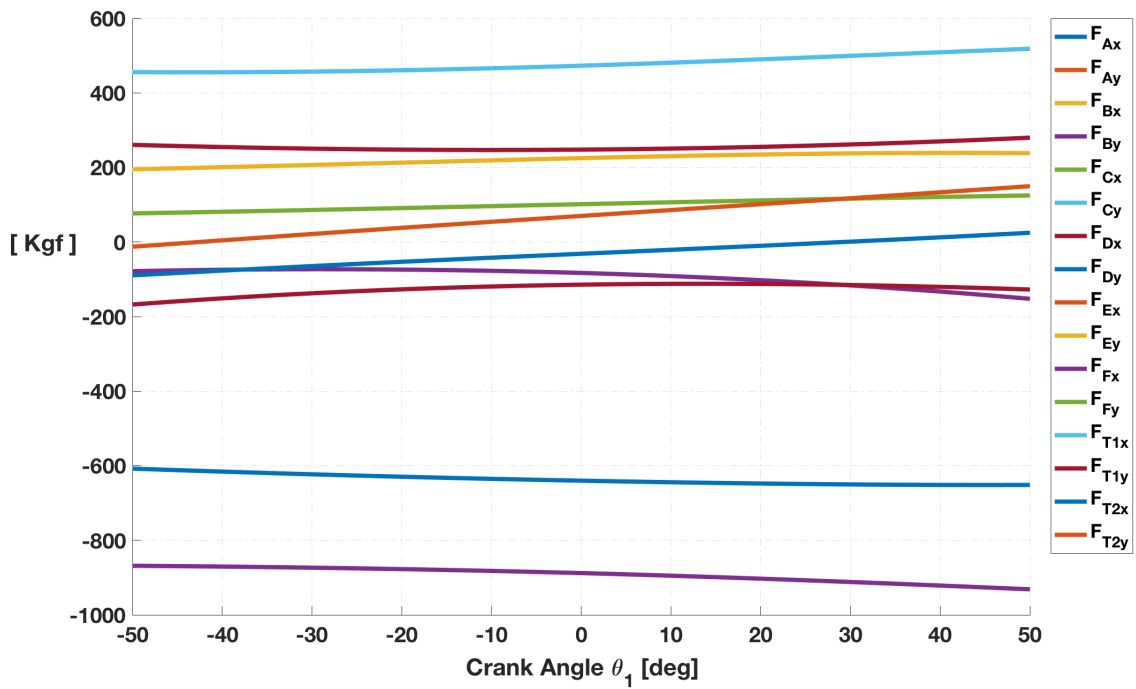
$$\text{M.S.}(Bending) = \frac{\mathcal{M}_{tu}}{\text{Bending Moment on pin}} - 1 \quad (5.35)$$

where, considering the method shown in Fig.5.13b, the arm *b* is equal to:

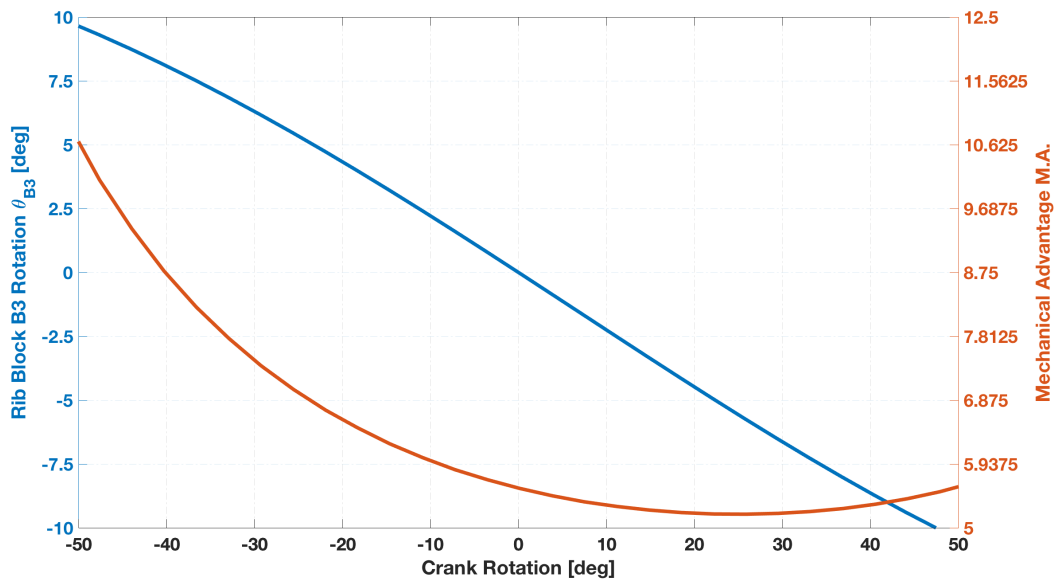
$$\text{Bending Moment on pin} = \frac{1}{2} * b * \text{Pin Force} \quad (5.36)$$

$$b = \frac{t_1}{2} + \frac{t_2}{4} + g \quad (5.37)$$

In Fig.5.15b, results of M.S.(*Bending*) are summarized. Ultimate Bending of AN steel pins, reported in [64], have been considered. All values are positive, and the minimum value is equal to 0.47 on hinge *F*.

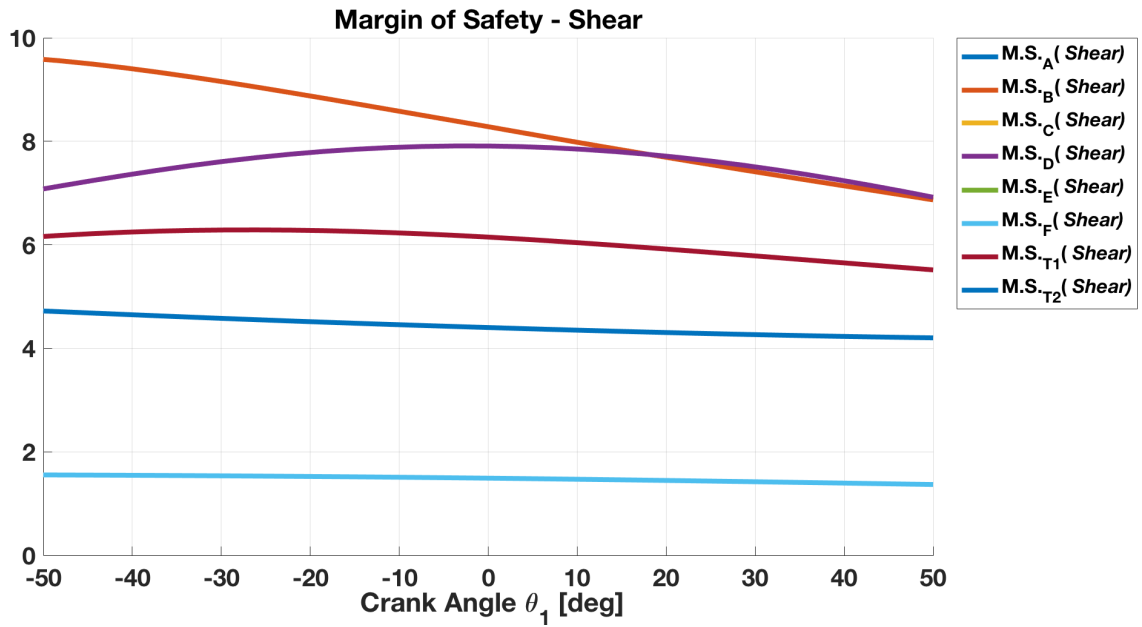


(a) Forces as function of the input crank angle θ_1 .

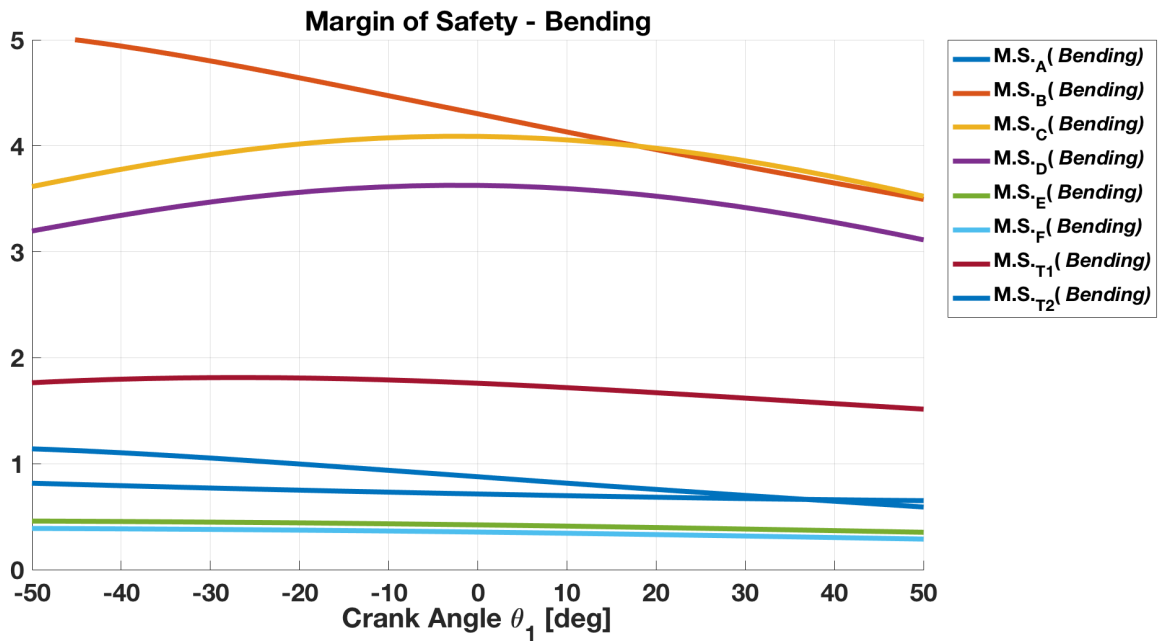


(b) Mechanical Advantage of IM2 (orange), and Output angle (blue) as function of crank rotation.

Figure 5.14: Inner mechanism (IM2): links forces and MA.



(a) Margin of Safety (M.S.) for Shear.



(b) Margin of Safety (M.S.) for Bending.

Figure 5.15: Inner mechanism (IM2): margin of safety for bolts as function of crank rotation θ_1 .

5.2.5 Finalized Layout (3D-CAD)

The first design loop was mainly driven by kinematic optimization of inner mechanisms (IM1 and IM2) according to the minimum available room within the tip section of the Fowler flap structure. The geometric parameters of leverages were synthesized to obtain high mechanical advantage as well as a large range of output angles (i.e. θ_{B2} and θ_{B3}).

As the smart rib is the core part of the adaptive structure, smooth control action of the morphing Fowler flap can be possible if no oscillations occur in the crank-rib block angle curves (i.e. $\theta_{B2}(\theta_{1,IM1})$ and $\theta_{B3}(\theta_{1,IM2})$). For this reason, final geometric parameters of linkages were chosen to avoid conditions where the output angle curves present peaks or inversions (i.e. $d\theta_{B2}/d\theta_{1,IM1} \neq 0$ and $d\theta_{B3}/d\theta_{1,IM2} \neq 0$).

In the second loop, using the instant centres analysis tool (Par.5.2.2), a fast evaluation of the linkages (IM1 and IM2) mechanical advantages was possible for the determination of the actuation torques provided in output along each rib-block hinge. In addition, the ICs tool was a very valuable tool to preliminary estimate the amount of torque that the actuator needs to hold the entire skeleton in static equilibrium.

In the third step, a static force analysis was developed to capture the forces applied on the entire linkage during morphing operations. The result of this analysis was able to support the structural design of each link (length and position) as well as the selection of pin diameter required.

After this three-step design process, the final mechanical layout of the smart rib was obtained. The exploded view of the smart rib is shown in Fig.5.16b. Each kinematic chain (IM1 and IM2) consists of a crank, two ternary links, and three binary links. All items are connected by cylindrical hinges. In additions, the crank and the ternary links are doubly supported on rib block plates to avoid out-of-plane rotations during the working range of the inner mechanisms.

Each mechanism (IM1 and IM2) uses a single actuator to provide the required output angle along the rib-block hinge during morphing operations. These inner mechanisms provide smoothness transition from the baseline configuration to the target airfoil shapes (i.e. mode 1, 2, and 3) without clashes or mechanical interferences.

5.2.6 Structural Design of the Smart Rib

Reliable and accurate finite-element models were defined to verify the kinematic chains, the actuating torques estimated with the instant centres (ICs) tool, as well as the structural integrity of the finalized smart rib layout.

A three-dimensional finite-element model of the smart rib was generated consisting of six-sided solid elements (CHEXA [88]) for links of the inner mechanisms and hinge

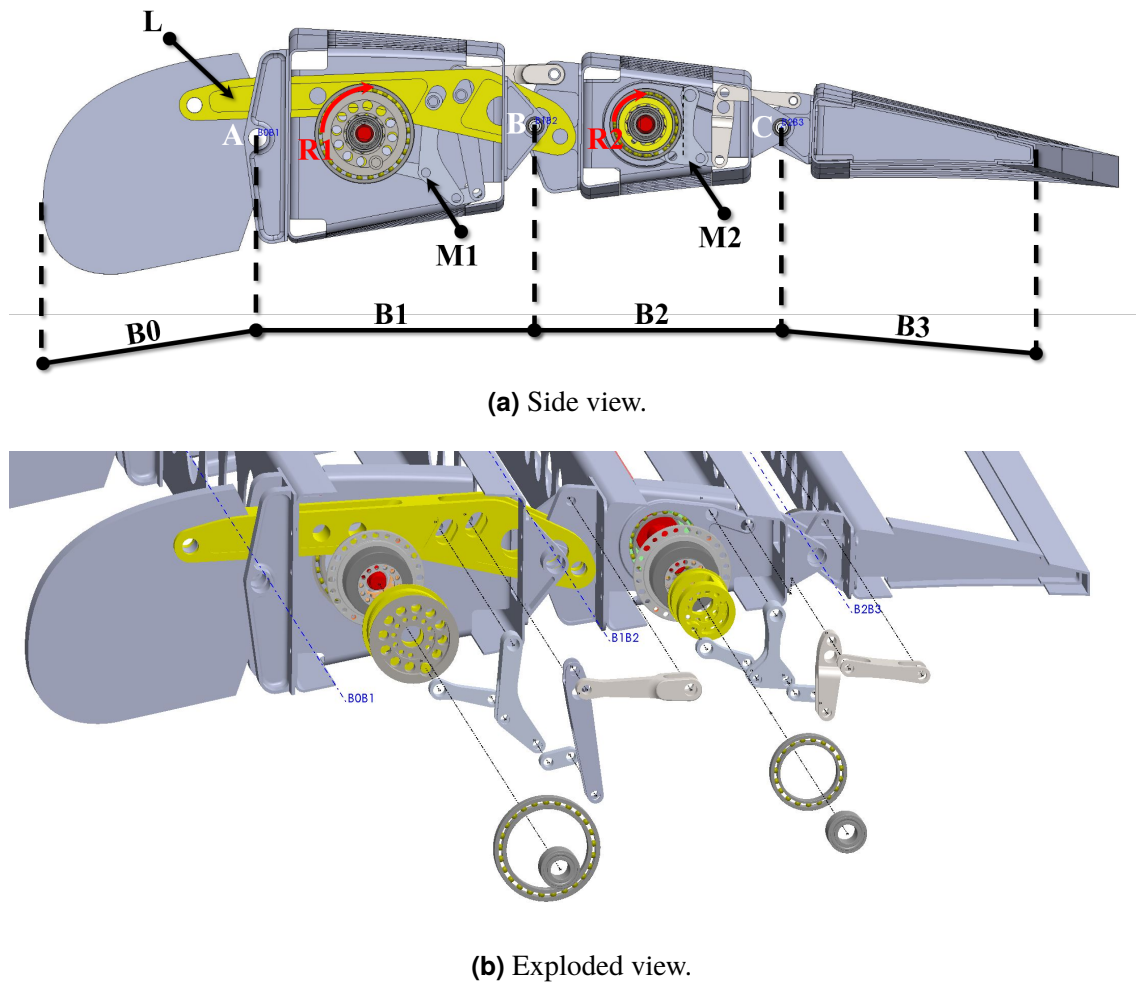


Figure 5.16: Smart rib: finalized layout (3D-CAD).

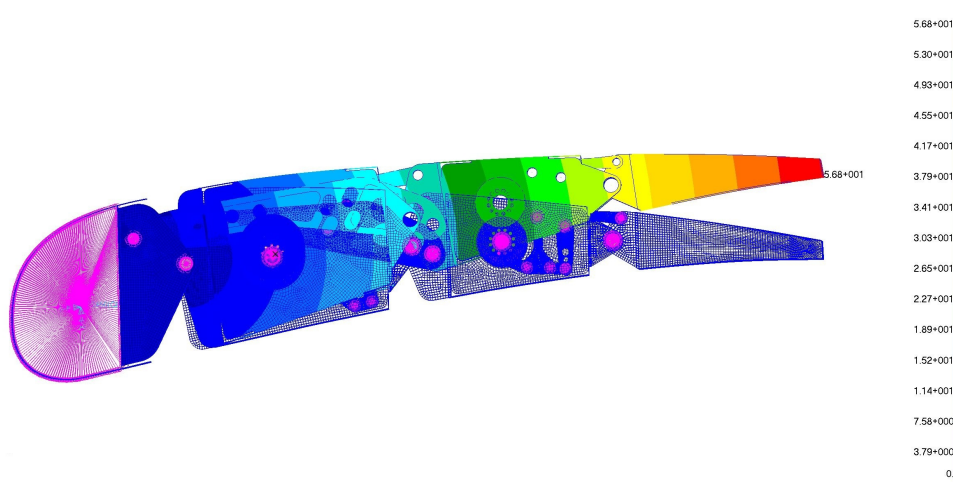
fittings, quadrilateral plane elements (CQUAD [88]) for the skin, beam elements (CBEA [88]) with rigid body elements (RBE2 [88]) for the cylindrical hinges.

The linear solver of Nastran (SOL 101) was used for structural analysis of the smart rib with the limit load condition pertaining to morphing mode 1. In addition, the following assumptions were made:

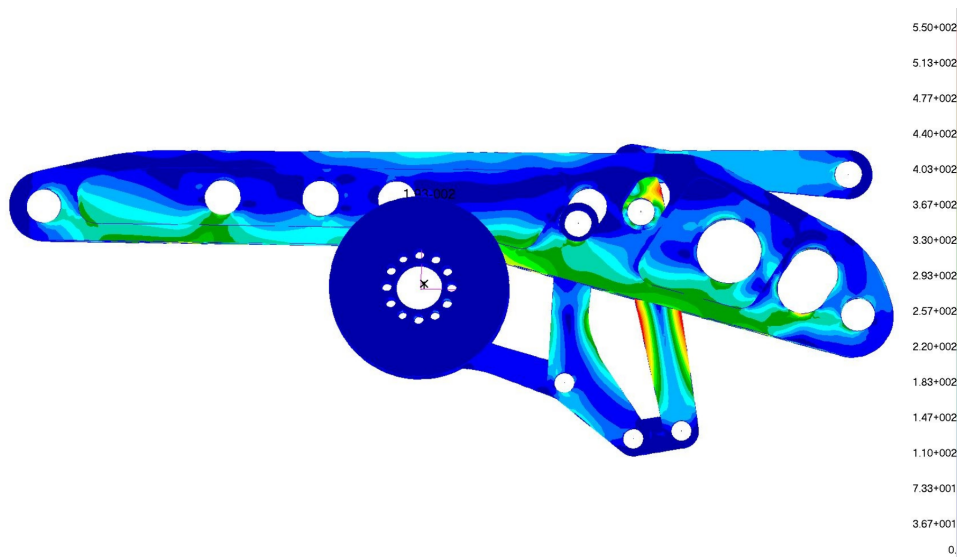
- Smart tip rib placed in baseline condition,
- Pressure loads, pertaining to the limit condition specified in Fig.4.4a, on upper and lower skins. The following resultant forces were applied: $F_{B0} = 2667\text{N}$, $F_{B1} = 1492\text{N}$, $F_{B2} = 974\text{N}$, $F_{B3} = 623\text{N}$,
- rib leading edge fixed (block B0).

As shown in Fig.5.17a, the maximum displacement is equal to 11 per cent of the local tip chord (58.6 mm). Von Mises stress distribution over the inner mechanism (Fig.5.17b) confirms the absence of any local plasticization at limit load condition: maximum peak stress is equal to 550 MPa and located in the “fork” link of M1 leverage made of 17-4PH steel with a Yield Strength higher than 700 MPa.

All the other items of the actuating mechanism made of Al2024-T5 alloy show stress lower than 330 MPa. Actuating torque required to hold the cranks leverages in the baseline position are equal to 42.9Nm for linkage M1 and 9.2Nm for linkage M2.



(a) Displacement [mm], Max value 58 mm.



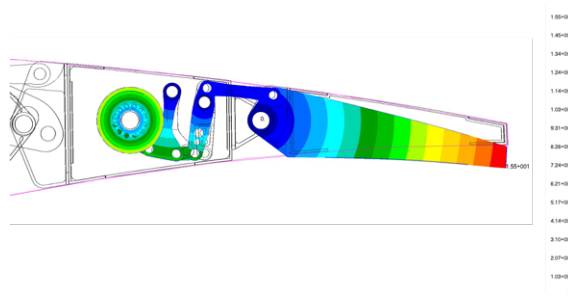
(b) Von Mises Stress [MPa], Max value 550 MPa.

Figure 5.17: Smart rib FE simulation: limit load for morphing mode 1.

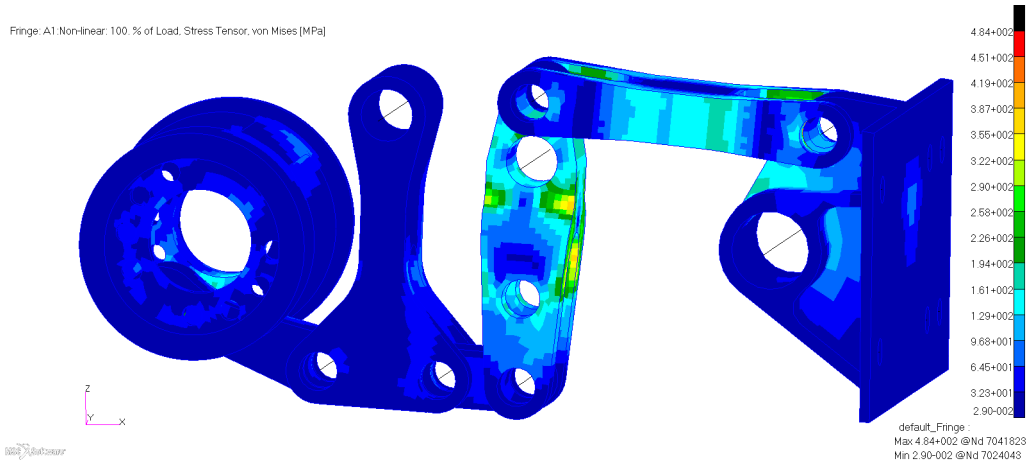
However, as explained in Sec.4.2.2, the 3MMF concept can operate also as prescribed by morphing modes 2 and 3. For this reason, when the flap is stowed, the flap tip segment has to be able to withstand the maximum pressure distribution at dive speed with $+3.33^\circ$ deflection (see Sec.4.2.2). In this case, the implicit non-linear solver (SOL 400 Nastran) was used to consider non-linear effects, and large rotations (rotations) updating the stiffness matrix at each step. The capability of the actuation system to enable morphing through smooth rigid-body kinematic of the inner mechanism was verified applying enforced displacements (SPCD [88]) to the crank and resistant torque (equal to 165 Nm) along the hinge axis to the actuator hinge fitting.

Von Mises stress distribution (Fig.5.18b) over the actuation mechanism confirms the absence of any local plasticization at limit load condition: maximum peak stress is equal to 484 MPa and located in the “fork” link made of 17-4PH steel with a Yield Strength higher than 700 MPa. All the other leverage’s items made of aluminium show lower stress than the Yield Strength of Al2024- T5 alloy. Finally, the actuation torque required to hold the leverage in the final position was equal to 23.25 Nm: MA is equal to 6.88 in accordance with the preliminary instant center tool.

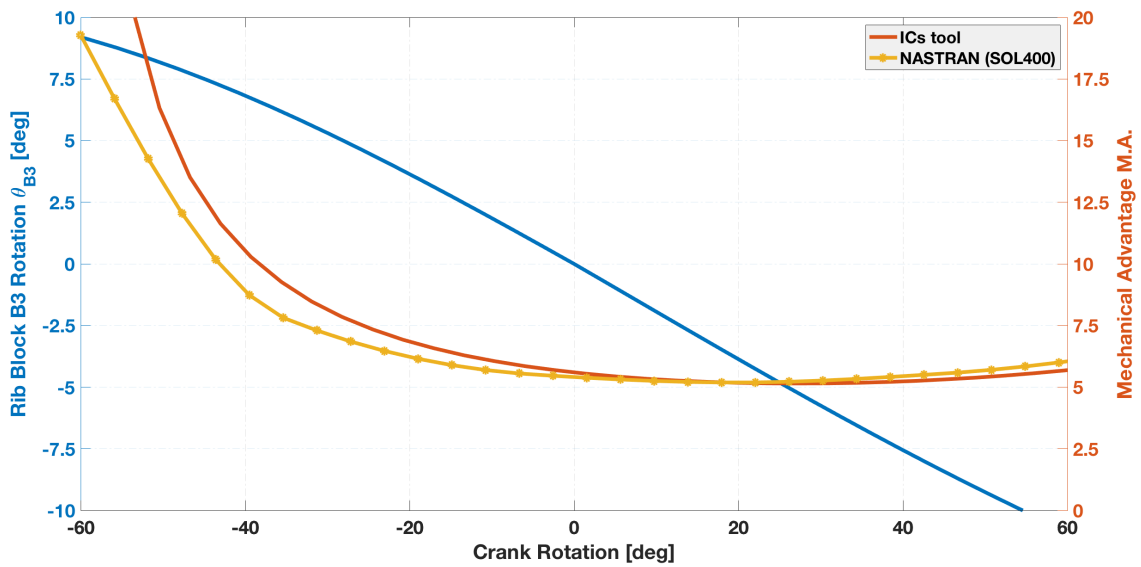
Several non-linear FE simulations were performed applying enforced rotations within the range $\theta_1 = [-80^\circ; 80^\circ]$ (SPCD [88]) to the crank and a resistant torque (equal to 165 Nm) along the hinge axis to the actuator hinge fitting. Obtained values are shown in Fig.5.18c: the preliminary ICs tool is in quite good agreement with NASTRAN SOL400.



(a) Displacement [mm], Max value 15.5 mm.



(b) Von Mises Stress [MPa], Max value 484 MPa.



(c) Mechanical Advantage estimated by ICs tool and NASTRAN (SOL400).

Figure 5.18: Smart rib FE simulation: limit load for morphing mode 2.

5.3 The Span-wise 3MMF Structural Skeleton

After the mechanism enabling rib morphing is defined in terms of the size of the rib blocks, and positions of hinges and links, the preliminary design of the structural system can be addressed. The ribs' kinematic chain is transferred to the overall 3MMF structure by means of a multi-box arrangement.

Considering preliminary attachment points of the fairing-less deployment system on the 3MMF skeleton, the ultimate bending moments and shear forces distributions will be evaluated and used for the pre-sizing of spars and skins. Finally, a simple FE model will be used to validate the followed procedure.

5.3.1 Structural Sizing of the Multi-Box Arrangement

Structural sizing process of the multi-box arrangement will be based on theory of thin-walled section beams [63].

Each box of the structural arrangement is assumed to be characterized by a single-cell configuration delimited along the span by homologue blocks of consecutive ribs, and along the chord by longitudinal stiffening elements (spars).

Upon the actuation of the ribs, all the boxes are put in movement, thus changing the external shape of the 3MMF. If the shape change of each rib is prevented by actuators, the multi-box structure is elastically stable under the action of external aerodynamic loads.

A statically equivalent system — based on lumped elastic properties — is then considered for each box; this equivalent system is sketched in Fig.5.19 with reference to a generic bay delimited by two consecutive 3MMF ribs.

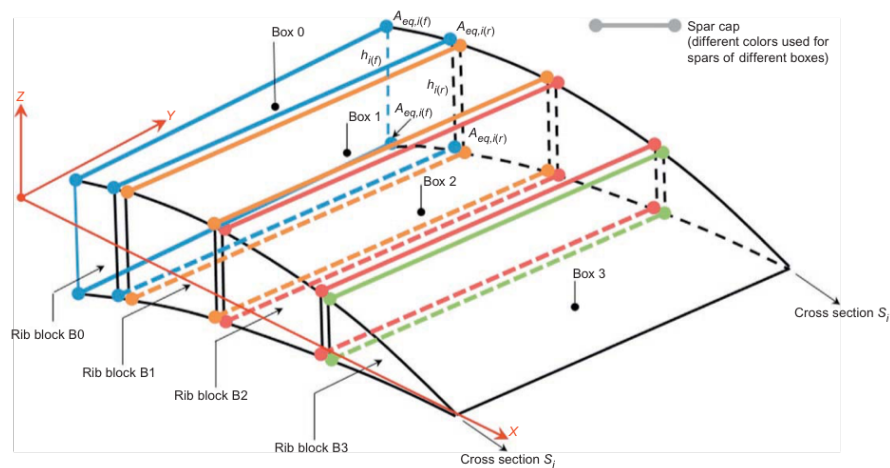


Figure 5.19: 3MMF Multi-box arrangement: lumped elastic properties.

The structural sizing of each box is carried out under the following assumptions:

- No load transfer between adjacent boxes; each box of the multi-box arrangement is treated separately;
- Most conservative condition in terms of multi-box configuration (morphed/unmorphed) and pertaining aerodynamic loads. This condition is identified as the one producing the highest internal solicitations (bending moments, shears, torque) along all the cross-sections of the multi-box arrangement.

For the cross-section of each 3MMF box, the following approaches can be used to assess the dimensions of the load bearing components: spar webs, spar caps, skin panels, rib plates.

Considering aerodynamic limit load condition (Par. 4.2.2, $q_\infty = 5858N/m^2$, airplane with flaps in landing configuration), the bending moment and shear force diagrams has to be evaluated for sizing the multi-box arrangement. The fairing-less deployment system is mainly composed of tracks and carriage fixed to the flap block $B0$ and attached in four points in correspondence of ribs 3, 4, 6, 7, as shown in Fig. 5.20a.

Each flap box can be reduced to a beam with supports in correspondence of the rib sections attached to the fairing-less deployment system. The vertical distributed load, pertaining to the limit load condition, is applied on each continuous beam model.

The five-span beam (Fig. 5.20b) is a redundant system with two hyper-static unknowns. This model can be reduced to a three-span beam with pinned supports with external moments ($\mathcal{M}_{OB} = 2q_{OB} \cdot L^2$ and $\mathcal{M}_{IB} = 2q_{IB} \cdot L^2$) at both beam ends (Fig. 5.20c), and the two unknown hyper-static moments (\mathcal{M}_I and \mathcal{M}_{II}).

If we consider that the rotation of the beam at the centre of each support is continuous across the support, the following conditions of congruence can be written for the rotation of each support using the principles of superposition [58]:

$$\left\{ \begin{array}{l} \phi_{I,left}^{(\mathcal{M}_I)} + \phi_{I,left}^{(\Pi_{II})} + \phi_{I,left}^{(\mathcal{M}_{II})} = \phi_{I,right}^{(\mathcal{M}_I)} + \phi_{I,right}^{(\Pi_I)} + \phi_{I,right}^{(\mathcal{M}_{IN})} \\ \phi_{II,left}^{(\mathcal{M}_{II})} + \phi_{II,left}^{(\Pi_{III})} + \phi_{II,left}^{(\mathcal{M}_{OUT})} = \phi_{II,right}^{(\mathcal{M}_{II})} + \phi_{II,right}^{(\Pi_{II})} + \phi_{II,right}^{(\mathcal{M}_I)} \end{array} \right. \quad (5.38)$$

where the generic term $\phi_{I,left}^{(\mathcal{M}_I)}$ is the left rotation of support I due to moment \mathcal{M}_I .

Making explicit each term of Eq. 5.38, we have the following system of equations:

$$\begin{cases} \frac{\mathcal{M}_I \cdot 2L}{3EI} - \frac{q_{II} \cdot (2L)^3}{24EI} + \frac{\mathcal{M}_{II} \cdot 2L}{6EI} = -\frac{\mathcal{M}_I \cdot L}{3EI} + \frac{q_I \cdot L^3}{24EI} - \frac{\mathcal{M}_{IB} \cdot L}{6EI} \\ \frac{\mathcal{M}_{II} \cdot L}{3EI} - \frac{q_{III} \cdot L^3}{24EI} + \frac{\mathcal{M}_{OB} \cdot L}{6EI} = -\frac{\mathcal{M}_{II} \cdot 2L}{3EI} + \frac{q_{II} \cdot (2L)^3}{24EI} - \frac{\mathcal{M}_I \cdot 2L}{6EI} \end{cases} \quad (5.39)$$

which are the three-moments equations [58] for the beam model of each flap box.

Solving Eq. 5.39, the hyper-static moments (\mathcal{M}_I and \mathcal{M}_{II}) can be obtained and the three-span beam becomes a statically determinate system. Therefore, reactions forces in supports can be evaluated by means of equilibrium equations. Bending moments and shear forces distributions can be obtained per each beam segment:

$$T_1(x) = R_{I,right} - q_I \cdot x, \quad M_1(x) = \mathcal{M}_I - R_{I,right} \cdot x + \frac{q_I \cdot x^2}{2} \quad (5.40)$$

$$T_2(x) = R_{II,right} - q_{II} \cdot x, \quad M_2(x) = \mathcal{M}_{II} - R_{II,right} \cdot x + \frac{q_{II} \cdot x^2}{2} \quad (5.41)$$

$$T_3(x) = R_{III} - q_{III} \cdot x, \quad M_3(x) = \mathcal{M}_{OB} - R_{III} \cdot x + \frac{q_{III} \cdot x^2}{2} \quad (5.42)$$

In Fig. 5.21, final distribution of bending moments and shear forces are reported; the highest solicitations are located near the root support (rib 3, at $x = 3.75m$). For the preliminary sizing of spars and skins, the ultimate bending moments and shear forces were obtained multiplying limit loads with a safety factor equal to 1.5.

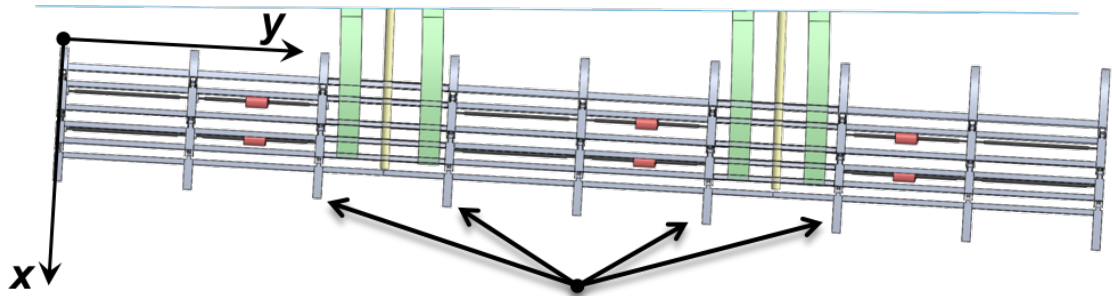
The ultimate bending moment $BM_{i(U)}$ at section S_i is supposed to be absorbed by front and rear spar caps according to:

$$BM_{i(f)} = \frac{h_{i(f)}^2}{h_{i(f)}^2 + h_{i(r)}^2} \cdot BM_{i(U)} = \gamma \cdot BM_{i(U)} \quad (5.43)$$

$$BM_{i(r)} = \frac{h_{i(r)}^2}{h_{i(f)}^2 + h_{i(r)}^2} \cdot BM_{i(U)} = (1 - \gamma) \cdot BM_{i(U)} \quad (5.44)$$

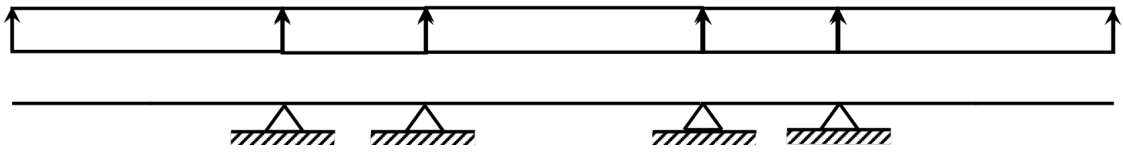
where $BM_{i(f)}$ is the amount of section ultimate bending moment absorbed by front spar caps; $h_{i(f)}$ is the height of the front spar; $BM_{i(r)}$ is the amount of section ultimate bending moment absorbed by rear spar caps; and $h_{i(r)}$ is the height of the rear spar. Normal stress induced by bending moments in front and rear spar caps is then imposed equal to σ_{ref} , with σ_{ref} being equal to $f \cdot \sigma_{tu}$, with σ_{tu} ultimate tensile stress of the material and f a safety factor equal to 0.7.

Required equivalent areas for front and rear spar are obtained as:

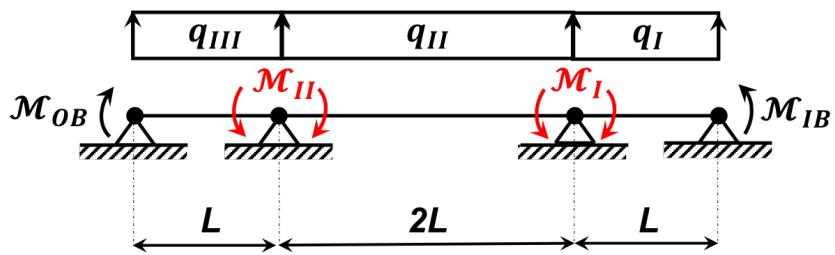


Deployment System attachment points

(a) Fairing-less Deployment System hosted in the 3MMF skeleton.



(b) Beam model of each flap box.



(c) Continuous-beam model.

Figure 5.20: 3MMF Multibox arrangement: beam model.

$$A_{eq,i(f)} = \frac{BM_{i(f)}}{\sigma_{ref}} \cdot \frac{1}{h_{i(f)}} \tag{5.45}$$

$$A_{eq,i(r)} = \frac{BM_{i(r)}}{\sigma_{ref}} \cdot \frac{1}{h_{i(r)}} \tag{5.46}$$

For practical reasons related to the manufacturability of the structural components, a lower boundary A^* is established for cap areas. The equivalent areas are considered equal to A^* in all cross-sections where Eqs. 5.45-5.46 provide values lower than A^* .

The chord-wise position of the ultimate shear force can be obtained as:

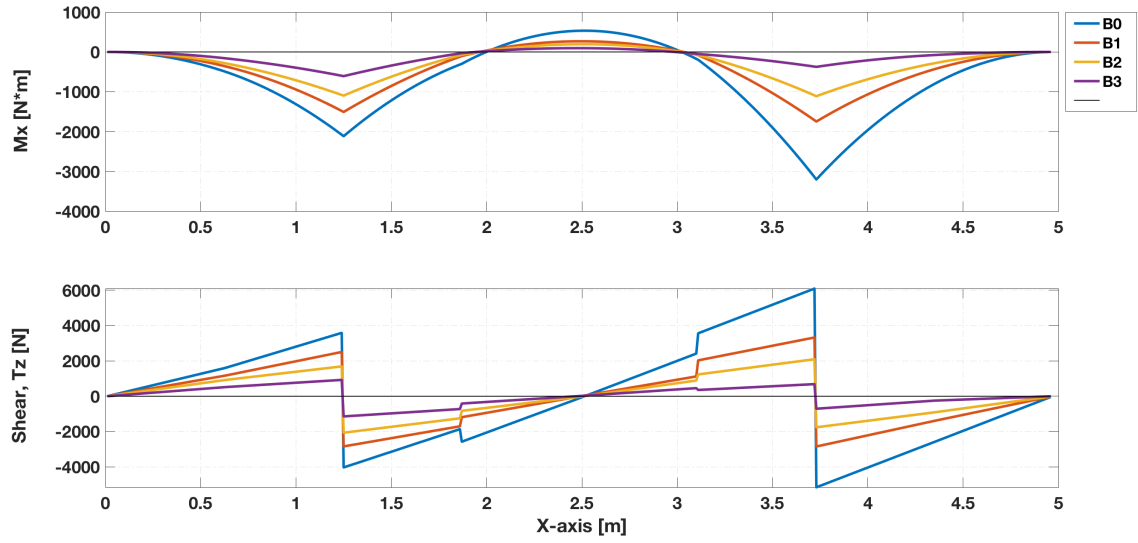


Figure 5.21: 3MMF Multibox arrangement: bending moments and shear forces distributions.

$$X_{S_i(U)} = \frac{TM^*_{i(U)}}{S_{i(U)}} \quad (5.47)$$

where $TM^*_{i(U)}$ is the ultimate torque moment at section S_i and $S_{i(U)}$ the ultimate shear at station S_i . The shear centre is assumed to be chord-wise located at the middle of the section:

$$X_{SC_i} = \frac{X_{i(f)} + X_{i(r)}}{2} \quad (5.48)$$

where $X_{i(f)}$ and $X_{i(r)}$, respectively, indicate the chord-wise coordinates of front and rear spar webs. According to the assumption about shear centre position, the effective ultimate torque moment can be replaced by a dummy value given by:

$$\overline{TM}_{i(U)} = S_{i(U)} \cdot |X_{S_i(U)} - X_{SC_i}| \quad (5.49)$$

By invoking Bredts formula, cell's shear flow results equal to:

$$q_i = \frac{\overline{TM}_{i(U)}}{2\Omega_i} \quad (5.50)$$

Ω_i being the area enclosed by the cell.

The shear flows, arising in each element of the section, are then obtained by referring

to the following equations:

$$q_{i(fw)} = q_i \cdot \frac{h_{i(f)}}{P_i} \quad (5.51)$$

$$q_{i(rw)} = q_i \cdot \frac{h_{i(r)}}{P_i} \quad (5.52)$$

$$q_{i(sk)} = q_i \cdot \frac{l_{i(sk)}}{P_i} \quad (5.53)$$

where $q_{i(fw)}$ is the shear flow in the web of the front spar; $q_{i(rw)}$ is the shear flow in the web of the rear spar; $q_{i(sk)}$ is the shear flow in the (upper/lower) skin panel; $h_{i(f)}$ is the height of the front spar; $h_{i(r)}$ is the height of the rear spar; $l_{i(sk)}$ is the length of the (upper/lower) skin panel; and P_i is the perimeter of the cell.

Shear stress induced by shear and torque moment along section elements are finally imposed to be equal to τ_{ref} , in which τ_{ref} is assumed equal to $\sigma_{ref}/\sqrt{3}$. Webs and skin panel thickness can be obtained by the equations:

$$t_{i(fw)} = q_{i(fw)}/\tau_{ref} \quad (5.54)$$

$$t_{i(rw)} = q_{i(rw)}/\tau_{ref} \quad (5.55)$$

$$t_{i(sk)} = q_{i(sk)}/\tau_{ref} \quad (5.56)$$

where $t_{i(fw)}$ is the thickness of the front spar web; $t_{i(rw)}$ is the thickness of the rear spar web; and $t_{i(sk)}$ is the thickness of the (upper/lower) skin panels.

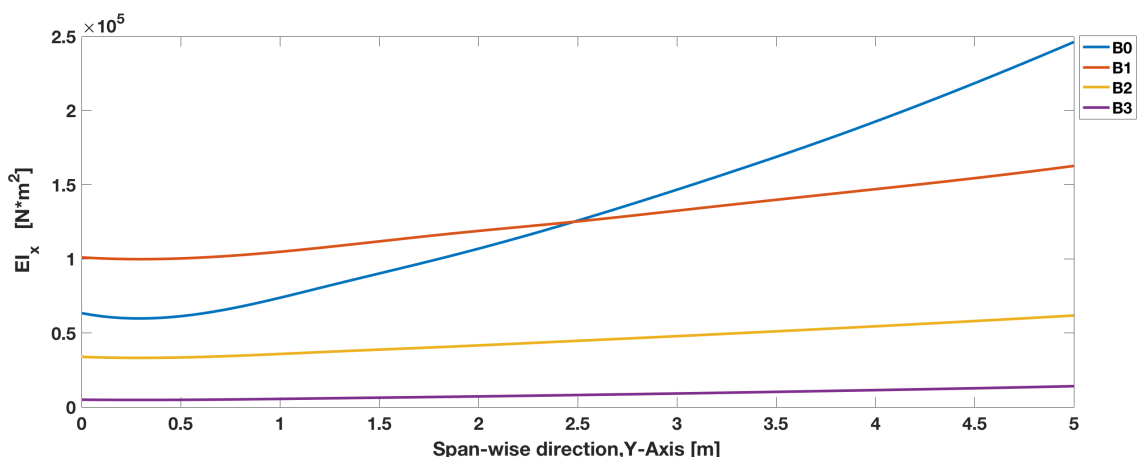
In order to take in account manufacturability constraints, Eqs.5.54-5.55-5.56 have to be combined with a lower boundary condition $t_{i(.)} \geq t^*$, where t^* is the minimum acceptable value for the thickness of the structural elements. In other terms, the thickness $t_{i(.)}$ is assumed equal to t^* if Eqs.5.54-5.55-5.56 provide values lower than t^* . For preliminary sizing purposes, at each cross-section S_i , the thickness of the rib is generally assumed to be equal to the greatest between $t_{i(rw)}$ and $t_{i(sk)}$.

It is evident that this approach allows for an iso-stress preliminary sizing of the structural elements at each cross-section, making the dimensions of the structural elements suitably distributed along the span so that at each section they aren't oversized with reference to the internal forces they must withstand.

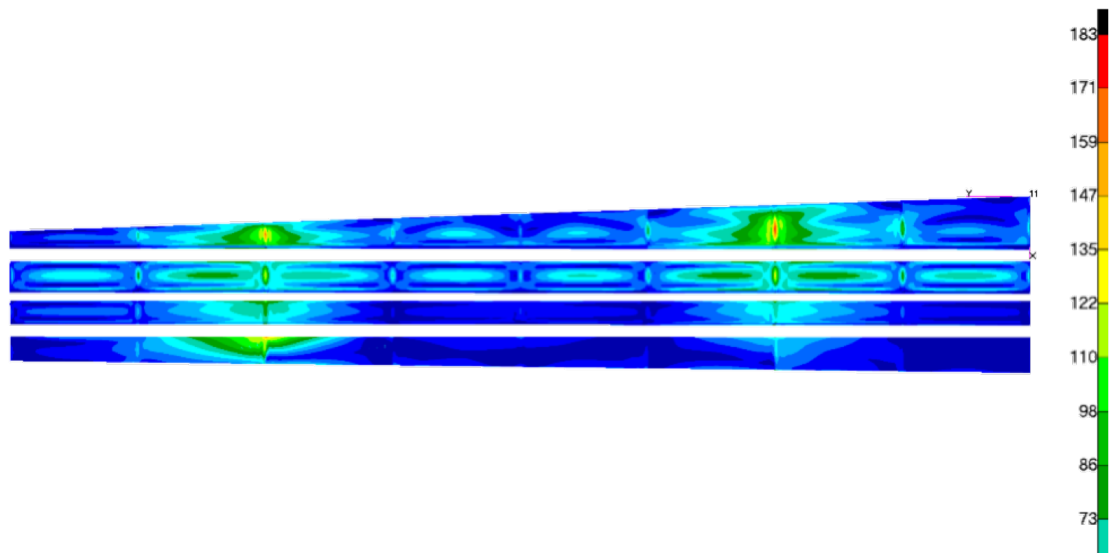
The preliminary sizing allows for the definition of a starting point for the main dimensions of the subcomponents and consequently for the elaboration of a detailed computer aided drawing (CAD) of the entire assembly. The adequacy of the adopted arrangements is then investigated and assessed during the advanced structural design phase. Finite element analyses are carried out to verify and — if necessary — to update the structural layout

while removing all the simplifications made in the preliminary design.

In addition, a simplified and representative structural model of the multi-box arrangement was generated: skins, and spar webs were modelled with shell elements (CQUAD4 [88]), spar caps were modelled with beam elements (CBAR [88]), rigid rib plates were modelled with rigid body (RBE2 [88]) with independent degree-of-freedom that are specified at a single grid point at the cell centre and with dependent degrees-of-freedom that are specified at the grid points on the perimeter of each cell section. Considering the limit load case provided in Sec.4.2.2 and the rib planes adjacent to the deployment system tracks fixed, Von Mises stress distribution (Fig.5.22b) confirms the assumptions made.



(a) Distribution of Bending stiffnesses for each box.



(b) Limit Load Condition, Von Mises Stress distribution [MPa].

Figure 5.22: 3MMF Multibox arrangement: results of pre-design process.

5.4 The Actuation System

If smart ribs are the core of the 3MMF structure because shape change capabilities can only be provided with proper control action of the inner mechanisms, the actuation system plays different roles in the set-up of a morphing device.

First of all, it is connected to the structural skeleton; therefore, it has a structural role because all the loads are transferred through its actuation arms. The most demanding task for design of full-scale morphing structures is to integrate within the structural skeleton one or more actuators. They must guarantee the mechanical power for transition from the baseline to target shapes.

Because the 3MMF concept was developed on the legacy of the bi-modal flap (fully tested with GST, see Sec.3.3.7), each actuation system was still based on two main components: a rotary brushless motor, and a Harmonic-Drive gear box. However, the final mechanical arrangement was completely improved.

In the new 3MMF concept, the kinematic chains were completely re-designed by a three-step design process. This approach was effective because improved performances were obtained in the finalized smart rib.

However, if compared to the kinematic chains of the bi-modal flap (see Fig.3.4 in Sec.3.3.7), the biggest improvement in the 3MMF was the type of linkage selected (Watt's Six-bar type) coupled with a new Harmonic-Drive gear box (CPL-17A [65]).

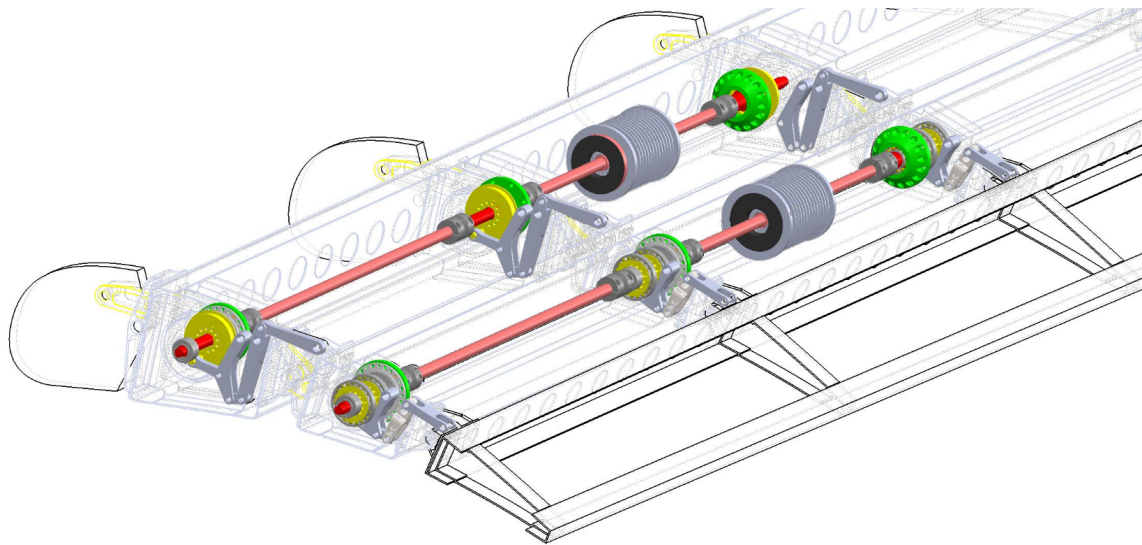
5.4.1 Through Shafts Solution: concept explained

The selected Watt's Six-bar mechanism provides adequate clearance between the crank and the transmission shaft. For this reason, actuation system based on through shafts can be enabled. This solution allows to actuate more than two rib blocks with a single hollow shaft brushless motor.

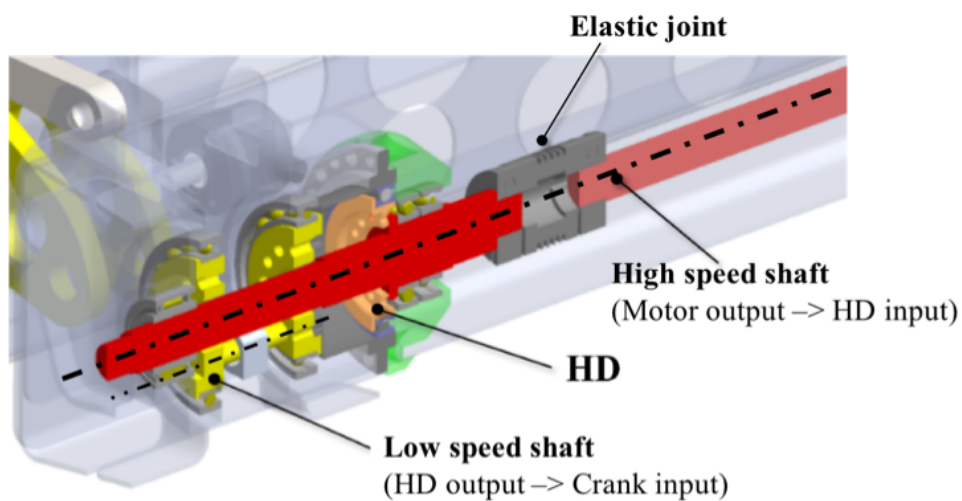
When the motor is activated, the high-speed shaft (Fig.5.24b) transfers the movement as input to the Harmonic-Drive gear box. Each block has a proper gear-box placed on each rib plate. Then, each gear-box reduces the speed with a factor equal to its gear ratio and transfer the movement as input to the IM crank (Fig.5.24b).

In such a way, a single motor can actuate three rib blocks. The high-speed shaft has been segmented in five parts connected by elastic joints (Fig.5.24b) in order to simplify the assembly process.

Using this solution for the actuation system, the overall number of actuators for the 3MMF concept was severely reduced saving weight and power. Only six motors were needed in the full-scale 5m prototype for enabling three morphing modes.



(a) Transmission shafts.



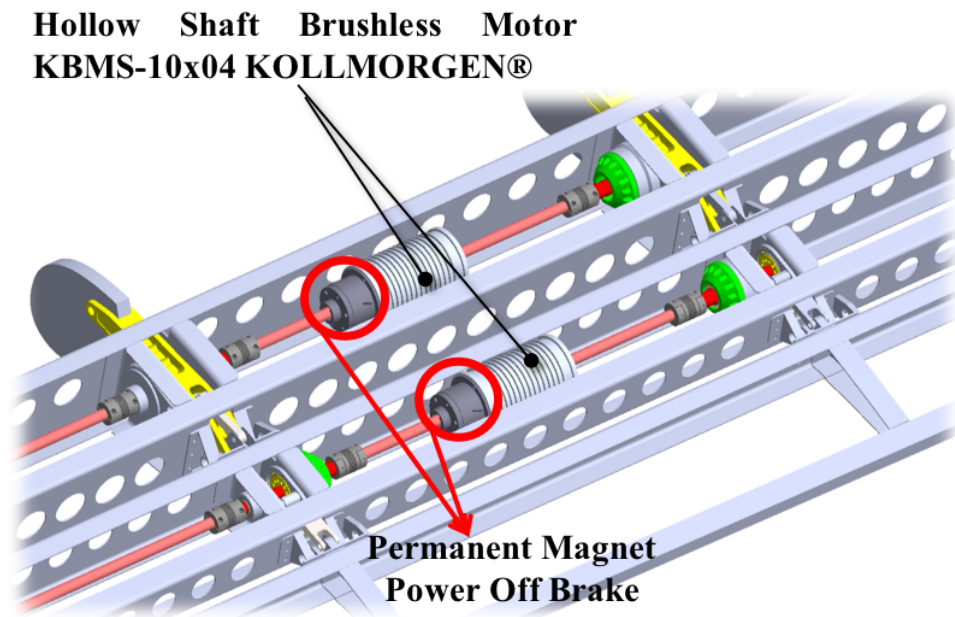
(b) High speed and low speed shafts (section view).

Figure 5.23: 3MMF actuation system: through shafts solution.

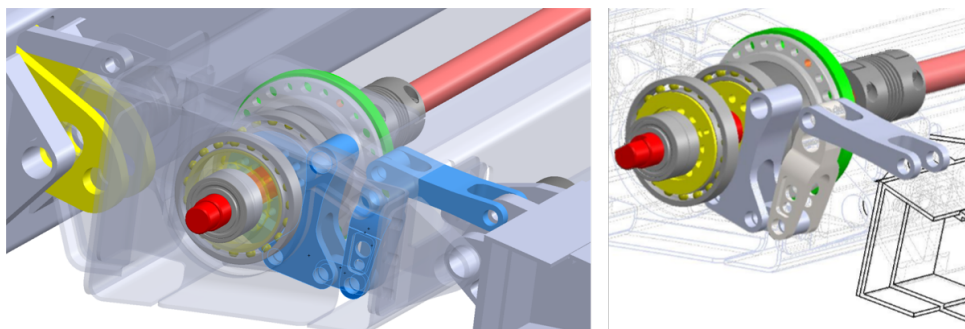
5.4.2 COTS selection & Mechanical Arrangement Definition

The aeronautical needs for compactness and lightness guided the choice of the mechanical arrangement of the interface between the actuation system and the rib.

Commercial Off-the-Shelf (COTS) actuator and gearbox were selected for the finalized design. The hollow-shaft Harmonic-Drive strain wave gear unit CPL-17A (Tab.5.2) was selected because of its high-power density (gear ratio equal to 120, weight 100 grams),



(a) Motors and power-off brakes.



(b) IM mechanical arrangement.

Figure 5.24: 3MMF actuation system: COTS components and IM mechanical arrangement.

reduced dimensions, and repeatability. The gear was connected to the crank of each mechanism and placed in a housing on each rib block plate; therefore, the torque provided by each brushless rotary motor was amplified and transferred by the gear unit to respective inner mechanism. The IM mechanical arrangement, shown in Fig.5.24b, consists of a crank, two ternary links, and three binary links. All items are connected by cylindrical hinges. The crank and the ternary links are doubly supported on the rib block plates and ball bearings were used to reduce friction between moving parts during operations. In such a way, out-of-plane rotations of the actuation system are strongly reduced, and the actuator moment is effectively transferred along the rib block main hinge axis.

In Fig.5.24a, permanent magnet power-off brake (Sepac PMB Series Model 197 [67]) were installed on each brushless motor. In such a way, the morphing system will be locked by brakes when no shape change are required.

On the other side, when transition from baseline to the selected morphing shape is requested, the permanent magnet brakes will be powered on and disengaged. So, the brushless motors can actuate the morphing system for shape change.

Table 5.2: Harmonic-Drive (CPL-17A) gearbox datasheet [65].



	Unit	CPL-17-2A		
Ratio	i []	120		
Repeatable peak torque	T_R [Nm]	54		
Average torque	T_A [Nm]	39		
Rated torque	T_N [Nm]	24		
Momentary peak torque	T_M [Nm]	86		
Maximum input speed (oil lubrication)	$n_{in(max)}$ [rpm]	10000		
Maximum input speed (grease lubrication)	$n_{in(max)}$ [rpm]	7300		
Average input speed (oil lubrication)	$n_{av(max)}$ [rpm]	6500		
Average input speed (grease lubrication)	$n_{av(max)}$ [rpm]	3500		
Moment of inertia	J_{in} [$\times 10^{-4}$ kgm ²]	0.049		
Weight	m [kg]	0.1		
Maximum hollow shaft diameter	$d_{H(max)}$ [mm]	18		
Transmission accuracy	[arcmin]	< 1.5		
Repeatability	[arcmin]	< ± 0.1		
Lost Motion	[arcmin]	< 1		
Torsional stiffness	K_t [$\times 10^3$ Nm/rad]	6.7	13	16
Ambient operating temperature	[°C]	Standard 0 ... 60, Special lubrication -40 ... 90		

Table 5.3: Kollmorgen (KBMS-10x04) brushless motor data-sheet [66].

Specification / Actuator Model		KBMS-10X04
Continuous Stall Torque	Nm	1.45
Peak Stall Torque	Nm	4.66
Speed at Rated Power	RPM	7050
Continuous Current	Arms	4.21
Weight	Kg	1.22
Inertia	Kgm ²	2.01E-5
Number of Poles	-	6

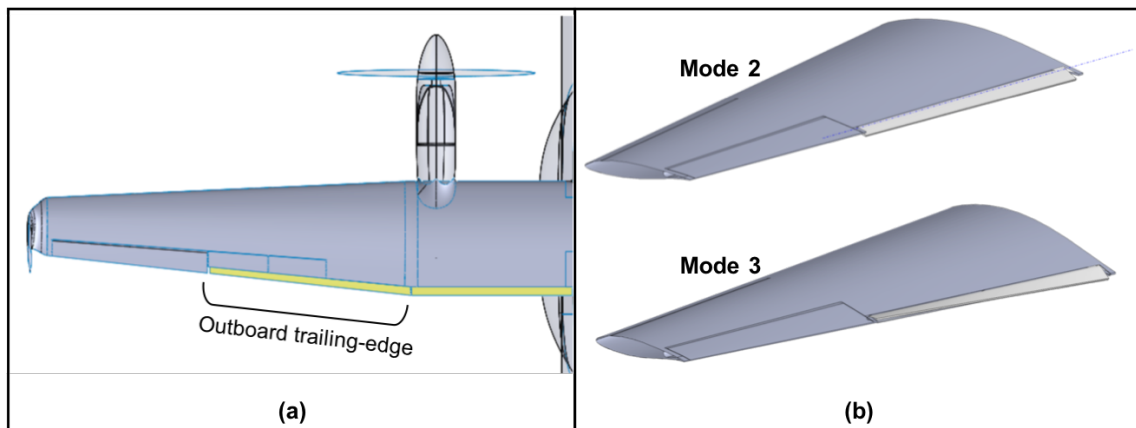


Figure 5.25: Adaptive Twist composite Tab (ATT) concept. (a) Investigation domain; (b) Enabled functionalities: rigid deflection (*upper*, mode 2), "continuous" span-wise twist (*lower*, mode 3).

5.5 The Adaptive Twist Composite Tab

The concept of Adaptive Twist Tab is based on the idea of retrofitting the metallic tip segment of an outer board Fowler flap (Fig.5.25a) with a device able to provide a new "continuous" span-wise trailing-edge twist (mode 3 in Fig.5.25b).

5.5.1 Working Principles and main design parameters

The structural concept is based on a thin-walled closed section beam layout (Fig.5.26). The tab skeleton is attached to the 3MMF device in nine points along the span-wise direction.

The root, central and tip sections will be connected with three independent actuation systems located in the 3MMF block B2. Three IM2, hosted in the 3MMF block B2, will transfer the torque to the actuator fitting of each ATT rib (root, central and tip in Fig.5.26).

Control action of the tab external shape can be provided by means of only three "active" ribs connected to three independent actuation systems. Each rib is bonded to the skin.

Two "C-shape" spars will be bonded to the skin and connected to the 3MMF block B2 by means of six hinge fittings. The "C" spars will provide proper bending stiffness to the ATT skeleton. These spars will not be connected with the "active" ribs.

Upon the actuation of the active ribs, the tab is put in movement thus changing the external shape of the trailing edge (Fig.5.25b); if the shape change of each rib is prevented by locking the actuation system, the tab is elastically stable under the action of external aerodynamic loads.

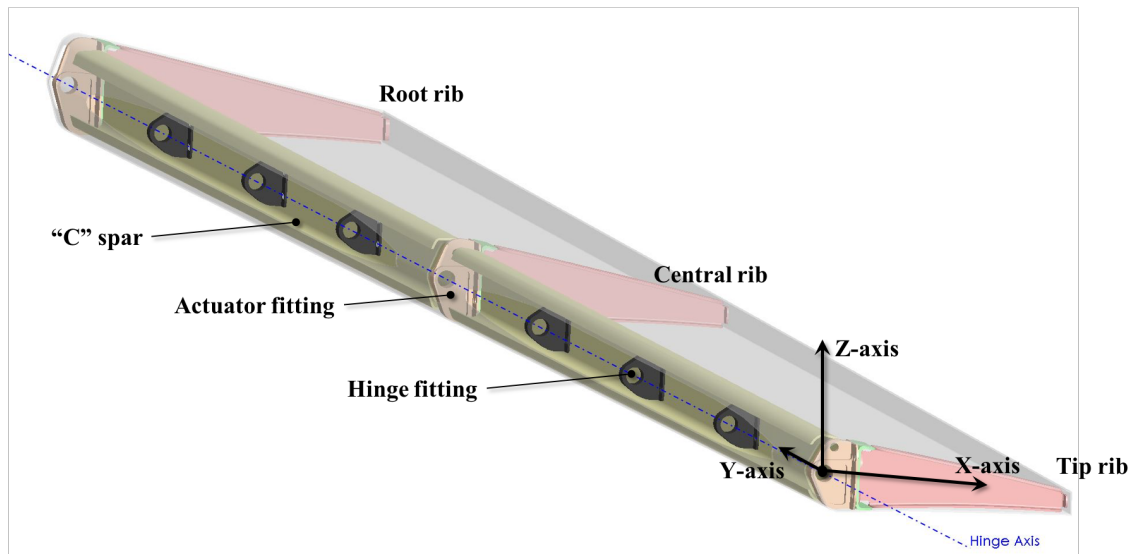


Figure 5.26: Adaptive Twist composite Tab (ATT) structural layout.

The rigid rotation of the tab (Fig.5.25b, upper) can be obtained synchronizing the three actuators. Differently, “continuous” span-wise trailing edge twist (Fig.5.25b, lower) can be activated providing different control actions. For instance, a linear span-wise tab twist (Fig.5.25b, lower) can be enabled providing clockwise rotation to the tip actuator and anti-clockwise rotation to the root actuator with the central one locked.

For the successful integration of such ATT skeleton in the 3MMF, it is evident that the most important parameter to be estimated in the preliminary design phase is the required twisting torque. Still from preliminary evaluation, a glass fibre prepreg with HexPly913 from Hexcel composites ([68]) was used for skin, “active” ribs, and C-shape spars.

The main mechanical properties considered [68] for the HexPly913 (120GL/R913; 37%;105AW) are: $E_x = 21.0$ GPa, $E_y = 7.5$ GPa, and $G_{xy} = 2.8$ GPa.

5.5.2 Torsion Equation for Thin-Walled Closed Section Beams

The energy required by the actuation systems for tab twisting is strictly related to geometric section layout and mechanical properties of the material. The geometric layout of the ATT closed section is shown in Fig.5.27.

According to the requirements for morphing mode 3 (Sec.4.2.1), the maximum twist angle to be provided at the flap tip segment must be equal to $\pm 5^\circ$. For this reason, for preliminary evaluation of maximum energy required for tab twisting, the central rib will be considered locked, and maximum twist angles will be applied respectively to tip and

root ribs. From the analytical point of view, the full-tab will be considered as a closed section beam fixed in the central section with tip and root sections free to rotate.

More in general, for a homogeneous cross section, the twist in case of restrained warping can be expressed by the following differential equation [71],

$$EC_{\omega} \frac{d^3\theta}{dy^3} - GJ_t \frac{d\theta}{dy} + \mathcal{M}_{OUT} = 0 \quad (5.57)$$

where J_t is the section's torsional constant, and C_{ω} is the sectorial moment of inertia for the generic cross section:

$$J_t = \frac{4A_m^2}{\oint \frac{ds}{t}} \quad (5.58)$$

$$C_{\omega} = \int_0^s \bar{\omega}^2 t \, ds \quad (5.59)$$

where $\bar{\omega}$ is the sectorial area and t is the section thickness.

The following notation is used: \mathcal{M}_{OUT} is the applied torsional moment to the single active rib by its respective actuation system; l length of the half-tab (tip/central rib or central/root rib span-wise distance); T_{tip} and T_{cen} are the reaction end torques at the ends of the half-tab; θ is the angle of rotation at the generic station y from origin (located at the tip section); θ' , θ'' , and θ''' are the successive derivatives of θ with respect to distance y .

The solution of Eq.5.57 describes the elastic deformations of uniform thin-walled closed section under concentrated torque applied at the tip end (tip rib), considering tip section free to twist but not warp and central section fixed (no twist or warp).

The boundary conditions for the half-tab can be expressed as follow:

- Tip (/root) section: $\theta'_{tip} = 0, T_{tip} = 0$;

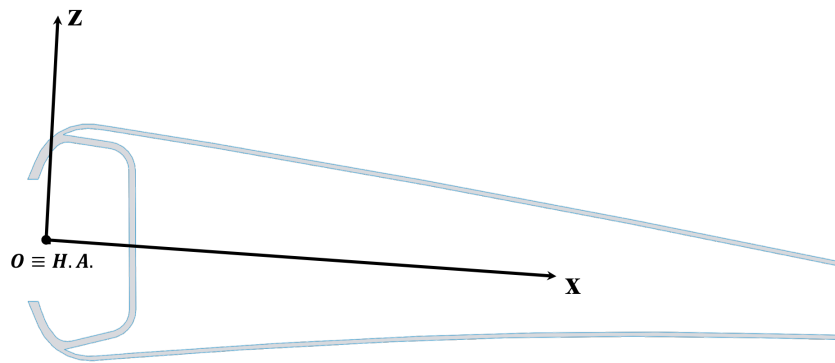


Figure 5.27: Adaptive Twist composite Tab (ATT) section layout.

- Central section: $\theta_{cen} = 0, \theta'_{cen} = 0, T_{cen} = -\mathcal{M}_{OUT}$;

With this assumptions, the final solution of Eq.5.57 is the following:

$$\theta = \frac{\mathcal{M}_{OUT}}{EC_{\omega}\beta^3} \left[\sinh(\beta y) + \beta(l - y) - \tanh\left(\frac{\beta l}{2}\right) \cdot \left(1 + \cosh(\beta y)\right) \right] \quad (5.60)$$

It is worth to notice that the solution of Eq.5.57, for an homogeneous closed section thin-walled beam loaded with a torque \mathcal{M}_t and that is free to warp at both ends, is equal to the expression provided by the Bredt theory [69],

$$\psi = \frac{d\theta}{dy} = \frac{\mathcal{M}_{OUT}}{4A_m^2} \oint \frac{ds}{Gt} = \frac{\mathcal{M}_{OUT}}{GJ_t} \quad (5.61)$$

where A_m is the area enclosed by the mid-line of the profile's wall, and θ is the twist angle about the Y-axis (coincident with the hinge axis, see Fig.5.26).

The successive derivatives of θ with respect to distance y can be obtained as follows:

$$\theta' = \frac{\mathcal{M}_{OUT}}{EC_{\omega}\beta} \left(\cosh(\beta y) - 1 - \tanh\left(\frac{\beta l}{2}\right) \cdot \sinh(\beta y) \right) \quad (5.62)$$

$$\theta'' = \frac{\mathcal{M}_{OUT}}{EC_{\omega}\beta} \left(\sinh(\beta y) - \tanh\left(\frac{\beta l}{2}\right) \cdot \cosh(\beta y) \right) \quad (5.63)$$

$$\theta''' = \frac{\mathcal{M}_{OUT}}{EC_{\omega}} \left(\cosh(\beta y) - \tanh\left(\frac{\beta l}{2}\right) \cdot \sinh(\beta y) \right) \quad (5.64)$$

The twist angle will be maximum at $y = 0$ (tab tip section),

$$\theta_{max} = \frac{\mathcal{M}_{OUT}}{EC_{\omega}\beta^3} \left(\beta l - 2 \tanh\left(\frac{\beta l}{2}\right) \right), \text{ at } y = 0 \quad (5.65)$$

For successive derivatives of θ , the maximum values are:

$$\theta'_{max} = \frac{\mathcal{M}_{OUT}}{EC_{\omega}\beta^2} \left[\frac{1}{\cosh(\beta l/2)} - 1 \right], \text{ at } y = \frac{l}{2} \quad (5.66)$$

$$\theta''_{max} = \frac{\pm \mathcal{M}_{OUT}}{EC_{\omega}\beta} \cdot \tanh\left(\frac{\beta l}{2}\right), \text{ at } y = 0 \text{ and } y = l, \text{ respectively} \quad (5.67)$$

$$\theta'''_{max} = \frac{\mathcal{M}_{OUT}}{EC_{\omega}}, \text{ at } y = 0 \text{ and } y = l, \quad (5.68)$$

where the parameter $\beta = \sqrt{GJ_t/EC_{\omega}}$ is the ratio between the Saint-Venant torsion rigidity GJ_t and the warping rigidity EC_{ω} which depends only on the member cross

section.

At any station y along the beam, the torsional moment T is equal to the sum of two effects:

$$T = T_{SV} + T_{\omega} \quad (5.69)$$

where the Saint-Venant part of the torsional moment is proportional to the first derivative of the angle of twist θ , and the warping torsion T_{ω} is proportional to the first derivative of the warping moment M_{ω} [72]:

$$T_{SV} = GJ_t\theta' \quad (5.70)$$

$$T_{\omega} = -M'_{\omega} = -(EC_{\omega}\theta'')' \quad (5.71)$$

The parameter χ can be defined to give indication to whether the Saint-Venant torsion or warping torsion predominates [72],

$$\chi^2 = \frac{l^2 GJ_t}{EC_{\omega}} = l^2 \beta^2 \quad (5.72)$$

For small values of χ only warping torsion needs to be considered, however there will be a certain region for χ where neither Saint-Venant torsion nor warping torsion may be neglected and thus the structural system must be analysed for mixed torsion. If the numerator in the expression for χ^2 is large as compared to the denominator, one may expect that Saint-Venant torsion is predominant. In the last, the Saint-Venant twist angle distribution will be described by the following equation:

$$\theta_{SV} = \frac{\mathcal{M}_t x}{GJ_t} \quad (5.73)$$

In the above equations, the elastic moduli are related to the generic section (Fig.5.27) and can be obtained as integration along the section profile contour [70],

$$\bar{E} = \frac{\int_0^s E ds}{\int_0^s ds} \quad (5.74)$$

$$\bar{G} = \frac{\int_0^s G ds}{\int_0^s ds} \quad (5.75)$$

where s is a coordinate following the profile's contour.

The actuation torque to be provided by the actuation system can be preliminary estimated with Eq.5.65 assuming the properties of the outer and inner tab mean geomet-

ric section, summarized in Tab.5.4. In addition, the sections have constant thickness equal to $t = 2$ mm; only one laminate has been considered with the following lay-up $[0^{\circ}_3; \pm 45^{\circ}; 0^{\circ}_3]_s$.

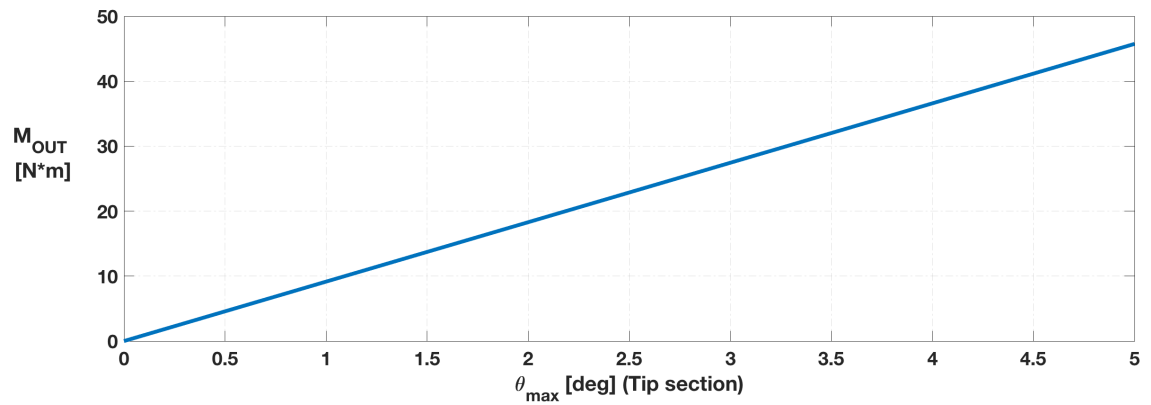
As shown in Fig.5.28a, the moment to be provided at the tip section ($\mathcal{M}_{OUT,tip}$) to obtain a 5° twist angle is equal to 45 Nm. On the other hand, the moment to be provided at the root section ($\mathcal{M}_{OUT,root}$) is equal to 72 Nm. An higher moment is required for inner half-tab twisting because of the higher torsional constant of the root section.

Torsional moments distributions can be evaluated with Eq.5.70-5.71. In Fig.5.29a, for the outer half-tab, the Saint-Venant part of torsional moment T_{SV} is dominant for large part of the span. On the opposite, the warping part of torsional moment T_{ω} is dominant near the ends of the half-tab: the tip and the central section. In addition, as shown in Fig.5.29c, if we consider the warping part of the torsional moment T_{ω} as function of the characteristic Torsional-Bending length ($d = \beta^{-1}$), for $y * \beta \geq 5$ the torsional moment will be due only to the Saint-Venant part.

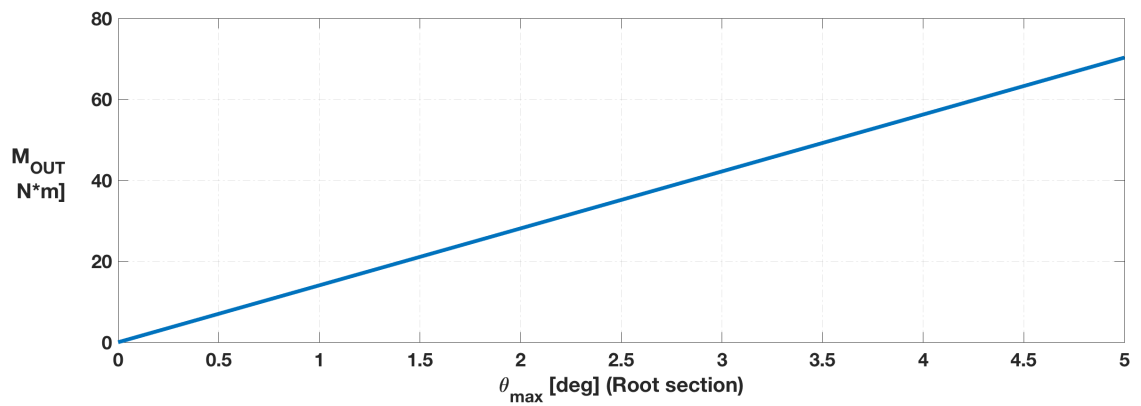
Further investigations will be performed by means of FE simulations to support the results obtained with the torsion equation.

Table 5.4: Tab section properties.

Outer Half-Tab (from tip to central rib) mean geometric section.	
Half-tab Span,	2500 mm
Chord,	176.29 mm
Torsional Constant, J_t	$2.919 * 10^5 \text{ mm}^4$
Warping Constant, C_ω	$7.561 * 10^7 \text{ mm}^6$
Characteristic Length (Torsional-Bending length), $d = \beta^{-1}$	35.495 mm
Torsion Parameter, $\chi = l * \beta$	70.43 mm
Inner Half-Tab (from central to root rib) mean geometric section.	
Half-tab Span,	2500 mm
Chord,	202.75 mm
Torsional Constant, J_t	$4.332 * 10^5 \text{ mm}^4$
Warping Constant, C_ω	$1.429 * 10^8 \text{ mm}^6$
Characteristic Length (Torsional-Bending length), $d = \beta^{-1}$	40.06 mm
Torsion Parameter, $\chi = l * \beta$	62.40 mm

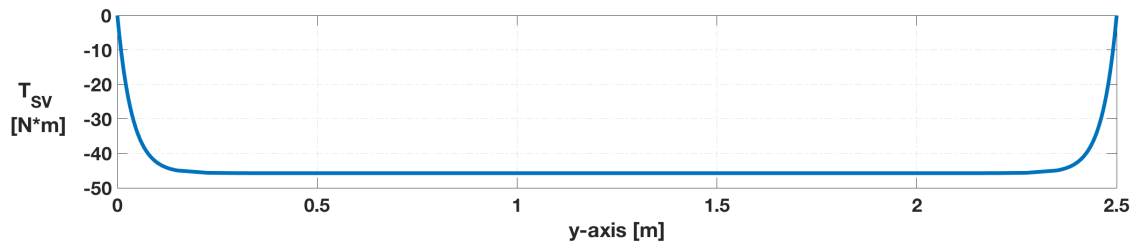


(a) M_{OUT} required at tip section for half-tab twist.

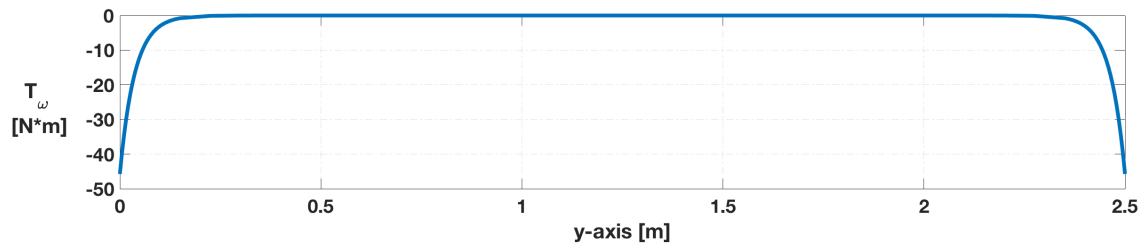


(b) M_{OUT} required at root section for half-tab twist.

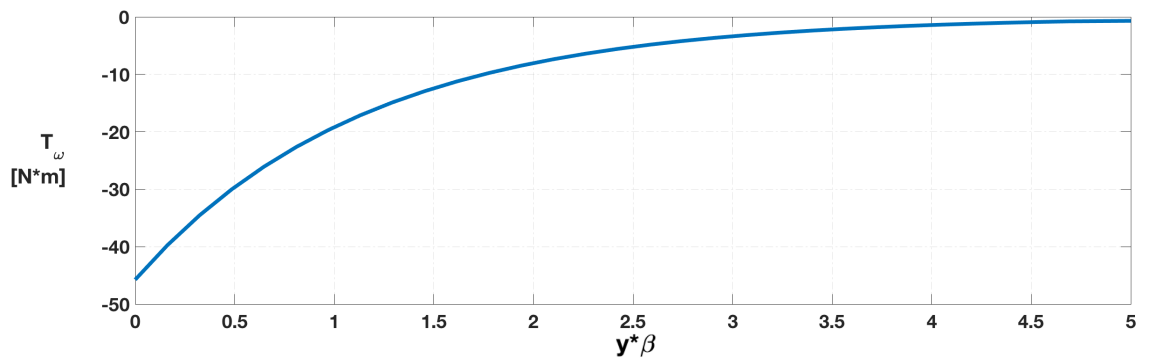
Figure 5.28: Required moments by actuation systems (M_{OUT}) for half-tab twist.



(a) The Saint-Venant part of Torsional Moment T_{SV} [N*m].



(b) The warping part of Torsional Moment T_{ω} [N*m].



(c) The warping part of Torsional Moment T_{ω} [N*m] as function of $y * \beta$.

Figure 5.29: Thin-walled Closed-Section beam: torsional moments distributions.

Chapter 6

Assessment of the 3MMF concept

6.1 Finalized Concept

In the Chap.5, the preliminary design of the 3MMF concept was fully addressed.

The first design loop of the smart rib was mainly driven by kinematic optimization of the inner mechanisms (IM1 and IM2) according to the minimum available room within the tip section of the Fowler flap structure. After that, in a second design loop, the geometric parameters of the leverages were synthesized to obtain high mechanical advantages as well as a large range of output angles (i.e. θ_{B2} and θ_{B3}). In the third design loop, a static force analysis was developed to support the definition of the mechanical arrangement of the smart rib. Preliminary FE simulation were used to verify the smart rib layout.

The smart rib layout was conservatively designed with reference to the flap tip section characterized by the minimum available room for actuation chains (IM1, IM2) installation. A parametric 3D-CAD was generated to quickly scale the tip rib layout according to the external aerodynamic surfaces. The final 3MMF (Fig.6.1a) has nine smart ribs equally spaced along the flap span by a distance of 0.6 m.

In addition, lengths of blocks B1 and B2, linking element (L1), and inner mechanisms (IM1 and IM2) were kept equal for all flap sections thus obtaining hinge lines perpendicular to ribs' reference planes. The full-scale outer-board flap has a taper ratio equal to 0.75, hence blocks B0 and B3 were properly scaled to match the chord of each flap section.

After that, the multi-box arrangement was defined to transfer the ribs kinematic to the overall 3MMF skeleton: each box was assumed to be characterized by a single-cell configuration delimited along the span by blocks of consecutive ribs, and along the chord by spars. Then, the novel layout of the actuation system was defined. A solution based on through shafts allowed to actuate three rib blocks with a single motor (Fig.6.1b). The final mechanical arrangement [73] was based on: a single hollow-shaft brushless motor, and

one hollow-shaft Harmonic-Drive properly connected on each rib-block. The working principles of each actuation system will be the following:

1. When the brushless motor is on, the main shaft will transfer the rotational speed to an HD gearbox connected on each rib-block plate;
2. As output of the HD, the rotational speed is then reduced (by a factor equal to the gear ratio). The crank of each leverage (IM1 and IM2) is directly connected to the HD output. In such a way, the kinematic chains are activated and the full morphing system can change its shape. In Fig.6.1c, the full-camber evolution is shown.

Only six motors are needed in the full-scale 5m prototype.

For morphing mode 1, all actuation systems must be enabled. The full-camber evolution will be mainly driven by rib block angles required for adequate high-lift performance in landing configuration (Fig.6.2a).

For morphing mode 2, the 3MMF is stowed in the wing. In order to enable flap tip upwards/downwards deflection, only actuation systems hosted within the block B2 will be enabled. These three motors will guide the transition of the tab, as shown in Fig.6.2b, in the deflection range $[-10^\circ; +10^\circ]$.

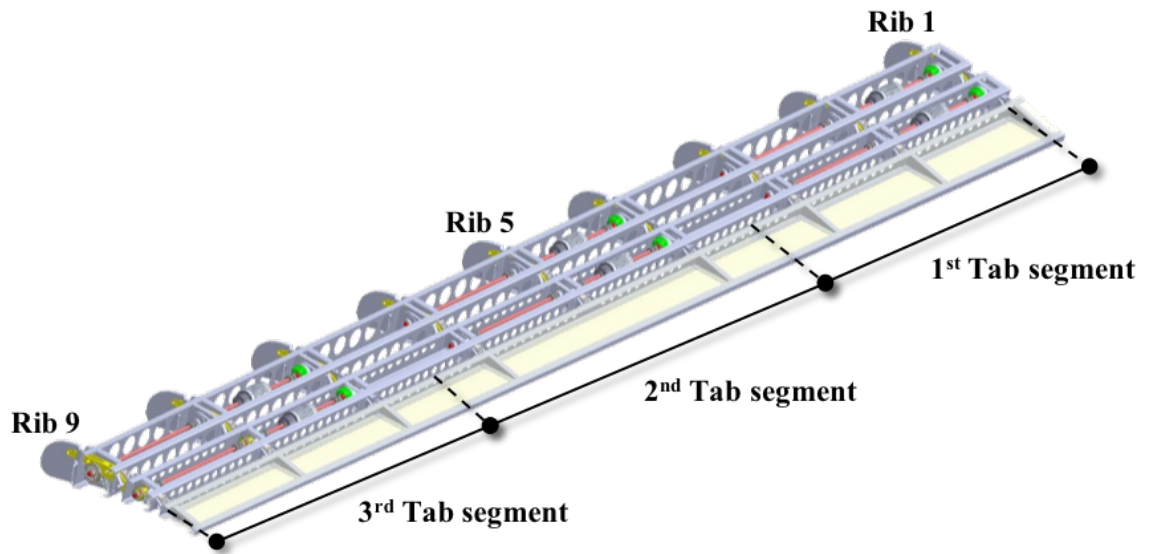
As shown in Fig.6.1a, the third box (i.e. the tab) of the 3MMF has been divided in three different (and independent) parts along the span to implement morphing mode 3 as segmented differential tip twist. The actuation system of each segmented tab will be properly controlled in order to provide shape transition as shown in Fig.6.2c.

Morphing modes 2 and 3 are supposed to be enabled during high-speed climb, cruise and off-design flight conditions. Thanks to this modes, load control functionalities can be implemented to improve the Natural Laminar Flow (NLF) wing aerodynamic efficiency.

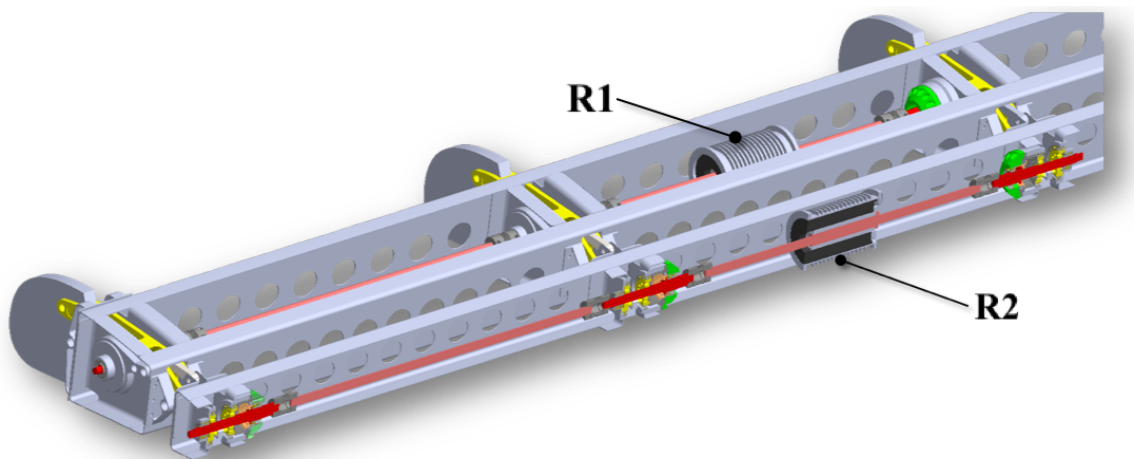
For this reason, a novel tab structural concept was investigated. The Adaptive Twist composite Tab (ATT) was based on the idea of retrofitting the segmented full-metallic flap tip (shown in Fig.6.2c).

The ATT skeleton, a thin-walled closed section beam, was preliminary analysed [74]. Three "active" are located in the root, central, and tip section. An actuator fitting connects each active rib to its respective actuation system which is located within the 3MMF block B2 (see Fig.6.3). Each active rib is bonded to the composite skin. Six hinge fittings are used to connect two "C" spars to the 3MMF block B2. The "C" spars are bonded to the composite skin and will provide adequate bending stiffness to the ATT skeleton.

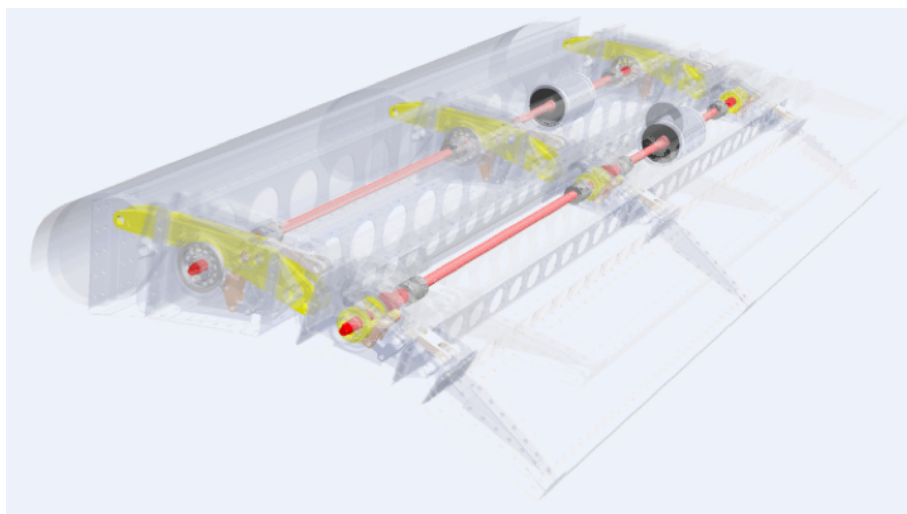
As shown in Fig.6.5, "continuous" span-wise twist can be enabled when each active rib is properly controlled. For instance, as in Fig.6.5, continuous span-wise twist law $(-5^\circ/0^\circ/+5^\circ)$ can be enabled providing counter-clockwise rotation to the tip rib, locking the central station, and with clockwise rotation of the root rib.



(a) 3D-CAD (isometric view).

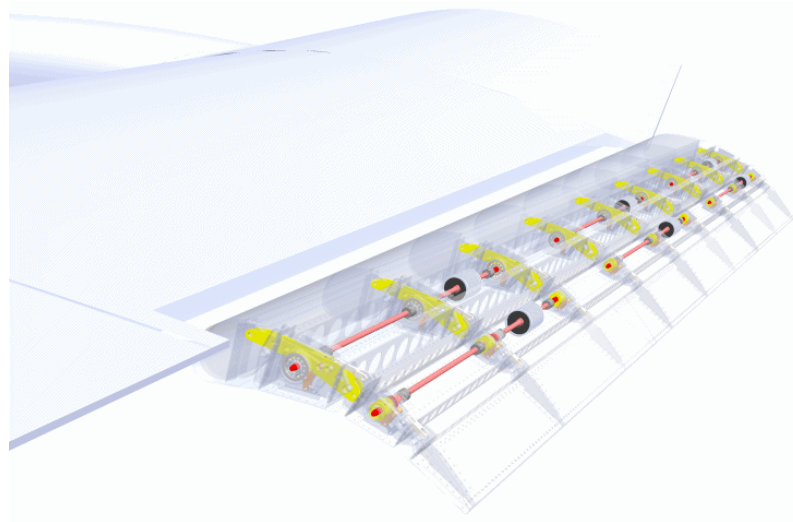


(b) Actuation System based on a segmented through shaft (section view).



(c) Two bays full-camber evolution.

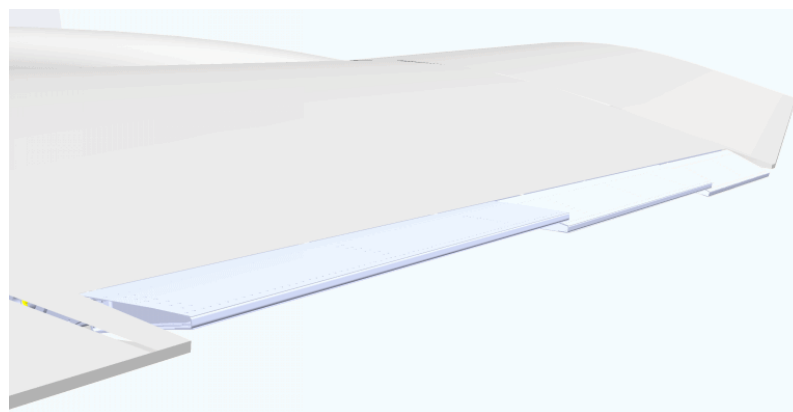
Figure 6.1: 3MMF finalized concept.



(a) Full camber **morphing mode 1**.



(b) Flap Tip upwards/downwards deflection (**morphing mode 2**).



(c) Flap Tip segmented twist (**morphing mode 3**).

Figure 6.2: 3MMF morphing modes.

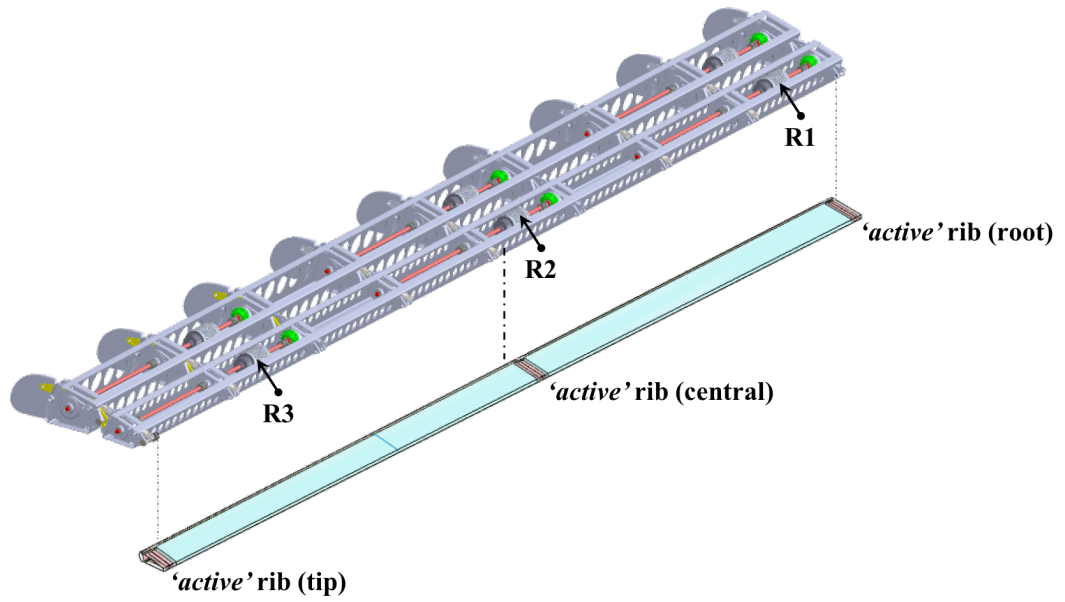


Figure 6.3: ATT composite tab installed on the 3MMF skeleton.

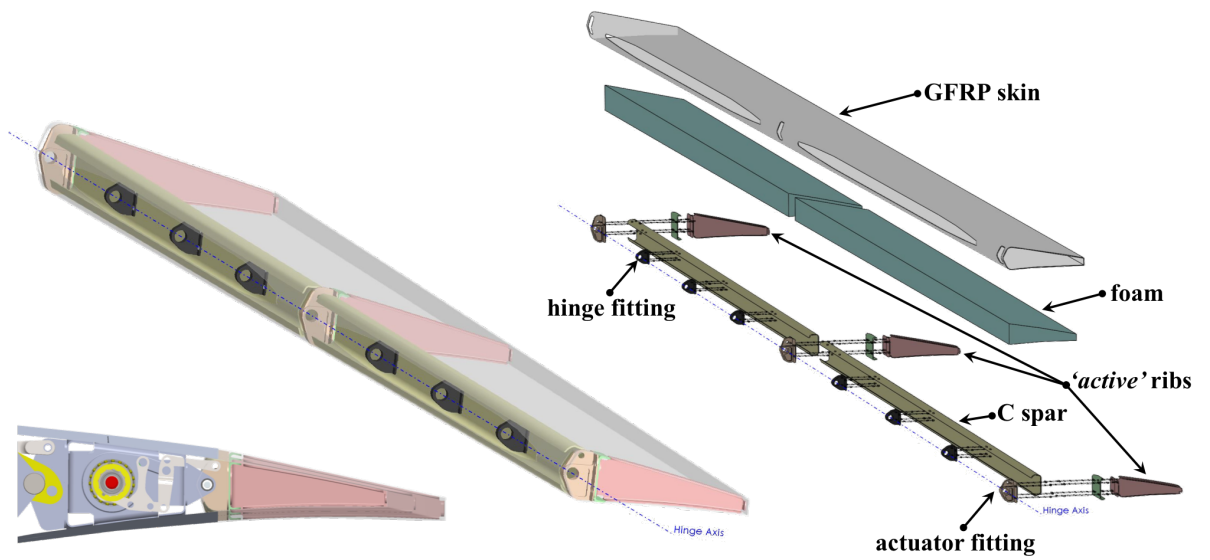


Figure 6.4: ATT composite tab structural layout.

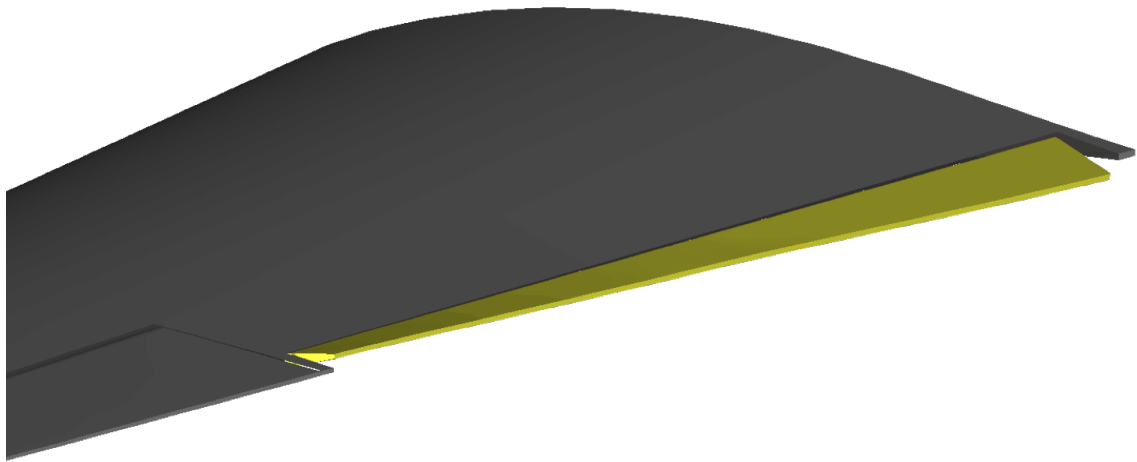


Figure 6.5: ATT composite tab: continuous span-wise twist from tip to root ($-5^\circ/0^\circ/+5^\circ$).

6.2 Aerodynamic Design and Performance Assessment

NLF (Natural Laminar Flow) technology has been identified as a promising technology in aerodynamics to improve the performance of aircraft and potential drag reductions up to 15% are expected. In the frame of CS–GRA platform, activities have been done to develop this technology as well as demonstrations and the general outcome was quite positive [75].

However, for such NLF applications, the design of high-lift devices for low speed flight conditions at take-off and landing is an important issue. First of all, if a leading-edge device is necessary, it has to be compliant with the NLF application at cruise conditions, when retracted. Then, for trailing-edge devices, a system with external fairings as small as possible is preferable, in order to limit the extra drag penalty due the friction on these fairings. And of course, the system has to provide a sufficient level of aerodynamic performance at take-off and landing conditions. Taking these constraints altogether, the morphing technology was considered for both leading-edge and trailing-edge devices.

The study presented in this document includes aerodynamic activities carried out at ONERA for the design and the performance evaluation of different morphing high-lift systems applied to the AG2-NLF wing [76].

In order to take system constraints into account, the high-lift results were obtained integrating: the fairing-less flap deployment system (designed by a Siemens team), a morphing flap (by UniNa, namely the 3MMF concept discussed in this Thesis), and a drooped nose (designed by with PoliMi). Different types of works have been done:

1. Flap system has been optimized for two wing sections of the AG2-NLF aircraft and

compared to the performance obtained for the reference TP90 when considering the same sections. This optimization considered first the landing conditions, and then the take-off ones.

2. Optimal movement of the Fowler flap deployment system was investigated.
3. Optimization of the flap morphing system (3MMF concept)
4. 3D assessment on a generic configuration of the R-IADP TP90 airplane.

6.2.1 Full-Camber Morphing Mode 1

In order to enable a mechanism without fairings, a roller-track type of deployment mechanism was selected (Fig.6.6c). The fairing-less deployment system consists of four deployment tracks, two linear ball-screw actuators distributed along the span of the wing and such that they can fit within the morphing flap structure when the flap is stowed in the wing box. The final solution for the integration of the deployment system within the 3MMF skeleton was to place the components of the deployment mechanism in two bays.

Position of the deployment systems were preliminary defined in Par.5.3.1 following two main driving design ideas: reduce internal solicitations (bending moments \mathcal{M}_y and shear forces T_z) on the multi-box 3MMF skeleton, and avoid clash with the 3MMF actuation system when the flap is stowed in the wing.

The main reason to use a fairing-less deployment system is because the use of external flap track fairing can lead to drag penalties during airplane flight mission. However, the maximum Fowler motion of a roller-track system can locate the flap in a position satisfactory only for take-off condition. As shown in Fig.6.6c, the roller-based system with curved track can provide a fowler motion up to $230mm$ (maximum extended). Indeed, the AG2-NLF aircraft requires at least a 20° flap deflection which can be provided by this deployment system, but the same system is not able to provide the expected landing performance.

Higher high-lift performance (i.e. higher $C_{L,max}$) can not be provided by any other fairing-less deployment mechanism, even using an enhanced drooped nose (Fig.6.10b). For the reference TP90 airplane in landing condition with conventional flap full-deployed at 33° , a $C_{L,max} = 3.0$ was requested. For this reason, a new high-lift technology must be used to provide the high-lift performance required for landing conditions.

Morphing technology (morphing mode 1) must be applied to recover the requested performance level for landing.

The main strategy was to deploy the flap in take-off configuration with a fairing-less deployment system and then use the morphing capability of the 3MMF device to reach

the requested landing performance.

As shown in Fig.6.7, several configurations were considered for morphed flap in landing configuration. At the end of the first loop of the smart rib kinematic design, the binary crossed link (BCL) mechanism was designed to provide specific gear ratio between consecutive blocks B1 and B2.

Considering the angles obtained in Fig.6.7c, three morphed airfoil shapes were considered for CFD simulations (Fig.6.8):

a) $\delta_1 = 2.75^\circ / \delta_2 = 7.25^\circ / \delta_3 = 10^\circ$;

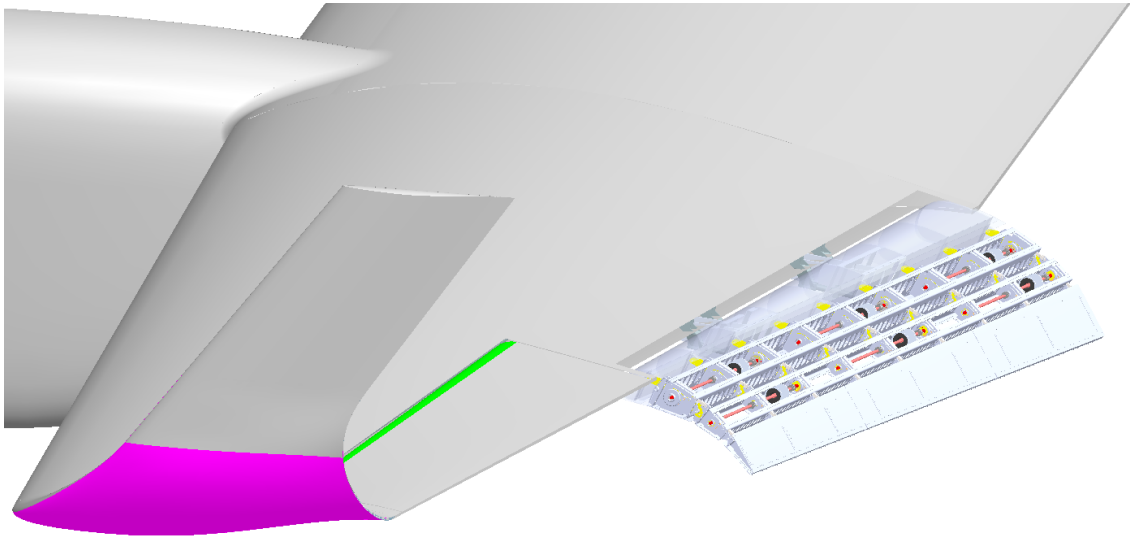
b) $\delta_1 = 4.5^\circ / \delta_2 = 10.5^\circ / \delta_3 = 10^\circ$;

c) $\delta_1 = 6.5^\circ / \delta_2 = 13.5^\circ / \delta_3 = 10^\circ$.

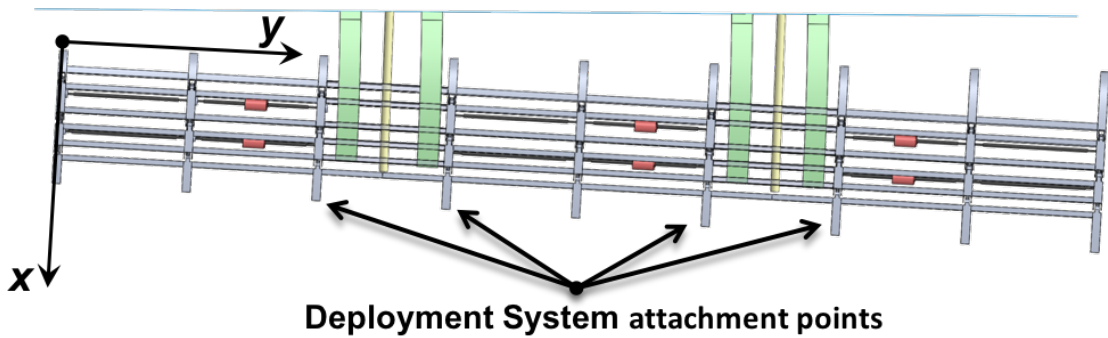
Symbols are explained in Fig.6.7a.

In Fig.6.10b, considering flow conditions for TO ($M_\infty = 0.197$ at sea level), maximum $C_{L,max}$ is equal to 2.87 when drooped nose and flap without morphing are used together. The use of the droop nose can bring +10% increase in the $C_{L,max}$.

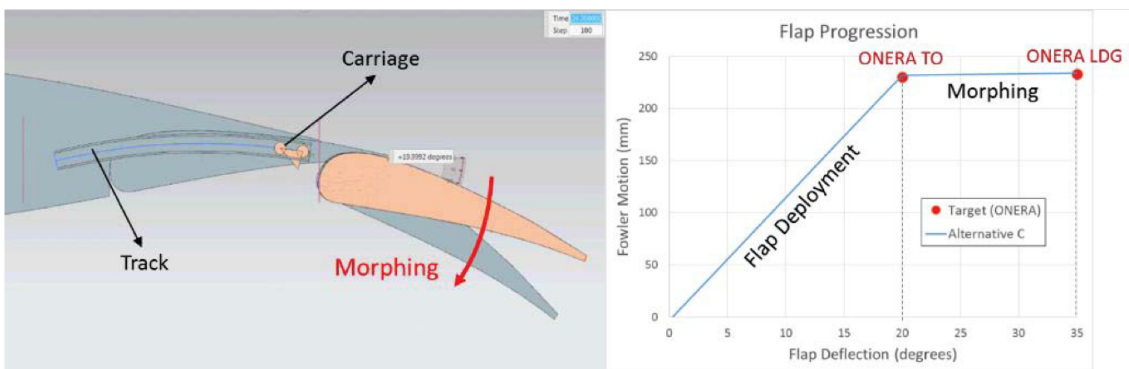
In Fig.6.10a, considering flow conditions for LDG ($M_\infty = 0.148$ at sea level), maximum $C_{L,max}$ is equal to 3.29 when drooped nose and morphing flap mode 1 ($\delta_1 = 4.5^\circ / \delta_2 = 10.5^\circ / \delta_3 = 10^\circ$) are used together. The use of the morphing flap mode 1 can bring +12.76% increase in the $C_{L,max}$. In addition, the stall angle is increased of 1.25° and occurs at wing root sections (Fig.6.9).



(a) Maximum Fowler motion (230mm) and 3MMF in landing configuration.

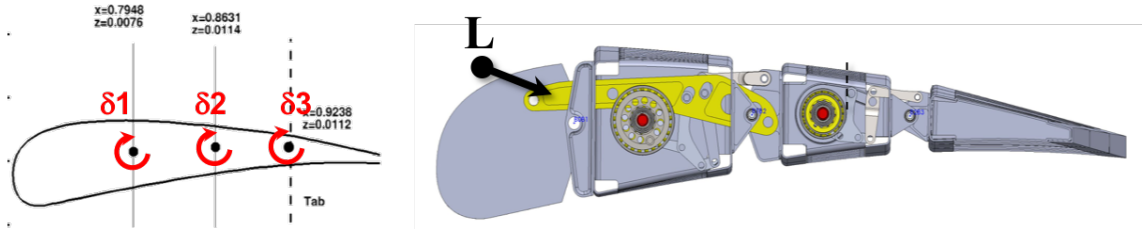


(b) Fairing-less Deployment System hosted in the 3MMF skeleton.

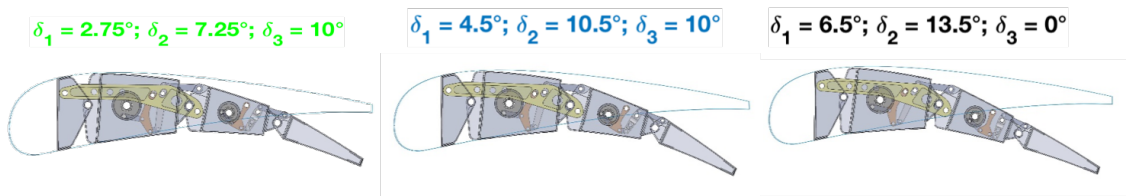


(c) Fowler motion provided by deployment system.

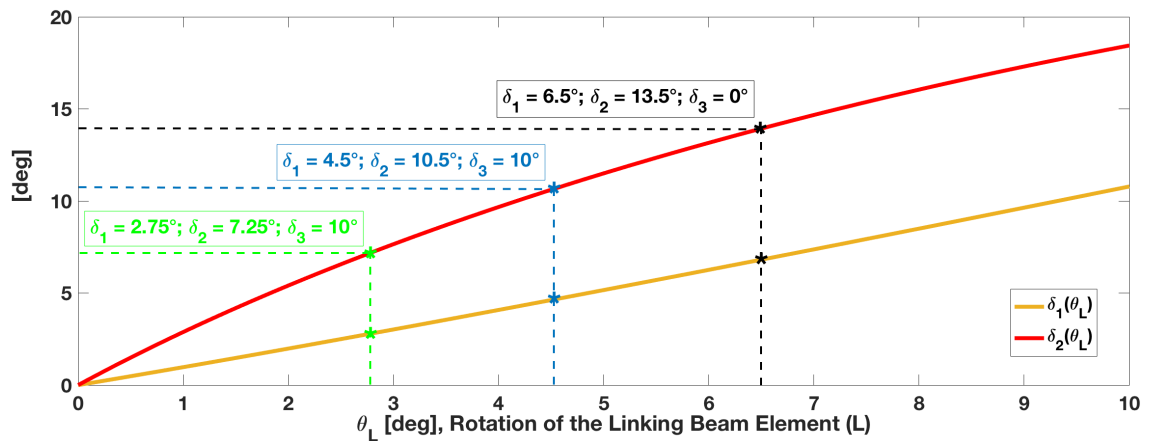
Figure 6.6: TP90 landing configuration.



(a) Angles nomenclature (left); Linking beam element marked in yellow (L, right).

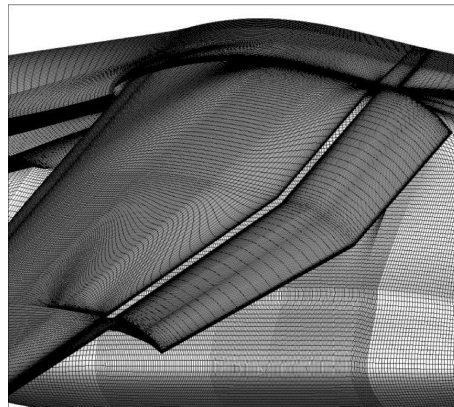
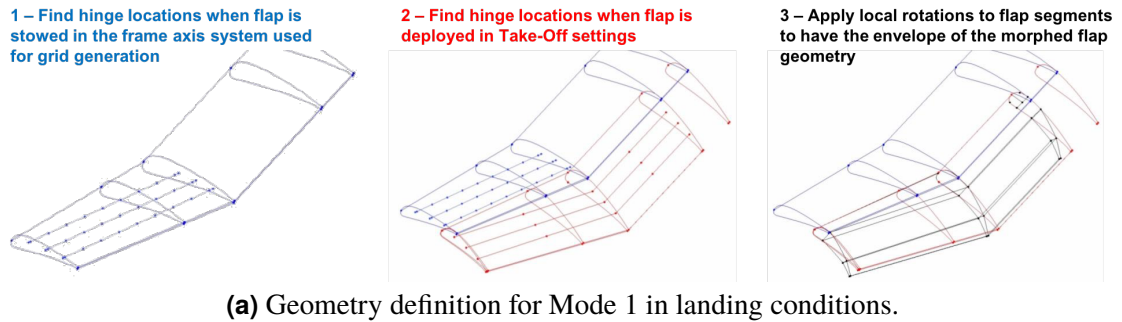


(b) Airfoil shapes considered in CFD simulations.



(c) Rib-block angles obtained as function of linking beam element rotation θ_L .

Figure 6.7: Configurations considered for morphed flap (Mode 1) at landing conditions.



(b) CFD grid used for Mode 1.

Figure 6.8: Process used for the generation of the morphed 3D flap configurations.

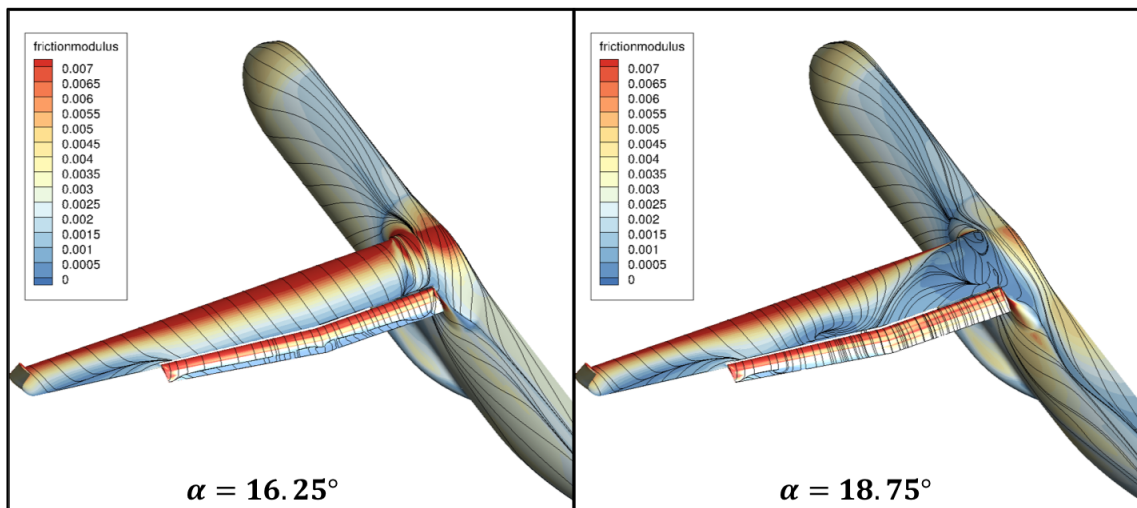
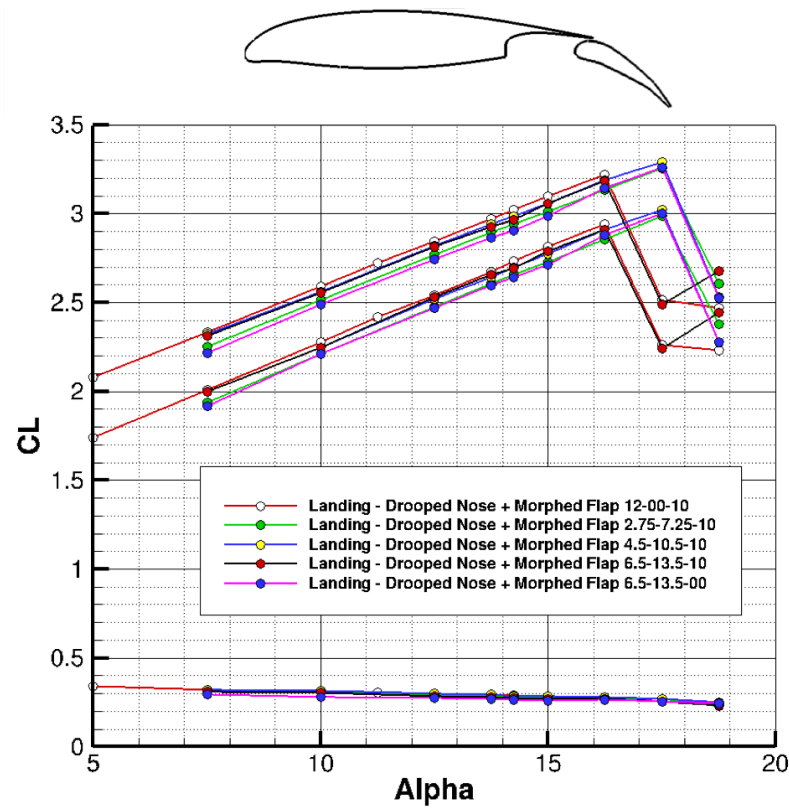
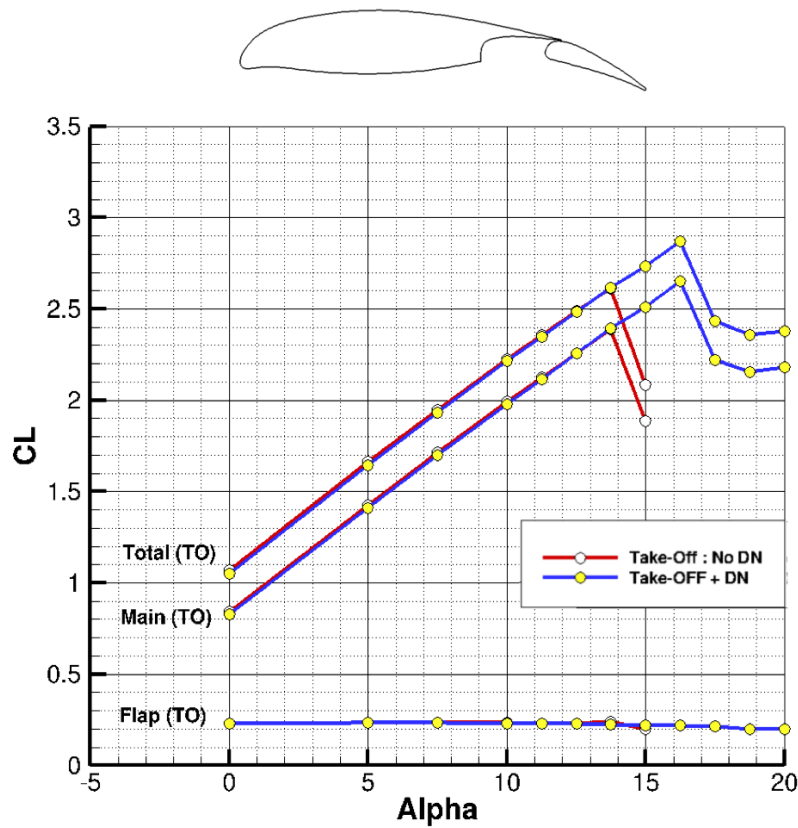


Figure 6.9: Computed stall process for the optimum morphed flap configuration [76].



(a) Landing conditions: droop nose + morphing flap Mode 1.



(b) Take-off conditions: droop nose + flap (without morphing)

Figure 6.10: TP-90 regional airplane: High-Lift Performance in Take-off and Landing conditions [76].

6.2.2 Tab rigid rotation and twist (Mode 2 & 3)

The activities, herein presented, have been developed with the objective to optimize morphing capabilities of the wing trailing-edge for performance improvement in high speed (climb) conditions [77].

Retrofitting the segment of the AG2-NLF wing flap system (designed in cruise condition) with a multi-functional trailing-edge, the span load distribution could be optimized aiming to improve the global aircraft aerodynamic performance. The computations of the aerodynamic flow around the 3D airplane configurations have been done with the ONERA elsA high fidelity software [78]. It solves the RANS equations on structured multi-block grids by a cell-centred finite volume technique. Spatial discretization uses the second order centred scheme of Jameson with 2nd and 4th order artificial dissipation. Convergence to steady flow solution is carried out thanks to a backward Euler technique with robust LU-SSOR implicit scheme method. The convergence is accelerated by the use of multi-grid techniques for steady flows. Different turbulence models are available in elsA and in this work the Spalart-Allmaras turbulence model was used with the QCR modification [79]. In the RANS computations, the ONERA elsA software has the capability to compute laminar flow regions and to determine the transition location, by using the so-called AHD compressible criterion for Tollmien-Schlichting instabilities [80] and the so-called C1 criterion for cross-flow instabilities [81], within the iterative convergence process. The generation of the wing shapes with morphed elements is done through the use of a grid deformation technique used in SARISTU project and described in [82]. The surface grid is firstly deformed according to the requested shape. Then, a displacement field of the grid nodes is derived for a volumic transfinite deformation technique applied to the initial grid. The advantage of this method is that the same scripts can be used for the different computations, as the topological information is kept. The drawback is that it is based on the initial topology, and some local grid inversion can be found if deformation is too large.

For the AG2-NLF regional airplane, multifunctional twistable trailing-edge could help to recover the laminar extent by an adaptation of pressure gradient in off-design condition. Considering C_L related to high speed climb flight condition, free transition computations show that laminar flow condition on the upper surface starts to be lost. Fig.6.12a present the different configurations considered for the multifunctional twistable trailing-edge. In Fig.6.12a(left), a rigid trailing-edge deflection (mode 2) equal to 2.5° was considered, while a continuous increase in deflection angles (mode 3) from tip to root ($4^\circ/3^\circ/2^\circ$) was additionally considered in Fig.6.12a(right). Fig.6.12b compares the computed Lift over Drag ratio (L/D) evolution with C_L in climb conditions for the different configurations considered. The reference case, with no morphing, is recalled as the black curve.

As expected, the efficiency of the trailing-edge morphing concept for the AG2-NLF airplane is visible for high C_L , where an increase of about 0.4 in Lift over Drag ratio is found: +1.75% compared to the NLF wing.

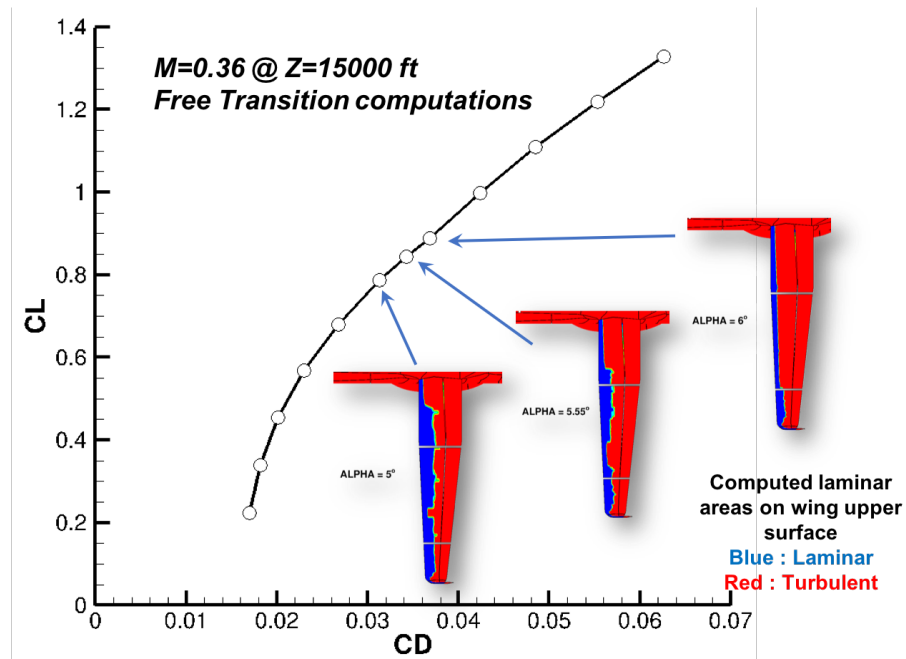
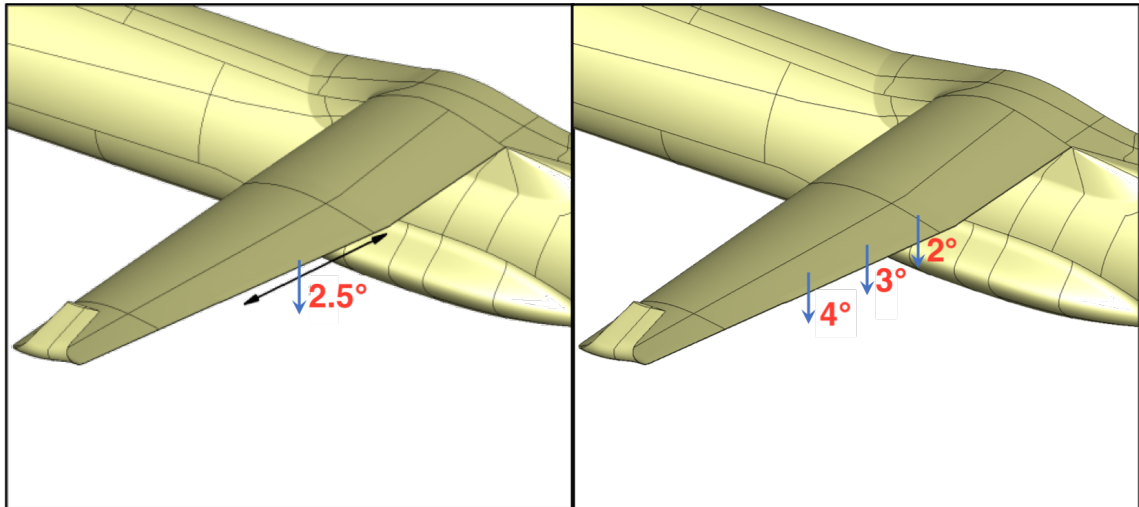
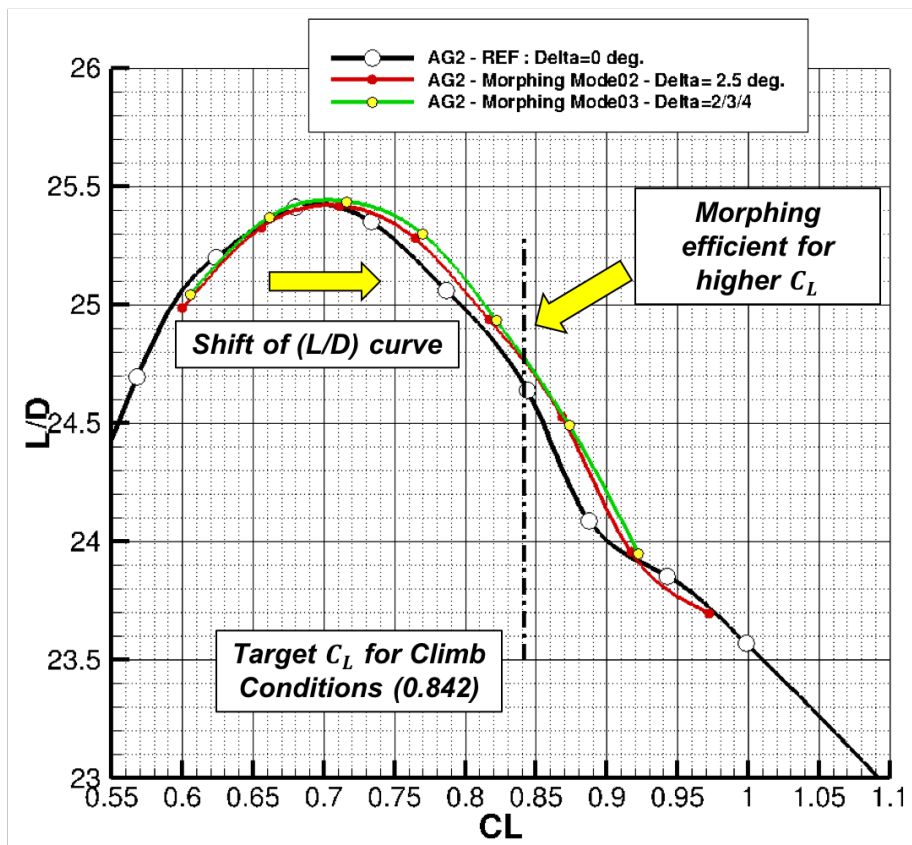


Figure 6.11: TP-90 Polar in climb condition without morphing (at $M_\infty = 0.36$ and $4572m$) [76].



(a) TE rigid rotation (left), TE twist morphing law (right).



(b) C_L versus aerodynamic efficiency L/D .

Figure 6.12: TP-90 Polar in climb condition with TE morphing mode 2 & 3 (at $M_\infty = 0.36$ and $4572m$) [77].

6.3 Finite Element (FE) Model

The higher level of complexity resulting for a multi-functional morphing structures makes it more challenging to meet standard aircraft airworthiness certification schemes without undergoing structural collapses. Indeed, because of the multi-functionality of the architecture several design loads conditions have to be fulfilled per each morphing mode.

The development of new architectures, together with the ever-present need for a practical realization of innovative solutions, makes any proposed morphing airframe a demanding platform to be simulated by means of Finite Element tools. Among the others, some key aspects have to be considered during the advanced design phase, such as:

- Simulation models of single parts (2D or 3D elements) to predict thin shell or thick solid components behaviour, that are typically present on morphing structures;
- Accurate modelling of local geometrical singularities (holes, fillets, local thickness variations) in order to capture stress concentration and possible plasticization effects;
- Detailed modelling of internal connecting members (pins, rivets);
- Correct modelling of single degrees of freedom (DOF) mechanisms: hinges and rotation centres, kinematic chain of actuation systems, avoiding an internal over constraining of the system.

For instance, the correct modelling of the two DOFs pertaining to each smart rib is of paramount importance to assure that the internal kinematic chains are not affected by misalignments and wrong rotation behaviour. This will assure that the correct load path in the kinematic chains will be obtained without over constraining the morphing system.

Nevertheless, such recommendations were considered to generate an accurate and predictable numerical model of a morphing structure. All the other general FE modelling checks (convergence analysis check, global equilibrium check) were taken into account to avoid any trivial mistake of final results.

The FE model presented in this section takes into account all the components that contribute to make up the 3MMF concept (Fig.6.1). The attention is particularly focused on the primary structure, and the actuation systems. The primary structure is intended as the reference skeleton, with the goal of distributing the efforts among the several elements of which it is composed. It is a kinematic system, and only the insertion of the actuation systems gives it load-bearing capabilities.

The electromechanical motors are the components that make the system capable of resisting the external loads. In the safe configuration, they work as a local clamp in the simulation; they are therefore imagined as infinitely rigid.

However, a final check will be performed on the actual capability of such systems to afford the resulting incident moments without failures in the Harmonic-Drive gearboxes of the actuation systems.

6.3.1 FE Modelling Guidelines

Frequently, the choice of the best element for a particular application may not be obvious. First, it must choose type, shape, and number of elements; these choices depend primarily on assessment of the effects that are important to represent in the model and on the cost and acceptable accuracy.

Going into the detail of the simulation process, various finite elements were taken into account in construction of the model, each with a different purpose:

- Linear quadrilateral elements (CQUAD4) for segmented skin, and spars modelling.
- Linear hexa elements (CHEXA) for rib blocks, inner mechanisms (IM1 and IM2), and linking beam elements (L1) modelling;

Generally, linear quadrilateral elements (CQUAD4) are preferred over the triangular elements (CTRIA3 and CTRIA6). The generic CTRIA3 element is a constant strain element. It is excessively stiff, and when used alone, it is generally less accurate than the CQUAD4 element, particularly for membrane strain. Therefore, CTRIA3 were not used. CQUAD elements were used for spars, and segmented skin (Fig.6.13d-6.13e). Each skin segment was properly screwed along spars and ribs' plates.

Since all items of the smart ribs are solid machined parts, solid elements were selected to model them. As well known in literature, tetrahedral elements can provide less accurate results [83]-[84]. For this reason, hexaedral solid elements (CHEXA, six-sided brick element with 8 grid points) were used. FE mesh of rib blocks is shown in Fig.6.13a. Details on the linking beam element and inner mechanisms (IM1 and IM2) are shown in Fig.6.13b-6.13c. Al 2024 was used for rib blocks, linking beam elements and leverages. While Steel 17-4-PH is only used for the fork shaped link of inner mechanisms (link 5).

One of the major issues is the modelling of the hinges and the relative motions of the different parts. In the preliminary design of the smart rib, absence of any mechanical interference was ensured during the movement of each leverages. Then, the finalized 3MMF concept with a through shafts actuation system was developed. Relying on 3D-CAD, kinematic simulations of the full-scale morphing system proved the absence of interferences between the actuation system and the inner mechanisms.

For this reason, a reliable FE model of the 3MMF was required for preserving the connections between the kinematic chains and the structural skeleton.

Cylindrical hinges were used to connect the different rib blocks as well as links of levers. Fasteners were used to connect segmented skins with spars and rib blocks.

The internal hinges were modelled according to the usual scheme of rigid body element (RBE) connections [88]. Such a connection is an algebraic representation of a kinematic constraint, which is an explicit equation that couples more DOFs of a set of nodes. In a RBE connection, the unknown DOF of a certain node (named master node) is equal to a combination of the DOFs of other nodes, belonging to the same RBE set (slave nodes).

In this way, the group has a single DOF for each direction, making it a rigid body with only six translational and rotational motion capability and no internal deformability.

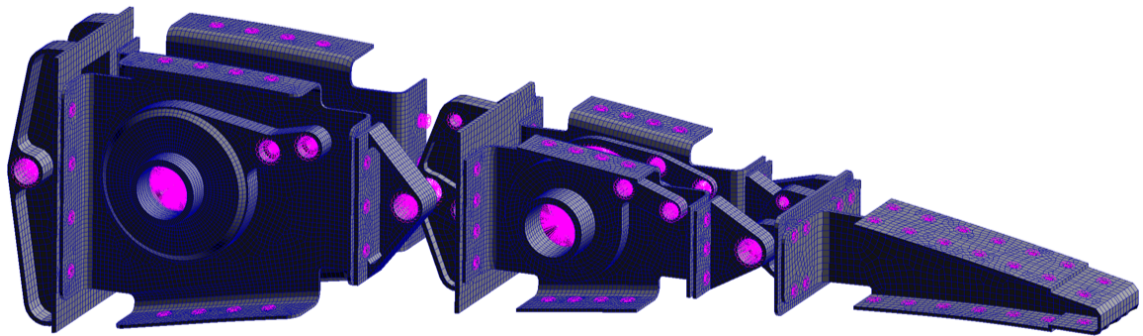
RBE is generally used for two different applications: 1) To simulate an extended rigid body, 2) to simulate joints (pins, fasteners or screws, hinges).

In fact, by properly modulating the constraints among the nodes, concurring into the RBE set, different architectures may be performed, leaving the DOFs that better represent a particular joint. In other words, namely rigid or partially rigid connections may be realized, as in the case of the link between two parts or two blocks, via a couple of hinges. Indeed, several types of joints may be simulated by establishing a link between two sets of RBEs, connected with a beam element:

- Fasteners for skin/spar and skin/rib interface: all DOFs are coupled.
- Pins for all internal hinges of the smart rib: all DOFs are coupled, except for a rotation around the pin axis RX (which is released).

An example of pin modelling is shown in Fig.6.13c(right). Therein, the independent node is seen as the ideal centre of rotation. The hinge is then modelled by coupling the DOFs of the master independent with the slave nodes, accordingly. For the case of a cylindrical hinge, all DOFs are coupled except for a rotation around the pin axis (RX). The mutual rotation between the connected parts is guaranteed by a BEAM, linking the two master nodes.

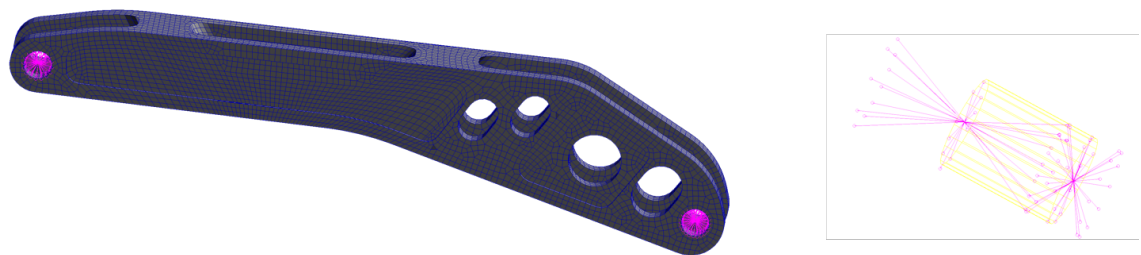
Finally, a generic fastener is modelled through a beam element whose extremities are rigidly linked to the connecting parts. Two RBE (with all DOFs coupled) were defined into holes of the two parts connected by a fastener. RBE's master node is defined at the hole centre, and RBE's slave nodes belong to the hole face. The two RBE's master nodes were the grid points of a beam.



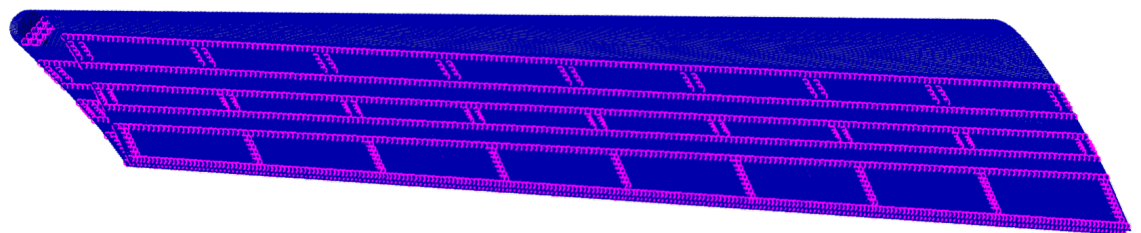
(a) Rib blocks (CHEXA elements).



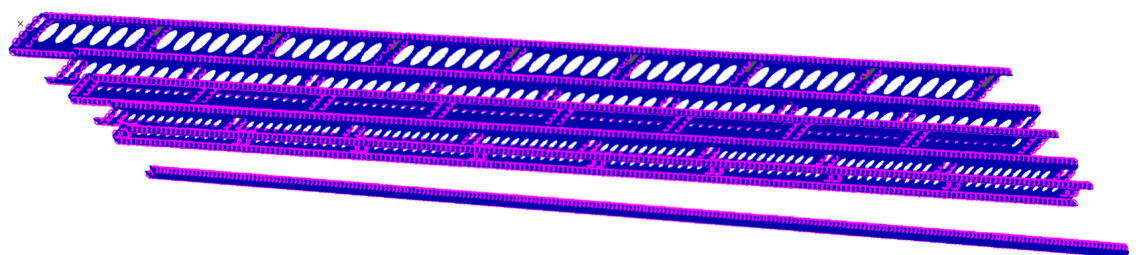
(b) Inner mechanisms IM1 & IM2 (CHEXA elements).



(c) Linking beam element (CHEXA) and hinge (CBAR with MPCs).



(d) Segmented Skin (CQUAD4 elements).



(e) Spars (CQUAD4 elements).

Figure 6.13: 3MMF Finite-Element Model: details of the smart rib.

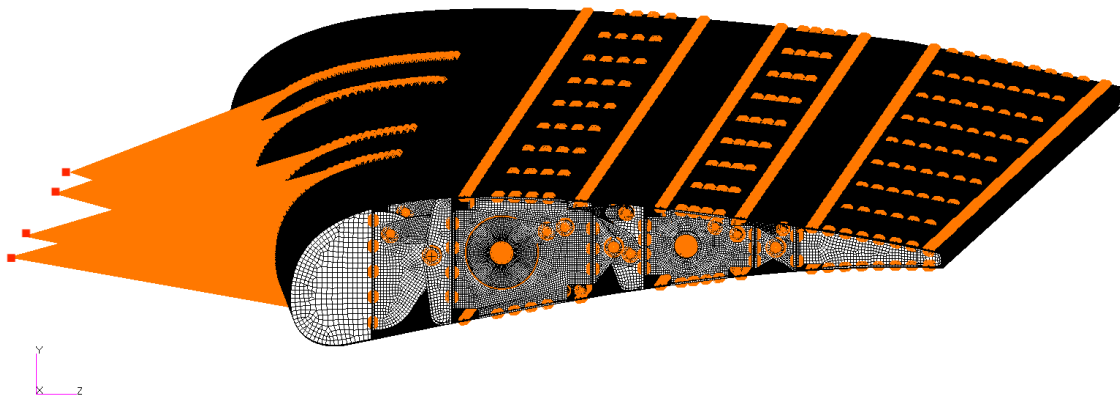


Figure 6.14: 3MMF finite-element model.

6.3.2 Modal Analysis

In order to check kinematic consistency of the entire finite element model, a modal analysis was performed with the flap leading-edge constrained in all degrees-of-freedom (Fig.6.14). Four RBEs were used to model the attachment to the flap leading edge of the fairing-less deployment systems.

Moreover, all actuator shafts, and harmonic drive gearboxes were removed: in such a way, all consecutive rib blocks might freely rotate around their respective hinge-axes.

For instance, when the actuation system is removed, the morphing system is only composed by its structural skeleton. In such a case, the kinematic behaviour of the full-scale FE model can be verified.

The FE model can be validated and used for static analysis only if the kinematic DOFs pertaining to 3MMF are simulated. As explained in Sec.5.2, each smart rib has two DOFs. It is of paramount importance to assure that all the internal kinematic chains are not affected by misalignments (along the span-wise direction) and wrong rotation behaviour are avoided.

This check will assure that the results provided by a static analysis will correctly predict the load path and the stress distribution in the kinematic chains. For instance, if all expected rigid modes are found removing the actuation systems, the FE model will be reliable and free from any over constraining on the kinematic chains.

Modal analysis was performed using Nastran [88]. Eigenvalues extraction was performed with Lanczos Method [88] in the frequency range of interest: [0 Hz; 50 Hz]. Method for normalizing eigenvectors was the maximum (i.e. NORM=MAX), which normalizes to unit value of the largest displacement in the analysis set.

Because flap blocks B0, B1 and B2 are connected by the linking element, we will expect one kinematic DOF which involves these items. Because flap tip segment was segmented in three parts (see Fig.6.2c), we will expect three DOFs for the flap tab (one per each segment).

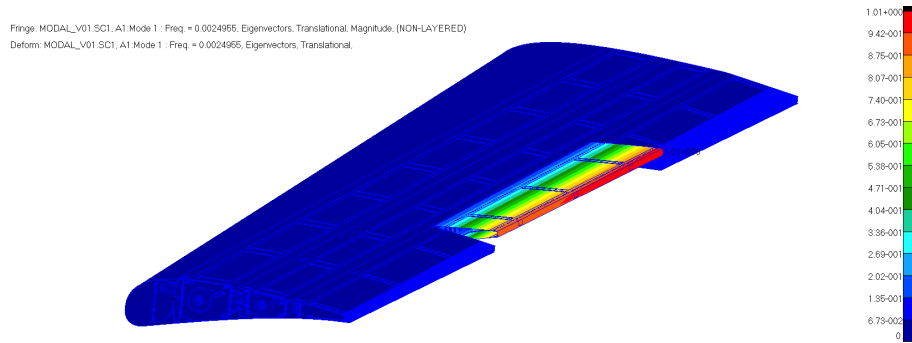
In Fig.6.15, four rigid modes were found. As expected, the whole 3MMF kinematics was properly modelled:

- First modal shape (Fig.6.15a) replicates the tab-like mode of the central segment;
- Second modal shape (Fig.6.15b) combines the camber-morphing mode (between blocks B0, B1, B2) with the tab-like morphing mode of the central segment;
- Third modal shape (Fig.6.15c) combines the tab-like mode of the inner and outer segments;
- Fourth modal shape (Fig.6.15d) replicates the tab-like mode of the outer segment.

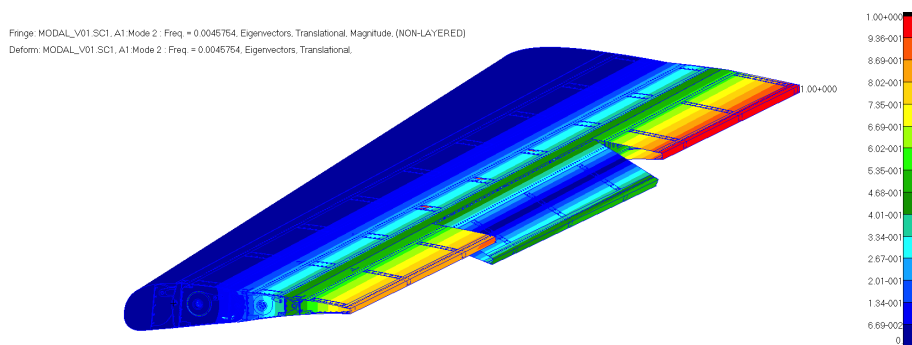
In Fig.6.16, relative to the range up to 50 Hz, three elastic modes were found. Analysis of these elastic modes gives hints about the dynamic behaviour of the 3MMF.

The principal conclusions that can be underlined are:

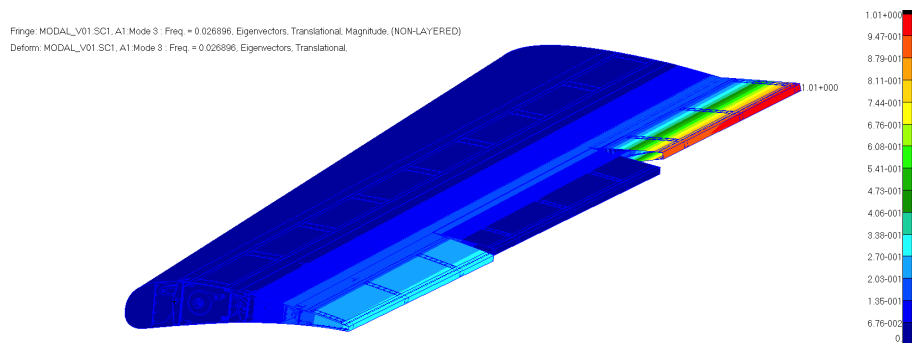
- Modal analysis shows that no local modes exist; in other words, all the shapes involve all the components;
- The first elastic modal shape is the morphing deformation mode (Fig.6.16a), confirming the peculiarity of the adaptive structural systems to include new DOF in the system;
- In addition, the first elastic mode occurs at relatively high frequencies (25.2 Hz), well beyond the “rigid mode zone” (namely, around 0 Hz); this is a clear signal that the selected configuration has a certain capability to resist the external loads;
- The modal density is reasonably low; this is a good index because many major instabilities, like flutter, derive from the coupling between two or more modes (flutter occurs when a torsional couples with a longitudinal bending eigenvector);
- The first torsional mode (Fig.6.16b) appears at 33.4 Hz, while the first bending mode takes place at 49.2 Hz; they are well identified and show a certain regularity;
- Segmented flap tip of the 3MMF does appear the one that is characterized by the largest motion; this is an index of potential aeroelastic problems investigated in [85].



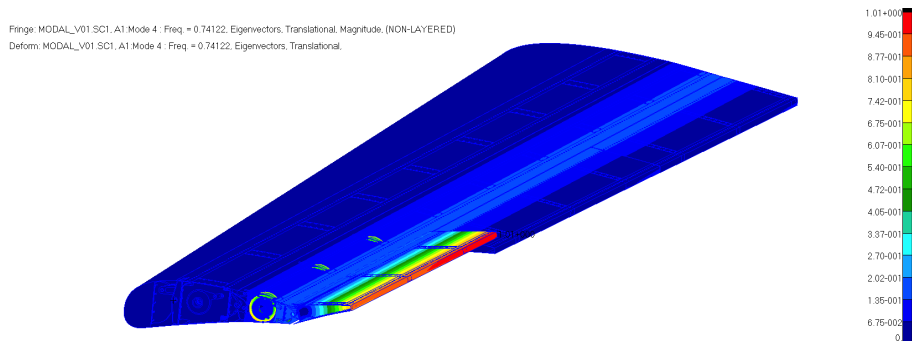
(a) 1st Rigid mode $f = 2.49 \times 10^{-3}$ Hz.



(b) 2nd Rigid mode $f = 4.57 \times 10^{-3}$ Hz.



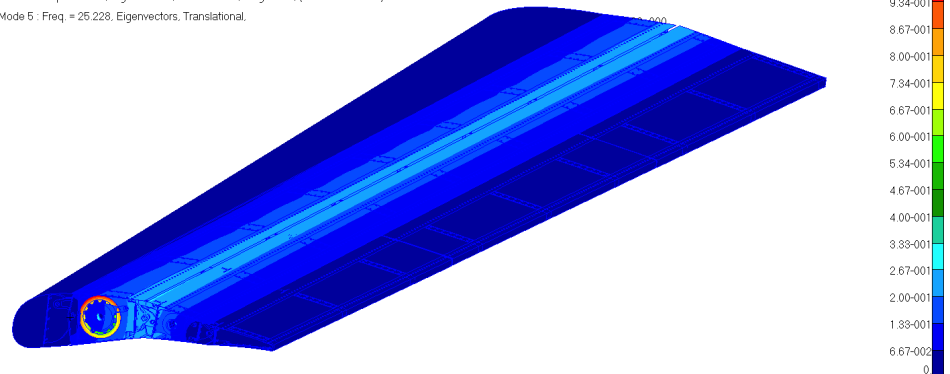
(c) 3rd Rigid mode $f = 2.68 \times 10^{-2}$ Hz.



(d) 4th Rigid mode $f = 0.74$ Hz.

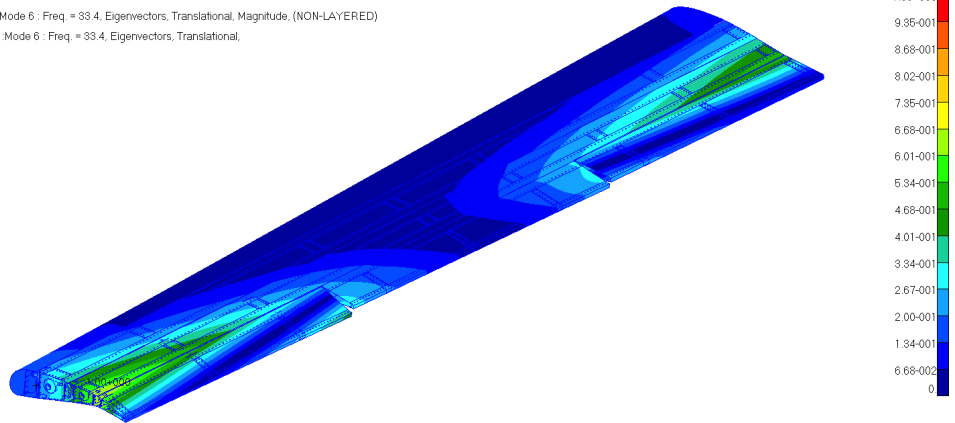
Figure 6.15: Modal analysis: rigid modes.

Fringe: MODAL_V01.SC1.A1.Mode 5 : Freq. = 25.228, Eigenvectors, Translational, Magnitude, (NON-LAYERED)
 Deform: MODAL_V01.SC1.A1.Mode 5 : Freq. = 25.228, Eigenvectors, Translational.



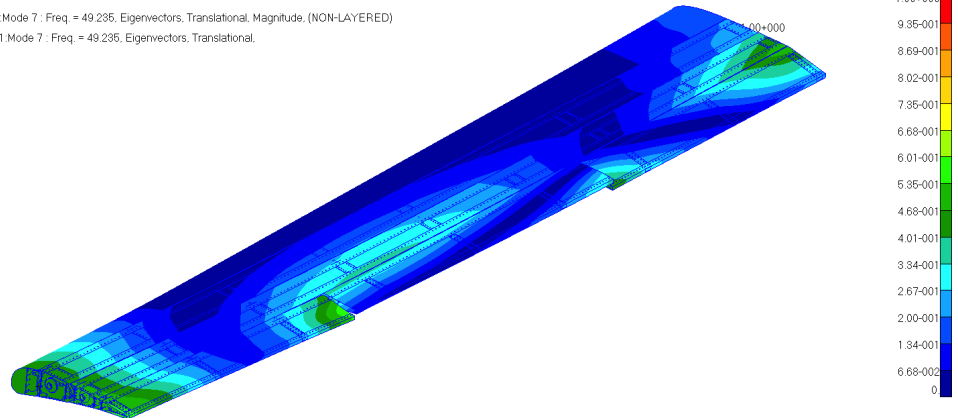
(a) 1st Elastic mode $f = 25.2$ Hz.

Fringe: MODAL_V01.SC1.A1.Mode 6 : Freq. = 33.4, Eigenvectors, Translational, Magnitude, (NON-LAYERED)
 Deform: MODAL_V01.SC1.A1.Mode 6 : Freq. = 33.4, Eigenvectors, Translational.



(b) 2nd Elastic mode $f = 33.4$ Hz.

Fringe: MODAL_V01.SC1.A1.Mode 7 : Freq. = 49.236, Eigenvectors, Translational, Magnitude, (NON-LAYERED)
 Deform: MODAL_V01.SC1.A1.Mode 7 : Freq. = 49.236, Eigenvectors, Translational.



(c) 3rd Elastic mode $f = 49.2$ Hz.

Figure 6.16: Modal analysis: elastic modes.

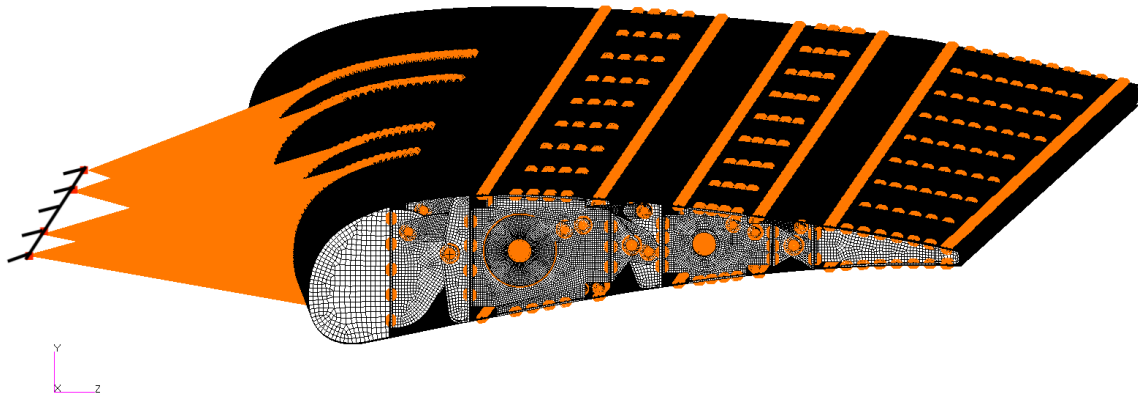


Figure 6.17: 3MMF finite-element model: BCs for static analysis.

6.4 Structural assessment of the full-metallic 3MMF

Preliminary FE static analyses of the single smart rib were performed to support the finalized layout (see Sec.5.2.6). In addition, these analyses confirmed the values of mechanical advantage evaluated with the ICs tool (see Fig.5.18c); VM stresses were below the material allowable on the kinematic chains.

After that, preliminary structural sizing procedures were used for the design of the 3MMF structural skeleton. Also in this case, VM stress distributions were below the material allowable for skins and spars (see Fig.5.22b).

Once the reliability of the model was proved in terms of smooth simulation of morphing kinematics (as supported by modal analysis results of the previous Sec.6.3.2), actuators transmission line was re-connected to the ribs and actuators shaft rotation was prevented in order to address static analyses.

In this section, a static analysis of the 3MMF demonstrator will be analysed considering the limit load distribution pertaining to morphing mode 1 (see Fig.4.4) in landing condition. The applied LL is a pressure distribution over the external surfaces of the upper and lower skins. This static analysis will be useful to prove structural integrity of the conceived layout up to LL conditions. In addition, interactions between the structural skeleton and the inner mechanisms will be assessed to estimate the load path in the morphing system up to the worst load condition.

As explained in Fig.6.6, the deployment system is connected to the 3MMF structural skeleton by means of four tracks along the span of the 3MMF block B0 (i.e. the flap leading edge). Four RBEs were used to model the attachment to the flap leading edge of the fairing-less deployment systems. The interface deployment system/flap was considered as

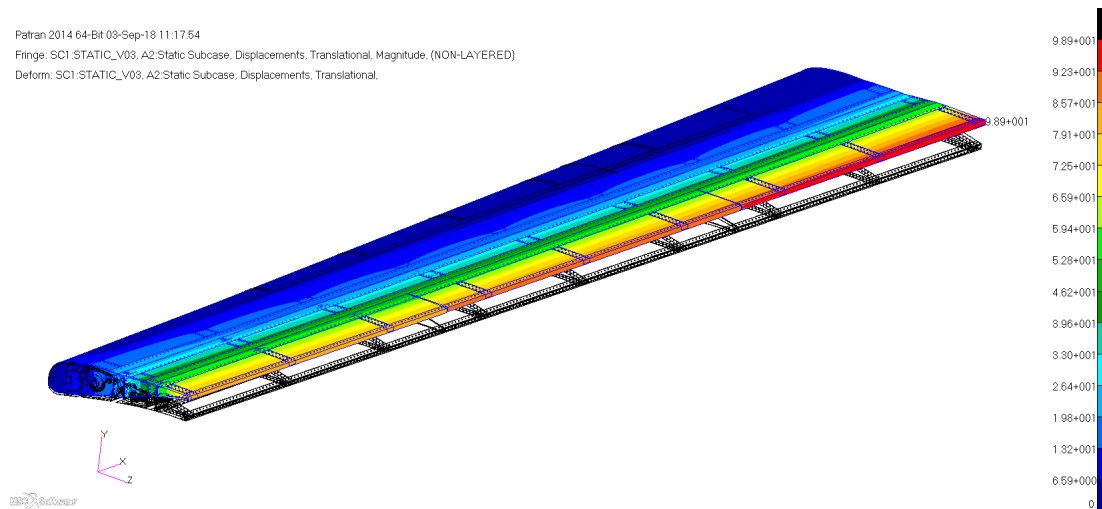


Figure 6.18: 3MMF static analysis with LL: displacements [mm].

perfect local clamps for the 3MMF: master grid points of RBEs, modelling the deployment systems, were constrained in all degrees-of-freedom (Fig.6.17).

In addition, the most conservative assumption was made on the actuation systems: each crank of each leverage (IM1 and IM2) was locked. No rotation around X-axis was allowed to each crank link. This boundary condition gives rise to the most critical stress distribution inside the inner mechanisms.

In Fig.6.18, the displacements distribution is shown. The maximum displacement of 98 mm was found at the trailing-edge of the root rib. This value corresponds to 11.3% of the local root chord.

In Fig.6.19, reaction moments at each IM crank were summarized. The maximum values are located on the cranks of IM1 hosted within 3MMF block B1. However, these values are below 20 Nm. This reaction torques are transferred to the actuation systems. For this reason, to be sure that any failures occur in the gear-boxes, the reaction torques must be lower than both

- Repeatable peak torque of the Harmonic-Drive CPL-17A [65] equal to 54 Nm (see Tab.5.2), which is the maximum available torque at HD output for a short period;
- Average torque of the Harmonic-Drive CPL-17A [65] equal to 39 Nm (see Tab.5.2), which is the maximum average torque at HD out for a variable load;

The results of the resistant torques assures that no damage will occur in the gearbox in the LL condition. For instance, the inner mechanisms assures satisfactory reductions of moment transferred to the HD gear-boxes because of their high mechanical advantage.

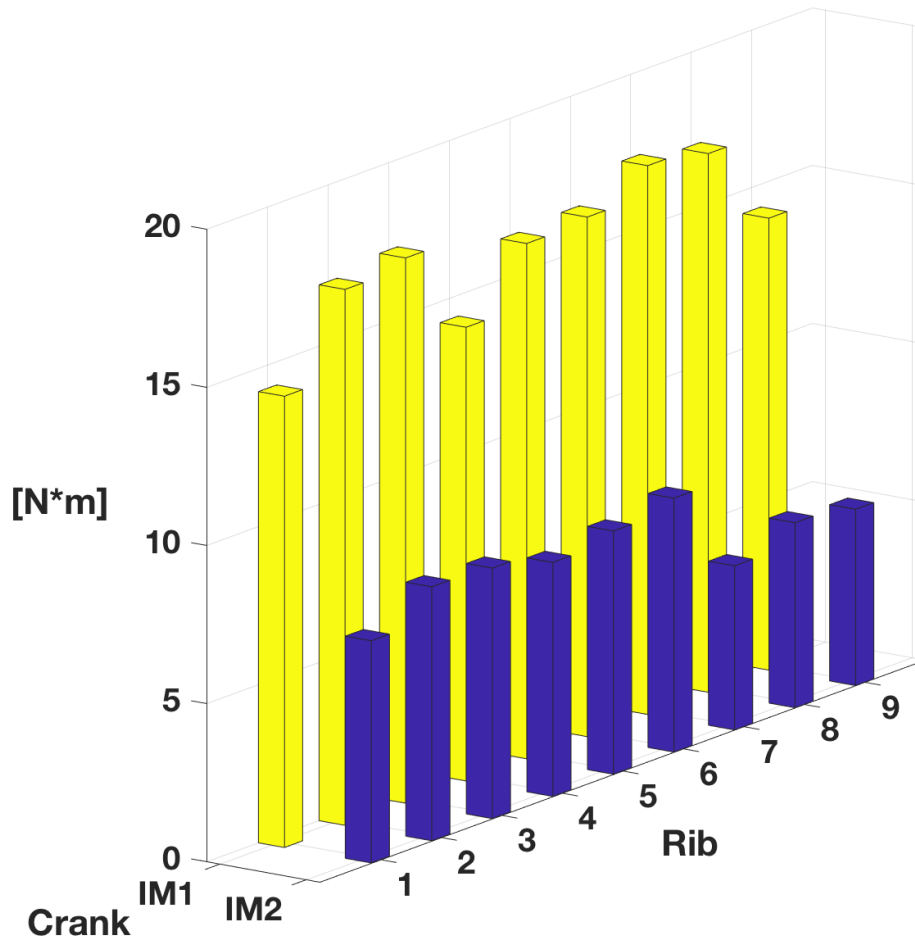
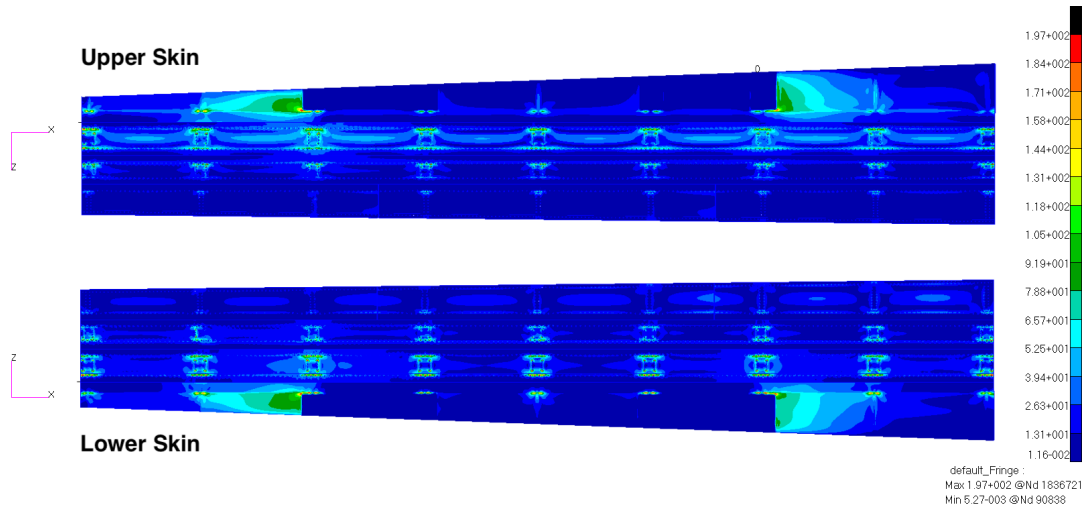


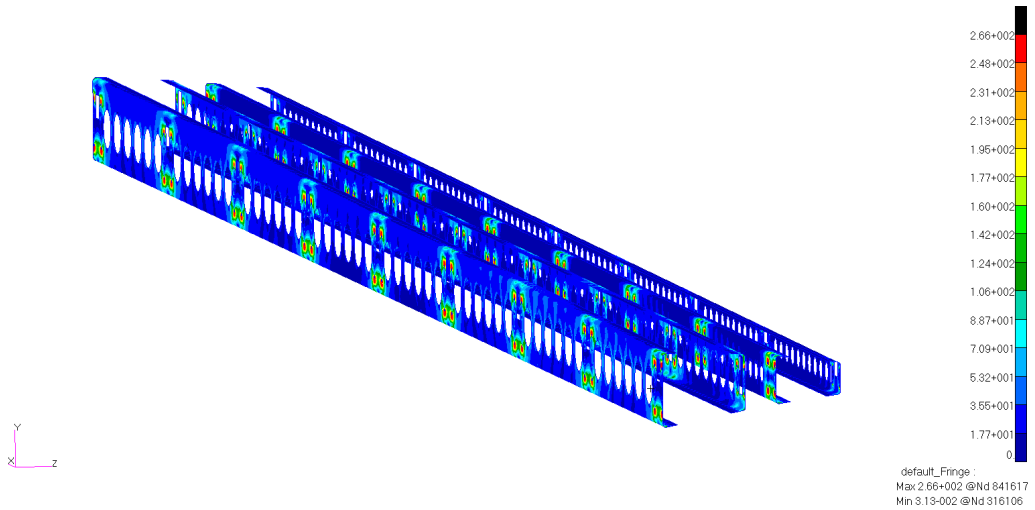
Figure 6.19: 3MMF static analysis with LL: reaction moments at each IM crank.

Finally, VM stress distributions are reported for each structural items. The strength of each component is evaluated by comparing the Von Mises (VM) stress with the yield material strengths: 330MPa for AL-2024, and 750MPa for 17-4PH steel. Peak values are reported for each part. Highest VM stress equal to 406 MPa is located on the fork link of IM1 (Fig.6.21a) which is the only item made of 17-4PH steel. Highest VM stress on items made of AL-2024 is located on the linking beam element: 302MPa in Fig.6.21b).

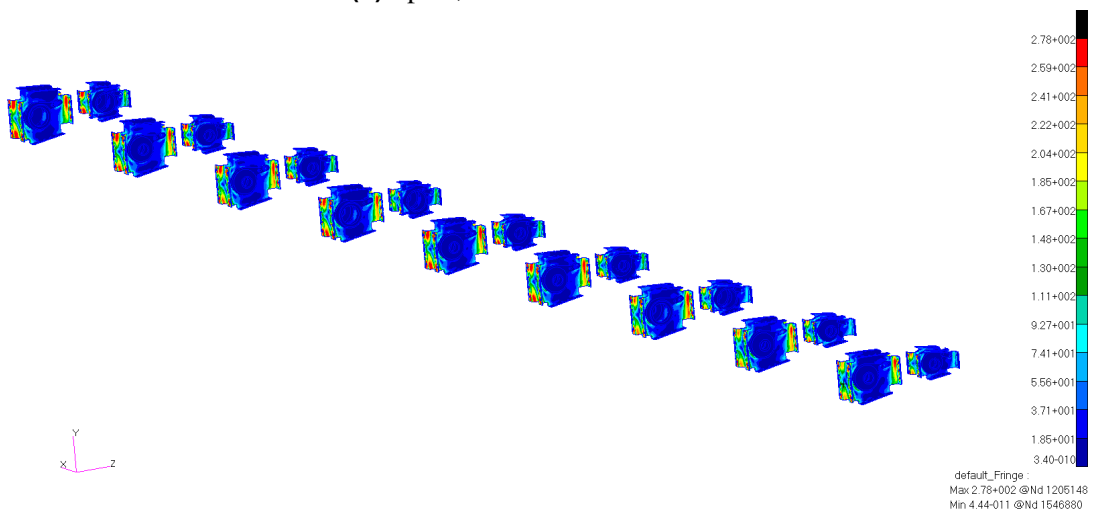
Static analysis results confirmed absence of any plastic deformations in the 3MMF structural skeleton in the LL condition.



(a) Upper and lower skin, Max Value 197MPa.

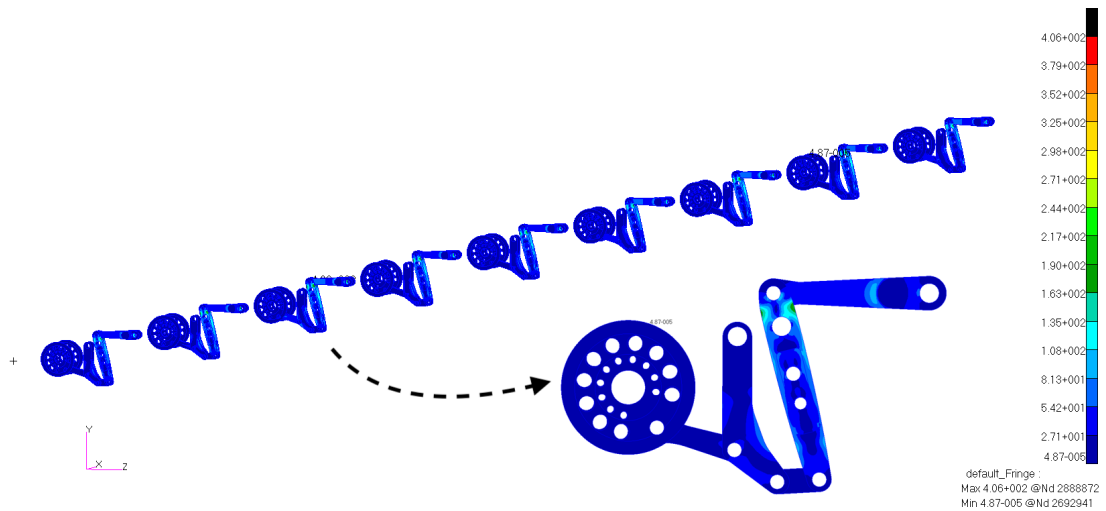


(b) Spars, Max Value 266MPa.

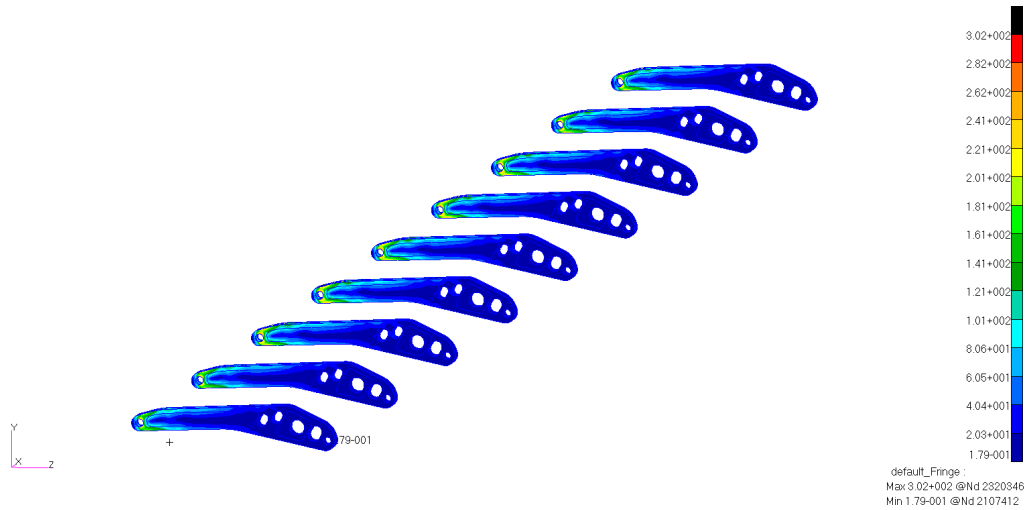


(c) Rib blocks, Max Value 278MPa.

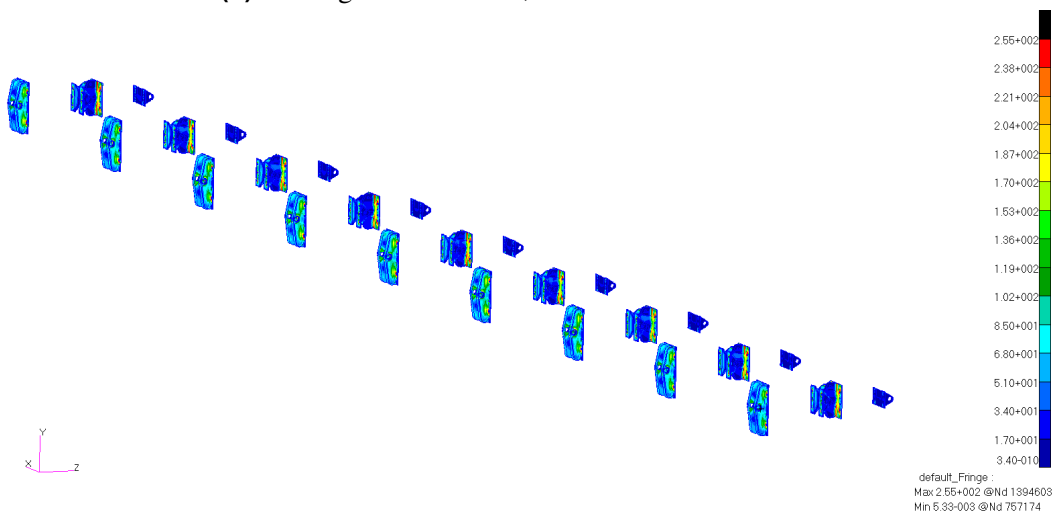
Figure 6.20: 3MMF static analysis with LL: VM stress [MPa].



(a) Inner Mechanisms, Max Value 406MPa.



(b) Linking beam element, Max Value 302MPa.



(c) Hinge fittings, Max Value 255MPa.

Figure 6.21: 3MMF static analysis with LL: VM stress [MPa].

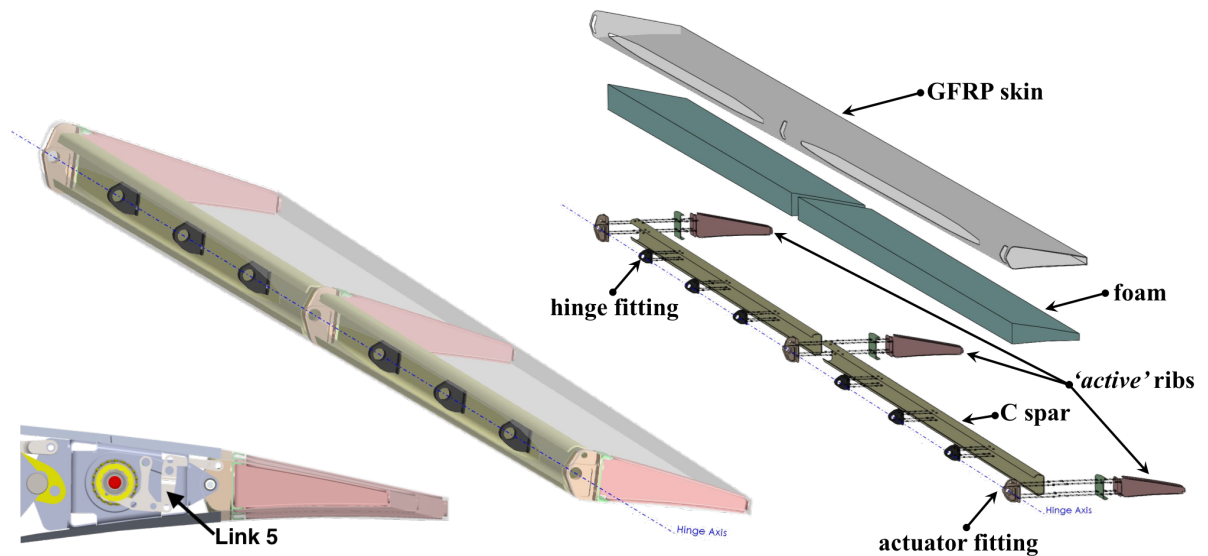


Figure 6.22: ATT structural concept.

6.5 Structural assessment of the composite ATT

The concept of Adaptive Twist Tab is based on the idea of retrofitting the segmented tab of the 3MMF with a device able to provide rigid deflections (morphing mode 2) and span-wise continuous twist (morphing mode 3). These new functionalities on a NLF wing can provide up to +2% aerodynamic efficiency improvement during cruise and climb flight conditions [77].

As explained in Sec.5.5.2, the ATT structural concept is a thin-walled closed section (Fig.6.22) whose functionalities are enabled thanks to actuation torque provided by three brushless rotary motor, properly amplified by harmonic drive gear units and inner mechanisms. As rotary actuators are activated, the inner mechanisms can transfer torque to the structural concept thus providing the required performance.

Upon the actuation of the active ribs, the Fowler flap tip is put in movement thus changing the external shape of the trailing edge; if the shape change of each rib is prevented by locking the actuation system, the composite tab is elastically stable under the action of external aerodynamic loads. The rigid rotation of the ATT (Fig.6.2b) can be obtained synchronizing the three actuators.

Differently, “continuous” span-wise trailing edge twist (Fig.6.5) can be activated providing different control actions. For example, linear span-wise tab twist can be enabled providing clockwise rotation to the tip actuator and anti-clockwise rotation to the root actuator (locking the central station).

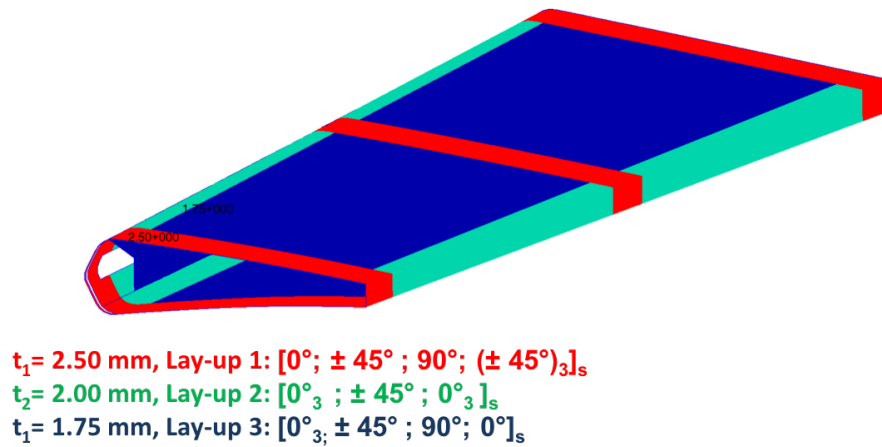


Figure 6.23: ATT thickness distribution.

In this section, the structural layout and the actuation system will be assessed with reference to the most severe load condition expected in service (LL condition) for the tab; AL2024-T5 alloy was used for most of the items of the inner mechanism, while 17-4PH steel was only used for the fork (link 5, see Fig.6.22) of the leverage. Rohacell® 51 FX was used for the foam [86].

A glass fiber prepreg with HexPly913 from Hexcel composites [68] was chosen as material for the upper and lower skins, the active ribs, and the “C-shape” spars. This material is widely used for the manufacturing of rotor blades. Indeed, the material assure good compromise between stiffness and large strain capabilities which are strictly related to operative performance under aerodynamic loading as well as static strength for twisting of the trailing-edge [74].

The final structural layout (Fig.6.22) was analyzed by means of advanced finite element model which finally proved:

- The capability of the actuation system to enable morphing through smooth rigid-body kinematic of the inner mechanisms;
- The absence of any local plasticization and elastic instability at limit load condition for the items made of aluminum and steel alloy;
- Strains for items made of GFRP (in parallel and perpendicular fiber directions) lower than the maximum allowed strains at the limit load;

In the preliminary design phase, analytical equations were an effective tool to estimate: moments required by the actuation systems (\mathcal{M}_{OUT}) for twisting, SV and warping parts of torsional moment (T_{SV} and T_w), and the torsional-bending length ($d = \beta^{-1}$).

However, to verify the mechanical behaviour of the multifunctional twistable tab in operative conditions, finite element (FE) simulations were required.

A three-dimensional finite-element was generated using quadrilateral plane elements (CQUAD4) for skin, C-shape spars and active ribs, while six-sided solid elements (CHEXA) for foam, actuator and hinge fittings. Thickness distributions for skin and C spars are summarized in Fig.6.23. A larger lay-up was considered for the skin near the active ribs because higher warping torsional moment were predicted in this area. The skin region with this lay-up has an extension equal to 200mm: five times the characteristic torsional-bending moment evaluated in Sec.5.5.2.

The numerical simulations were performed using linear solver of Nastran [88].

A preliminary analysis was performed on the composite tab without aerodynamic loads to assess the maximum twisting torque required by actuation systems for mode 3 as well as the structural strength of the twisted skin. The central “active” rib was constrained in all degrees of freedom; enforced rotations (SPCD) equal to +5 degrees (downward) to the tip active rib and -5 degrees (upward) to the root active rib were applied. As shown in Fig.6.24, the maximum strain of about 1.34 per cent is reached near the cut-out of the central section. For the most part of the remaining structure the strains stay below 0.8 per cent. According to [87], the maximum allowed strain in fiber direction is equal to 2.5 per cent and 0.5 per cent perpendicular to the fiber. The torque required for enabling linear twist is equal to 64.05Nm for tip actuation system and 103.6Nm for root one.

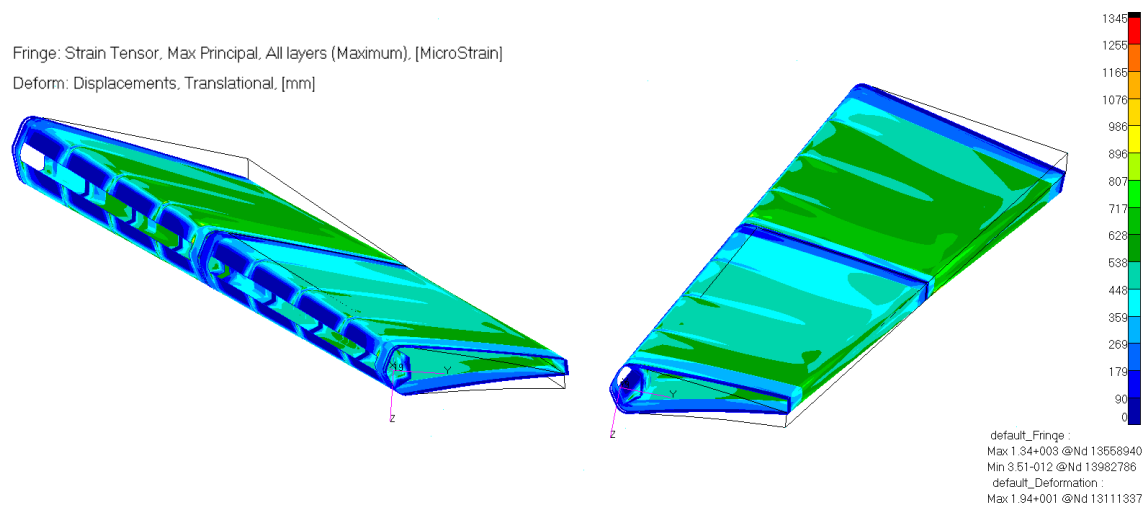


Figure 6.24: Continuous span-wise TE twist (Mode 3): +5° (root); 0° (central); -5° (tip).

A second analysis was performed to prove the structural integrity of the composite structure upon the limit load condition (reported in Tab.4.2) pertaining to Mode 2 (TE

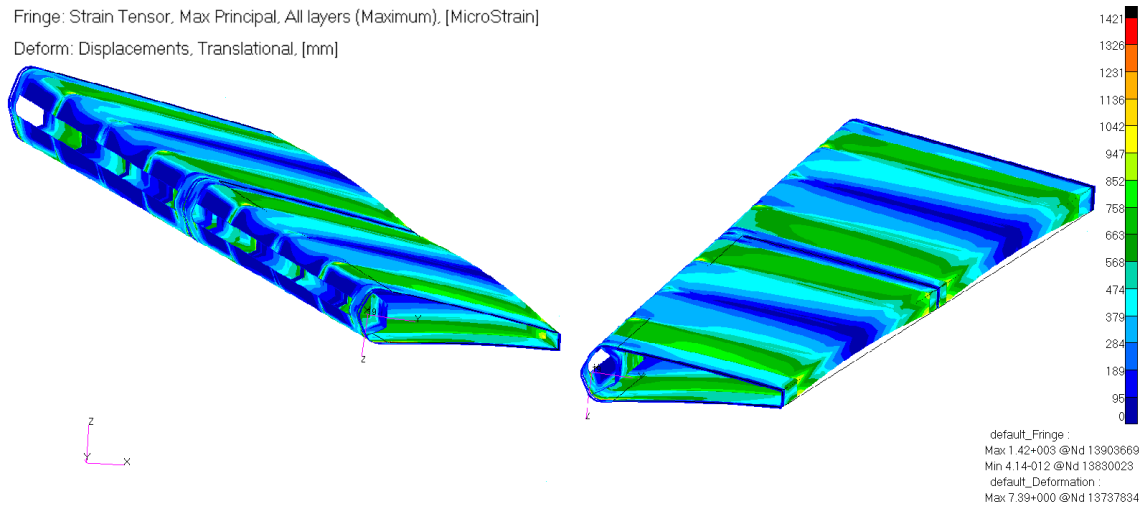


Figure 6.25: Rigid downward deflection equal to $+5^\circ$ (Mode 2): Strain Distribution [μ Strain].

rigid rotation equal to $+5$ deg downward). As shown in Fig.4.2, the maximum strain of about 1.42 per cent is reached near the central section. Maximum displacement is equal to 7.39mm in the midpoint of the inboard tab region. In the remaining part of the structure the overall displacement is below 3mm which demonstrates sufficient stiffness of the system; in compliance with regulations (EASA CS 25.305(a)) the deformation levels don't interfere with the safe operation at limit load condition.

According to airworthiness requirements [41], aircraft structures must comply with limit load conditions to prove their structural integrity with the overall flight envelope.

However, during the regular airplane flight mission profile, load-bearing aircraft structures have to withstand aerodynamic loads lower than the ones prescribed in the limit condition. In such case, the multifunctional twistable trailing-edge used on the AG2-NLF wing is expected to be activated in high speed climb flight conditions (as explained in Sec.6.2.2). For enabling transition from baseline configuration to the rigid trailing-edge deflection (mode 2 in Fig.6.12a) equal to 2.5° , all rotary brushless motors have to be activated (R1, R2, and R3) transferring to their respective "active" ribs the same angle. In this case, the actuating torques required to enable this transition are reported in Fig.6.26. Continuous increase in deflection angles (mode 3 in Fig.6.12a) can be enabled with the three independent actuation systems transferring from tip to root angles equal to $(4^\circ/3^\circ/2^\circ)$ to their respective "active" ribs. Considering aerodynamic load pertaining to the climb condition ($M_\infty = 0.36$ at 4572m) with TE morphing in Mode 3 ($4^\circ/3^\circ/2^\circ$), the structural layout shows the maximum strain equal to 0.28 per cent, and the required actuating torques (per each active rib) are summarized in Fig.6.26.

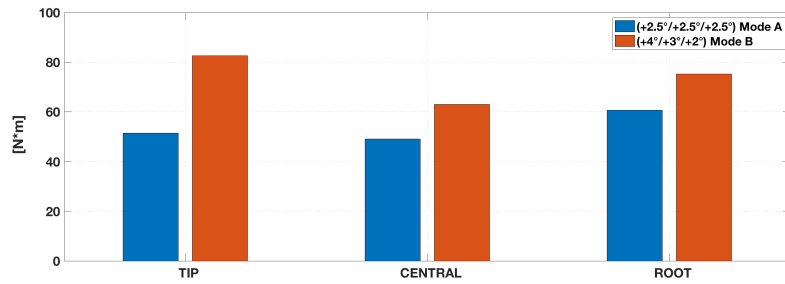
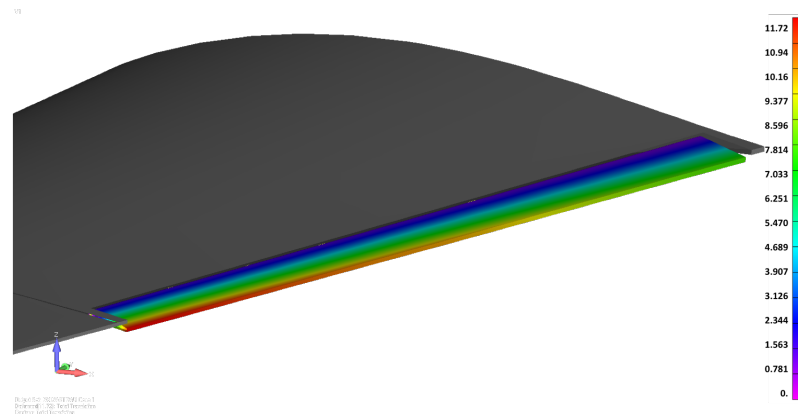
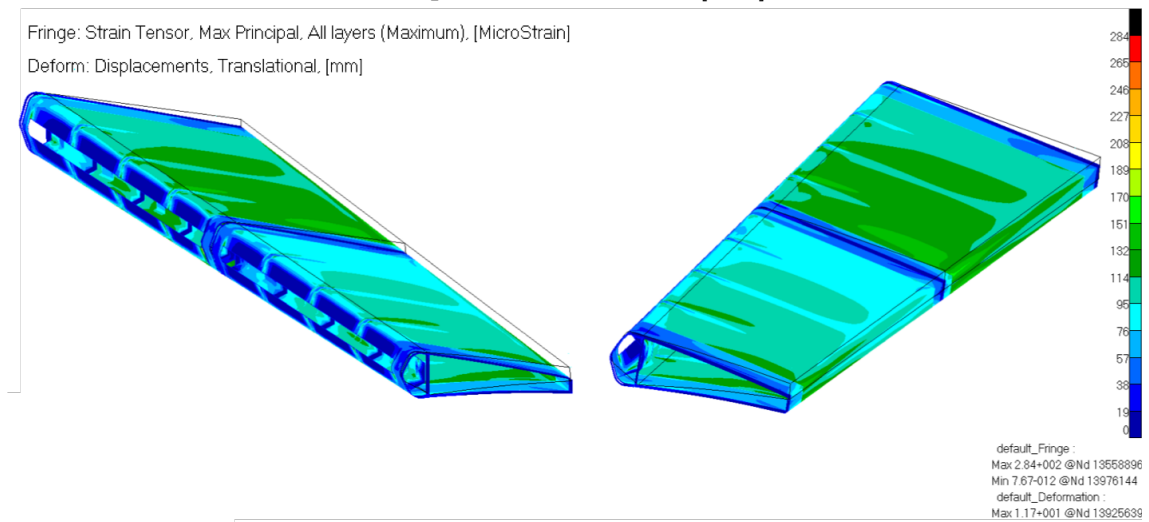


Figure 6.26: Actuating torques required by the actuation systems for enabling morphing TE modes during high speed climb flight conditions ($M_\infty = 0.36$ at 4572m).



(a) Displacement distribution [mm].



(b) Strain Distribution [μ Strain].

Figure 6.27: Continuous span-wise TE twist (Mode 3): +2° (root); +3° (central); +4° (tip).

6.6 Estimated Weight

At each design loop, the concept was constantly improved to reduce number of parts (i.e. rotary actuators, smart ribs), and total weight. According to [1], the weight of a conventional flap system is approximately 3 per cent of the airplane MZFW. The final weight of the outboard 3MMF results equal to 92.5kg that is 12 per cent lower than the weight estimated for a conventional outboard flap (104.6kg) for a regional Turbo-prop aircraft. Weight estimation of the finalized 3MMF concept is shown in Tab.6.1.

In addition, it is possible to estimate the benefits in terms of fuel saved at aircraft level obtained with this innovative high-lift solution: fairing-less deployment system and the morphing flap.

Change in aircraft range due to morphing flap and fairing-less flap deployment system can be estimated by the Breguet formula (which gives the range for an airplane flying at a constant speed):

$$R = \frac{V_{\infty}}{(SFC)g} \cdot \frac{C_L}{C_D} \ln\left(\frac{M_1}{M_2}\right) \quad (6.1)$$

where R is the range (m), V_{∞} is the velocity (m/s), $g = 9.81m/s^2$, $SFC(= M/T)$ is the specific fuel consumption with M fuel massflow consumed per second (kg/s) and T engine thrust (N); M_1 is the initial mass of the airplane including the fuel, and M_2 is the final mass of the airplane at the end of the mission.

Assuming constant specific fuel consumption, same cruise speed and same lift, the increase of aircraft range can be approximated as a function of change in drag and empty mass of the aircraft:

$$\% \text{Range increase} = \left\{ \frac{\left[\frac{1}{C_D} \cdot \ln\left(\frac{M_1}{M_2}_{\text{new}}\right) \right]}{\left[\frac{1}{C_D} \cdot \ln\left(\frac{M_1}{M_2}_{\text{ref}}\right) \right]} - 1 \right\} * 100\% \quad (6.2)$$

In more details, the following assumptions can be made for a regional turbo-prop airplane:

- $M_{1,\text{ref}} = \text{MTOW (Maximum Take-Off Weight)} = 33200\text{kg}$;
- $M_{2,\text{ref}} = \text{MZFW (Maximum Zero Fuel Weight)} = 31200\text{kg}$;
- $m_{\text{flap}} = 0.03 \cdot M_{1,\text{ref}}$, the overall conventional flap weight is approximately 3% of the weight of a conventional aircraft [1];

- Mass of the deployment mechanism is expected to be in the same order with the conventional mechanisms

In such a case, the range can be mainly affected by three factors related to this high-lift solution and compared to a conventional flap and deployment system:

- ΔM_{3MMF} increase of weight due to 3MMF technology;
- $\Delta M_{fairing}$ decrease of weight due to elimination of flap track fairings;
- $\Delta C_D = 0.0075$ decrease of drag coefficient due to elimination of flap track fairings equal to 0.75%;

In the same way, the amount of fuel saving due to 3MMF technology and a fairing-less Flap Mechanism can be calculated for the same (design) range travelled with a conventional high-lift system.

Considering the design range R_{design} of $100NMiles = 1852Km$, using the Breguet formula, we can estimate for the reference configuration that:

$$\eta_{ref} = \left[\frac{V_{\infty}}{(SFC)g} \cdot \frac{C_L}{C_D} \right]_{ref} = \frac{R_{design}}{\ln\left(\frac{M_1}{M_2}\right)} = 29807.6km \quad (6.3)$$

If the A/C range is assumed to be a typical range ($300NMiles = 555Km$), the typical fuel weight can be estimated with the Breguet formula:

$$M_{1,ref,typical} = M_{2,ref} \cdot \exp\left(\frac{R_{typical}}{\eta_{ref}}\right) \implies M_{fuel,ref} = 587kg \quad (6.4)$$

We can equate the range given by the new high-lift TE system R_{new} with the one obtained with the conventional flap R_{ref} ; thus, for the same range travelled $R_{new} = R_{ref}$, we can estimate the fuel mass required for the new configuration and the decrease in fuel consumption:

$$M_{fuel,new} = \left[\exp\left(\frac{1}{1 + \Delta C_D} \cdot \ln\left(1 + \frac{M_{fuel,new}}{M_{2,ref}}\right)\right) - 1 \right] * M_{2,ref} \quad (6.5)$$

$$\%Fuel\ Decrease = M_{fuel,ref} - M_{fuel,new} \quad (6.6)$$

The weight increase due to the 3MMF morphing technology is “recovered” considering “only” the benefits induced by the adoption of a fairing-less deployment system.

As shown in Fig.6.28, a 25% weight increase for the 3MMF can provide a 0.32% benefit in fuel consumption because of the fairing-less deployment system.

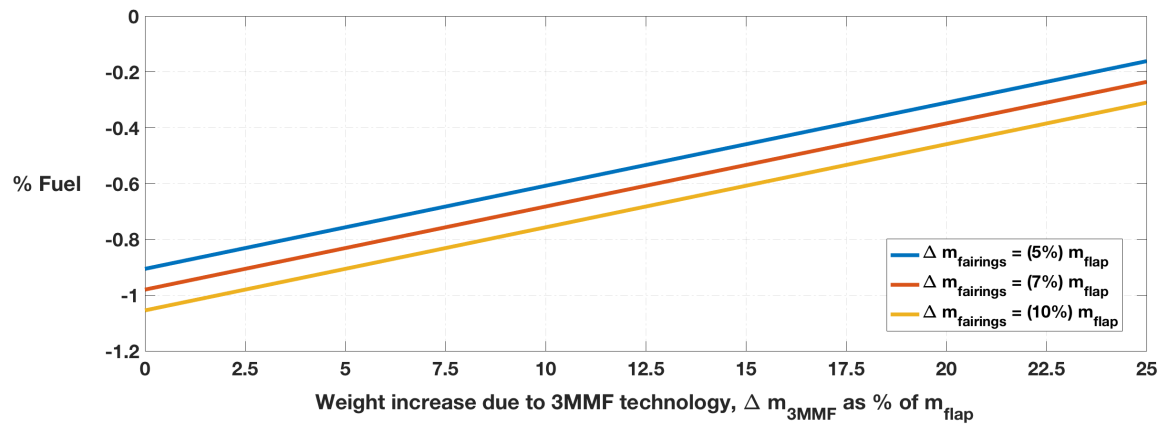


Figure 6.28: Fuel weight decrease as function of 3MMF technology weight increase.

In a different way, if the 3MMF final weight is equal to the one of a conventional flap (i.e. $\Delta m_{3MMF} = 0$), a fuel consumption benefit up to 1.05% can be provided using a fairing-less deployment system.

Components	Weight [Kg]
Rib,Spars	34.65
Skin (aluminium 1.5 mm tick)	23.70
Total Structure	58.35
Cinematism,Bearings,joints	18.79
Actuators, sensors	15.36
Total Actuation	34.15
Total Flap	92.50

	Part Number	nr	Weight [Kg]	Total [Kg]	
S t r u c t u r e	Block 0	Rib and spar	1	12	12.00
		skin	1	5	6.80
	Block 1	Rear Spar	1	2.500	2.50
		Front Spar	1	3.300	3.30
		Rib	9	0.450	4.05
		Skin	1	3.400	5.10
	Block 2	Rear Spar	1	2.000	2.00
		Front Spar	1	2.500	2.50
		Rib	9	0.350	3.15
		Skin	1	2.600	4.00
	Block 3	Rear Spar	1	0.400	0.40
		Front Spar	1	0.520	0.52
		Rib	9	0.470	4.23
		Skin	1	5.200	7.80
	A c t u a t i o n	Shaft_bay	6	0.135	0.81
		Shaft_Motor	6	0.150	0.90
Shaft_Rib		18	0.051	0.92	
Harmonic Drive support		18	0.067	1.21	
Block 2		Link	9	0.103	0.93
		Crank	18	0.042	0.76
Block 1		Link	9	0.141	1.27
		Crank	18	0.100	1.80
		External_Link	9	0.290	2.61
Commercial off-the-shelf		Joint MKH 20-35-10	24	0.036	0.86
		Encoder Kubler	6	0.060	0.36
		Harmonic Drive CPL 17-100	18	0.100	1.80
		SKF 61807	18	0.029	0.52
		SKF 61903	36	0.015	0.54
		SKF 61710	36	0.035	1.26
		SKF NA 4901	18	0.028	0.50
	Pins_main	27	0.078	2.11	
KBMS 10-X04	6	2.150	12.90		
PMagnet Power-Off Brakes	6	0.350	2.10		
TOTAL ESTIMATE WEIGHT [Kg]				92.50	

Table 6.1: 3MMF final weight.

6.7 Mechanical Power

In addition to final 3MMF weight, it is interesting to give estimation about the mechanical power provided during morphing operations.

In the preliminary design phase (Sec.5.2.3), the mechanical advantages of inner mechanisms were estimated. Then, in Sec.5.2.6, the ICs tool was proved to be in quite good agreement with Nastran SOL400 (Fig.5.18c).

For this reason, the expression obtained for the MA can be used for estimation of mechanical power provided by each actuation system. During morphing TE operations, each actuation system can provide the respective active rib an output torque evaluated as follow

$$\mathcal{M}_{OUT} = M_{mot} \cdot (M.A.) \cdot F_{HD} \cdot \eta_{HD} \cdot \eta_{IM} \quad (6.7)$$

Where $M_{mot}(= 1\text{Nm})$ is the torque provided by each rotary hollow-shaft brushless motor, $F_{HD} = 120$ is the gear ratio of the Harmonic Drive (CPL 17-2A) [65], $\eta_{HD} = 0.7$ is the efficiency of the Harmonic Drive [65], and $\eta_{IM} = 0.7$ the efficiency of the inner mechanism. The output torque of each actuation system can be expressed as function of the crank position. In Fig.6.29, the total torque provided by each actuation system hosted in 3MMF block B2 is shown.

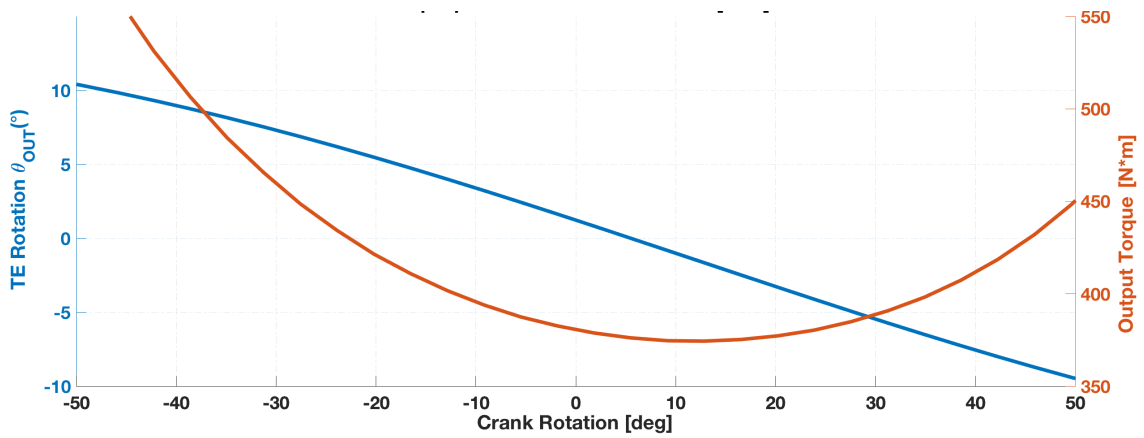


Figure 6.29: Actuating torque provided by each actuation system hosted in 3MMF block B2.

Chapter 7

Conclusions & Recommendations

The design of a Three-Modal camber Morphing Flap (3MMF) was outlined in this thesis. Starting from the bi-modal flap architecture experimentally validated by means of Ground Static Test (GST), the 3MMF was designed according to the challenges posed by real wing installation issues.

The investigation domain was the full-scale outboard flap region of a turboprop regional aircraft spanning 5.15m with a root chord equal to 0.87m and a taper ratio equal to 0.73.

The minimum design space at the tip section of the outboard flap resulted 37% smaller than the minimum room available at the tip section of the bi-modal flap. This resulted in a more challenging design effort for the new 3MMF concept.

In addition, this new concept was required to further develop and mature the integration of morphing technologies on next regional aircraft. For this reason, a complete re-design of the architecture was required with the main outcome to fulfil more demanding industrial requests:

- integration of a fairing-less deployment system;
- minimization of spare parts;
- enhancement of the overall system robustness;
- simplification of the overall flap assembly
- reduction of the installed power thanks to a lower number of actuators.

The novel multi-functional morphing flap technology was requested to improve the aerodynamic performances of the next TP90 along its entire flight mission. For this reason, this morphing flap system layout added new and more demanding functionalities.

Three different functions were enabled:

- Morphing mode 1: overall airfoil camber morphing (up to 28° equivalent rigid deflection);
- Morphing mode 2: $+10^\circ / -10^\circ$ (upwards/downwards) deflection of the flap tip segment (from the 90% to 100% of the local chord);
- Morphing mode 3: Tip twist ($\pm 5^\circ$ along the outer flap span);

In the preliminary design phase, several components of the morphing system were addressed:

- Smart rib: The core of the 3MMF layout with the capability to provide the morphing as an inner movable articulation of the flap structure.
- Multi-box arrangement: the skeleton of the 3MMF layout with the main goal to provide overall load-bearing property and host the actuation system.
- Through Shafts Actuation System: the element of the 3MMF layout which guarantees the mechanical power for transition from the baseline to target shape.

The final layout of the 3MMF resulted from the optimal integration of these components leading to:

- weight reduction of 35% compared to the bi-modal flap;
- reduction of installed power thanks to only six motors required (instead of 12 required in case of a design solution based on the bi-modal flap);
- larger morphing shapes: full-camber morphing up to 28° (instead of 14° for the bi-modal flap), $\pm 10^\circ$ flap tip deflection (instead of $\pm 8^\circ$);
- new morphing mode: $\pm 5^\circ$ tip twist along the span enabled with the Adaptive Twist composite Tab (ATT) structural concept.

Following the final assessment, the 3MMF concept was able to assure the following benefits at aircraft level:

- 1.1% fuel reduction because of reduction of aerodynamic drag obtained with a fairing-less deployment system
- 12% high-lift performance improvement (comparing take-off and landing conditions)

- 2% aerodynamic efficiency improvement in high-speed climb, and off-design cruise conditions

Based on six hollow-shaft brushless motors, the 3MMF concept answers the request of aircraft versatility providing several morphing modes to be enabled along the entire flight mission profile on the next generation regional aircraft.

Nowadays, automated manufacturing processes for composite materials (AFP and ATL) are widely employed to obtain large composite aircraft structures with the highest performance [90]. The actual application of the 3MMF technology in a new aircraft can be even more attractive if a fully-composite solution will be adopted for the structural skeleton (i.e. the multi-box arrangement) as a further development.

In such a way, final manufacturing and assembly costs will be severely reduced because of fewer parts and fasteners required. Indeed, the adoption of a fully-composite solution will be able to better answer the actual requirements of aircraft manufacturing industry where time and costs are crucial for enabling efficient in series production.

A building-block approach, as industry standard practice [91], has to be defined to prove the feasibility of a fully-composite solution. Firstly, tests on elements and subcomponents should be arranged to establish the material properties and the internal load paths on the structural behaviour. Then, the concept design should be developed considering manufacturing processes scale-up requirements. Finally, the full-scale prototype will be obtained applying design for manufacturing best practices.

Besides the choice between a fully-composite solution and a metallic one, the simultaneous need for monitoring target morphed shapes, actuation forces and flight controls require the use of a ground demonstrator for the physical integration of systems. The Iron Bird is the most suitable way to optimize and validate such systems including electromechanical components such as actuators and flight controls.

This ground demonstrator will include different morphing devices installed on a aircraft wing box as well as the basic equipment needed to carry out “hardware in the loop simulations”. Such a concept may be used to demonstrate advanced control technologies in a modular multi-level design that provides the robustness and the flexibility of a real aircraft integration.

Manufacturing, assembly and integration issues including electrical and flight control may be extensively addressed in relation to the actual configuration of the aircraft.

Such full-scale ground demonstrator is the perfect tool to confirm the characteristics of all system components or to discover an incompatibility that may require modifications during early development stages and thereby it accelerates the transition to test in a relevant environment.

The “Iron Bird” for testing morphing wing architectures will enable test engineers to evaluate the real-time capabilities of morphing devices with the purpose of:

- demonstrating maturity, reliability and integrated performance of morphing devices;
- investigating aircraft safety-related aspects by simulating system failures, such as jamming to validate fault tree analyses and hazard assessments;
- evaluate the elastic response of the device to specific loads related to simulated operative flight conditions;
- detailing cable routing and pathways;
- validating the electrical consumption of each actuation system, in stationary and dynamic conditions, and the required command to A/C surface in each test case.

“Virtute enim ipsa non tam multi praediti esse quam videri volunt.”

Laelius seu De amicitia

Marco Tullio Cicerone

“Be quick, be quiet, and be on time.”

Clarence “Kelly” Johnson

Acknowledgements

I would like to acknowledge Leonardo (Aircraft Division), CIRA (*Centro Italiano Ricerche Aerospaziali*), ONERA (*Office National d'Etudes et de Recherches Aérospatiales*), and Siemens PLM for their technical support as partners of Airgreen 2 Consortium (Clean Sky 2, REG-IADP). Special acknowledgements go to Leonardo Company (Aircraft Division) for having provided the industrial guidelines and the necessary support.

I would like to thank Prof. Francesco Marulo and Prof. Leonardo Lecce for their insightful and effective way of approaching complex engineering problems that I sincerely admired during courses in Aerospace Structures.

Special thanks to Prof. Rosario Pecora and Prof. Francesco Amoroso for their guidance and constant support and for the chance I received to broaden my knowledge.

I would like to thank Prof. Hans Peter Monner and Dr. Markus Kintscher for hosting me at the Institute of Composite Structures and Adaptive Systems (DLR e.V., Braunschweig, Germany) for a six-months research stay. This experience really enriched me from a cultural and human point of view.

Bibliography

- [1] Rudolph P.K.C, High-lift systems on commercial subsonic airliners, Technical Report, NASA/CR-4746, 1996.
- [2] Barbarino S., Bilgen O., Ajaj R.M., Friswell M.I., Inman D.J. A review of morphing aircraft, (2011) Journal of Intelligent Material Systems and Structures, 22 (9), pp. 823-877. <https://doi.org/10.1177/1045389X11414084>.
- [3] Wright O., Wright W. Flying Machine, US Patent N. 821393A, Priority Date, Mar. 23rd, 1903; Publication Date, May 22nd, 1906.
- [4] Wright O. How we invented the airplane: An Illustrated History. Dover republication (1988), New York (USA), ISBN 0-486-25662-6.
- [5] Brissenden R.F., Heath A.R., Conner D.W., Spearman M.L. (technical monitors), The Boeing Preliminary Design Department. Assessment of variable camber for application to transport aircraft. NASA Contractor Report CR-158930, National Aeronautics and Space Administration Langley Research Center, Hampton, VA, October, 1980.
- [6] Hardy R., AFTI/F-111 mission adaptive wing technology demonstration program. Proceedings of the 1983 AIAA Aircraft Prototype and Technology Demonstrator Symposium, Air Force Museum Dayton, OH, March 23-24, 1983.
- [7] Smith J. W., Lock W. P., Payne G. A. Variable-Camber Systems Integration and Operational Performance of the AFTI/F-111 Mission Adaptive Wing, NASA TM-4370, April 1992.
- [8] AFTI/F-111 Mission Adaptive Wing Briefing to Industry, U.S. Air Force Wright Aeronautical Labs., Rept. AFWAL-TR-88-3082, Wright-Patterson AFB, OH, Oct. 1988.

- [9] DeCamp R., Hardy R., and Gould D., Mission-Adaptive Wing, SAE Technical Paper 872419, 1987, <https://doi.org/10.4271/872419>.
- [10] Thornton S. V., Reduction of structural loads using maneuver load control on the Advanced Fighter Technology Integration (AFTI)/F-111 mission adaptive wing, NASA Technical Memorandum TM-4526, National Aeronautics and Space Administration, Edwards, CA, September, 1993.
- [11] Bolonkin A., Gilyard G. B., Estimated benefits of variable-geometry wing camber control for transport aircraft, NASA Technical Memorandum TM-1999-206586, National Aeronautics and Space Administration, Edwards, CA, October, 1999.
- [12] Pfeiffer N.J., and Christians J.G., Active Tailoring of Lift Distribution to Enhance Cruise Performance, NASA Technical Report, CR-213543, 2005.
- [13] Hilbig R., Koerner H., Aerodynamic Design Trends for Commercial Aircraft, NASA Technical Memorandum TM-77976, National Aeronautics and Space Administration, Washington, DC 1986 January.
- [14] Szodruch J., Hilbig R., Variable wing camber for transport aircraft, Prog. Aerosp. Sci., Vol. 25, N.3, pp. 297–328, 1988.
- [15] Sinapius M., Monner H.P., Kintscher M., Riemenschneider J., DLR's morphing wing activities within the european network, Proceedings of the 23rd International Congress of Theoretical and Applied Mechanics (ICTAM), Beijing, August 19-24, 2012, <https://doi.org/10.1016/j.piutam.2014.01.036>.
- [16] Monner H. P., Hanselka H., Breitbach E. J. (1998). Development and design of flexible Fowler flaps for an adaptive wing. Smart Structures and Materials 1998: Industrial and Commercial Applications of Smart Structures Technologies. <https://doi.org/10.1117/12.310673>.
- [17] Stanewsky E., Adaptive wing and flow control technology, Prog. Aerosp. Sci. 37 (7) (2001) 583–667.
- [18] Monner H. P., Breitbach E., Bein T., Hanselka H. (2000). Design aspects of the adaptive wing — the elastic trailing edge and the local spoiler bump. The Aeronautical Journal (1968), 104(1032), 89-95. <https://doi.org/10.1017/S0001924000017814>.

- [19] Monner H. P., Realization of an optimized wing camber by using formvariable flap structures, *Aerospace Science and Technology*, Vol. 5, No. 7, 2001, pp. 445–455. [https://doi.org/10.1016/S1270-9638\(01\)01118-X](https://doi.org/10.1016/S1270-9638(01)01118-X).
- [20] Kudva M., Scherer J., McGowan L., Overview of the DARPA/AFRL/NASA Smart Wing Program. *SPIE Proceedings*, Vol. 3674, 230, (1999).
- [21] Di Matteo N., Guo S., and Li D., Morphing Trailing Edge Flap for High Lift Wing, 52nd AIAA/ASME/ASCE/AHS/ASC Structures, Structural Dynamics and Material Conference, 4-7 April 2008, Denver, Colorado.
- [22] Wölcken P. C., Papadopoulos M. (Editors), *Smart Intelligent Aircraft Structures (SARISTU)*, Proceedings of the Final Project Conference, 2015. <https://doi.org/10.1007/978-3-319-22413-8>.
- [23] Kintscher M., Kim J., Storm S., Peter F., Assessment of the SARISTU enhanced adaptive droop nose, Proceedings of the Final Project Conference, Springer International Publishing, 2016, ISBN 978-3-319-22413-8.
- [24] Storm S., Kirn J. (2017) Towards the Industrial Application of Morphing Aircraft Wings—Development of the Actuation Kinematics of a Droop Nose. In: Araujo A., Mota Soares C. (eds) *Smart Structures and Materials. Computational Methods in Applied Sciences*, vol 43. Springer. https://doi.org/10.1007/978-3-319-44507-6_10
- [25] Wildschek A., Storm S., Herring M., Drezga D., Korian V., Roock O., Design, optimization, testing, verification and validation of the wingtip adaptive trailing edge, Proceedings of the Final Project Conference, Springer International Publishing, 2016, ISBN 978-3-319-22413-8.
- [26] Wildschek A., Prananta B., Kanakis T., Van Tongeren H., Huls R. Concurrent optimization of a feed-forward gust loads controller and minimization of wing box structural mass on an aircraft with active winglets (2015) 16th AIAA/ISSMO Multidisciplinary Analysis and Optimization Conference. <https://doi.org/10.2514/6.2015-2490>
- [27] Concilio A., Dimino I., Pecora R. An adaptive trailing edge for large commercial aircraft. (2016) ECCOMAS Congress 2016 - Proceedings of the 7th European Congress on Computational Methods in Applied Sciences and Engineering, 3, pp. 6496-6504. <https://doi.org/10.7712/100016.2272.14442>.

- [28] Pecora R. et al. Structural Design of an Adaptive Wing Trailing Edge for Large Aeroplanes. In: Wölcken P., Papadopoulos M. (eds) Smart Intelligent Aircraft Structures (SARISTU). Springer, 2016.
- [29] Dimino I., Ciminello M., Concilio A., Grati A., Schueller M., Pecora R. (2017) Control System Design for a Morphing Wing Trailing Edge. In: Araujo A., Mota Soares C. (eds) Smart Structures and Materials. Computational Methods in Applied Sciences, vol 43. Springer.
https://doi.org/10.1007/978-3-319-44507-6_9.
- [30] Dimino I., Flauto D., Diodati G., Concilio A., Pecora R. Actuation System Design for a Morphing Wing Trailing Edge. Recent Patents on Mechanical Engineering (2014) 7: 138. <https://doi.org/10.2174/2212797607666140429005538>.
- [31] Schorsch O, Luhning A, Nagel C, Pecora R, Dimino I, Polymer based morphing skin for adaptive wings. 7th ECCOMAS thematic conference on smart structures and materials, SMART 2015, Azores, Portugal, 3–6 June 2015.
- [32] Recksiek M., Advanced High Lift System Architecture with Distributed Electrical Flap Actuation, Aviation System Technology Workshop 2009, 29-30 March, Hamburg, Germany
- [33] Reckzeh D. Aerodynamic design of the high-lift-wing for a Megaliner aircraft. (2003) Aerospace Science and Technology, 7 (2), pp. 107-119.
[https://doi.org/10.1016/S1270-9638\(02\)00002-0](https://doi.org/10.1016/S1270-9638(02)00002-0).
- [34] Strüber H., The Aerodynamic Design of the A350 XWB-900 High Lift System, Proceeding of ICAS 2014, St. Petersburg, Russia, 7-12 September 2014.
- [35] Reckzeh D. Multifunctional wing moveables: Design of the A350XWB and the way to future concepts. (2014) 29th Congress of the International Council of the Aeronautical Sciences, ICAS 2014.
- [36] Arguelles P., Bischoff M., Busquin P., Drost B. A. C., Evans R., Kroll W., Lagardere J., Lina A., Lumsden J., Ranque D., Rasmussen P., Reutinger P., Robins R., Terho H., Wittlov A., *European aeronautics: a Vision for 2020 - Meeting society's needs and winning global leadership*, European Commission for Research, 2001.
- [37] High Level Group on Aviation Research Rept. *Flightpath 2050: Europe's Vision for Aviation*, EUR-098-EN, European Commission, Belgium, 2011.

- [38] Clean Sky Joint Undertaking (CSJU) website.
Available at: <http://www.cleansky.eu>
- [39] BLADE Project, Clean Sky (CS) Programme SFWA-ITD. Available at: https://www.airbus.com/newsroom/press-releases/en/2017/09/airbus_-_blade_-_laminar-flow-wing-demonstrator-makes-first-flight.html
- [40] Clean Sky 1(CS1) Green Regional Aircraft (GRA) ITD website.
Available at: <http://www.cleansky.eu/green-regional-aircraft-gra>
- [41] EASA, CS-25, *Certification specifications and acceptable means of compliance for large aeroplanes*, Amendment 11, July 2011.
- [42] Pecora R., Amoroso F., Amendola F. and Concilio A., Validation of a smart structural concept for wing-flap camber morphing, *Smart Structures and Systems*, vol. 14, no. 4, pp. 659–678, 2014.
- [43] Mingione G., Preliminary Design of Wing Trailing Edge Morphing Architectures, JTI-GRA deliverable no. GRA2.2.1- TN-CIRAPlus-TECH-210105A, (confidential).
- [44] Pecora R., Barbarino S., Concilio A., Lecce L., and Russo S., Design and Functional Test of a Morphing High-Lift Device for a Regional Aircraft, *Journal of Intelligent Material Systems and Structures*, Vol. 22, No. 10, 2011, pp. 1005–1023.
- [45] Van Dam C. P., Shaw S. G., Vander Kam J. C., Rudolph P. K. C., & Kinney, D. (1999). Aero-mechanical design of high-lift systems. *Aircraft Engineering and Aerospace Technology*, 71(5), 436–443. <https://doi.org/10.1108/00022669910296873>.
- [46] Dimino I., Ciminello M., Concilio A., Pecora R., Amoroso F., Magnifico M., Schueller M., Grati A., Volovick A., Zivan L. Distributed actuation and control of a morphing wing trailing edge, *Smart Intelligent Aircraft Structures (SARISTU)—Proceedings of the Final Project Conference*, Springer International Publishing, Cham, Switzerland, 2016, ISBN 978-3-319-22412-1.
- [47] Riva R. Synthesis of Stephenson’s six-bar linkages by an interactive technique. *Meccanica* (1981) 16: 157. <https://doi.org/10.1007/BF02128444>.
- [48] Pecora R., Amoroso F., Arena M., Noviello M.C., Rea F., Experimental validation of a true-scale morphing flap for large civil aircraft applications, *Proceedings of SPIE - The International Society for Optical Engineering*, 10166, 2017.
<https://doi.org/10.1117/12.2259878>

- [49] Rea F., Arena M., Noviello M.C., Pecora R., Amoroso F., Preliminary failure analysis of an innovative morphing flap tailored for large civil aircraft applications, Proceedings of 7th International Conference on Mechanical and Aerospace Engineering, 2016, <https://doi.org/10.1109/ICMAE.2016.7549598>.
- [50] Noviello M.C., Rea F., Arena M., Pecora R., Amoroso F., Actuation and control of a novel wing flap architecture with bi-modal camber morphing capabilities, Proceedings of 7th International Conference on Mechanical and Aerospace Engineering, 2016, <https://doi.org/10.1109/ICMAE.2016.7549578>
- [51] Bowman J., Sanders B., Weisshaar T. Evaluating the Impact of Morphing Technologies on Aircraft Performance, 43rd AIAA/ASME/ASCE/AHS/ASC Structures, Structural Dynamics, and Materials Conference, Structures, Structural Dynamics, and Materials and Co-located Conferences. <https://doi.org/10.2514/6.2002-1631>
- [52] Prock B., Weisshaar T., Crossley W. Morphing Airfoil Shape Change Optimization With Minimum Actuator Energy As An Objective, 9th AIAA/ISSMO Symposium on Multidisciplinary Analysis and Optimization, Multidisciplinary Analysis Optimization Conferences. <https://doi.org/10.2514/6.2002-5401>.
- [53] Pecora R., Ameduri S., Rea F. (2018). Active Metal Structures. In Morphing Wing Technologies: Large Commercial Aircraft and Civil Helicopters (pp. 279–320). Elsevier Inc. <https://doi.org/10.1016/B978-0-08-100964-2.00010-1>.
- [54] Moorhouse D., Sanders B., Von Spakovsky M., Butt J. Benefits and design challenges of adaptive structures for morphing aircraft, (2006) Aeronautical Journal, 110 (1105), pp. 157-162. <https://doi.org/10.1017/S0001924000001135>.
- [55] Joo J.J., Sanders B., Washington G. Energy based efficiency of adaptive structure systems (2006) Smart Materials and Structures, 15 (1), pp. 171-181. <https://doi.org/10.1088/0964-1726/15/1/046>
- [56] Dimino I., Diodati G., Concilio A., Volovick A., Zivan L., Distributed electromechanical actuation system design for a morphing trailing edge wing, Proc. SPIE 9801, Industrial and Commercial Applications of Smart Structures Technologies 2016, 980108 (16 April 2016). <https://doi.org/10.1117/12.2219223>.
- [57] Raven, F.H. Velocity and Acceleration Analysis of Plane and Space Mechanisms by Means of Independent-Position Equation. Trans. of the ASME. Journal of Applied Mechanics, Vol. 25, 1958, pp. 1-6.

- [58] Timoshenko S.P., Strength of Materials: Advanced Theory and Problems, Part II, Second Edition, Van Nostrand Company, 1940.
- [59] Hartenberg R. S., Denavit J., Kinematic Synthesis of Linkages. McGraw-Hill, New York (1964).
- [60] Norton R.L. Design of Machinery: an introduction to the synthesis and analysis of the mechanism and machines; McGraw-Hill, Third Edition, 2004.
- [61] Erdmann A.G., Sandor G.N., Kota S. Mechanism Design: Analysis and Synthesis. Prentice Hall, New Jersey, Fourth Edition, 2001, ISBN 0-13-040872-7 (v. I).
- [62] Berkof R.S. The input torque in linkages. (1979) Mechanism and Machine Theory, 14 (1), pp. 61-73. [https://doi.org/10.1016/0094-114X\(79\)90042-9](https://doi.org/10.1016/0094-114X(79)90042-9).
- [63] Bruhn E.F., Analysis and design of flight vehicle structures, chapter A19, Tri-State Offset Company, Cincinnati, OH, 1969.
- [64] Bruhn E.F., Analysis and design of flight vehicle structures, chapter D1, Tri-State Offset Company, Cincinnati, OH, 1969.
- [65] HarmonicDrive AG. CPL-2A Component Sets. https://harmonicdrive.de/fileadmin/user_upload/2014_12_ED_1019655_CPL_2A.pdf (visited on 28/10/2018).
- [66] Kollmorgen KBM Series Brushless Motors. Selection Guide. <https://www.kollmorgen.com/en-us/products/catalogs/kollmorgen-kbm-series-brushless-motors-selection-guide> (visited on 28/10/2018).
- [67] Datasheet Power-off brakes Sepac PMB Series Model 197. <https://sepac.com/wp-content/uploads/protected/SEPAC-Data-Sheet-PMB-Brake.pdf>
- [68] HexPly913 from Hexcel composites. https://www.hexcel.com/user_area/content_media/raw/HexPly_913_us_DataSheet.pdf (visited on 28/10/2018).
- [69] Bredt R. Kritische Bemerkungen zur Drehungselastizitat, Zeitschrift des Vereines deutscher Ingenieure, 40(29): Pages 813–817, 1896.
- [70] Raither W., Heymanns M., Bergamini A., Ermanni P. Morphing wing structure with controllable twist based on adaptive bending-twist coupling (2013) Smart Materials and Structures, 22 (6), art. no. 065017. <https://doi.org/10.1088/0964-1726/22/6/065017>.

- [71] Vlasov V.Z. Thin-Walled Elastic Beams. 2nd Edition, Israel Program for Scientific Translation, Israel, 1961.
- [72] Kollbrunner C.F., Basler K. Torsion in Structures: An Engineering Approach, Springer-Verlag, Berlin, 1969.
- [73] Rea F., Amoroso F., Pecora R., Noviello M., Arena M. Structural Design of a Multifunctional Morphing Fowler Flap for a Twin-Prop Regional Aircraft. ASME. Smart Materials, Adaptive Structures and Intelligent Systems, Volume 1, (SMASIS 2018): V001T04A003. <https://doi.org/10.1115/SMASIS2018-7937>.
- [74] Rea F., Amoroso F., Pecora R., Kintscher M. Design of an Adaptive Twist Trailing Edge for Large Commercial Aircraft Applications. ASME. Smart Materials, Adaptive Structures and Intelligent Systems, Volume 1, (SMASIS 2018): V001T04A004. <https://doi.org/10.1115/SMASIS2018-7939>.
- [75] Forte M., Piot E., Perraud J., Hue D., Duchemin J., et al.. Research activities of ONERA on laminar airfoils in the framework of JTI Clean Sky SFWA-ITD: transition prediction. Greener Aviation 2016, Oct 2016, BRUXELLES, Belgium. <https://hal.archives-ouvertes.fr/hal-01411673>
- [76] Frédéric Moens (ONERA), Design of Aerodynamic Shapes and Loads for Wing Advanced High-Lift device (Leading-edge and Trailing-edge), Deliverable Nr. O2.1.3-07 (Confidential).
- [77] Rea F., Amoroso F., Pecora R., Moens F. Exploitation of a Multifunctional Twistable Wing Trailing-Edge for Performance Improvement of a Turboprop 90-Seats Regional Aircraft. Aerospace. 2018; 5(4):122. <https://doi.org/10.3390/aerospace5040122>
- [78] Cambier L., Heib S., Plot S. The Onera esLA CFD software: input from research and feedback from industry. Mechanics & Industry, Volume 12 (No3), pp. 159-174, 2013.
- [79] Spalart P.R. Strategies for Turbulence Modelling and Simulation. International Journal of Heat and Fluid Flow, Volume 21, pp 252-263, 2000.
- [80] Houdeville R., Bardoux P., Moreux V. 3D Boundary Layer Computations on Wing-Pylon-Nacelle Configuration. Workshop on Aspects of Airframe Engine Integration for transport Aircraft, March 1996.

- [81] Casalis G. Arnal D. ELFIN II, Sub-task 2.3: Data Base Method. Development and Validation of the Simplified Method for Pure Crossflow Instability at Low Speed, ELFIN Technical Report No 145, 1996.
- [82] Morphing Wing Technologies – Large Commercial Aircraft and Civil Helicopters. [Chapter 5 – pages 148- 154]. Edited by A. Concilio, I. Dimino, L. Lecce, R. Peccora. Elsevier, 2017, ISBN: 9780081009642.
- [83] Carl J., Muller-Hoeppe D., Meadows M. Comparison of tetrahedral and brick elements for linear elastic analysis, Term Project AFEM Spring 2006, ASEN 5367, Department of Aerospace Engineering Sciences, University of Colorado, Boulder, .
- [84] Wang E., Nelson T., Rauch R. Back to elements—tetrahedra vs. hexahedra, ANSYS 2004 International Conference, Pittsburgh, PA, May 24th–26th, 2004.
- [85] Pecora R., Amoroso F., Noviello M.C., Dimino I., Concilio A. Aeroelastic stability analysis of a large civil aircraft equipped with morphing winglets and adaptive flap tabs, Proc. SPIE 10595, Active and Passive Smart Structures and Integrated Systems XII, 105950L (15 March 2018); <https://doi.org/10.1117/12.2300173>.
- [86] Evonik Corporation Rohacell® 51 FX Polymethacrylimide (PMI) Rigid Foam Plastic. <https://mychem.ir/uploads/tds/16728.pdf>
- [87] Kintscher M., Wiedemann M., Monner H.P., Heintze O., Kuhn T., Design of a smart leading-edge device for low speed wind tunnel tests in the European project SADE, International Journal of Structural Integrity, Vol 2, 2011.
- [88] MSC Software (2012), *MSC Nastran 2012 - Quick Reference Guide*.
- [89] MSC Software (2012), *MSC Nastran 2012 - Linear Static Analysis User's Guide*.
- [90] McIlhagger A., Archer E., McIlhagger R. (2015). Manufacturing processes for composite materials and components for aerospace applications. Polymer Composites in the Aerospace Industry, 53–75.
<https://doi.org/10.1016/b978-0-85709-523-7.00003-7>
- [91] Harris C., Starnes J.H., Shuart M.J. Design and Manufacturing of Aerospace Composite Structures, State-of-the-Art Assessment, Journal of Aircraft, Vol. 39, No. 4 (2002), pp. 545-560. <https://doi.org/10.2514/2.2992>